A reconfigurable, LTCC-based, ultra-wideband periodic leaky-wave antenna with circular polarization at 60 GHz

by

Mahdi EMAMI

THESIS PRESENTED TO ÉCOLE DE TECHNOLOGIE SUPÉRIEURE
IN PARTIAL FULFILLMENT OF A MASTER'S DEGREE
WITH THESIS IN ELECTRICAL ENGINEERING
M.A.Sc.

MONTREAL, AUGUST 13th, 2021

ÉCOLE DE TECHNOLOGIE SUPÉRIEURE
UNIVERSITÉ DU QUÉBEC

BOARD OF EXAMINERS

THIS THESIS HAS BEEN EVALUATED

BY THE FOLLOWING BOARD OF EXAMINERS

Mr. Dominic Deslandes, Memorandum Supervisor
Department of Electrical Engineering, École de technologie supérieure

Mr. Frédéric Nabki, President of the Board of Examiners
Department of Electrical Engineering, École de technologie supérieure

Mr. François Blanchard, Member of the jury
Department of Electrical Engineering, École de technologie supérieure

THIS THESIS WAS PRESENTED AND DEFENDED

IN THE PRESENCE OF A BOARD OF EXAMINERS AND THE PUBLIC

ON AUGUST 11th, 2021

AT ÉCOLE DE TECHNOLOGIE SUPÉRIEURE

ACKNOWLEDGEMENTS

I would like to express my sincere gratitude to my advisor Prof. Dominic Deslandes for his continuous and earnest support that made my Master experience fruitful and practical. I deeply appreciate his great positive energy, patience, motivation, enthusiasm, and immense knowledge which guided me throughout my study and research. The achievements of this research project would not be possible without his guidance and heartwarming encouragement.

I would also like to thank all my colleagues as well as the support staff of the LACIME research center. My special thanks go to Normand Gravel from LTCC@ÉTS, who performed the whole fabrications' process and also shared his invaluable experiences and expertise with me while working in the laboratory. I express my profound appreciation to the technicians in Poly-Grames laboratories at École Polytechnique de Montréal, Jules Gautier and Maxime Thibault, who performed the radiation pattern measurements of the antennas. Moreover, I would like to acknowledge CMC Microsystems for the provision of CAD tools that facilitated this research.

My heartfelt thanks go to all of my family and friends who encourage me and support me throughout my whole life to follw my dreams; especially, my parent that their unconditional love always get me through difficult times. I really appreciate all you have done for me.

Finally, I would like to thank everyone who contributed to this thesis. Especially, Mohammad Hassan Rahmani, who was a great help for me since the beginning of this project and his doctoral thesis was the main inspiration for this research.

Une antenne périodique à ondes de fuite, ultra-large bande, reconfigurable, à polarisation circulaire à 60 GHz, fabriquée en LTCC

Mahdi EMAMI

RÉSUMÉ

Au cours de la dernière décennie, la demande pour des débits de données plus élevés dans les applications de communication sans fil à courte portée a rapidement augmenté. C'est ainsi que les débits binaires de l'ordre de plusieurs Gb/s sont très attrayants, en particulier lors de l'utilisation de la bande sans licence de 7 GHz autour du spectre de 60 GHz, qui est connue sous le nom de « Wireless Gigabit Alliance » (WiGig Alliance). Le Wi-Fi traditionnel ne permet plus d'offrir des performances multi-gigabit, une latence quasi nulle et de faibles interférences aux applications intérieures et extérieures à courte portée. Les marchés potentiels pour les applications WiGig sont la VR/RA (réalité virtuelle et réalité augmentée), le streaming de téléphone intelligent vers un télévision à haute définition HD, la synchronisation mobile à l'aide du cloud, les points d'accès publics ultrarapides et le haut débit fixe sans fil 5G.

Les antennes en boîtier (AiP), en tant que plateforme d'antenne à faible coût, compactes et à haute performance, sont une solution appropriée pour les communications en ondes millimétriques. Cependant, en raison du niveau élevé d'atténuation dans cette gamme de fréquences, un système d'antenne à bande ultra-large efficace, avec un gain de rayonnement élevé et prenant en charge la polarisation circulaire, est nécessaire afin de surmonter la portée de connexion limitée. De plus, une antenne à faisceau étroit doit être équipée d'une capacité d'orientation du faisceau en deux dimensions pour couvrir la zone maximale de la pièce. Malheureusement, les systèmes d'antennes existants qui sont développés pour la bande 60GHz n'offrent pas toutes ces caractéristiques à la fois dans un seul boîtier. D'autres solutions ont été développées, toutefois ces conceptions incluent des dispositifs actifs tels qu'une plate-forme motorisée et des déphaseurs actifs qui rendent le système total encombrant et coûteux.

Dans ce projet de recherche, nous introduisons une antenne périodique à ondes de fuite (PLWA) efficace avec un diagramme de rayonnement hautement directif et reconfigurable dans deux directions (orientation du faisceau 2-D). Cette antenne a une structure très simple et occupe un espace très petit, elle est conçue pour la technologie LTCC, ce qui la rend facile à fabriquer pour les applications AiP pour les ondes millimétriques et permet une production de masse à moindre coût pour un produit commercialement. De plus, il supporte une polarisation circulaire. Nous présentons ici un modèle empirique pour l'antenne proposée, le processus de conception et d'optimisation, les défis de la fabrication sur le substrat LTCC et les considérations pour les mesures. Nous proposons un réseau phasé de structures PLWA alimenté par une lentille de Rotman avec un angle de balayage du faisceau de $-43°$ à $+34°$ sur le plan Y-Z et de $-31°$ à $+28°$ sur le plan X-Z dans la gamme de fréquences de 50GHz à 70GHz. La structure complète fabriquée sur le substrat Dupont 9K7 LTCC ne comprend que des composants microbandes passifs et a une empreinte de $15\,mm \times 38\,mm$. La largeur de bande d'adaptation d'un seul PLWA optimisé est de 29GHz de 43GHz à 72GHz (largeur de bande d'impédance

fractionnelle de 48.3%) et son efficacité moyenne et son gain maximal réalisé sur cette gamme de fréquences sont respectivement de 87.42% et 11.25 *dBi*. De plus, les valeurs du rapport axial et du SLL sont maintenues en dessous de 3 dB et -10 dB respectivement.

Mots-clés: antenne reconfigurable, antenne microruban sur substrat LTCC, antennes périodique à ondes de fuite, antenne dans en boîtier, communication à ondes millimétriques à ultra-large bande, polarisation circulaire.

A reconfigurable, LTCC-based, ultra-wideband periodic leaky-wave antenna with circular polarization at 60 GHz

Mahdi EMAMI

ABSTRACT

Over the last decade, demand for higher data rates in the short-range wireless communication applications has rapidly grown. Bit-rates in the order of multi-Gb/s are very appealing these days; especially, utilizing the 7 GHz unlicensed bandwidth around the 60 GHz spectrum which is also known as the Wireless Gigabit Alliance (WiGig). Bringing multi-gigabit performance, near-zero latency and low interference to short-range indoor and outdoor applications, is not possible with traditional Wi-Fi anymore. The potential markets for the WiGig applications are VR/AR (Virtual Reality and Augmented Reality), smartphone-to-HDTV streaming, mobile cloud sync, super-fast public hot spots and 5G fixed wireless broadband.

Antenna in Package (AiP) as a low-cost, low-profile and high performance antenna platform, has been proved to be a suitable solution for the mm-Wave communications. However, due to high attenuation level at this frequency range, an efficient, ultra-wideband antenna system with high radiation gain that supports circular polarization seems inevitable to overcome the limited connection range. Moreover, a narrow beam antenna must be equipped with 2-D beam steering capability to cover the maximum area of the room. Unfortunately, the existing antenna systems that are developed for 60 GHz band will not offer all these features at once in a single package. Other solutions have been developed, however, such designs include active devices such as motorized platform and active phase shifters that make the total system bulky and expensive.

In this research project, we introduce an efficient periodic leaky-wave antenna (PLWA) with a high directive, reconfigurable radiation pattern in two directions. This antenna has a very simple and small-footprint structure, designed for the LTCC technology, which makes it easy to fabricate for the mm-Wave AiP applications and allows the budget-efficient repeatability of the mass production for a commercially suitable product. Moreover, it supports the circular polarization. Here, we will present an empirical model for the proposed antenna, the design and optimization process, the fabrication's challenges on the LTCC substrate and the considerations for the measurements. We propose a phased-array of PLWAs structure fed by a Rotman lens with the beam scanning angle of $-43°$ to $+34°$ on the Y-Z plane and $-31°$ to $+28°$ on the X-Z plane for the frequency range of 50 GHz to 70 GHz. The complete structure fabricated on the Dupont 9K7 LTCC substrate includes only passive microstrip components and has a footprint of $15\,mm \times 38\,mm$. The matching bandwidth of a single optimized PLWA is 29 GHz from 43 GHz to 72 GHz (fractional impedance bandwidth of 48.3%) and its average efficiency and peak realized gain over this frequency range are 87.42% and 11.25 *dBi* respectively. Also, the values of Axial Ratio and SLL are kept under 3 dB and -10 dB respectively.

Keywords: reconfigurable antenna, LTCC substrate microstrip antenna, periodic leaky-wave antennas, antenna in package, ultra-wideband mm-Wave communication, circular polarization.

TABLE OF CONTENTS

Page

LIST OF TABLES

LIST OF FIGURES

LIST OF ABREVIATIONS

2D	Two Dimensions
3D	Three Dimensions
AiP	Antenna in Package
AoC	Antenna on Chip
AR	Axial Ratio
BFN	Beam Forming Network
CRLH	Composite Right/Left Hand
CP	Circular Polarization
EMI	Electromagnetic Interference
FEM	Finite Element Method
Gbps	Giga bits per second
GHz	Giga Hertz
HDTV	High Definition Television
UHDTV	Ultra-High Definition Television
HFSS	High Frequency Structural Simulator
HTCC	High Temperature Co-Fired Ceramic
LCP	Liquid Crystal Polymers
LHCP	Left Handed Circular Polarization
LTCC	Low Temperature Co-Fired Ceramic

MTM	Microstrip-to-Microstrip
MTS	Microstrip to Strip-line
OSB	Open Stop Band
PAN	Personal Are Networks
PCB	Printed Circuit Board
PNA	Programmable Network Analyzer
PLWA	Periodic Leaky-Wave Antennas
PSO	Particle Swarm Optimization
RFIC	Radio Frequency Integrated Circuit
RHCP	Right Handed Circular Polarization
RL	Rotman Lens
SFP	Series Fed Patch Antenna
SIW	Substrate Integrated Waveguide
SiP	System in Package
SoP	System on Package
SLL	Side Lobe Level
SNR	Signal to Noise Ratio
TEN	Transverse Equivalent Network
WiFi	Wireless Fidelity
WiGig	Wireless Gigabit
WPAN	Wireless Personal Area Networks

LISTE OF SYMBOLS AND UNITS OF MEASUREMENTS

BW	Beamwidth
dB	Decibels
dBi	Decibels relative to an isotropic radiator
GHz	Giga Hertz
Ω	Impedance
θ_m	Angle of the maximum beam
n	Space harmonic number
β	Phase Constant
$\beta-1$	Phase constant of (n = -1) Space harmonic
$\beta-2$	Phase constant of (n = -2) Space harmonic
βn	Phase constant of an infinite number of harmonics
α	Attenuation constant
$\alpha(z)$	Attenuation constant along the antenna length
γ	Complex propagation constant
k_0	Free space wave number
λ_0	Free space wavelength
λ_g	Guided wavelength
$A(z)$	Aperture illumination along the antenna axis
e_r	Radiation efficiency

ε_r	Relative permittivity
μ_r	Relative permeability
μ_0	Free space permeability
A	Transmission parameter (ABCD matrix)
D	Transmission parameter (ABCD matrix)
Z_0	Characteristic impedance
Z_{rad}	Radiating edge impedance
Z_p	Transverse network characteristic impedance
Z_{via}	Equivalent impedance of vias
k_x	Transverse network propagation constant
k_y	Propagation constant in the propagation direction
Γ_{in}	Reflection coefficient of the transverse network
X_b	Series capacitance
X_a	Parallel inductance
χ	Kuester method parameter
ω	Angular frequency
η_0	Free space impedance
Z_{in}	Input impedance of the unit-cell
Z_1	Characteristic impedance of the high impedance line
Z_2	Characteristic impedance of the low impedance line

$Z_{a,b,c}$	Impedance parameter of the T network
$Z_{11,12,21,22}$	Impedance parameters of the unit-cell
β_{lw}	Phase constant of the line with vias
θ	Azimuth angle
ϕ	X-Y plane angle
$E(\theta)$	Radiation pattern of the series fed antenna array
$EF(\theta)$	Element pattern of the series fed antenna array
P_m	Total length of each unit-cell for m variation
Q	Quality factor
P	Total length of the unit-cell
L_1	Length of the lower impedance part of the unit-cell
L_2	Length of the higher impedance part of the unit-cell
W_1	Width of the lower impedance part of the unit-cell
W_2	Width of the higher impedance part of the unit-cell
d	Diameter of the shorting via
s	Distance of the vias' centers from the edge of the unit-cell
c	Distance between centers of adjacent vias in the unit-cell
h	Height of the dielectric
t	Metal thickness printed on the dielectric
L_t	Total length of the PLWA

R	Radius of the Rotman lens
F	Upper focal length of the Rotman lens
G	Central focal length of the Rotman lens
W	Length of the output transmission line from port's arc
W_0	Minimum length of the output transmission line from port's arc
N	Array elements position of the Rotman lens
o	Rotman lens center
α	Off-center focal angle of the Rotman lens
β	Focal Ratio of the Rotman lens: G/F
θ	Scan angle of the Rotman lens
$AF(\theta)$	Array factor of the Rotman lens
d	Array elements distance
S_{mn}	S-parameter of the port number n to m
εeff	Effective microstrip permittivity
IL	Insertion loss
RL	Return loss

INTRODUCTION

These days, the number of smart electronic devices around us are increasing exponentially. Each device requires the data exchange with other devices (for example within an IoT network). Besides, the size of data for transferring has also grown with the popularity of the applications like uncompressed, high-quality images, musics and videos streaming. Therefore, the necessity of the higher data transfer rates can not be avoided. The maximum data rates supported by the existing Wi-Fi technologies (IEEE 802.11a/b/g/n) are between 54 and 300 Mbps at 2.4 and 5.2 GHz bands. Fortunately, the new unlicensed 60GHz protocol of 5G technology (WiGig), with a higher carrier frequency, offers preferable bit-rates of up to 7Gbps. Another newly developed standard, named 802.11ax, provides wide bandwidth. It is marketed as Wi-Fi 6 (2.4 and 5GHz) and Wi-Fi 6E (6 GHz) and operates in license-exempt bands between 1 and 7.125 GHz.

Due to the excessive growth of wireless applications, carriers and the need for wider bandwidth, the migration to the higher frequency bands in the near future is inevitable. The availability of an unlicensed spectrum around 60GHz has attracted the attention of many researchers recently (Hansen, 2011). The dedicated bandwidth around the 60GHz frequency is about 7GHz with a carrier ranging from 57GHz to 64GHz (for U.S. and Canada). This compares very well with the 83.5MHz bandwidth of Bluetooth at 2.4GHz band and moreover, enables the wider channel support and faster data rates for the multimedia applications.

Despite its wide bandwidth, the only drawback of the telecommunication at 60GHz band is the high attenuation level in the wave propagation. Due to high value of the propagation loss at these frequencies, the transmitted wave cannot pass through the physical objects which would limit the communication range to a small room or an office (about 10 meters range). However, it has been suggested to take advantage of an antenna system with a more directive radiation beam pattern along with a suitable beamforming technique in order to overcome this challenge (Kai Chang *et al.*, 2002). Moreover, the mechanical solutions exist to orient the antenna on the

proper direction in order to mitigate this issue; however, they are mostly bulky and expensive solutions which normally need to include the design of motorized parts.

Motivation

Because, in a typical communication system, the transceiver circuit and the antenna usually are designed and fabricated in two separate procedures, there will be some special considerations that should be taken into account. The interconnection system, the matching circuit and the antenna coupling effect on the rest of elements are some examples of the important aspect of the design which need a careful attention and any failure to do so will lead to a reduction in the overall performance of the system. There is no need to remind that, normally, such a complex and complicated system could be really bulky and expensive.

Using the Antenna in Package (AiP) techniques in the mm-Wave applications like WiGig, we could preserve a lot of space and the costs, while maintaining high performance. A multi-layer system, containing all the essential elements of the transmission and reception along with the antenna in one package would be a compact and low-cost design which its performance could be maximized by taking advantage of a low loss inter-layer connection circuit. Moreover, the antenna coupling effect on the other elements could be considered and minimized during the optimization procedure. Besides, the mass production of such a communication circuit will be fast and cheap, especially when all the antenna system is designed using the passive elements. Recently, one of the main interesting research topics on the 60GHz telecommunication is an adaptive directional antenna with the capability to change its radiation pattern direction in order to adapt to a new configuration of its working environment.

Problems and challenges statement

Because of significant level of the attenuation at 60GHz band duo to the electromagnetic waves' interaction with oxygen molecules in the atmosphere, a highly directive and efficient antenna

is the most crucial requirement for any short-range WiGig application in order to have a potent and continuous communication. This implies, the narrow-beam antenna must attain the beam-forming capability in two perpendicular directions (2-D beam scanning) to cover the maximum area of the room. Furthermore, this adaptive and directive antenna should be an ultra-wideband, operating throughout the entire dedicated bandwidth and even more to have a margin of safety.

Beside being ultra-wideband and having a reconfigurable radiation pattern, side lob level (SLL) must be kept as low as possible while the efficiency set to the highest feasible value. Circular polarization is highly recommended to support any devices' orientation relative to each other in the communication. The circular polarization of an electromagnetic wave is a polarization state in which, at each point, the electromagnetic field of the wave has a constant magnitude and is rotating at a constant rate in a plane perpendicular to the direction of the wave. This will require an axial ratio (AR) of less than 3dB. The Axial Ratio of an antenna is defined as the ratio between the major and minor axis of a circularly polarized antenna pattern. If an antenna has perfect circular polarization then this ratio would be 1 (0 dB). The size, cost and complexity of the structure are also important issues that need to be investigated and addressed. Moreover, the fabrication at mm-Wave frequencies on LTCC substrate and the packaging (AiP) are the other challenges in design procedure of an antenna for the WiGig application.

The existing beamforming structures proposed for 60GHz communication, to best knowledge of the author, did not cover all these issues at once. Some solutions are just linearly polarized antennas with beam scanning in one direction (Murano *et al.*, 2017; Tekkouk *et al.*, 2017). Some others are low efficiency structures, using the digital phase shifters in their beamforming networks which leads to lack of continuous beam steering capability, limited bandwidth, and an increase in the cost and power consumption of the whole system (Ding *et al.*, 2014; Nikfalazar *et al.*, 2017; Townley *et al.*, 2017). There are structures with 2-D beam scanning capability but their scanning range and bandwidth both are very limited (Moulder *et al.*, 2010).

As mentioned earlier, the performance and the level of integrity of whole antenna system could be extremely improved using a 2-D beamformer with all passive components, while keeping the costs minimum. However, the existing structures mostly have some issues regarding to the large dimensions, limited bandwidth and scanning range, costly implementation techniques, and lack of circular polarization. Another suggested solution for reducing the size of structure is to take advantage of the multi-layer design configuration. The loss level and dimension of the interconnections between the layers is the most important challenges for these structures.

Objectives and goals

Based on aforementioned issues and challenges, this research project is focused on the study, design, simulation, and fabrication of a ultra-wideband reconfigurable directive antenna using all passive components in order to have a seamless 2-D radiation beam scanning over a wide scanning range. This structure will be really low-profile, low-cost, high efficient and also have a radiation pattern with great radiation gain, low SLL and support circular polarization.

The WiGig unlicensed 60GHz frequency band has almost 7GHz bandwidth. The beamforming network and antenna system must be designed so that to operate in a wide bandwidth without any stop-band. Moreover, the 2-D beam scanning angle of the system should be wide enough to cover the maximum space of the radiation sphere. Besides, it have to realize the maximum possible radiation gain to overcome the high attenuation in these frequencies while maintaining its high efficiency (more than 80 percent) and low SLL value (below -10 dB).

The size, costs and simplicity of the structure are other objectives that we are looking for. To integrate the proposed antenna with the transceiver and other necessary circuits in one package, the structure size must be as small as possible. This is achievable by all passive components, multi-layer structure that is fabricated on a LTCC substrate. This proposed structure also is extremely low cost and has a simple structure to be easily manufactured in mass production.

Another favorite objective in the peer to peer communications is to have a circular polarization. By using CP, the sender and receiver devices could have a powerful data communication at any orientation relative to each other and there will be no need to realignment. A high gain antenna supporting CP and beamforming capability, establishes a potent communication link with other devices anywhere within the room which makes it the perfect candidate for a WiGig wireless system, allowing multiple devices connectivity and high data exchange rate.

The summary of main objectives for this research project is as follows:

- Study and review the current developments in AiPs with radiation beam scanning capability.
- Propose a solution for the bandwidth and scanning range limitation problems related to the current beamforming networks.
- Design, fabrication, and modeling of a new type of circularly polarized scanning antenna operating at 60GHz with wide scanning angle and large impedance bandwidth.
- Investigate and suggest a method to reduce the SLL level and axial ratio value in order to improve the antenna's performance.
- Design and fabrication of a compact, low-cost antenna with simple structure.
- Design and simulation of a passive beamformer network for the frequency band of 60GHz.
- Design, simulation, optimization, fabrication, and measurement of a LTCC based 2-D beam scanning antenna system, operating on the 60GHz band (WiGig applications), containing all passive elements, with a wide scanning range and high radiation gain and efficiency.

Methodology

To realize a reconfigurable antenna with 2-D scanning capability, we propose a phased-array of the periodic leaky-wave antennas (PLWA). A PLWA, which is designed to be very directive,

is able to steer its radiation pattern seamlessly from backward to forward quadrant including the broadside by changing its input frequency (Jackson & Oliner, 2008). This unique feature provides the beamforming in first direction (direction of the waves propagation in antenna). A phased-array of the proposed PLWA, which is properly designed and placed next to each other, creates a suitable radiation aperture that makes the beam scanning in the second direction (perpendicular to the direction of waves propagation) possible (Pozar, 2011).

The main challenges in design of a leaky-wave antenna are its limited impedance bandwidth (which affects the scanning range), the existence of open-stopband (OSB) in the broadside radiation and its high scanning sensitivity to the input frequency (Jackson & Oliner, 2008; Williams *et al.*, 2013). We will demonstrate later in chapter 3 that the open-stopband could be suppressed around the broadside region by matching the input impedance of unit-cell (UC) to the characteristic impedance of transmission line. A wider input impedance matching of the unit-cell leads to a larger impedance bandwidth for the periodic leaky-wave antenna (which is technically a linear series fed array of the unit-cells). We can actually realize an ultra-wideband PLWA through a proper optimization-matching procedure of the unit-cell (Rahmani, 2017).

The scanning sensitivity of a PLWA to the input frequency has a positive relationship with the relative permittivity of the substrate. A higher value of ε_r increases the scanning sensitivity to input frequency, that leads to a wider scanning angle over the designated bandwidth. However, in a PLWA only one space harmonic must radiate among the infinite number (Jackson & Oliner, 2008). Hence, the scanning sensitivity can be adjusted for the desired application by choosing a suitable value for the dielectric constant of substrate, considering the requirement that only one space harmonic must exist inside the radiation region (Rahmani, 2017).

Design and fabrication of a compact and low-cost antenna system with a simple structure, high radiation gain and efficiency, circular polarization and reduced SLL is the main objective of this research project. All these features will be achieved by proposing a PLWA structure composed

of a cascade of a few optimized unit-cells with a very simple geometry. As a matter of fact, the simplicity of its structure makes it really tolerant to the fabrication's inaccuracies which is very important for fabrications at high frequencies. Moreover, fabricating on the LTCC substrate and using only passive elements in the design, makes the whole system very compact and low-cost. On the other hand, the linear series-array structure of the antenna increases the radiation gain and efficiency of the final system that will lead to a larger communication range.

A tapering function could be applied to the antenna structure along the direction of propagation to shape the radiation aperture and control its SLL (Rahmani, 2017), but as we will present later in this thesis, it won't be necessary and also is not practical in the mm-Wave fabrications. In fact, the SLL could be reduced during the optimization process of the unit-cell, that will lead to a reduced SLL for the final structure of the PLWA. Because of the longitudinal asymmetry of the proposed unit-cell structure, an elliptical polarization will be obtained. It is possible to reduce the axial ratio to 3dB via the optimization process and realize the circular polarization.

In this research project, a Rotman Lens (RL) is suggested as the feeding network of antennas' phased-array, which makes the beamforming possible in second direction. The Rotman lens is a passive phase-shifter network with a true time delay line which has a wideband scanning performance and can be implemented using the mmWave passive circuits (Attaran *et al.*, 2016).

Finally, it is practical to reduce the size of system further and increase the level of integration, using a multi-layer configuration by including the wideband band-pass filter (Rahmani, 2017). However, this part has not been included in the current research project. To prove the antenna's concept and perform the optimizations, our proposed structure has been full-wave simulated using FEM-based ANSOFT HFSS software; then, fabricated and tested on a LTCC substrate. The S-parameter measurements were performed using N5225A Programmable Network Analyzer (PNA) at the LACIME LTCC Lab of ÉTS and the radiation patterns were measured in an anechoic chamber provided by the PolyGrames group at École Polytechnique de Montréal.

Main Contributions and Novelties of the Thesis

As we mentioned in the problems and challenges section, several research projects currently exist which attain some of our objectives presented in this thesis. But, to the best knowledge of author, the current research project is the first work that realizes all these features at the same time in one complete system, that makes it an ideal candidate for the WiGig applications.

- It is a low-profile and low-cost periodic LWA structure fabricated on the LTCC substrate that makes it an ideal candidate for the AiP applications at mm-Wave frequencies.
- It has a really simple structure compared to similar designs, which reduces the complexity of fabrication and increases the coherency of designed and fabricated product's features.
- The antenna has a really high resistant against the fabrication's inaccuracies. As a matter of fact, there is a great agreement between the simulation's and measurement's performance, even in the case of very poorly fabricated prototypes.
- Only passive components are used in the form of microstrip structures to minimize the costs and size of total system and make it ready for an easy integration in one package (AiP).
- Its 2-D beamforming capability covers the most area of the room to create a potent, effective wireless link at highly attenuated 60GHz band, which is suitable for any WiGig application. The system contains a phased-array of the optimized PLWAs, fed by a Rotman lens.
- The proposed structure is a novel reconfigurable periodic leaky-wave antenna with seamlessly beam scanning capability from backward to forward quadrant including the broadside radiation and a wide scanning range. This antenna specially designed, optimized and tested for the WiGig application band (57GHz to 64GHz at U.S. and Canada).
- The beam scanning angle span can be adjusted for the desired application. The substrate's permittivity affects the scanning range in the direction of waves propagation within the antenna. Also, beam angle could be tuned to any desired value in the perpendicular direction

by modifying the Rotman lens's phase-shift. Current designed scanning angle in this project is $-43°to+34°$ in propagation's direction and $-31°to+28°$ in perpendicular direction.

- The antenna system has an ultra-wide fractional impedance bandwidth of 48.3 percent. The matching bandwidth of the proposed PLWA is almost 29GHz from 43GHz to 72GHz.
- The radiation efficiency is very high and almost constant over the desired frequencies. The average efficiency of the proposed antenna is 87.4% from 50GHz to 70GHz.
- It has a high gain value over the desired frequency band which is needed at highly attenuated 60GHz communications. The average radiation gain for a single antenna is 12.4 dBi. This value reachs up to 20 dBi for the whole structure containing a phased-array of five antennas.
- Side Lobe Level (SLL) for the simulation and the measurement is less than -10dB.
- The antenna supports the circular polarization as an essential requirement for any WPAN device. The average measured Axial Ratio is about 2.57 dB from 50GHz to 67GHz.

Thesis Outline

This thesis is organized into 5 chapters. In the first chapter, we will cover the general concept and motivation of this research project along with the literature review of the recent related works in this area. A summary of the wireless WiGig applications, the reconfigurable antenna and antenna in package (AiP) used in this domain will be shortly discussed.

In the second chapter, the general theory and mathematical model of the proposed structure will be introduced. Since the mathematical equations are very complicated, an empirical model for our periodic LWA will be presented, which is more practical for the design purpose. The main features of the proposed structure will be investigated, considering the geometrical parameters. Then, a study of the geometrical parameters of the antenna will be conducted.

A comprehensive optimization process for the proposed PLWA along with the feeding network (Rotman lens) and a phased-array of the antennas for beam-steering in the second direction will be discussed in the third chapter. We present the actual design procedure and optimization process of each component to achieve a certain goal. However, the procedure can be repeated for different objectives like having the maximum bandwidth, higher gain, wider beam scanning angle, improved axial ratio, better efficiency and etc, we will demonstrate the simulation results for some of these objectives in this chapter. Moreover, an alternative antenna design without any via will be introduced in order to make the fabrication process much easier.

In the fourth chapter, we will talk about the fabrication process of our proposed PLWA structure on the LTCC substrate and its challenges. We explain a brief summary of the whole procedure from constructing the circuit film mask to the LTCC baking in the oven, pointing out some tips and guidelines at each stage. We will discuss the advantages of using a LTCC technology and what range of options we have for choosing a suitable substrate. Then, we explain the methods for connecting the measurement instruments to our structure in order to have a precise measurement at mm-Wave frequencies. Next, our fabrication batches, the method of inspection after each fabrication and some practical experiences obtained while fabricating on the LTCC substrate at high frequencies will be shared.

Finally, we will present the antenna's measurement results in the fifth chapter. Generally, the performance of an antenna is measured in two steps; first, S-Parameter measurement using a Vector Network Analyzer (VNA) to check the matching bandwidth of the antenna and second, the radiation pattern measurement in an Anechoic Chamber to verify other antenna's features such as radiation gain, main beam angle and polarization. The setup for each measurement will be explained in this chapter and then, we compare the measurement results with the simulation results from chapter 3 to investigate the antenna's performance and fabrication quality.

At the end of this thesis, you will find a quick summary of the whole antenna system's features and performance parameters in the conclusion chapter. Furthermore, some recommendations and suggestions for the future works will follow in this section.

CHAPTER 1

BACKGROUND

1.1 Introduction

This chapter will provide the background information for the presented research project. First, the application domain of this thesis, the Wireless Gigabit Alliance (WiGig), will be introduced shortly, followed by two important concepts that are widely used in the mm-Wave applications extent: Reconfigurable Antenna and Antenna in Package (AiP). Duo to high attenuation level and extreme directivity of the antennas which are designed for this frequency range, having a reconfigurable radiation pattern seems inevitable. Moreover, considering the total compact size of fabricated antennas' structure for 60 GHz band, packaging the transceiver chip and its all necessary circuits with the antenna system would be very advantageous for these applications. Finally, we will present the literature review and investigate the existing antenna systems which are designed and fabricated for the same scope of this research project. The theoretical and mathematical model of our proposed structure will be presented in the next chapter.

1.2 Wireless Gigabit (WiGig)

Wireless Gigabit (WiGig) is a category of the wireless protocols which operates in a frequency band around 60 GHz. WiGig, which is also known as 60GHz-WiFi, includes a set of wireless network protocols that holds the current IEEE 802.11ad standard as well as the upcoming IEEE 802.11ay standard. The IEEE 802.11ad specification is a revision of the IEEE 802.11 wireless networking protocol that was originally developed by the WiGig Alliance in 2009 to provide a Multiple Gigabit Wireless System (MGWS) standard at 60 GHz frequency. It was completed in 2010 and added to the IEEE 802.11 family in December 2012. IEEE 802.11ay specification is a proposed enhancement to the IEEE 802.11ad standard by quadrupling the bandwidth and adding MIMO up to 8 streams. WiGig standard operates on the V-band of mm-Wave frequency, which makes the range of communication rather limited (just a few meters range and difficult

to pass through obstacles or walls). However, duo to its higher operating frequency compared to the existing wireless protocols, such as LTE (0.7 GHz to 2.6 GHz) and conventional WiFi (2.4 GHz or 5 GHz), it offers significantly wider bandwidth (about 7 GHz).

WiGig technology could enhance the communication experience for virtual reality, augmented reality, high quality multimedia streaming, gaming, wireless docking, and obviously, enterprise applications requiring high speed, data-intensive connections. WiGig allows Wi-Fi devices to access the uncongested 60 GHz frequency band with wide channels to transmit data efficiently at multi-gigabit per second speeds. Users will benefit from the expanded capacity and focused transmission between devices to reduce interference, even in crowded environments.

The potential market for the WiGig products includes the wireless docking between devices such as smartphones, laptops, TVs, projectors, tablets, and IoT devices. In addition to that, the simultaneous streaming of multiple ultra-high definition videos, more immersive gaming, augmented reality and virtual reality experiences, fast download of high-definition movies, convenient public kiosk services, easier handling of bandwidth intensive applications in the enterprise are considered as some of the popular applications for the WiGig technology.

As mentioned, WiGig standard was first announced in 2009 by the Wireless Gigabit Alliance, a trade association that pushes this technology. In 2013, the Wireless Gigabit Alliance merged with the Wi-Fi Alliance, which oversees the Wi-Fi standards like Wi-Fi 6. The original version of WiGig, which published in 2012, uses the 802.11ad standard and provides the speeds of about 5 Gbps over a maximum distance of 10 meters. The enhanced and faster IEEE 802.11ay standard was scheduled for release in 2019, that is already delayed. Some silicon companies are working on developing products using this new technology. Qualcomm has developed its first 802.11ay 60GHz Wi-Fi chipset for WiGig devices in 2018, allowing for speeds of up to 10 Gbps and latency under a millisecond. Although, the product still requires the line-of-sight between transmitter and receiver, but, it can reach top speed at up to 100 meters away.

The available bandwidth of unlicensed 60 GHz frequency is more than all the other unlicensed bands combined. Table 1.1 shows the worldwide spectrum availability of WiGig. The allocated

bandwidth expands from 3 to 9 GHz and most regions allow use of 7 GHz. In comparison, the 5 GHz Wi-Fi exploits about 500 MHz and the 2.4 GHz band has less than 85 MHz of bandwidth in most regions (Hansen, 2011). Although, wider bandwidth increases the channel capacity for high-speed communications, but the real challenge for any WiGig application is to overcome the severe path loss from transmitter to receiver at 60 GHz band.

Table 1.1 60 GHz worldwide spectrum availability
Taken from Hansen (2011).

Country	From (GHz)	To (GHz)
U.S. and Canada	57.05	64.00
Japan	59.00	66.00
Australia	59.40	62.90
Europe	57.00	66.00
China	59.00	64.00
South Korea	57.00	64.00

Because the total noise power of a wider bandwidth is normally very extreme, a WiGig system should operate at 10 dB higher received power than a conventional Wi-Fi system. Moreover, the loss of 60 GHz band is typically 21 to 28 dB more than the 2.4 and 5 GHz band due to the shorter wavelength (Hansen, 2011). Therefore, to compensate for this excessive loss, either we must reduce the maximum operating range or increase the antenna gain. Fortunately, compact antennas with high gain are feasible at high frequencies, since the gain is directly related to the antenna aperture and inversely to the square of the wavelength. However, a high antenna gain will result in a narrow antenna beamwidth, which demands a beamforming system for the communication. Hence, devices that are designed for the 60 GHz band, need to find each other, coordinate operation, and optimize antenna settings in an efficient and interoperable method. The MAC/PHY specification of WiGig standard considered these challenges with the design of its network architecture, access protocol, and PHY layer. Furthermore, a specific beamforming protocol is an indispensable part of the specification (Hansen, 2011).

1.3 Reconfigurable Antennas

A reconfigurable antenna can dynamically modify its radiation properties and/or frequency. These type of antennas normally exploit two inner switching mechanisms to produce a dynamic response in a controlled and reversible way to provide a purposeful redistribution of the RF surface currents through the antenna in order to achieve the desirable properties. These two mechanisms are the electrical and the mechanical switching using components such as RF switches, varactors, tunable materials or mechanical actuators (Dubal & Chaudhari, 2020).

There is also another category of antenna, known as the smart antenna, that instead of using an inner mechanism like the reconfigurable antenna, takes advantage of an external beamforming network. However, in both cases, the reconfiguration ability of the antennas will be used to optimize the antenna performance in a dynamic environment or to adapt to a variable operating requirements. Hence, a single reconfigurable antenna replaces multiple conventional antennas resulting in a compact, low-cost system (Dubal & Chaudhari, 2020). Reconfigurable antennas can be categorized based on the dynamically adjusted parameter of the antenna: the frequency of operation, radiation pattern, polarization (Huff & Bernhard, 2008).

1.3.1 Frequency Reconfiguration

In a situation where multiple communication systems operate in different bands, a frequency reconfigurable antenna can adjust its operation frequency dynamically in order to communicate with each device and hence, replaces the required multiple antennas. Generally, a physical or electrical modifications to the antenna's structure/dimension - while operating - using the RF switches (Panagamuwa *et al.*, 2006), impedance loading (Erdil *et al.*, 2007) or tunable materials (Liu & Langley, 2008), would realize the frequency reconfiguration feature.

1.3.2 Radiation Pattern Reconfiguration

This type of reconfigurable antennas can intentionally change the spherical distribution of its radiation pattern in order to direct its radiation power in any arbitrary direction and establish a

potent communication link with the devices in different spatial positions. The beam steering, which navigates the direction of the maximum radiation to maximize the antenna gain in a link with mobile devices, is the most common application of the pattern reconfigurable antennas. The radiation pattern reconfigurability can be achieved using movable or rotatable structures (Rodrigo *et al.*, 2012; Chiao *et al.*, 1999), or the switchable and reactively-loaded parasitic elements (Aboufoul *et al.*, 2013; Harrington, 1978; Hum & Perruisseau-Carrier, 2014). In the last decade, the metamaterial-based reconfigurable antennas, which provide a small form factor and wide beam steering range, have been designed for many applications (Mookiah & Dandekar, 2009; Gulati & Dandekar, 2014). Moreover, plasma antennas with tunable directivities have been considered as alternatives (Borg *et al.*, 1999; Kumar & Bora, 2010; Alexeff *et al.*, 2006). Throughout this thesis, the reconfigurability capability refers to this category of antennas.

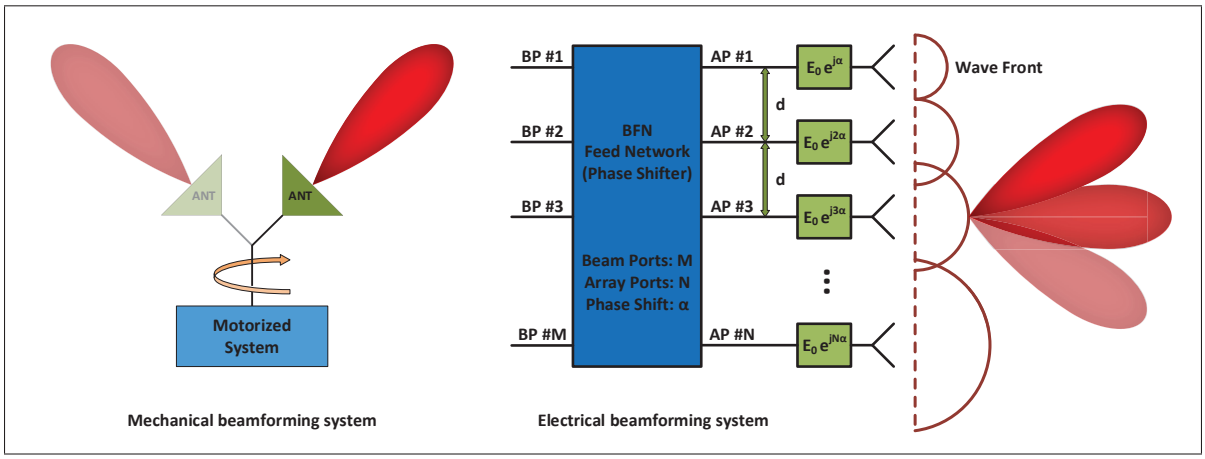

Figure 1.1 Mechanical and electrical beamforming systems.

1.3.3 Polarization Reconfiguration

Polarization reconfigurable antennas can switch between different polarization modes. In case of the portable devices' communications, the ability to switch between horizontal, vertical and circular polarizations could result in a minimum polarization mismatch losses. The polarization reconfigurability feature can be realized by modifying the balance between the different modes of a multi-mode structure (Simons *et al.*, 2002).

1.3.4 Compound Reconfiguration

These reconfiguration antennas are able to simultaneously adjust several antenna's parameters. The combination of frequency agility and beam-scanning is the most common application of the compound reconfiguration that provides an improved spectral efficiencies. It is possible to achieve this reconfigurability by combining different single-parameter reconfiguration techniques in the same structure (Yang *et al.*, 2007; Aboufoul *et al.*, 2014) or reshaping dynamically a pixel surface (Rodrigo *et al.*, 2014; Pringle *et al.*, 2004). However, an ultra-wideband antenna which supports 2-D beam steering and the circular polarization can provide almost everything expected from a compound reconfigurable antenna.

1.4 Antenna in Package

AiP is an IC (Integrated Circuit) package that is integrated with an antenna system. The AiP package may include the required network elements for the antenna system. The AiP designs at the mmWave band applications are very popular due to the miniaturized size of the antenna at this frequency range. This technology made it possible to integrate the complex microwave circuits into a single package in order to save the overall size and cost of the mass production (Zhang *et al.*, 2009). The AiP eliminates bulky interconnection network between the antenna and other elements of the communication system, which has generally high losses and costs, and increases the efficiency of the whole system. An AiP system provides a low insertion loss interconnections as well as low impedance matching (Zhang & Liu, 2009; Zhang *et al.*, 2013).

Comparing to AoC (Antennas on Chip), the AiPs will provide higher radiation efficiency, gain enhancement, better impedance matching, and improved packaging techniques. Moreover, it is possible to integrate the antenna in a package with other antennas (as an array), beamforming networks, and filters in order to build a complete system which could be optimized in terms of the size, losses, costs and performance (Zhang & Liu, 2009).

There are several packaging methods and different material types and technologies that can be exploit to perform the microwave circuit packaging (AiP). A vast range of materials from

co-fired ceramics to organic materials are available for the chosen technology by designers. These packaging technologies, which are listed briefly below, can provide different electrical and physical performance based on the desired application. More detailed information about these methods and their advantages and disadvantages can be found in Rahmani (2017).

- Co-Fired Ceramics (low dielectric and conductor loss, reliability, high packaging density).
- Thick and Thin Film Ceramics (pre-fired ceramic base).
- High frequency laminates (wide range of electrical and physical properties).
- Liquid Crystal Polymers (light weight, low cost, and hermetic organic material).

The most important challenges in the design of an AiP system, which have to be addressed carefully in order to have a performant system, are the implementing a low loss interconnection, electromagnetic shielding of the AiP, and preventing cavity resonances. Failing this task results in poor overall system efficiency. Moreover, the antenna configurations, integration of required elements such as filters and beamforming network in the package, multi-layer design, and circular polarization are very interesting matters that might be considered in the system design.

1.5 Literature review

As the integrated devices at mm-Wave frequencies becomes more popular, the contributions to the AiPs advancements have been considerable by the academic and industrial researchers. The footprint of AiP systems can be traced in several communication applications such as 5G technology, point-to-point and point-to-multi-point WiGig telecommunications, as well as automotive radars. Hence, all sorts of reconfigurable AiP systems have been developed for these applications at 60GHz band during last years, supporting different features.

Zwick *et al.* (2006) studied and suggested an integrated folded dipole structure on a fused silica substrate which was designed for ISM band at the center frequency of 60GHz. Although, the proposed antenna showed a good efficiency of 90% and the maximum gain of 7 dBi, but there

was only a limited fractional bandwidth of 10%. In an effort to improve the bandwidth of the structure, Grzyb *et al.* (2007) proposed a cavity-backed folded dipole superstrate antenna on the plastic package that increased the impedance bandwidth up to 35%, proving the undeniable effect of appropriate packaging on the AiP's performance. Later in 2011, the same research team developed a 16-element arrays of aperture coupled patch antenna in a multi-layer organic package structure to enhance the radiation gain. They succeeded to realize 17 dBi gain with almost 80% efficiency and more than 10 GHz of impedance bandwidth (Liu *et al.*, 2011).

In another research, an AiP system of $28mm \times 28mm$, consist of 16 patch antennas printed on a LTCC substrate and integrated with a flip-chip attached transceiver working at 60 GHz, was reviewed and studied by Kam *et al.* (2011). At the same time, an integrated multilayer AiP for 60 GHz band presented by Hong *et al.* (2011), which includes an array of 24 stacked circular patch antennas integrated in an LTCC package. The proposed antenna has a maximum gain of 14.5 dBi at boresight and more than 9 GHz bandwidth. Moreover, it is capable of 45º beam-steering in both E-plane and H-plane. Following their work, these researchers developed a FR4 PCB version of their previous proposed structure later, in order to reduce the cost and fabrication complexities considerably (Hong *et al.*, 2013). The aforementioned works were mainly sponsored by gigantic IT companies such as IBM and Samsung.

On the other hand, the advancements in AiP technologies were not possible without the contribution of research groups in academia. In an effort, Zhang *et al.* (2008) proposed a slot antenna grid array printed on an LTCC package at 60 GHz, which had a maximum gain of 11 dBi and a -7 dB impedance bandwidth of 6 GHz. Later, in order to increase the radiation gain, a dual grid array (Zhang *et al.*, 2011) and a quadruple grid array (Zhang *et al.*, 2013) were developed with the maximum radiation gain of 13.5 dBi and 15 dBi respectively. These structures had a fractional bandwidth of 15% and 25% respectively. Liao *et al.* (2015) proposed a differentially fed planar aperture antenna supporting 21.5% of impedance bandwidth and peak gain of 15.3 dBi at 60 GHz. To develop this work further, Bisharat *et al.* (2016) redesigned a circularly polarized antenna version as a fit candidate for 5G communications. Then, Liao & Xue (2017) introduced a dual polarized aperture antenna in an LTCC package, which provided a bandwidth

of 7 GHz from 57 to 64 GHz with a peak gain of 12 dBi. In 2014, Kim *et al.* (2014) suggested a compact LTCC-based Yagi-Uda AiP system that was designed for the 60 GHz mobile wireless application. This antenna which used integrated CMOS chip connected wire-bonding for AiP, demonstrated about 90% efficiency and 6.2 dBi gain over its 9 GHz bandwidth.

More recent designs at 60GHz are performed on FR4 PCB substrate by GUO & WONG (2019); Al-Alem & Kishk (2019); Wu *et al.* (2019) which showed an impedance bandwidth of 24%, 27.5%, 21.6% and the maximum radiation gain of 17.6 dBi, 12.6 dBi, 26.2 dBi respectively. At the same year, Zhu *et al.* (2019) proposed a single-ended-fed planar aperture antenna (SPAA) fabricated on the LTCC substrate. This aperture antenna consists of 4×4 element arrays which demonstrates a maximum gain of 20.4 dBi from 57.5 to 65.7 GHz. Another low-cost, compact AiP system was suggested by Xia *et al.* (2020) for 60 GHz low-power radar sensor applications using a glass integrated passive device (Glass-IPD) manufacturing process. The proposed taper slot antenna has been realized in 1×2 array and featured 6.5 dBi gain with an impedance bandwidth of 47.2 to 67 GHz. Reddy Kota *et al.* (2020) presented a 1×4 rectangular patch array antenna on a Silicon Nitride (Si_3N_4) substrate for IoT applications. This low-profile antenna showed 12 to 15 dBi of radiation gain over its 5 GHz bandwidth.

In the literature, the first AiP system with beam steering capability was introduced by Hong *et al.* (2011) which had 45° range. This structure employed a RFIC to generates the necessary phase shifts in order to modulate the phase delivered to each of the array elements. After that, Yoshida *et al.* (2013) presented a planar dipole array in which several substrates were stacked vertically using a 3-D SiP technology. The proposed antenna was able to perform 2-D beam scanning with a scanning range of 75° and 95° in theta and phi directions, respectively. Nonetheless, since this system used the active phase shifters for beamforming, the cost and power consumption of the product would be considerably high. Following that, Tekkouk *et al.* (2017) worked on a wideband beam steering slotted plate antenna at 60 GHz with a scanning range of 120° in one direction and an impedance bandwidth of 13%. Due to 1-D beam steering, mechanical movement between antenna parts would be required.

Recently, Aziz *et al.* (2019) suggested a connected slots linear phased array that feeds a high gain semi-symmetric lens antenna at 60 GHz. An array of 16 connected slots provides 90° 1-D beam-steering in the H-plane and demonstrates a maximum gain of 24.6 dBi over more than 33% impedance bandwidth. Another integrated antenna with 2-D beam scanning capability was introduced by Li *et al.* (2021). The proposed structure designed and fabricated on a Rogers substrate in a 5×5 array configuration. The scanning ranges were 80° and 90° in the E-plane and H-plane respectively. Although, its impedance bandwidth was limited to 6%, but it showed a radiation gain of 18.5 dBi and a boresight efficiency of up to 85% at 60 GHz.

As mentioned earlier, the importance of circular polarization cannot be overlooked in the AiP applications, especially for highly directive antennas at mm-Wave band. The first AiP system at 60 GHz supporting the circular polarization was introduced byWeily & Guo (2009). They utilized an 4×2 array of circular slot antenna loaded with an elliptic patch fed by a microstrip line implemented on a liquid crystal polymer (LCP) substrate. There is a plethora of research groups who have studied and designed several types of AiPs with circular polarization at 60 GHz (Bisharat *et al.*, 2016; Liu *et al.*, 2012; Shen *et al.*, 2012; Sun *et al.*, 2013).

Rafiei *et al.* (2018) presented an antenna structure consist of a pair of tilted bow-tie radiators with planar semi-helix unit-cells which supports circular polarization from 54 to 64.3 GHz. This antenna was fabricated on RT/duroid substrate and exhibits 10 to 12.5 dBic radiation gain over 46.6% impedance bandwidth. Zhu *et al.* (2018) proposed an aperture-coupled patch antenna array with quadri-polarization at 60 GHz. Two linear polarizations were realized by differential feeding of the array, while two CP radiations were achieved by sequential rotation feeding. This structure provides an impedance bandwidth of 11.6% and 12.2 dBic gain. Later, a U-slot with two parasitic elements at 60 GHz was designed by Ibrahim (2019) that supported circular polarization over a very limited bandwidth. This PCB fabricated antenna had 7.2 dBi radiation gain and 87% efficiency from 53.3 GHz to 60.8 GHz.

A summary of the latest developments in AiP design is presented in Tables 1.2 and 1.3.

Table 1.2 Summary of the recent AiP developments.

Reference	Substrate	Antenna Type	Pol.	Gain	Array	BW
Zwick *et al.* (2006)	Fused silica	Folded Dipole	Linear	7 dBi	Single	13%
Grzyb *et al.* (2007)	Plastic	Folded Dipole	Linear	8 dBi	Single	35%
Liu *et al.* (2011)	Organic	Folded Dipole	Linear	17 dBi	16 El.	20%
Kam *et al.* (2011)	LTCC	Aperture Coupled Patch	Linear	8 dBi	16 El.	N.R.
Hong *et al.* (2011)	LTCC	Circular Patch	Linear	14 dBi	24 El.	15%
Hong *et al.* (2013)	FR4	Circular Patch	Linear	12 dBi	8 El.	15%
Zhang *et al.* (2008)	LTCC	Slot Antenna Grid Array	Linear	11 dBi	Single	10%
Zhang *et al.* (2011)	LTCC	Slot Antenna Grid Array	Linear	14 dBi	2 El.	15%
Zhang *et al.* (2013)	LTCC	Slot Antenna Grid Array	Linear	15 dBi	4 El.	25%
Liao *et al.* (2015)	FR4	Planar Aperture	Linear	15 dBi	Single	21%
Bisharat *et al.* (2016)	FR4	Planar Aperture	Circular	14 dBi	Single	16%
Liao & Xue (2017)	LTCC	Planar Aperture	Dual	12 dBi	Single	11%
Yoshida *et al.* (2013)	LTCC	Planar Dipole	Linear	10 dBi	Single	11%
Tekkouk *et al.* (2017)	Hollow Waveguide	Slotted Plate	N.R.	29 dBi	13 El.	13%
Weily & Guo (2009)	LCP	Circular Slot Elliptic Patch	Circular	14 dBi	8 El.	50%
Liu *et al.* (2012)	LTCC	Helical	Circular	15 dBi	16 El.	21%
Shen *et al.* (2012)	LTCC	Patch	Circular	10 dBi	4 El.	12%
Sun *et al.* (2013)	LTCC	U-Slot Patch	Circular	16 dBi	16 El.	27%
Kim *et al.* (2014)	LTCC	Yagi-Uda	Linear	6 dBi	Single	15%

Table 1.3 Summary of the recent AiP developments.

Reference	Substrate	Antenna Type	Pol.	Gain	Array	BW
GUO & WONG (2019)	FR4	Fabry-Perot Cavity (FPC)	Linear	17 dBi	Single	24%
Al-Alem & Kishk (2019)	Rogers	Rectangular Dielectric Resonator	Linear	12 dBi	Single	27%
Wu *et al.* (2019)	Rogers	Patch	Linear	26 dBi	64 El.	21%
Zhu *et al.* (2019)	LTCC	Single-Ended-Fed Planar Aperture	Linear	20 dBi	16 El.	13%
Xia *et al.* (2020)	Glass-IPD	Taper Slot Antenna	Linear	6 dBi	2 El.	33%
Reddy Kota *et al.* (2020)	Silicon Nitride	Rectangular Patch	Linear	15 dBi	4 El.	8%
Aziz *et al.* (2019)	Megtron 7 R5785	Connected Slots Linear Phased-Array	Linear	24 dBi	16 El.	33%
Li *et al.* (2021)	Rogers	Patch	Linear	18 dBi	25 El.	6%
Rafiei *et al.* (2018)	RT/duroid	Bow-Tie Antenna	Circular	12 dBi	2 El.	46%
Zhu *et al.* (2018)	Rogers	Aperture Coupled Patch	Linear Circular	12 dBi	4 El.	11%
Ibrahim (2019)	FR4	U-Slot Microstrip Patch	Circular	7 dBi	Single	13%

1.6 Conclusion

In this chapter, we presented the background information and existing literature in the scope of current research project. Several designs, by considering the selected technology, antenna's structure, beam-steering capability, and circular polarization were reviewed. It is clear that the researchers in industries and academia are trying to design and develop a performant product

to be integrated in the next generation of communication systems by achieving the higher radiation gain using arraying techniques, impedance bandwidth improvement, low-cost packaging techniques, enhanced system efficiency, beam steering capability and circular polarization.

CHAPTER 2

THEORETICAL MODEL OF STRUCTURE

2.1 Introduction

The path loss due to extreme amount of the attenuation in the mmWave applications such as WiGig communication at 60 GHz band challenges the communication range and makes the high directivity antennas an indispensable, demanding solution. Recently, many radiation gain enhancement techniques were developed to address this requirement. However, more directive antenna indicates less space coverage by the radiation beam for an effective communication. It means, two communicating devices in such applications must have a reconfigurable radiation pattern, adjusted toward each other, to avoid the communication link failures. The mechanical beam-steering of the antenna is a very costly and bulky system which makes it an inconvenient, impractical solution for the AiP applications. Moreover, the circular polarization is generally an inseparable part of the WPAN telecommunication systems to compensate for the antennas' orientation relating to each other. The Side Lobe Level (SLL) in the radiation pattern is another important issue for these communication systems to be considered, because we want to have the maximum radiation power in our desired direction to increase the total efficiency.

A microstrip antenna structure containing all passive components with an acceptable circular polarization (Axial Ratio lower than 3 dB) and a reduced Side Lobe Level (SLL lower than -10 dB), seems a perfect candidate for these applications. A leaky-wave structure is an interesting solution that can meet all the requirements. The Periodic Leaky-Wave Antenna (PLWA) has a seamless beam-steering ability from backward to forward quadrant including the broadside radiation with input frequency variations (Jackson & Oliner, 2008). Although, a reconfigurable radiation pattern with frequency for some applications is undesirable, but it could be highly advantageous for the WiGig telecommunications because its dedicated bandwidth is divided into some frequency channels. Hence, two devices need to find the right frequency channel that creates the radiation beams toward each other for a potent communication link.

A PLWA is composed of a cascade of the smaller blocks named unit-cells (UC), which makes the design procedure easier, because we could design a single UC separately and then expand it to the whole structure. Besides, this antenna is considered a linear series fed array structure which needs a really simple feeding network. The main issues that we have to address in the design process of a PLWA are the bandwidth matching, the scanning range limitation and the open-stopband (OSB) suppression. Moreover, a suitable circular polarization and an acceptable side lobe level are attainable through an optimized PLWA (Otto *et al.*, 2014).

In this chapter, the general theory and mathematical model of the proposed structure will be introduced. Since the mathematical equations are very complicated, an empirical model for our periodic LWA will be presented which is more practical for the design procedure. The main features of the proposed structure will be investigated considering the geometrical parameters. Then, a study of the geometrical parameters of the antenna will be covered. However, the comprehensive optimization process along with the feeding network and an phased-array of the antenna for beam-steering in the second direction will be discussed in the next chapter.

2.2 Leaky-wave antenna

Leaky-wave antennas (LWAs) was introduced first at 1940s as a slotted rectangular waveguide (Jackson *et al.*, 2012). A Leaky-wave structure is a traveling wave antenna, in which, there is a perturbation (uniform or periodic) in the wave propagation that leads to wave leakage alongside the antenna's structure while traveling through guidance medium (Otto *et al.*, 2014). These antennas, unlike resonant antennas, use a travelling wave on the guiding structure for propagation (Walter, 1965). Since these antennas have generally a simple structure that can realize high directivity without a need for the complex and expensive feeding network like a phased-array, they are well suited for the microwave band and above (Jackson *et al.*, 2012).

Duo to the power leakage along the length of leaky structure, the propagation wavenumber $k_z = \beta - j\alpha$ on the guiding structure of LWA is complex, consisting of both a phase constant β and an attenuation constant α, even if the structure is lossless (Jackson & Oliner, 2008).

Generally, the LWA has a planar or nearly planar structure fed by a simple feed network which could generate a narrow beam pattern with the limited bandwidth (Jackson & Oliner, 2008). The specific characteristic of leaky-wave antenna is its inherent beam scanning ability with the input frequency (Walter, 1965). It is possible to have a seamlessly backward to forward beam scanning with frequency, including the broadside and endfire radiation (Lei Liu *et al.*, 2002).

The leaky-wave structure can be categorized based on the feeding source to the unidirectional and the bidirectional structures (Jackson & Oliner, 2008). In unidirectional structure, wave will be guided in only one direction and usually there is just a simple feed source at one end of the structure and a matched load on the other end. On the contrary, the bidirectional structure can be fed in the center with two matched loads on both ends of the structure and the wave may propagate in two opposite directions. The bidirectional structure can be advantageous in many applications such as producing the broadside radiation pattern (Jackson *et al.*, 2012).

It is possible to design a leaky-wave structure so that the wave propagates through a line (1-D) along the guiding structure or in 2-D guiding surface to have more advanced radiation beam shapes (Jackson & Oliner, 2008). Because of its ability to steer the beam angle with the input frequency, LWA usually has a fairly narrow pattern bandwidth from 1% to 10%. The pattern bandwidth is defined as the radiated power density at a fixed observation angle (Jackson *et al.*, 2012). Although, this feature might be undesirable for the point to point communications, but for the beam scanning applications will be quite beneficial (Jackson & Oliner, 2008).

As mentioned, the LWAs are very popular for the microwave and millimeter-wave frequencies due to their high directivity and simple structure (Jackson & Oliner, 2008). Moreover, they are low-profile and low-cost structures that could be easily manufactured in mass production for the AiP applications. The only issue that should be addressed in their design process is the open-stopband (OSB) elimination in the radiation. Of course, the antenna bandwidth matching, side lobe level (SLL), limited radiation pattern bandwidth and polarization are also the matter of concern. However, later we will show that all of these problems could be solved at once in the proposed structure, because they are not completely independent from each other.

1-D LWA could have a uniform (or quasi-uniform) or periodic structure (Jackson *et al.*, 2012). Uniform LWA has a uniform guiding structure along the length of antenna and it supports the fast-wave propagation ($0 < \beta < k_0$). On the other hand, a periodic LWA is composed of the repetition of a unit-cell along its length and the guiding structure supports slow-waves ($\beta > k_0$). A quasi-uniform LWA has a periodic structure but it shows the features of a uniform LWA, because it has a periodicity of much less than a wavelength which has no major effect on the radiation (Jackson & Oliner, 2008; Jackson *et al.*, 2012).

In order to have the leaky-wave radiation in a uniform structure, only the dominant mode should be excited to propagate. Usually, a complex feeding network is necessary to suppress the lower modes (Oliner & Lee, 1986). Besides, in most conventional uniform LWAs, the broadside radiation is not achievable, because they don't cover $\beta = 0$ (normally forward quadrant $\beta > 0$) in their operating region (Jackson & Oliner, 2008). On the contrary, the periodicity along a periodic LWA makes the fundamental non-radiating mode to radiate (Collin & Zucker, 1969). This lead to infinite number of space harmonics (Floquet waves) ,which could be fast or slow, having the wavenumbers of (Oliner & Lee, 1986; Jackson *et al.*, 2012):

$$k_{z,n} = k_{z,0} + \frac{2\pi n}{p} \tag{2.1}$$

where p is the period in the z-direction. Normally, periodic LWA is designed in such a way that only one harmonic (β_{-1}) radiates and others are non-radiating. Because β_{-1}, which is the real part of $k_{z,-1}$, can have a positive, negative or zero value, the periodic LWA could have the radiation at forward, backward or broadside direction respectively (Jackson *et al.*, 2012).

In a LWA structure, the phase constant is dependent on the input frequency and it controls the radiation beam angle of the antenna. Equation 2.2 shows the relation between phase constant β and radiation beam angle θ_m with respect to the broadside direction. Attenuation constant α, on the other hand, is responsible of the wave leakage (radiation) along the antenna structure. The Larger value of the attenuation constant means a higher leakage per unit length which

leads to a shorter effective aperture for the antenna and consequently, a wider radiation beam (Jackson & Oliner, 2008). Equation 2.3 specifies the half power beam width BW_{HP} in term of the beam angle θ_m and the normalized attenuation constant α:

$$sin\theta_m \approx \frac{\beta}{k_0} \tag{2.2}$$

$$BW_{HP} = 2csc(\theta_m)(\frac{\alpha}{k_0}) \tag{2.3}$$

where θ_m is the angle of the maximum radiation beam with respect to the broadside direction (perpendicular to the leaky waveguide axis), k_0 is the wave number in free space and BW_{HP} is the half power beam width. According to equation 2.3, smaller attenuation constant can creates narrower beam (even pencil beam), but the antenna needs longer structure for the radiation with high efficiency. As a general rule, the phase constant of the leaky wave controls the beam angle, while the attenuation constant controls the beam width. It is possible to taper the aperture distribution to control the side lobe level or the beam shape (Jackson & Oliner, 2008).

The side lobe level of a LWA structure depends on the length of its aperture. Although, a longer LWA has a higher efficiency duo to more radiations along its length, but it also has a higher value of SLL which is undesirable. Moreover, longer antenna means more space occupied by the structure that could be an issue for the AiP applications. Therefore, there would be a trade-off between SLL and efficiency for the length of LWA. As a general rule, the length of a LWA is chosen so that 90 percent of the incident wave radiates while propagating through the guiding structure. It should be mentioned that when the efficiency is close to the unity, the value of attenuation constant will be impractically large. To realize a LWA structure which is 90 percent efficient, the equation 2.4 must be hold (Jackson & Oliner, 2008):

$$\frac{L}{\lambda_0} \approx \frac{0.18}{\alpha/k_0} \tag{2.4}$$

where L is the length of LWA that creates the aperture of the line-source antenna. Considering an antenna structure in the direction of z axis, the amplitude and phase of traveling wave along the aperture are dependent of the values of α and β as a function of z. In a completely uniform leaky-wave structure, α and β are constant along z axis which leads to an aperture distribution with exponential amplitude and linear phase. This aperture distribution will creates a high value of SLL. However, we can limit the SLL value using some techniques involving the control of attenuation variation with respect to z (Jackson & Oliner, 2008; Wanchu Hong *et al.*, 2003; Gomez-Tornero *et al.*, 2005).

2.3 Proposed Microstrip PLWA

The proposed antenna structure in this research project has a periodic leaky-wave structure, composed of a cascade of a few optimized unit-cells (UCs). This unidirectional 1-D periodic LWA has a very simple structure with respect to the design and fabrication processes, which is capable of producing the high directivity circularly polarized radiation pattern. High value of efficiency at 60 GHz band with low side lobe level (SLL) is achievable taking advantage of the proposed antenna. Moreover, wideband impedance matching and wide scanning range, from backward to forward including the broadside radiation, over the frequency are possible through suitable optimization procedure. Therefore, the very first step in the design procedure is to introduce the proper unit-cell that fulfil the desired features. The main issues that have to be addressed to achieve this objective are:

- Only one radiating space harmonic should be in the radiation's range
- Impedance matching bandwidth of the single UC
- Eliminating the open-stopband (OSB)
- Circular Polarization (CP)
- Reducing Side Lobe Level (SLL)

2.3.1 Unit-Cell Model

Figure 2.1 presents the proposed LWA's unit-cell (UC) structure and its geometrical parameters. This antenna is composed of the periodic repetition of a single unit-cell along the direction of propagation. The unit-cell itself is made of a microstrip line with the characteristic impedance of Z_0 that is loaded by two step discontinuities and shorted by three vias in the middle.

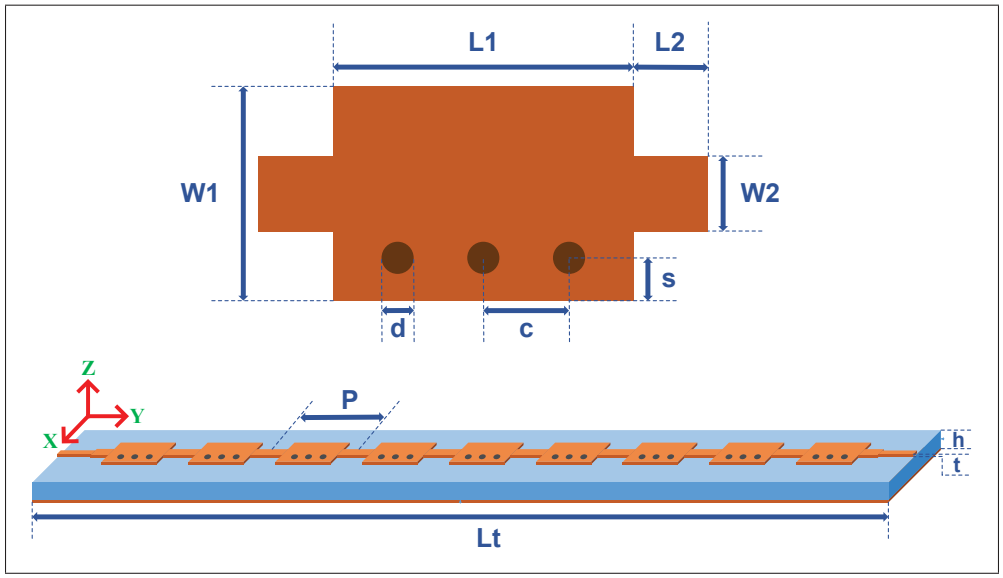

Figure 2.1 The unit-cell's geometrical parameters and Antenna's periodic structure on LTCC substrate.

The vias in UC construct a SIW wall on one side of the transmission line and create half mode SIW through altering propagation mode in the transmission line (Henry & Okoniewski, 2016). The positions and number of the via will affect the propagation constant and the radiation pattern, which is well studied in Deslandes & Wu (2001) and Deslandes & Ke Wu (2006).

The proposed periodic LWA can be considered as a series fed array antenna. In this way, each unit-cell as an element of the array must show a minimum reflection over the frequency band with an enhanced radiation feature. Using this analysis, the performance of the antenna could be predicted by means of the single element factor of a unit-cell and the total complex propagation constant of the periodic structure (Caloz & Itoh, 2004).

2.3.2 Propagation Constant

The propagation constant of a LWA structure is the most important parameter that specifies the radiation performance of the antenna. To obtain the dispersion characteristic of the proposed periodic LWA, the Bloch wave analysis will be helpful. Using the infinite periodic structure formulation in Pozar (2011), we can obtain the propagation constant of the antenna as:

$$\gamma = \frac{1}{P}(cosh^{-1}\frac{A+D}{2}) \tag{2.5}$$

where $\gamma = \alpha + j\beta$ is the propagation constant, A and D are the transmission parameters of a single unit-cell and $P = L_1 + 2 \times L_2$ is the period or length of one UC (refer to figure 2.1). This method gives us the attenuation and phase constant of an infinitely long structure based on the transmission parameters and periodicity, which is a good estimation of our finite structure.

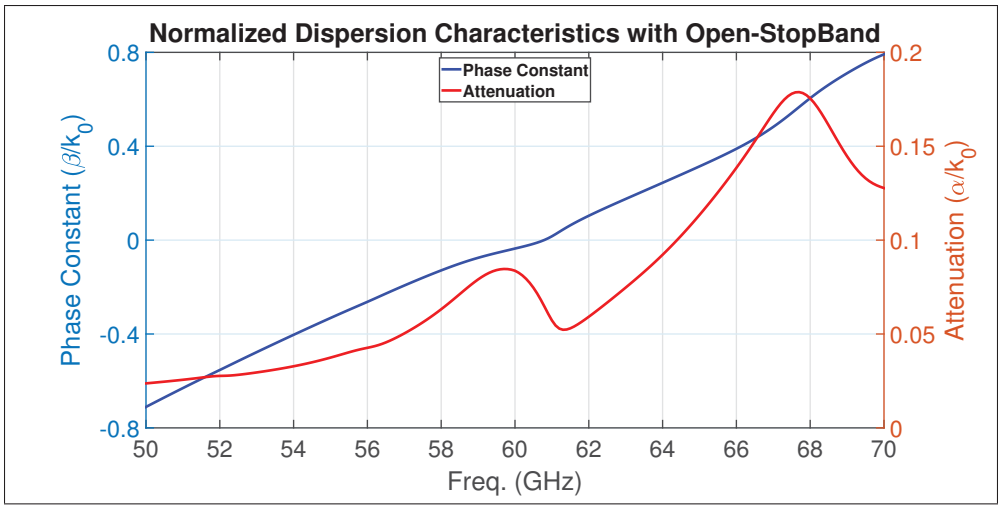

Figure 2.2 The propagation constant of an unoptimized Unit-Cell.

Figure 2.2 shows an example of the phase constant and attenuation constant of a unit-cell that is not optimized. In this figure, two open-stopbands (OSB) are clearly detectable as a bump in the attenuation graph: one around 60 GHz and the other near 68 GHz. An abrupt increase in attenuation constant accompanied by phase constant drop in these frequencies can be observed.

2.3.3 Empirical model of the unit-cell

As mentioned previously, in order to know the radiation behaviour of our antenna, we should obtain the propagation constant of the periodic structure and for this purpose, we need to find the transmission parameters of the unit-cell. (Itoh, 1989) suggests an analytical method based on the transmission line theory and TEN (Transverse Equivalent Network) for specifying the transmission matrix. Figure 2.3 shows the unit-cell model based on this analytical method (Rahmani, 2017). As we can see in the figure 2.3(a), the unit-cell presented as a cascade of two ports networks: two microstrip transmission lines, two step discontinuities, and a transmission line with three shorted vias on the side. The most important block in the UC's model is the transmission line with via which its proposed TEN model is introduced in figure 2.3(b).

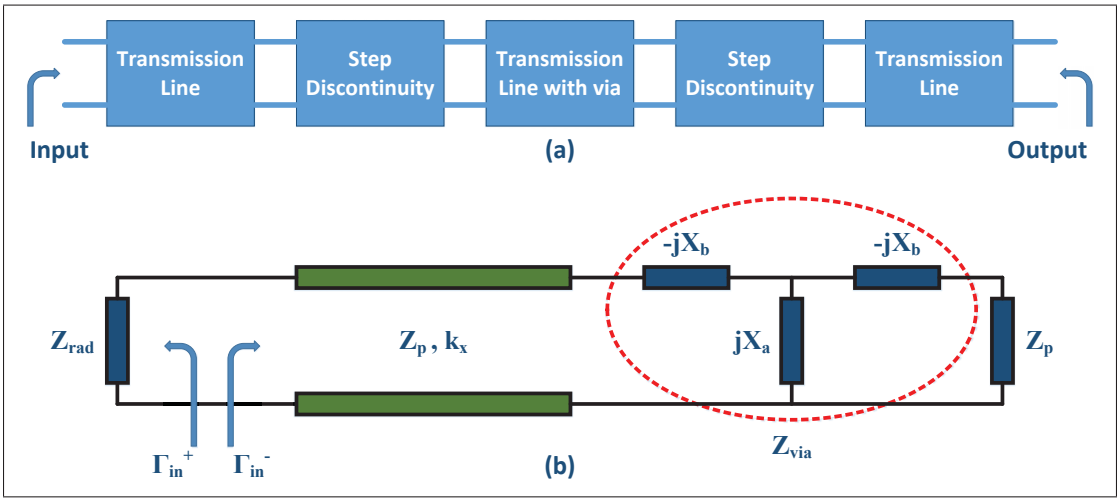

Figure 2.3 UC Model, a) Decomposed 2 ports network model of the UC, b) Proposed TEN for the transmission line with vias Taken from Rahmani (2017).

The analytical model of the unit-cell and how to find the mathematical presentation of its blocks are well formulated and studied in Rahmani (2017). The reader may refer to this reference for more in detail analysis. Although, the transmission parameters of a unit-cell can be specified using these mathematical equations, but the easier and more accurate method in the design and optimization process is to take advantage of a full-wave simulator software to obtain these parameters. We will cover this subject completely in the next chapter.

2.3.4 Input Impedance and OSB Elimination

In order to increase the impedance bandwidth of the proposed periodic LWA, the unit-cell must be self-matched with $Z_0 = 50\,\Omega$ over the desired frequency band. In this way, there will be no need for an extra matching circuit when cascading the UCs to build the periodic antenna structure. This ensure us that the periodic repetition of the UCs in PLWA structure will still be matched over the entire bandwidth. On the other hand, (Paulotto *et al.*, 2009) has proven that a matched unit-cell will not show an open-stopband (OSB). The input impedance of the proposed unit-cell can be obtained from the equivalent T network presented in figure 2.4.

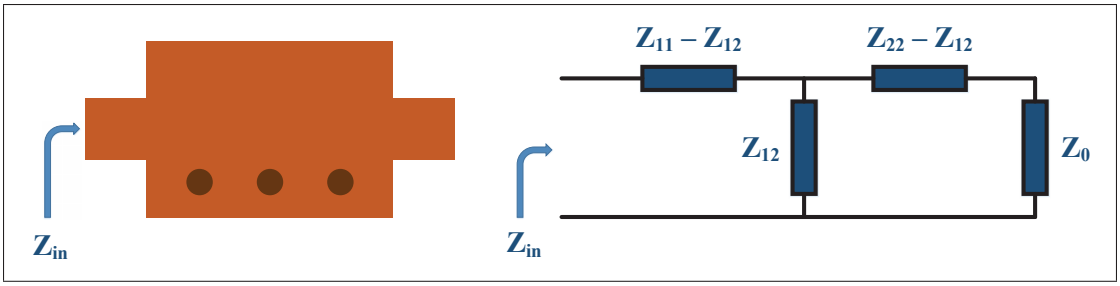

Figure 2.4 Equivalent T network of a unit-cell.

As we know, one side of the structure will be terminated by a matched load of $Z_0 = 50\,\Omega$. Thus, the input impedance of a single unit-cell can be determined by:

$$Z_{in} = [\,(Z_0 + Z_{22} - Z_{12}) \,||\, Z_{12}\,] + Z_{11} - Z_{12} \tag{2.6}$$

where Z_{in} is the input impedance of a single unit-cell based on the impedance matrix of the structure. In order to have a self-matched UC, the input impedance have to be close to Z_0, but in a unoptimized UC normally the imaginary part has a high value and the real part is non-constant, especially in the broadside. Fortunately, this problem can be solve through a proper optimization process of the unit-cell. In the next chapter, we will present an optimized unit-cell that is self-matched over a wide frequency range and we will show that there will be no OSB over the radiation region and the final antenna structure stay matched on that frequency band.

2.3.5 Scanning Range Limitations

In order to have a single beam radiation using a periodic LWA without emerging the grating lobes, only one space harmonic ($n = -1$) among infinite number must exist in the radiation region. This requirement implies two conditions of $\beta_{-2} < -k_0$ and $\beta_0 > k_0$, while β_{-1} stays inside the radiation region (Collin & Zucker, 1969). The relative permittivity of the structure's substrate has a major role in controlling the scanning sensitivity of the periodic LWA with the input frequency (Yang *et al.*, 2010; Henry & Okoniewski, 2016).

Choosing low values of the relative permittivity ε_r for structure's substrate results in a higher fundamental group velocity which in turn lowers the scanning sensitivity of the antenna with respect to the input frequency (Collin & Zucker, 1969). This means, the slope of β_{-1} versus frequency will decrease which it allows the scanning to occur over a larger frequency range. Hence, while choosing the suitable substrate for our application, we have to consider two conditions that restrict the radiation region and one criteria on the scanning angle range over the desired frequency band. Of course, we also need to keep in mind that our choice have to be among the available technologies for the fabrications.

2.3.6 Study of Geometrical Parameters

Here, we investigate the effect of each unit-cell's geometrical parameter on the radiation performance by monitoring the attenuation constant. This study will be more helpful during the fine-tuning process after the optimization of unit-cell. Among nine independent geometrical parameters that were introduced in the figure 2.1, we keep three of them constant, considering the available technology for the fabrication (d via diameter, h substrate thickness and t metal thickness). Figures 2.5 and 2.6 present the attenuation constant of a cascade of five unit-cells (to consider the mutual coupling between UCs) versus six geometrical parameters, which is performed using Ansoft HFSS (Ansoft, 2020). The increase or decrease in the attenuation level and the movement of the OSB into higher or lower band versus the parameter's variation are noticeable in these figures. More parametric study can be found in Rahmani (2017).

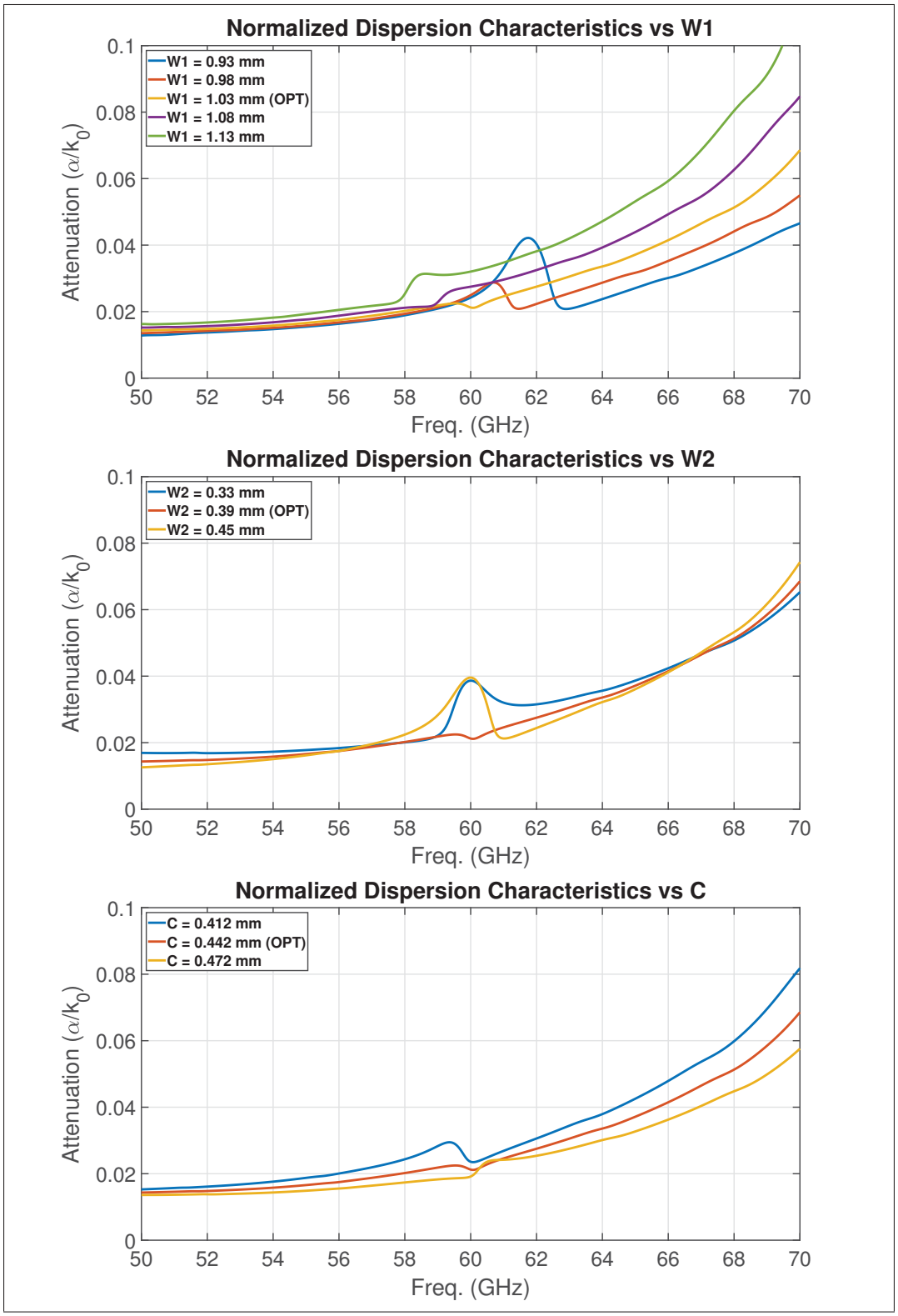

Figure 2.5 Study of the geometrical parameters (W_1, W_2, C).

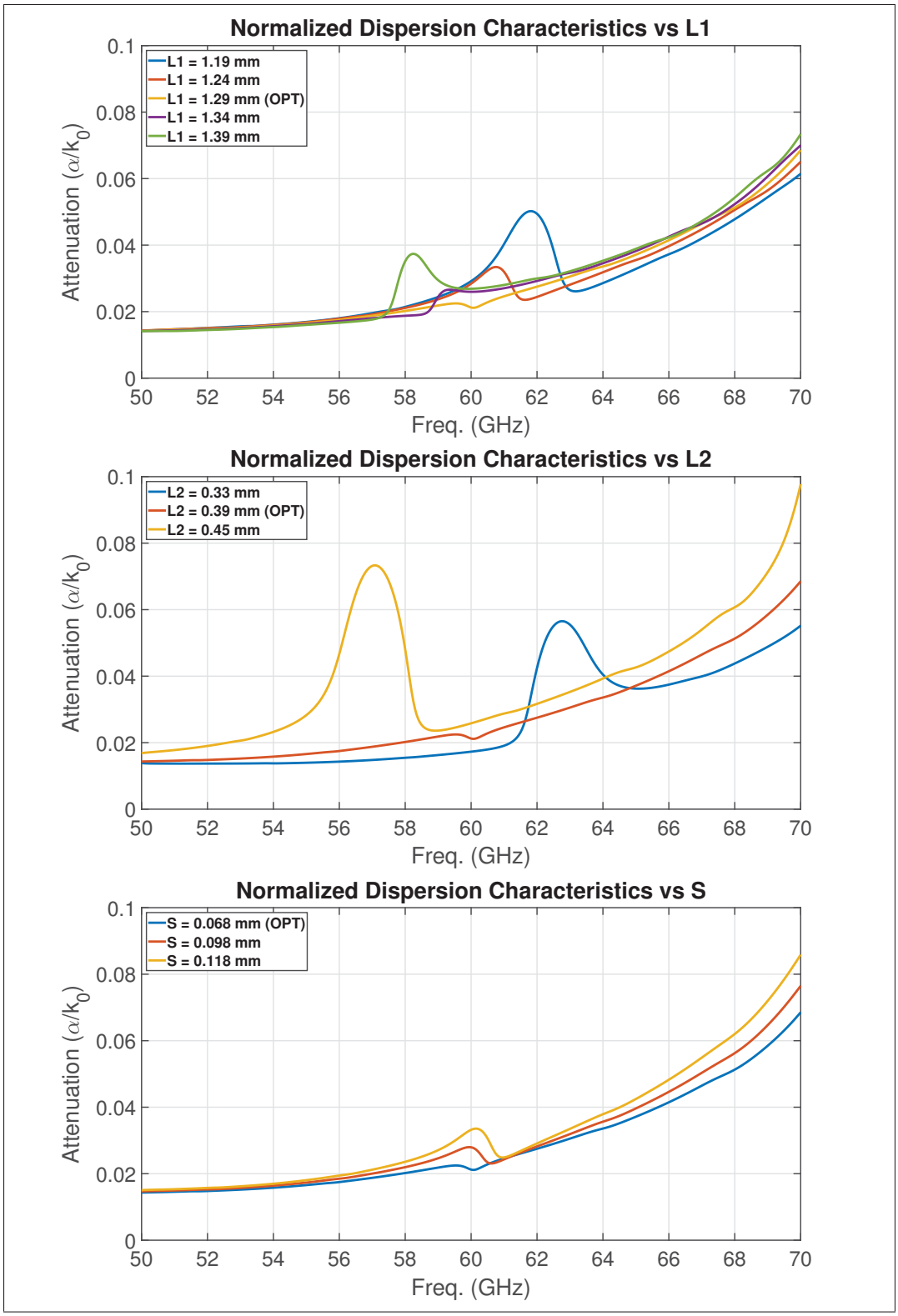

Figure 2.6 Study of the geometrical parameters (L_1, L_2, S).

2.3.7 Side Lobe Level

A periodic LWA could be considered as an array of series fed radiators. Thus, there will be side lobes in the radiation pattern and the SLL which must be kept as low as possible. The side lobes emerge because our structure is not infinite and the aperture distribution is uniform. However, it is possible to reduce the SLL by controlling the aperture distribution using the tapering technique (Jackson & Oliner, 2008). This technique on a periodic LWA is performed by reshaping the attenuation constant of each unit-cell in the antenna to the desired aperture distribution, while holding all the phase constants fixed-slope with the frequency. It means, all of the unit-cells in the periodic structure have the same phase constant variation over the bandwidth, but their attenuation constant is unique and follows a specific distribution.

The first step of tapering is to determine the aperture distribution function based on the desire SLL (Rahmani, 2017). It should be noticed that not all the distributions are feasible duo to impractical value of the attenuation constant. The tapering on the proposed PLWA can be achieved by a slight movement of the vias in the unit-cell body while the dimension stays the same. It is a really time-consuming, difficult procedure, because each unit-cell should be optimized according to its position on the structure. Moreover, it is very unlikely to achieve the desire aperture distribution in the fabrication for high frequency applications due to small dimension of the structure and the fabrication's accuracy in these frequency bands.

2.3.8 Circular Polarization

The axial asymmetry caused by the vias on one side of the proposed unit-cell provides an elliptical polarization. This is because of the quadrature phase relationship between the series and shunt radiation contributions in the periodic LWA (Otto *et al.*, 2014). If the axial ratio (AR) of the antenna is reduced to zero through the optimization process, we will have a circular polarization. The axial ratio optimization could be achieved by adjusting the asymmetry of the unit-cell in such a way to obtain the Q-balance state where series and shunt radiation quality factors are equal. This procedure can be performed using a full-wave simulator software by

changing the position of the via with respect to asymmetrical axis and monitoring the AR value on the main beam direction at the desired frequency. It should be considered that the position of the vias affects the impedance bandwidth, radiation characteristic at broadside and the axial ratio. Therefore, there will be a trade-off between these features while adjusting the position of vias. A study related to this trade-off is presented in Rahmani (2017). Figure 2.7 illustrates a simple visual presentation of the surface current flow on the proposed unit-cell when different ports are excited. These current flows produce the RHCP and LHCP radiation depending on the direction of circulation.

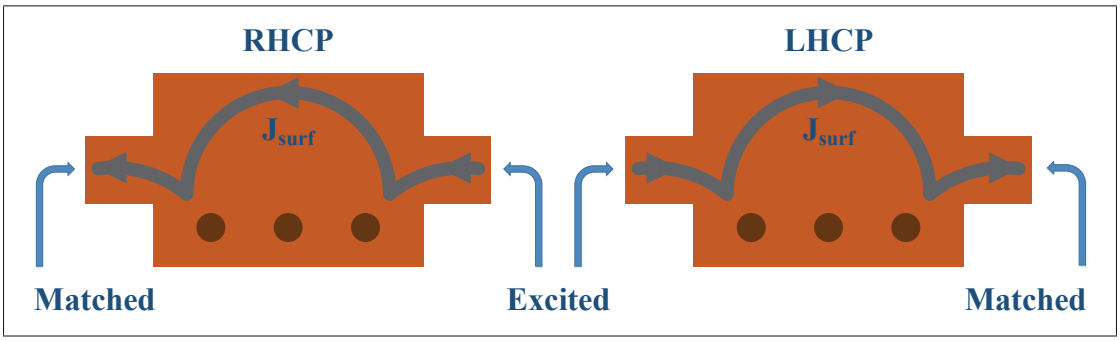

Figure 2.7 Circular polarization with respect to the surface current.

2.4 Conclusion

Here, a general introduction to the leaky-wave antenna was presented and its advantages for our application were discussed. Then, the proposed PLWA was introduced and its features and performance were investigated in separate sections. An empirical model for the proposed unit-cell along with the reference to the mathematical model was suggested. Main issues in the design procedure of suggested PLWA were reviewed. Also, one study on the effect of the geometrical parameters of a unit-cell on the performance of the whole antenna was presented.

CHAPTER 3

DESIGN AND OPTIMIZATION PROCESS

3.1 Introduction

In the previous chapters, the background theory and mathematical model of all components of the proposed structure were introduced. This section is about the design and simulation part of the project. Here, we present the actual design procedure and optimization process of each component to achieve the certain goal. Obviously, the procedure can be repeated for different objectives: having the maximum bandwidth, higher gain, wider beam-scanning angle, improved axial ratio, higher efficiency and etc. We will present the simulation results for some of these objectives in this chapter.

The proposed antenna has a periodic leaky-wave structure, which means it is made by repetition of smaller parts named unit-cell. First, we are going to explain the design and optimization procedure for a single unit-cell which is easier and faster than designing the whole antenna. Then, we extend it to have a complete structure by considering some challenges. One of the challenges is the mutual coupling between adjacent unit-cells and another one is wave-leakage from the SIW wall that we are going to address them. We conducted a study on the second challenge which will be presented as the study on number of vias.

In the next section, an alternative antenna design will be introduced. The proposed antenna contain vias to the ground plane forming a SIW's wall. These vias sometimes are difficult to get aligned with the structure in the fabrication procedure. They add one extra step in manufacturing procedure and there is a possibility of poor connection or no connection at all. Therefore, elimination of via from the structure would save a lot of time and costs. We will present an antenna without via as an alternative. This would be a fully-printed antenna.

Using leaky-wave structure, we have a reconfigurable radiation beam pattern in the direction of propagation. To have the radiation beam which steers in two perpendicular directions and

scans 3D space, we exploit an array of the same antenna. This phased-array makes possible the perpendicular scanning to the direction of propagation. The feed network of a phased-array can be very bulky and costly. Rotman lens is used as the feeding network to have a simple and low-cost structure. This low-profile, passive element is printed on the same layer of the antenna. Rotman lens design and simulation will be discussed in the next part, followed by an array of proposed antenna.

3.2 Unit-Cell design

Design, simulation and optimization of the whole structure of antenna is a very complicated and time-consuming process. Fortunately, by having a periodic structure, we don't need to perform the entire design procedure at once (Pozar, 2011; Rahmani, 2017). Instead, we start with the single unit-cell design which is faster and easier to carry out. Then, after achieving the desired features in that unit-cell, we can extend it to the periodic antenna structure by a little fine-tuning, considering mutual coupling between unit-cells (Rahmani & Deslandes, 2017).

In the first step, we sketch the model of proposed unit-cell structure in the HFSS simulator software (Ansoft, 2020). As mentioned earlier, the unit-cell is composed of two transmission lines with different width which creates two discontinuities. The wider transmission line is shorted to the ground plane on one side through three vias, constructing a SIW-wall. Later in this chapter we will explain why we chose three vias for this purpose. Figure 3.1 shows the unit-cell structure with its all dimension parameters.

Next step is to setup the Optimetrics feature of the simulator software to find an optimized unit-cell for our objective. For that purpose, we should specify the parameters that we want to be optimized, determine their initial values and their sweep ranges. Then, we should define the output variables which are our target in the process of optimization. According to chapter two, the unit-cell should be designed and optimized so that to eliminate the open-stopband. That will be achieved by impedance matching over the entire frequency range. This procedure can be accomplished using a full-wave simulator software, Ansys HFSS (Ansoft, 2020).

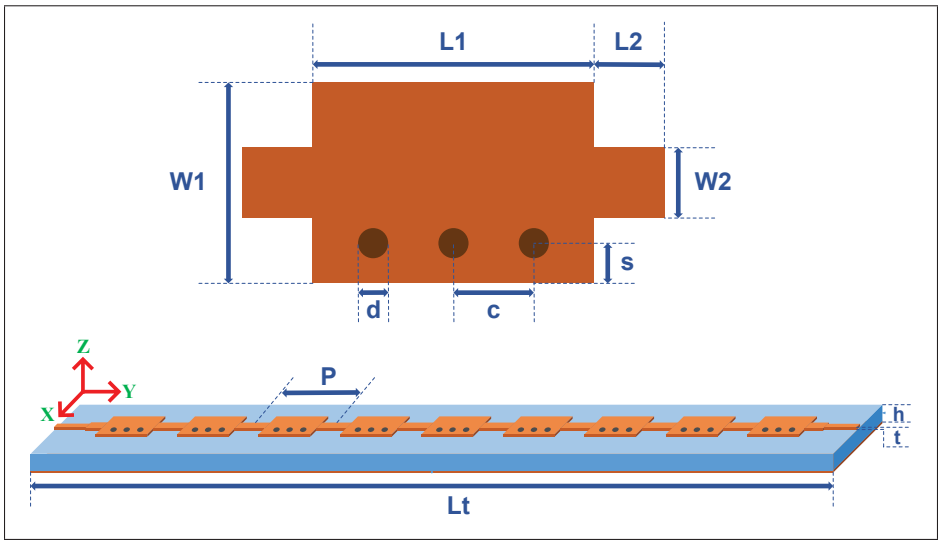

Figure 3.1 The unit-cell's dimension parameters and Antenna's periodic structure on LTCC substrate.

3.2.1 LTCC substrate and metal

There are some limitations for the substrate that we can actually employ in this project. As mentioned earlier, the periodic repetition of the unit-cells in the LWA's structure produces an infinite number of space harmonics that can be fast or slow. To have the single beam radiation, only one space harmonic must exist inside the radiation region; Otherwise, grating lobes will appear (Jackson & Oliner, 2008). This will imply the condition sets of $\beta_{-2} < -k_0$ and $\beta_0 > k_0$ while β_{-1} have to stay in the radiation region (Collin & Zucker, 1969). On the other hand, the relative permittivity of the substrate has the most important role in the scanning sensitivity of the periodic LWA over the frequency range (Henry & Okoniewski, 2016; Yang *et al.*, 2010). The higher values of the dielectric constant will result in more scanning sensitivity of phase constant to the frequency. It means, by increasing the relative permittivity ε_r, the slope of phase constant β will also increase, which lead to lower fundamental group velocity and wider beam scanning angle over the desired bandwidth. A study on the scanning range limitations is presented in Rahmani (2017) and Rahmani & Deslandes (2017). You can refer to the dispersion diagram of the optimized unit-cell showing the space harmonics and the radiation range for more information in this subject.

Our target bandwidth for WiGiG application is 57 to 64 GHz (Hansen, 2011) which is not very wide for this band (fractional bandwidth of 11.6%). In addition, we want to have the maximum beam scanning angle over this range of frequency to cover more spatial area (at least 45°). As aforementioned, to have wider beam scanning angle, we need a substrate with higher dielectric constant. But, we are limited to choose our LTCC substrate among the accessible material. The dielectric and conductor losses at high frequency and substrate's shrinkage after baking are other factors that should be considered while choosing the suitable substrate.

For this project, we decided to fabricate our antenna structure on the LTCC substrate in Microelectronics and Communications Research Lab (LaCIME) of École de Technologie Supérieure (LTCC@ÉTS, 2020). In this laboratory, we are able to perform all the steps of fabrication on the LTCC including metal printing, via filling, punching, layer stacking, laser ablation, cutting and etc. We have access to the different types of substrate and metal. Summary specification of the available material can be found in the tables 3.1 and 3.2.

Table 3.1 Available LTCC Systems

		GREEN TAPE			
		DUPONT		**FERRO**	
		951	9K7	L8	L6M
METAL	Gold	Not Available	Available	Available	Available
	Silver	Available	Available	Available	Available
	Copper	Not Available	Not Available	Available	Available

Table 3.2 Substrates Properties

Parameter	**Condition**	**951**	**9K7**	**L8**	**L6M**
Dielectric Constant	@10GHz	7.5±0.2	7.1±0.2	7.2±0.2	5.7±0.2
Loss Tangent	@10GHz	0.006	0.001	0.002	0.001
X,Y Shrinkage	%	12.7±0.3	9.1±0.3	13.2±0.3	15.8±0.3
Z Shrinkage	%	13.0±0.2	11.8±0.5	30.0	26.0

We need a substrate with high dielectric constant and low loss tangent to have the maximum beam scanning angle with the minimum dielectric loss. Therefore, We chose DUPONT 9K7 Green Tape as the substrate of our periodic LWA. This LTCC substrate is designed for high frequency application. Besides, It has the smallest percentage of the shrinkage after baking, which means the structure would have the minimum change in the dimension. Then, for the antenna printing and via filling, we use silver as the metal duo to its high electrical conductivity (6.3×10^7) which lead to less conductor loss. Although, it is more prone to the oxidation than the copper and gold; but it won't be a problem, if we devise a coating for the antenna or complete all the measurements as soon as possible after the fabrication.

The next thing we must designate is the thickness of the LTCC sheet. For DUPONT 9K7 substrate, we possess the sheets with thickness of 2, 5 and 10 mil in LaCIME. Working with a thin sheet of LTCC not only is difficult due to its fragility, but also increases the surface waves in the leaky-wave structure which result in low efficiency. We simulated an optimized unit-cell on two substrates with thicknesses of 5 and 10 mil. The 5 mil substrate showed almost half of the efficiency of 10 mil substrate. So, we employed the 10 mil LTCC sheet for our project which considering the shrinkage, the final height of substrate would be 224 micron.

Height of printed metal is not very important as long as it is not very low or high. Low value of the height results in high conductor loss and high value does not have any advantage. Actual height of metal would be specified by the stencil which we use for the metal printing. The height of 8 micron is very common that we adopt as well.

There are two options for creating via holes: laser and punch machine. Laser can deliver more accurately positioned via in the metal patch and we have more options for the size and shape of hole. But it is slower and sometimes the shape of via is deformed because of edge's burr caused by laser working. On the other hand, punch machine is fast and creates clean, round via. But only the size of 150 micron is available in our punch machine. We tried both methods for the comparison that will be presented in the chapter 5. So, the same size of via was taken for both methods which, by considering the shrinkage of substrate, would be 136 micron.

3.2.2 Input parameters and initialization

All parameters in the figure 3.1 should be determined during the design phase. These parameters define the structure of the unit-cell. Some of them already have the fix value due to the prerequisites of project that we introduced in the previous section. The rest are optimization's parameters, for which we have to specify the initial value and the sweeping range. The purpose of the optimization procedure is to find an optimal value for each one of them in the sweeping range so that the whole unit-cell shows our desired features. Table 3.3 shows all of the input parameters and their values including the fix and optimization's parameters.

Table 3.3 Input Parameters of proposed Unit-cell

Fixed Parameters				**Optimization Parameters**		
Name	**Symbol**	**Fix Value**	**Unit**	**Symbol**	**Initial Value**	**Unit**
Relative Permittivity	ε_r	7.1		L_1	1.319	mm
Dielectric Loss	$tan\delta$	0.001		L_2	0.388	mm
Metal Conductivity	σ	6.3×10^7	S/m	W_1	1.039	mm
Substrate Height	h	224	micron	W_2	0.388	mm
Metal Thickness	t	8	micron	s	0.170	mm
Via Diameter	d	136	micron	c	0.465	mm

Start point for the optimization process is very important, because in most of cases it determine whether the solution is converging or not. Besides. it affects the processing time. The next step is specifying the sweeping range of each parameter. This will determine also the sweeping step. We should be careful about choosing the range because the final value may not be practical. Here, we fix the sweeping range to 30 percent of the initial value.

There are two ways to choose initial value for the optimization's parameters. First one is to take advantage of the mathematical model presented in Rahmani (2017) to estimate the size of structure. This approach is very time-consuming and the result is not very accurate duo to the difference existing between mathematical and actual model in reality. An easier solution is to

exploit the optimized values of the similar structure presented in Rahmani & Deslandes (2017) using a proper scaling factor. That unit-cell was designed for the center frequency of 25 GHz with relative permittivity of 6.15. Our target is to have an antenna at center frequency of 60 GHz with relative permittivity of 7.1. The height of substrate for both structure is almost the same and the size of via is very complicated to be considered. Therefore, we can ignore these parameters in the calculation of the scale factor. The optimization parameter's initial values in the table 3.3 are estimated based on this equation:

$$L_2 = L_1 \times \sqrt{\frac{\varepsilon_{r1}}{\varepsilon_{r2}}} \frac{f_{c1}}{f_{c2}} \tag{3.1}$$

Where L_1 and l_2 are old and new lengths, ε_{r1} and ε_{r2} are old and new relative permittivities and f_{c1} and f_{c2} are old and new center frequencies. This formula is extracted from the microstrip line length formula in the reference book of (Pozar, 2011). By looking at the equation 3.2 and considering a constant phase ϕ, we observe that the length L is in reverse relationship with the effective permittivity ε_e and frequency f. As we expected, increasing the value of relative permittivity and frequency will decrease the length of microstrip line.

$$\phi = \sqrt{\varepsilon_e} k_0 L = \sqrt{\varepsilon_e} \frac{2\pi f}{c} L \tag{3.2}$$

3.2.3 Target features

The final structure of our antenna must shows certain specifications relating to the Matching, Bandwidth, Gain, Efficiency, Circular Polarization, Grating Lopes and etc. However, we don't need to check all of these features in the unit-cell's design and optimization procedure. Setting different criteria for each feature and running the simulator using diverse Optimetrics Analysis Functions, gives us multiple good candidates for further evaluation. Below is the specifications which are our target features of the periodic LWA:

- The periodic LWA should be matched over the entire bandwidth to 50 Ω microstrip line. It means, Return Loss $|S_{11}|$ is supposed to be better than 10 dB from 57 to 64 GHz.
- At least 90% of the input power have to dissipate by radiation along the periodic LWA's body. So, Insertion Loss $|S_{21}|$ must be close or higher than 10 dB from 57 to 64 GHz.
- Center frequency of the antenna is 60 GHz. Therefore, phase constant β should be zero at this frequency and the Return Loss $|S_{11}|$ be in its maximum value.
- Antenna must have a seamless, constant beam scanning over the desired bandwidth showing no open-stopband. This implies that the phase constant β to have a smooth slope versus the frequency and the attenuation constant α to be as flat as possible.
- Antenna supports the circular polarization. Hence, Axial Ratio should be less than 3 dB.
- Gain and efficiency must be as high and constant as possible with the frequency.

The output variables which we need to monitor and inspect for achieving our target features in the periodic LWA are listed bellow. We employed some of them in the simulation setup to gain a certain goal. But the others are only used to plot and check the functionality of the antenna.

- Return Loss $|S_{11}|$
- Insertion Loss $|S_{21}|$
- Phase Constant β
- Attenuation Constant α
- Input Impedance Z_{in}
- Axial Ratio
- Gain
- Efficiency

Return Loss and Insertion Loss are accessible in the HFSS full-wave simulator (Ansoft, 2020). Also, HFSS can compute Axial Ratio, Gain and Efficiency of the antenna through its post process mechanism. We have to define Phase Constant, Attenuation Constant and Input Impedance in the output variables of the project. Propagation Constant was calculated using equations 3.3 to 3.9 (Pozar, 2011) and Input Impedance by equations 3.10 (Rahmani & Deslandes, 2017).

$$k_0 = \frac{2\pi f}{c} \tag{3.3}$$

$$A = \frac{(1+S_{11})(1-S_{22})+S_{12}S_{21}}{2S_{21}} = \frac{Z_{11}}{Z_{21}} \tag{3.4}$$

$$D = \frac{(1-S_{11})(1+S_{22})+S_{12}S_{21}}{2S_{21}} = \frac{Z_{22}}{Z_{21}} \tag{3.5}$$

$$\alpha = \frac{real(\gamma)}{k_0} = \frac{1}{nPk_0}\, real(cosh^{-1}\frac{A+D}{2}) \tag{3.6}$$

$$\alpha = -\frac{ln(S_{21}^2) - ln(1-S_{11}^2)}{2nPk_0} \tag{3.7}$$

$$\beta = \frac{imag(\gamma)}{k_0} = \frac{1}{nPk_0}\, imag(cosh^{-1}\frac{A+D}{2}) \tag{3.8}$$

$$\beta = -\frac{angle(S_{21})}{2nPk_0} \tag{3.9}$$

$$Z_1 = Z_0 + Z_{22} - Z_{12} \quad , \quad Z_2 = \frac{Z_1 Z_{12}}{Z_1 + Z_{12}} \quad , \quad Z_{in} = Z_2 + Z_{11} - Z_{12} \tag{3.10}$$

3.2.4 Optimization Solution

In the previous sections, we defined our input and output variables for the optimization procedure of one unit-cell. Also, we specified our target features that we seek in the final product. But it is not practical to add all of these conditions to the Optimetrics setup. Fortunately, the most important conditions which should be met are the matching-bandwidth and having no open-stopband. If these two conditions, which are not completely independent, are satisfied, the other ones are most likely will be fulfilled as well. We will verify this part manually in the fine-tuning of the whole periodic antenna array.

Table 3.4 shows the calculations that we actually defined for the optimization solution. The first condition will assure the center frequency of antenna at 60 GHz (broadside radiation). The second condition is for achieving the matching over the entire bandwidth. Third and forth one will try to make the normalized attenuation constant α as flat as possible and closed to our desired value. Having flat α vs frequency will guarantee that we have no open-stopband and seamless radiation with constant gain. The value that we chose for α is a empirical value to have the minimum possible number of unit-cells in the periodic LWA.

Table 3.4 Setup Optimization

Solution	Calculation	Condition	Goal	Range	Weight
Last Adaptive	$abs(\beta)$	<=	0.01	$f = 60GHz$	1
Sweep	$dB(S_{11})$	<=	-10	$f = 56GHz : 64GHz$	1
Sweep	α	<=	0.201	$f = 55GHz : 65GHz$	1
Sweep	α	>=	0.199	$f = 55GHz : 65GHz$	1

As optimizer engine, we found Genetic Algorithm (Random Search) the best solution for our optimization setup. It maybe slower to converge compared to the other methods like Newton, but it gives more feasible candidates and also every time you run it, you can have different answers due to its random search feature. While other optimizers follow a certain path to find one proper solution, Genetic Algorithm provides more options to have variety of solutions.

The process starts by using optimization parameter of the simulator to find the closest antenna's feature to satisfy our conditions. It should be mentioned that not all of optimization outputs are practical. For example, some of them are not possible to fabricate due to the impractical dimensions or when via is very close to the edge of metal patch.

To save time, we setup our Driven Solution Analyzer for the single unit-cell to be single frequency solved at 60 GHz, the maximum number of pass equal to 6, the maximum delta S equal to 0.02 and the sweep type is Interpolating from 55 to 65 GHz. In this way, we could have more than 1000 iterations in one day, running the optimizer. After finding some realistic candidates, using manual fine-tuning, we try to find the best feature out of that unit-cell. We seek these features from the fine-tuning process of the unit-cell:

- ☐ Return Loss $|S_{11}|$ is higher than 10 dB from 57 to 64 GHz with the maximum at 60 GHz.
- ☐ Insertion Loss $|S_{21}|$ is as high as possible from 57 to 64 GHz.
- ☐ Phase Constant β has a smooth slope vs the frequency with a zero value at 60 GHz.
- ☐ Attenuation Constant α is as flat as possible with no bump.
- ☐ Input Impedance Z_{in} is close to $50\,\Omega$ from 57 to 64 GHz..

3.2.5 Optimization Results

As previously mentioned, running the simulator with Genetic Algorithm (Random Search), the optimizer provides us the answers with different features. In this section, we are going to present some of our desirable optimization's results after the fine-tuning. Table 3.5 shows the dimension parameters of an optimized unit-cells. Tables 3.6 and 3.7 demonstrate parameters of the unit-cells which have an improved bandwidth and circular polarization respectively. Figures 3.2, 3.3 and 3.4 present the return loss, insertion loss and input impedance of a single unit-cell and the propagation constant of a cascade of five unit-cells for each structure.

Table 3.5 Parameters of an optimized UC.

Parameter	Value	unit	Parameter	Value	unit
L_1	1.290	mm	L_2	0.385	mm
W_1	1.030	mm	W_2	0.390	mm
s	0.136	mm	c	0.442	mm

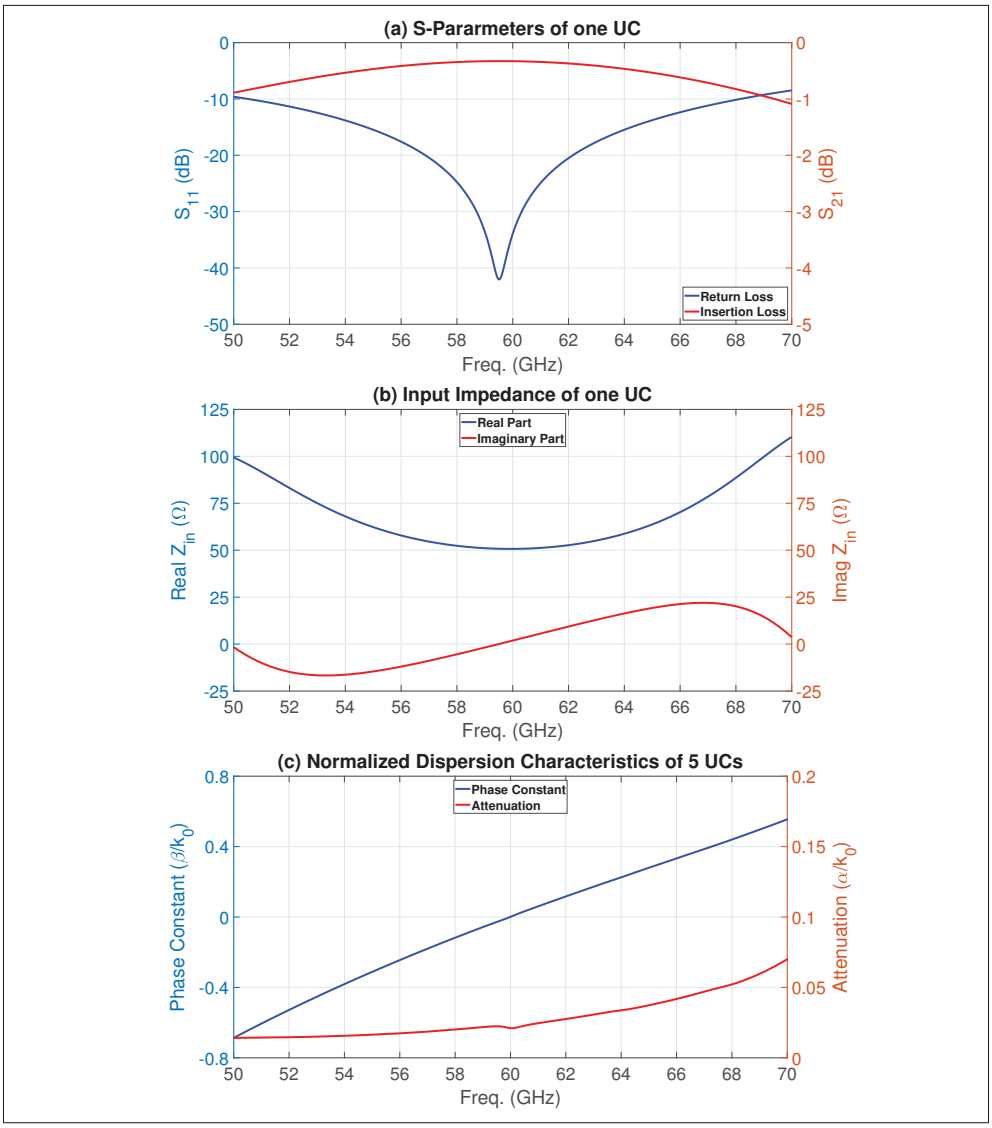

Figure 3.2 (a) S-Parameters of single UC (b) Input impedance of single UC (c) Normalized propagation constant of a cascade of 5 UCs.

Table 3.6 Parameters of an optimized UC with improved BW.

Parameter	Value	unit	Parameter	Value	unit
L_1	1.386	mm	L_2	0.352	mm
W_1	0.900	mm	W_2	0.330	mm
s	0.136	mm	c	0.375	mm

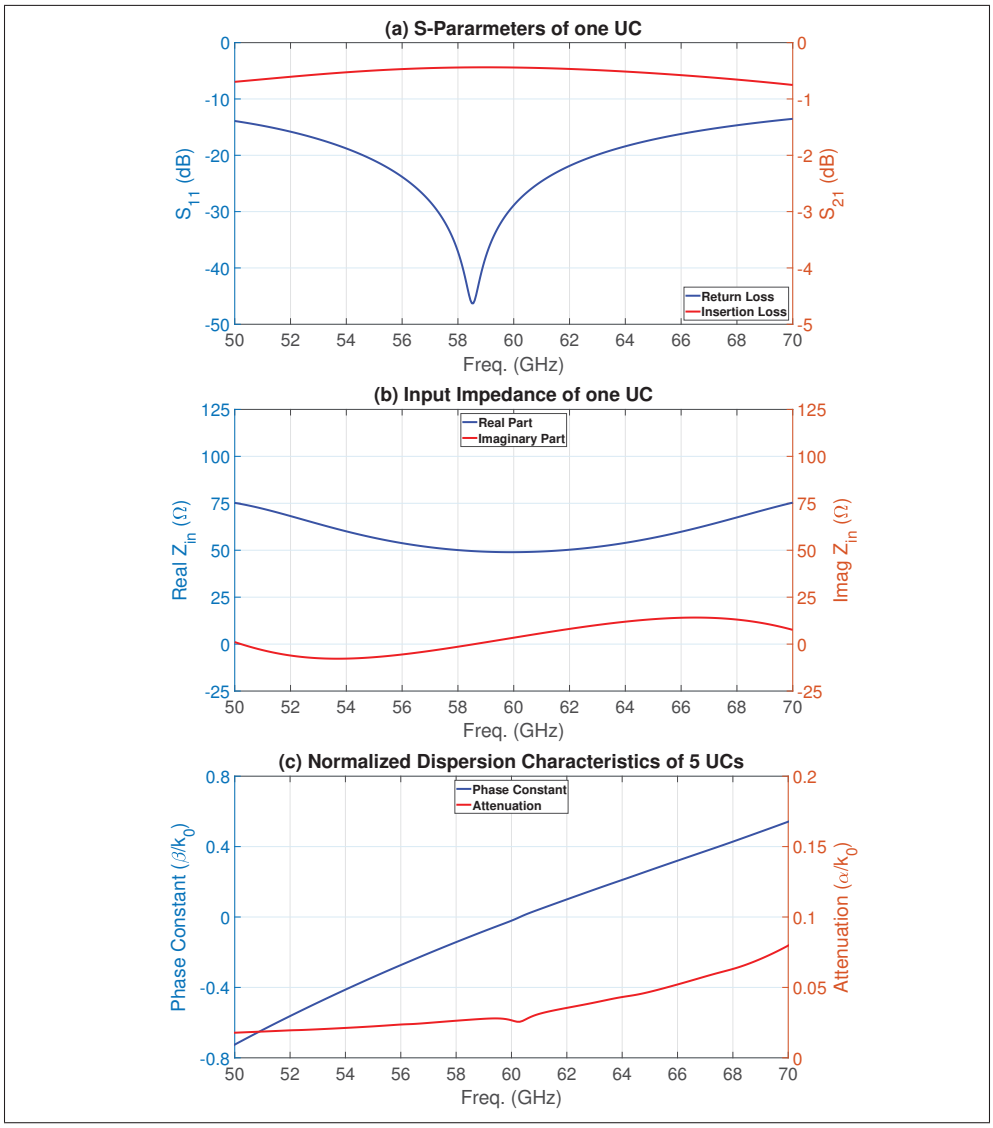

Figure 3.3 (a) S-Parameters of single UC (b) Input impedance of single UC (c) Normalized propagation constant of a cascade of 5 UCs.

Table 3.7 Parameters of an optimized UC with improved CP.

Parameter	Value	unit	Parameter	Value	unit
L_1	1.300	mm	L_2	0.330	mm
W_1	1.020	mm	W_2	0.340	mm
s	0.136	mm	c	0.332	mm

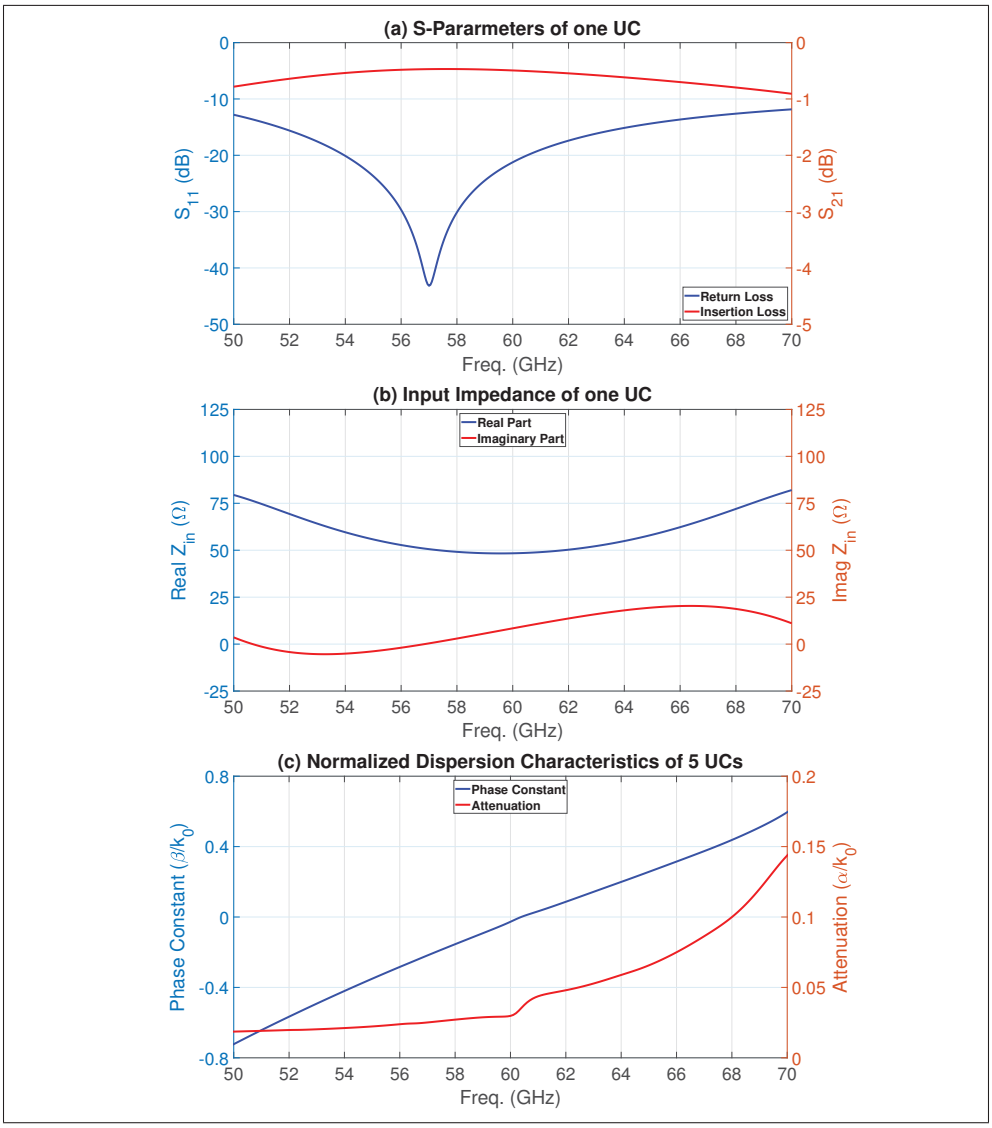

Figure 3.4 (a) S-Parameters of single UC (b) Input impedance of single UC (c) Normalized propagation constant of a cascade of 5 UCs.

3.3 Antenna optimization and fine-tuning

The process of fine-tuning takes place in three phases. First, when the optimizer delivered some viable candidates, we try to find an ideal unit-cell by slightly changing the input parameters, considering the conditions introduced at the end of section "Optimization Solution". Then, we put a series of five unit-cells next to each other to observe how it works as a periodic LWA. In this way, we can examine all the interactions between UCs. Five UCs seems the perfect number for this purpose, because the structure shows almost the same features as infinite numbers of UCs does and also it is very fast to simulate in HFSS.

When we cascade some unit-cells to create a periodic LWA, propagation constant would change slightly. That is due to mutual coupling between adjacent unit-cells and also some effects like wave-leakage through SIW-wall which is intensified by accumulation. One advantage of the proposed antenna is that we could design one small structure named unit-cell and then expand it easily to full antenna structure. Moving from one UC to multiple UCs does not change the output features so much and by a little fine tuning, desirable features can be achieved. Figures 3.2, 3.3 and 3.4 part (a) and (b) show S-Parameters and input impedance of one unit-cell which are only things we need from this step of the design procedure. If one unit-cell is matched over desired bandwidth, the entire periodic LWA after cascading of some unit-cells will be matched. Part (c) of the figures 3.2, 3.3 and 3.4 presents the propagation constant of a cascade of five unit-cells after second fine tuning which shows no open-stopband.

The third time that we may need fine tuning is after constructing the whole antenna. For this purpose, we can put any number of unit-cells next to each other and add a $50\,\Omega$ microstrip line to both side of antenna. Normally, there is no need for fine tuning in this step, but if we have a slight deviation from our target goal, it could be useful. Figures 3.5, 3.6, 3.7 and 3.8 show performance parameters of three presented antenna with 9 unit-cells. Based on efficiency and gain, it seems that 9 unit-cells will be enough for our application; however, insertion loss is a little lower than expected. Figures 3.9, 3.10 and 3.11 demonstrate scanning properties of antenna in three frequencies through antenna's 3-D gain.

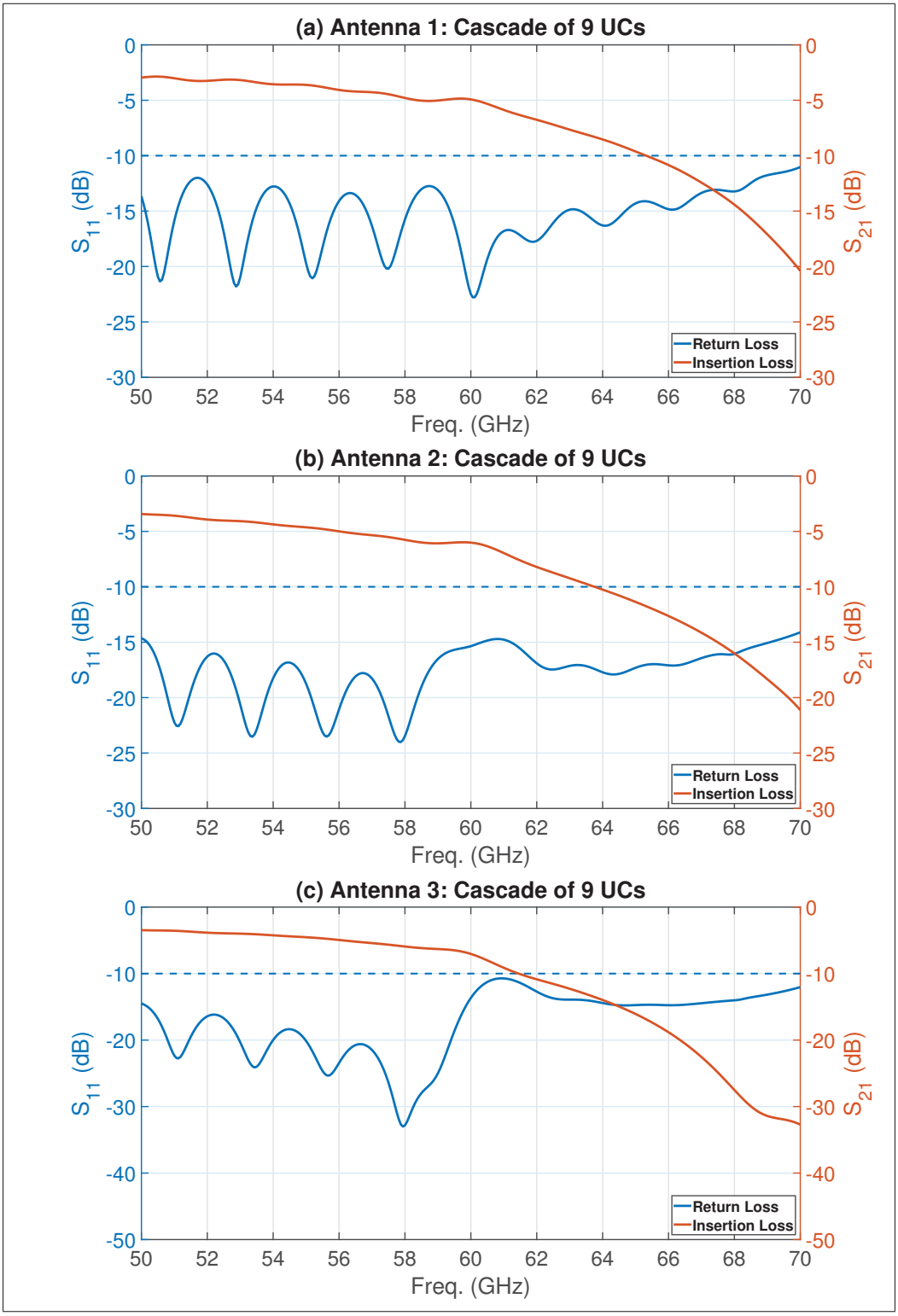

Figure 3.5 Return Loss and Insertion Loss vs Frequency of 9 UCs
(a) Antenna in table 3.5 (b) Antenna in table 3.6 (c) Antenna in table 3.7.

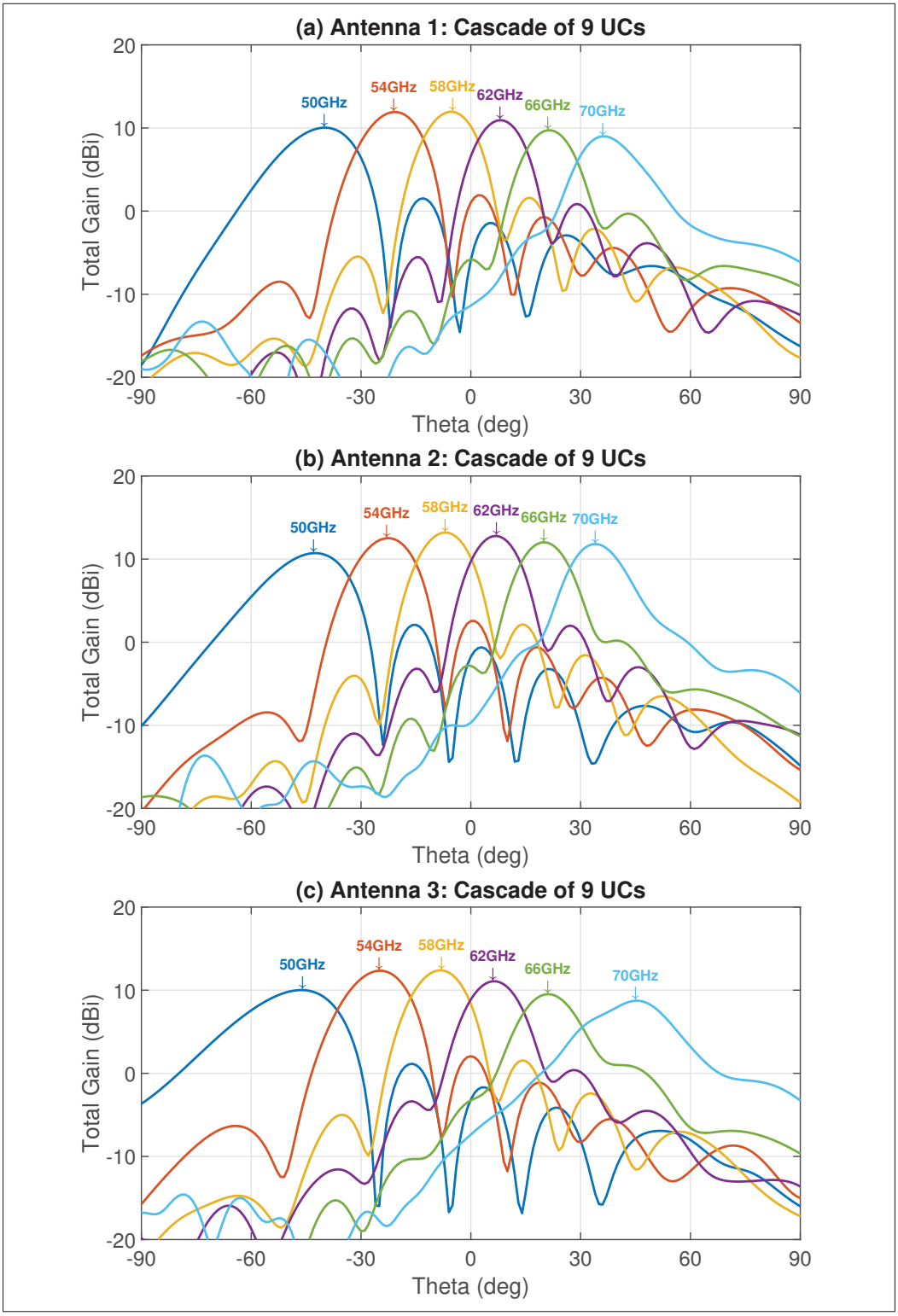

Figure 3.6 Radiation Beam Scanning with Frequency of 9 UCs
(a) Antenna in table 3.5 (b) Antenna in table 3.6 (c) Antenna in table 3.7.

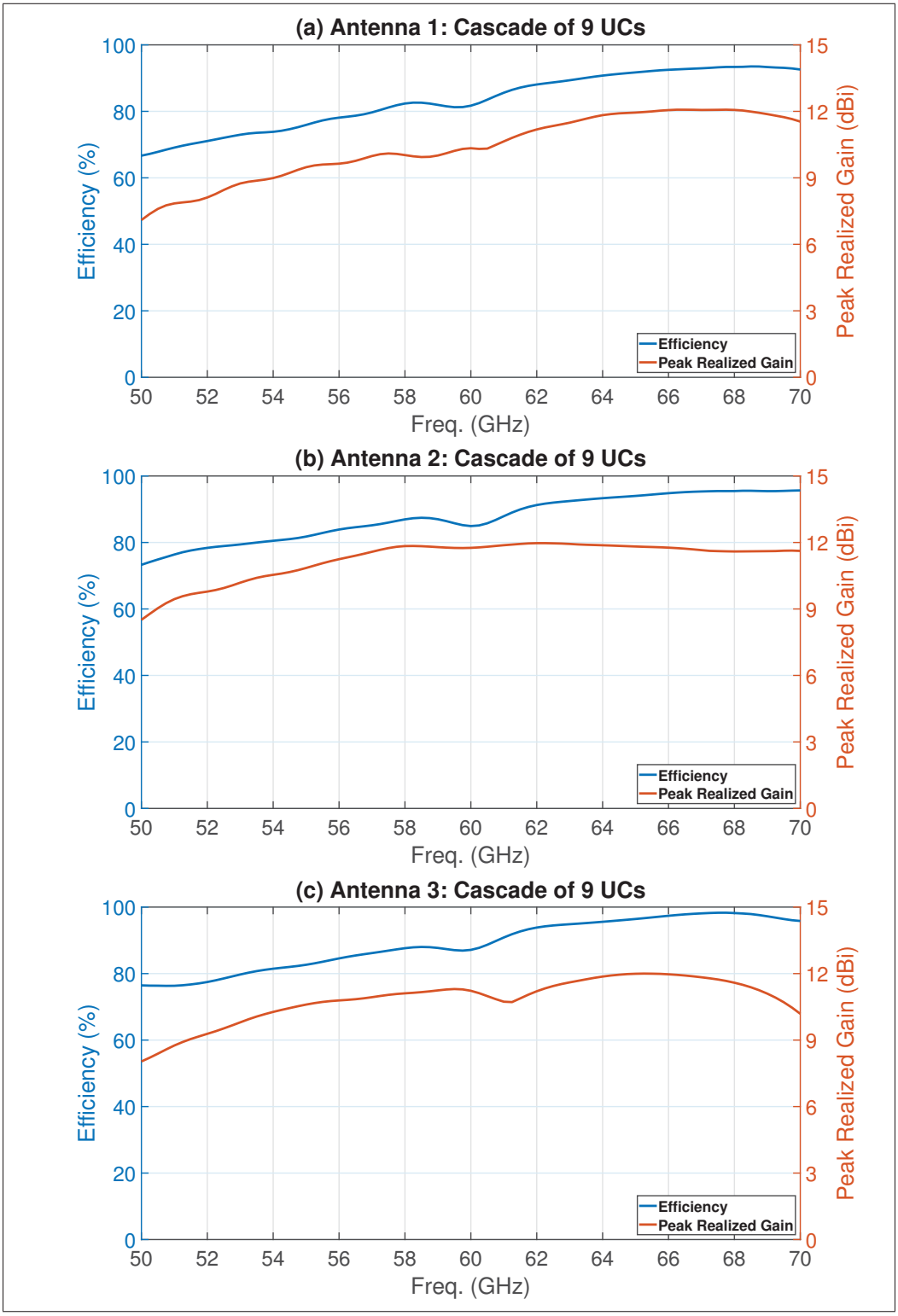

Figure 3.7 Efficiency and Peak Realized Gain vs Frequency of 9 UCs
(a) Antenna in table 3.5 (b) Antenna in table 3.6 (c) Antenna in table 3.7.

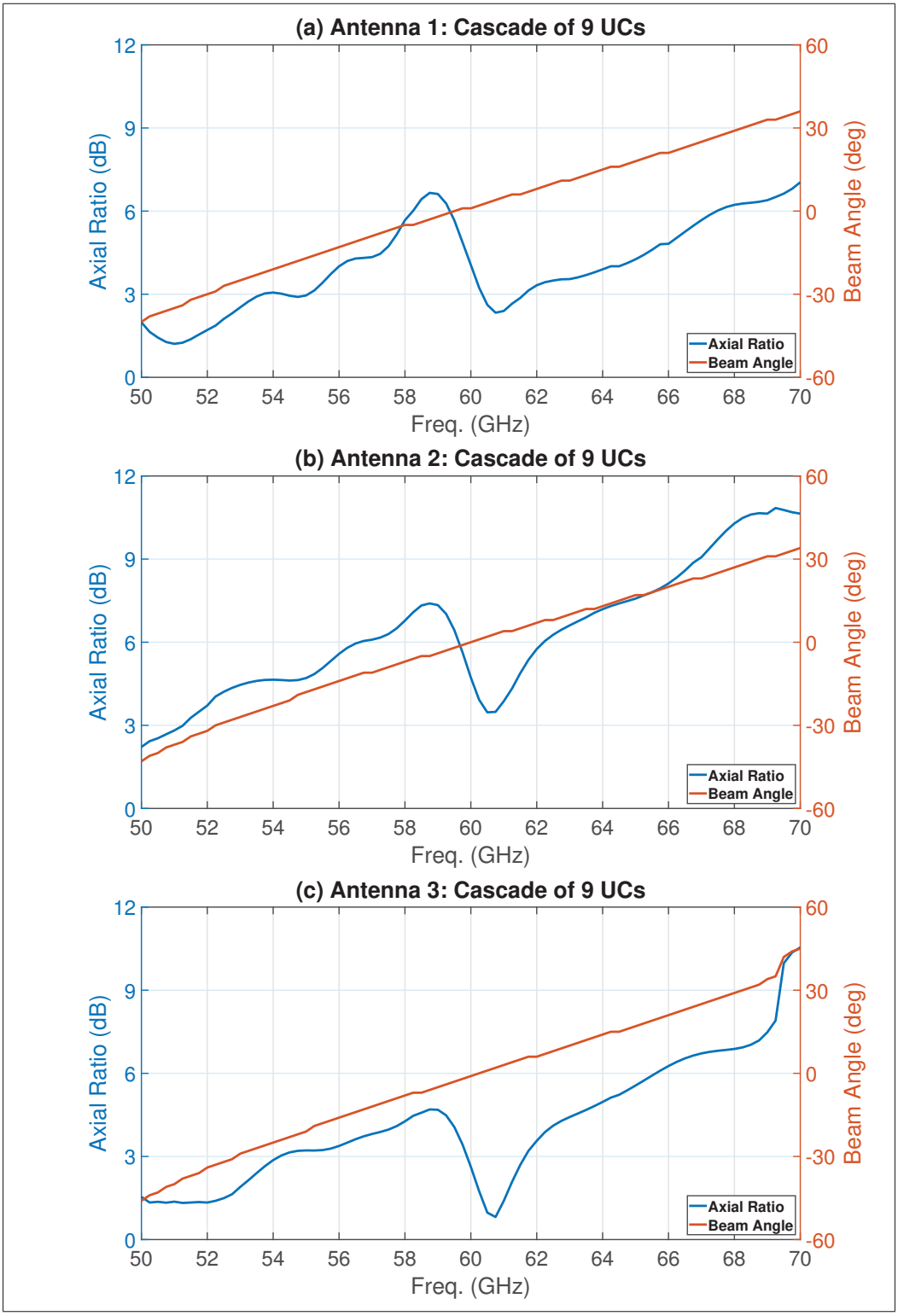

Figure 3.8 Axial Ratio and Main Beam Angle vs Frequency of 9 UCs
(a) Antenna in table 3.5 (b) Antenna in table 3.6 (c) Antenna in table 3.7.

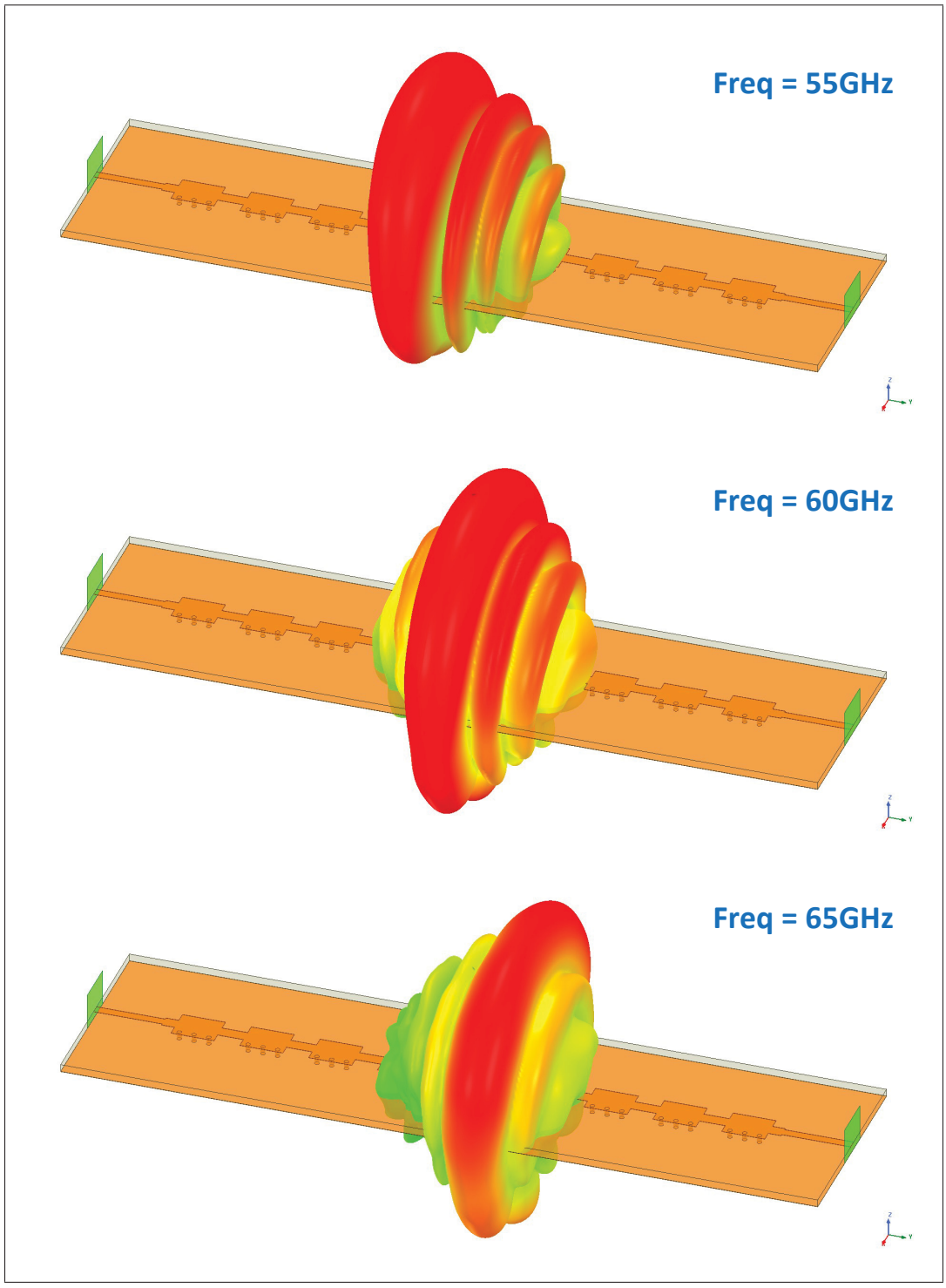

Figure 3.9 3D Gain of Antenna in table 3.5 at 55GHz, 60GHz and 65GHz (backward to forward beam scanning with frequency).

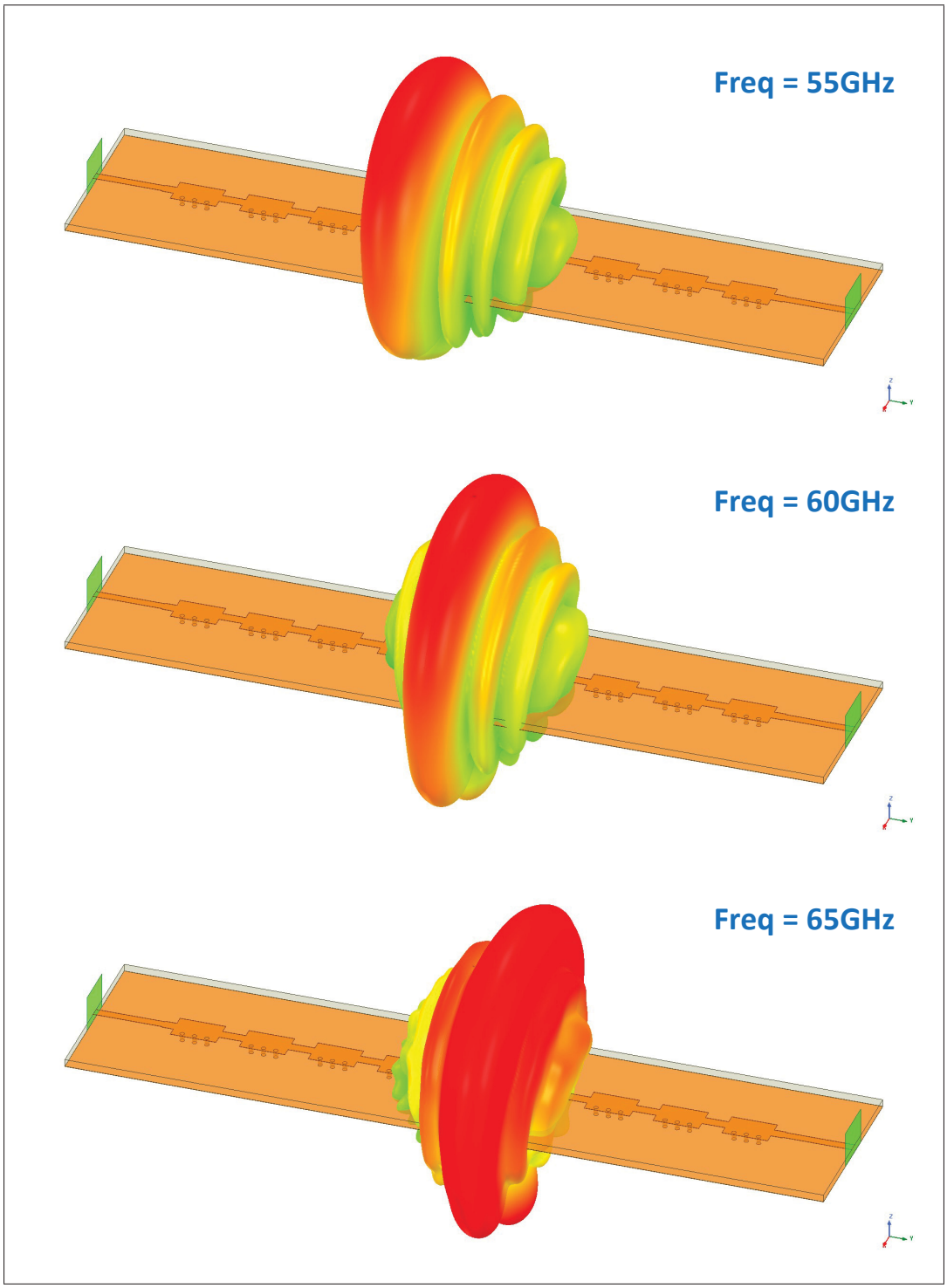

Figure 3.10 3D Gain of Antenna in table 3.6 at 55GHz, 60GHz and 65GHz (backward to forward beam scanning with frequency).

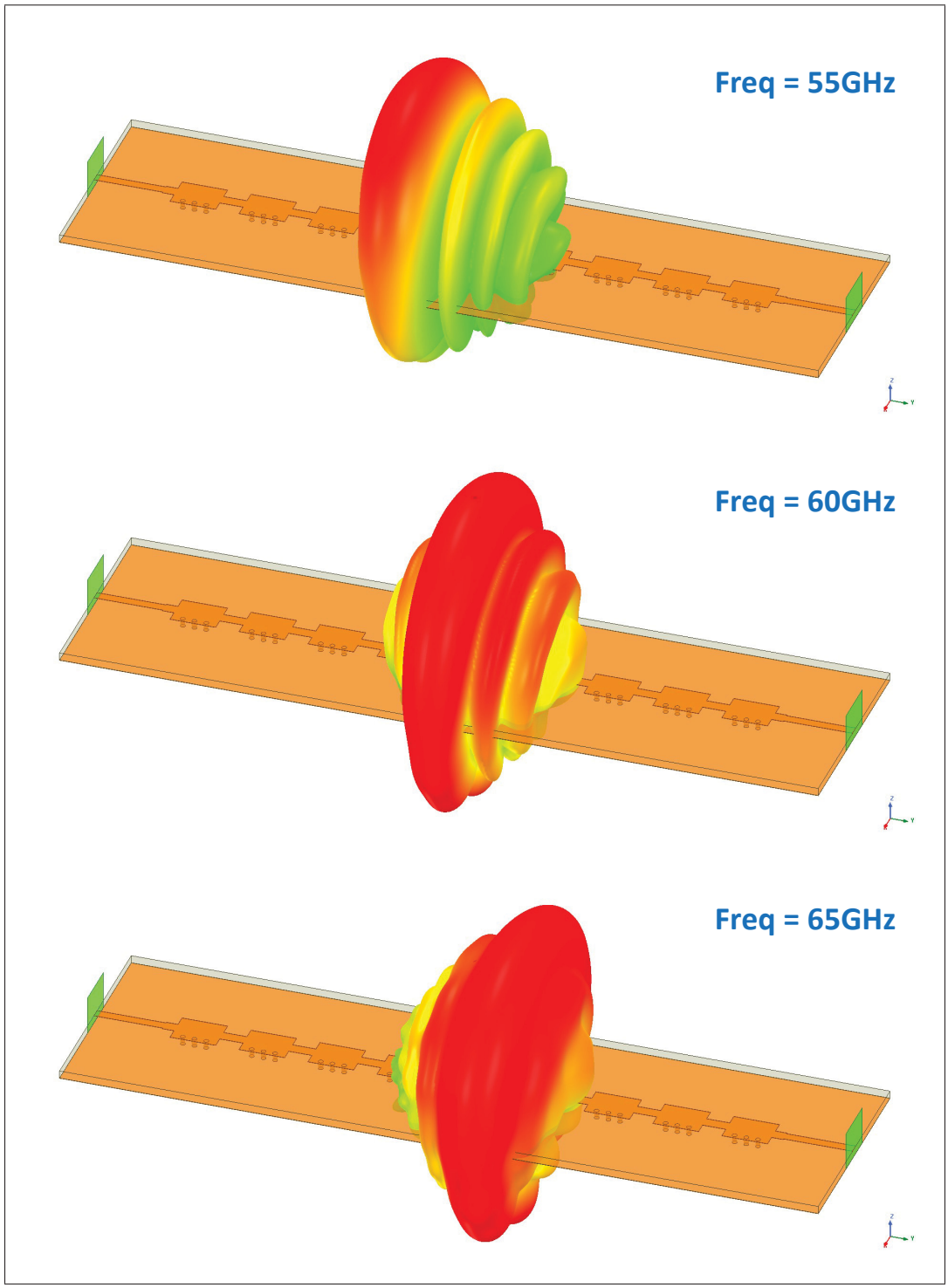

Figure 3.11 3D Gain of Antenna in table 3.7 at 55GHz, 60GHz and 65GHz (backward to forward beam scanning with frequency).

3.3.1 Mutual coupling and wave-leakage from sidewalls

In periodic LWA structure, unit-cells are placed next to each other. Analysis of infinite periodic structure can be found in Pozar (2011). Adjacent unit-cells can load each other. There will be mutual coupling between radiating elements in two neighboring unit-cells that causes a shift in center frequency and some deviations in propagation constant. However, these changes are not significant and could be resolved through the fine tuning of the cascade of five UCs.

As mentioned earlier, the vias in the proposed unit-cell structure build a SIW-wall on one side to construct a Half Mode Substrate Integrated Waveguide (HMSIW) by altering propagation mode in the transmission line. It means, this wall must prevent the wave from escaping SIW. But, there will be some wave leakages through the wall (the gap between vias). It gets worse in higher frequencies due to smaller wavelengths. That is the main reason for the increase of the insertion loss in high frequencies. Of course, there are also the wave leakages from the places with no walls. A complete study of the dimension and distance of vias in SIW for the desired bandwidth is presented in Deslandes & Ke Wu (2006).

3.3.2 Study on the number of via

The number of via in a unit-cell structure is very important because it controls wave leakage from SIW-wall. The antenna in Rahmani & Deslandes (2017) takes advantage of two vias in the unit-cell structure at 25GHz. Here, we present a study on the number of via at 60GHz band by keeping the size of wall constant. Figures 3.12 and 3.13 show respectively the S-Parameters and propagation constants of a cascade of five unit-cells for 2 to 5 vias and the groove.

As expected, when the number of via increases, the insertion loss becomes more flat at higher frequencies and the open-stopband observed in propagation constant at higher frequencies will move outside the band. It is notable that the structure with three vias has shown some improvements relating to two vias. Although, there is not much different among 3 to 5 vias and the groove. Therefore, we chose the unit-cell with three vias as our proposed structure which offers improved bandwidth and is not difficult to fabricate.

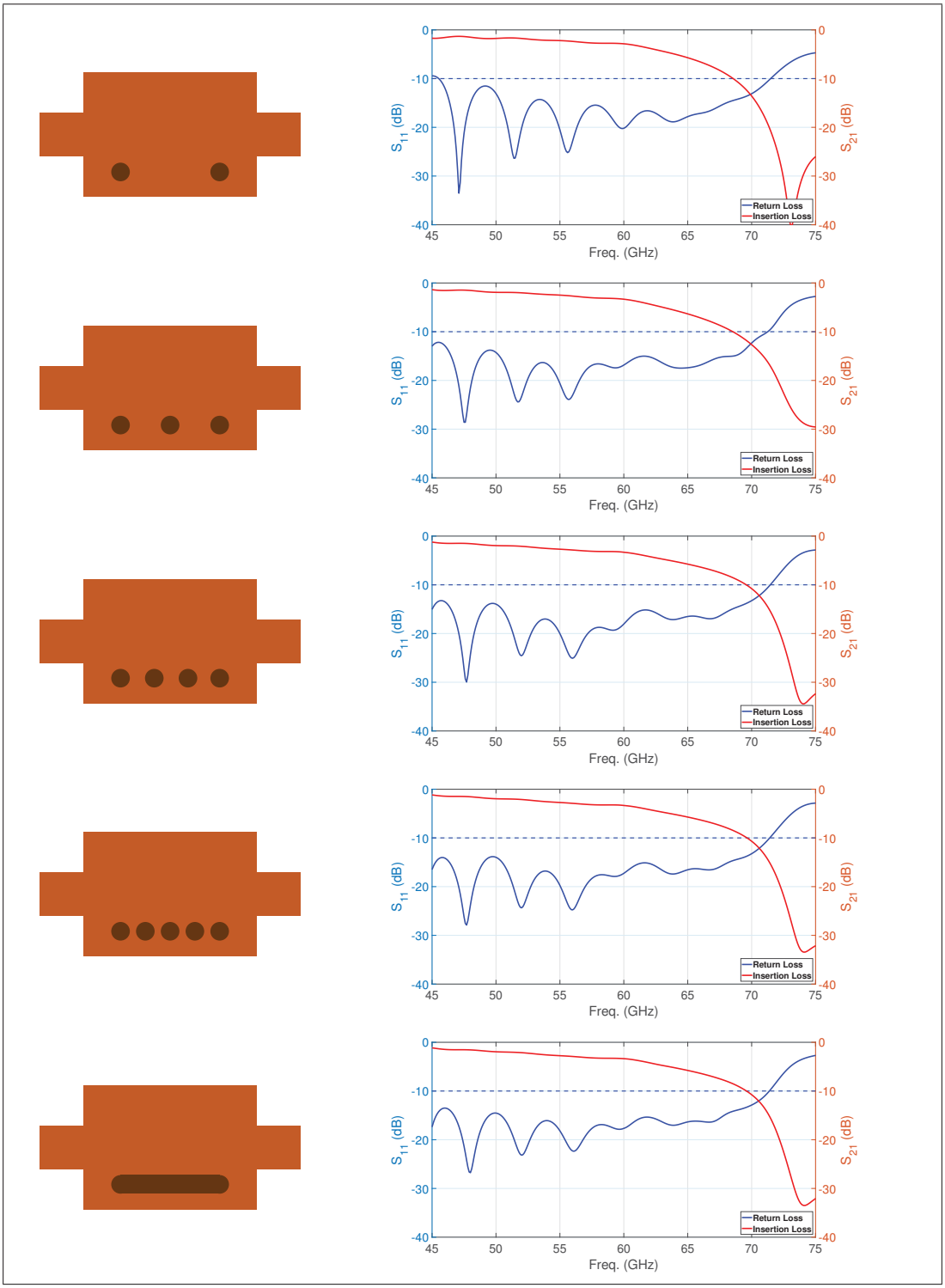

Figure 3.12 S-Parameters for the cell structure with different via numbers.

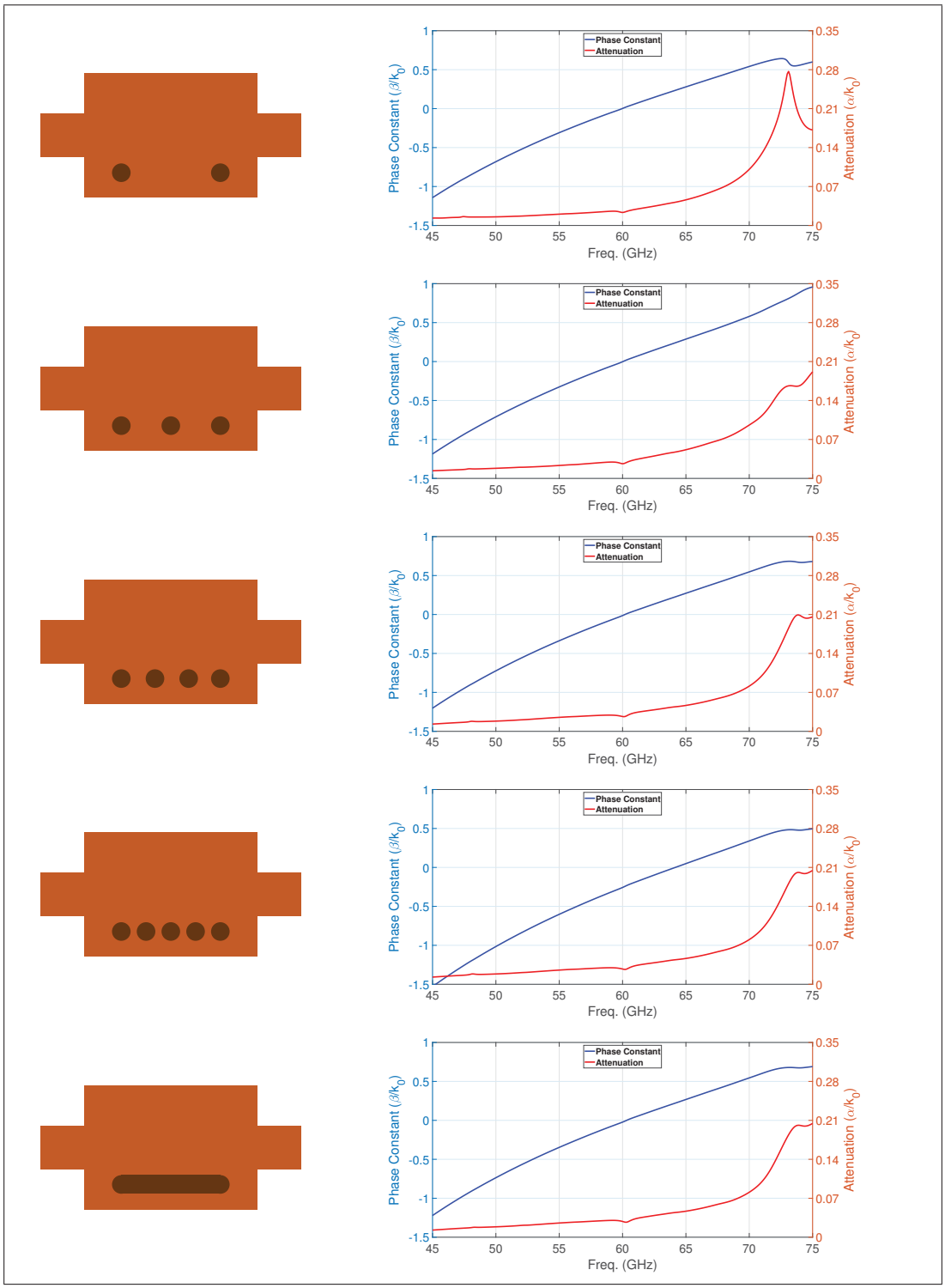

Figure 3.13 Propagation Constant for the cell structure with different via numbers.

3.3.3 Study on the number of unit-cells

As introduced in chapter 2, the ideal length of a periodic LWA structure would be attained when 90 percent of the input power dissipates through radiation. A shorter structure will not be efficient and a longer structure will be a waste of resources in the fabrication. Therefore, we performed a comprehensive study on the length of our periodic LWA to find the optimum number of unit-cells. For this purpose, the proposed antenna in table 3.6 were considered with 9, 11, 13 and 15 unit-cells configuration. Figure 3.14 presents the comparison of all output features of these antennas simulated in HFSS.

The return loss for all configurations are above 10dB (all matched and almost in the same level). As expected, the insertion loss rises when the number of unit-cells increases. Total gain and peak realized gain increase for higher number of unit-cells and the radiation beam becomes more directive (narrow). The efficiency improves a little but axial ratio and beam angle would stay the same. It seems the feature improvement from 9 UCs to 15 UCs is not significant, however the difference in the length is huge for the SIP applications. Also, cascading more unit-cells in the structure will add more grating lobe to the radiation pattern. So, we found 9 unit-cells configuration is good enough for our application.

3.3.4 Study on Ground Plan

The size of ground plane in any antenna structure is very important because it can change performance of the system (Huynh & Stutzman, 2003). Normally, a larger ground plane has better efficiency, higher gain and improved bandwidth; but it also increases the whole size of structure. Here, we present the simulation of our antenna on two ground planes.

Figure 3.15 shows 3D and polar gain of the proposed antenna in table 3.6 with ground plane width of 5.4mm and 20.9mm. Figure 3.16 represents the comparison of all output features of this antenna for two mentioned ground planes. The antenna is optimized for the smaller ground plane; that's why it has almost the same or better performance. However, it is noticeable that the larger ground plane has improved axial ratio and is slightly better in higher frequencies.

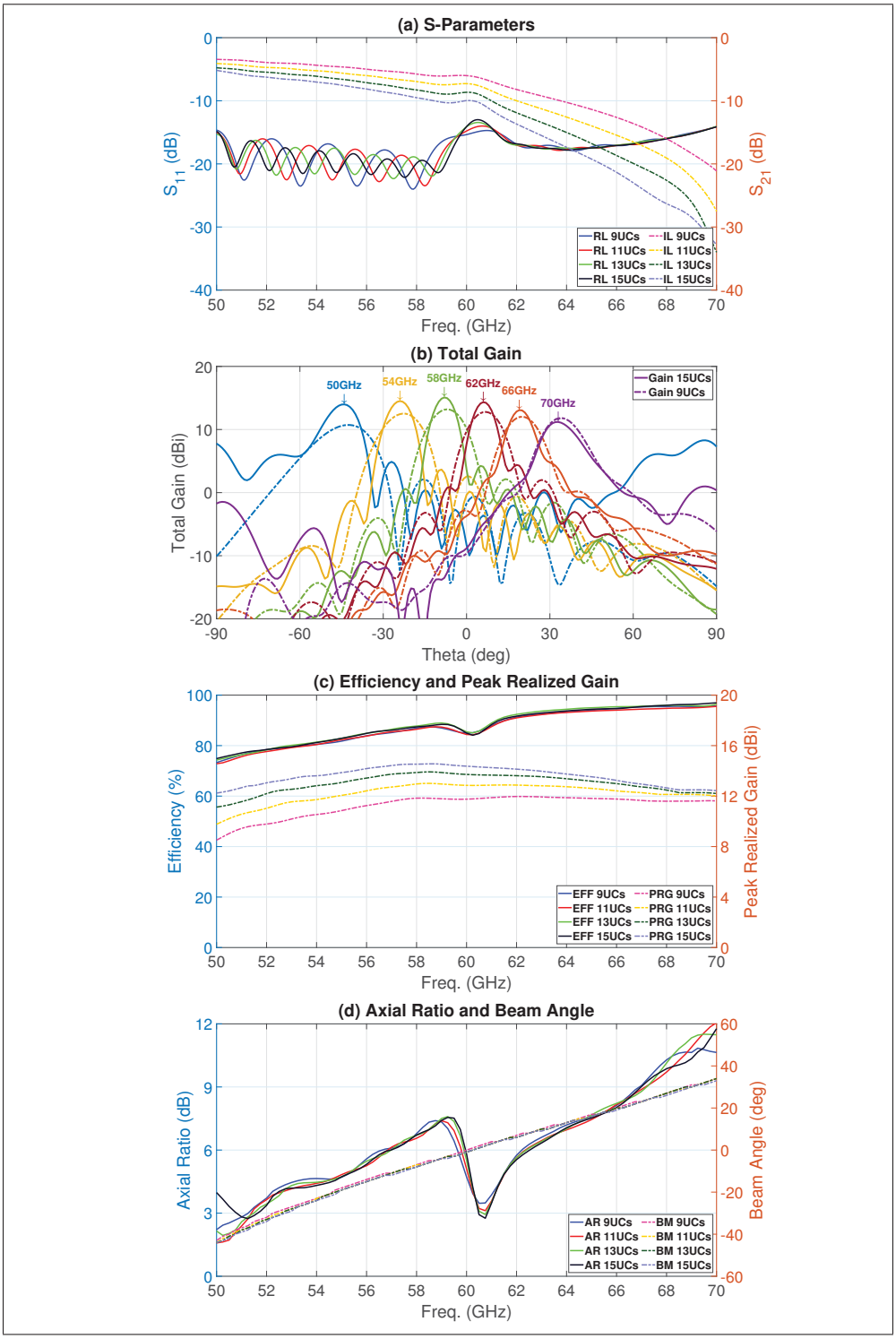

Figure 3.14 Antenna in table 3.6 with different UC's number.

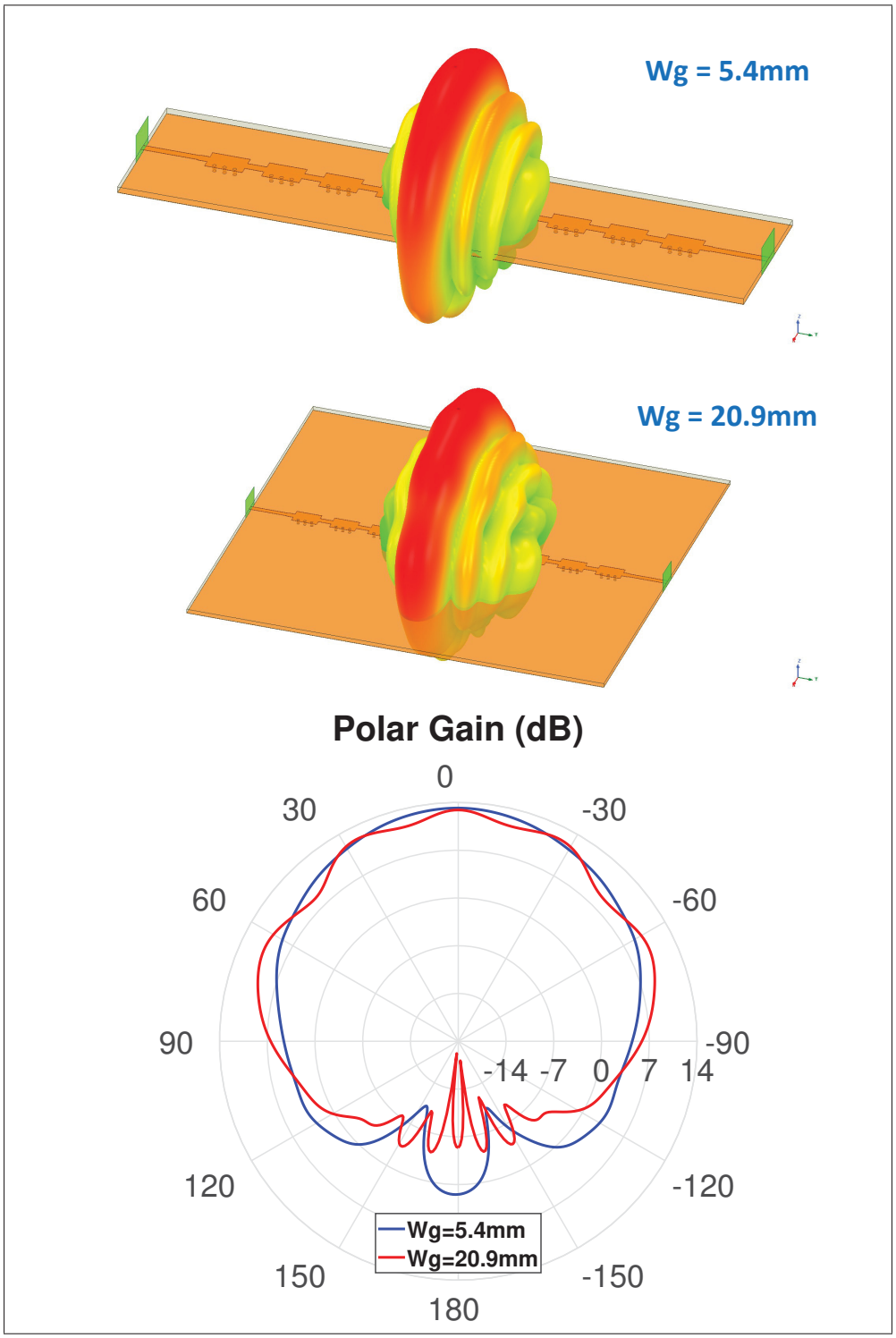

Figure 3.15 Effect of Ground Plane Width on Antenna in table 3.6. 3D Gain and Polar Gain at 60 GHz.

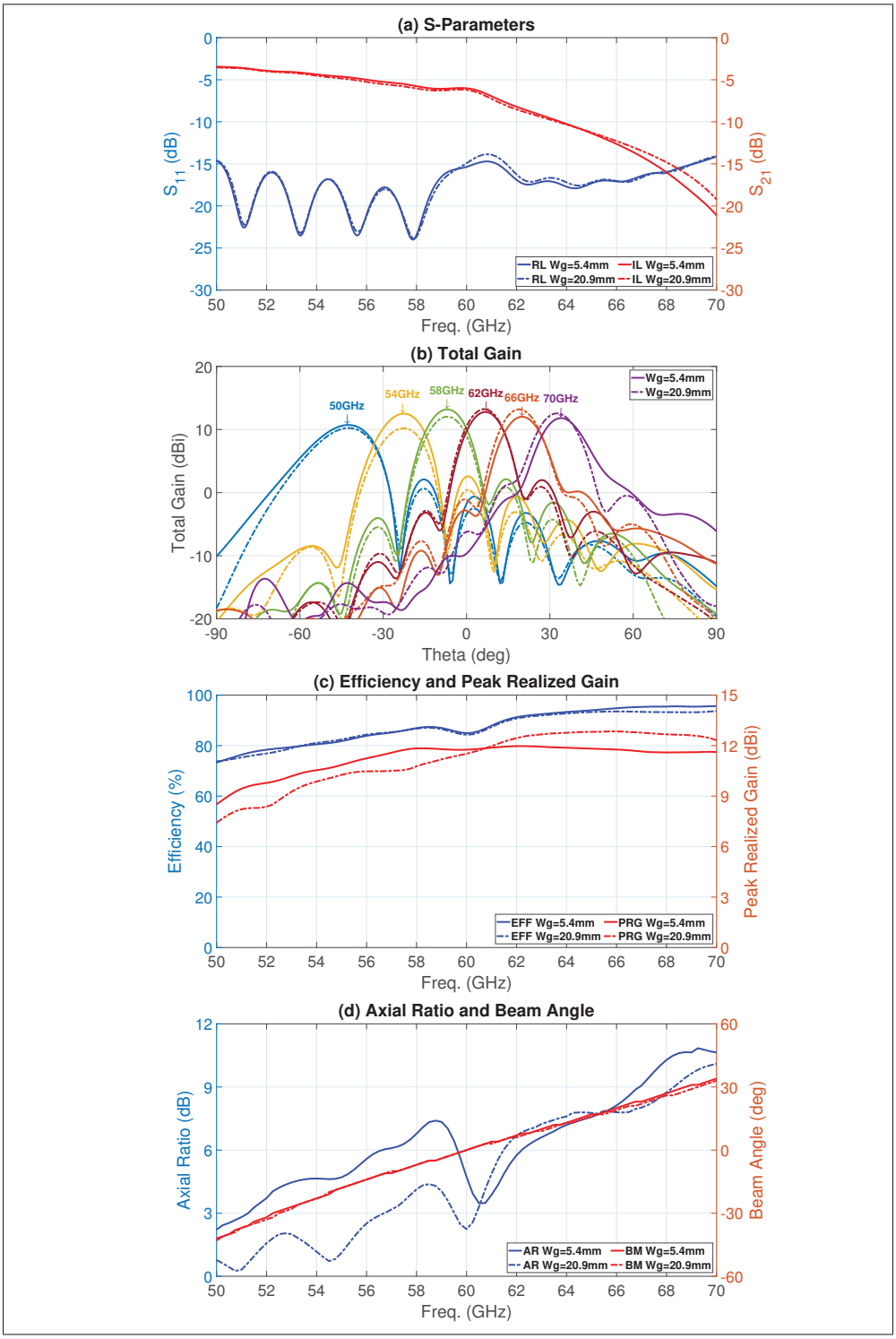

Figure 3.16 Effect of Ground Plane Width on Antenna in table 3.6.

3.4 Alternative design: an antenna without via

Fabrication of a LTCC structure containing the via has some challenges. For example, it will add two steps to the fabrication process that will be time and budget consuming. Moreover, it is possible that the final product shows unacceptable features due to misalignment of the vias relating to the antenna's body. In the fabrication process, we normally deploy the punch or laser machine to create the via's holes in the substrate; then, we proceed to print the metal and perform the via filling. If the structure does not have any via, we would eliminate the punching and via filling steps which will be a great saving in the resource. Besides, the via alignment to the metal patch would not be necessary anymore which may improve the fabrication accuracy and subsequently antenna's performance.

The drilling and printing steps will be accomplished in two different machines which need separate alignments. Even though, we use the same reference (printed fiducial marker) to adjust the position of vias relating to the metal patch in both machines, there will be some misalignments that may lead to poor positioning of the vias in the printed antenna structure. This will affect the propagation property of the antenna. It should be mentioned that there is a laser oblation process after the metal printing which trims the metal patch to the specified dimension and it has its own alignment as well.

It is noticeable that employing the punch machine for drilling of the via is not very accurate in the localization (our machine has the accuracy of about 20 μm); and using laser machine, although it is very accurate (less than 5 μm), sometimes the shape of the hole is deformed (not cylindrical). This could cause a problem for the via filling part. In addition, after stacking the layers and pressing them together, the via diameter will expand.

All these deficiencies in the fabrication could be resolved by proposing a structure without any via. The via in the proposed periodic LWA constructs a path to the ground plane and provides a SIW-wall on one side of unit-cell. Instead of using the via for this purpose, we suggest to take advantage of the quarter-wavelength radial stub which can provide a virtual ground potential over a frequency band rather than actual physical connection to the ground plane.

3.4.1 Quarter-wavelength radial stub vs via

The open-circuited radial stub is a convenient way to achieve the desired impedance for a range of frequencies. Looking into its input, considering the other side of stub is open-circuited (an infinite impedance), we can obtain our desired reactance by varying the electrical length of stub. Neglecting transmission line losses, the input impedance of the stub is purely reactive. It has some advantages over the straight open-stub. Input port of the radial stub (L_g) can be designed as small as desired and also the reactance of stub shows less variations with frequency near resonance comparing to the straight stub (Gardner & Wickert, 1988). It means, the radial stub have almost constant impedance over wider bandwidth. Reference (Gardner, 1987) provides the input impedance of a modified radial stub geometry as follow:

$$Z_{in} = -jZ_0(l)\,\frac{Y_0(\beta(l_0-l))\,J_1(\beta l_0) - J_0(\beta(l_0-l))\,Y_1(\beta l_0)}{Y_1(\beta(l_0-l))\,J_1(\beta l_0) - J_1(\beta(l_0-l))\,Y_1(\beta l_0)} \tag{3.11}$$

where l is the physical length of the stub, $Z_0(l)$ is the characteristic impedance of the stub at $z = l$, β is the effective phase constant of the transmission line, l_0 is a positive constant used to describe the characteristic impedance along the stub and the functions $J_n(x)$ and $Y_n(x)$ are Bessel functions of the first and second kind respectively. We should notice that in this equation, the actual length l is considered a little shorter than physical one due to the effect of fringing field at the open-circuit end. Equation 3.11 can be expressed in a simplified form for the frequencies below the resonance to:

$$Z_{in} = -jZ_0(l)\,cot[\frac{\beta}{2}\,\{\frac{l_0^2}{l_0-1} - (l_0-1)\}] = -jZ_{max}\,cot[\frac{\beta l}{2}\,(1+\frac{Z_{max}}{Z_{min}})] \tag{3.12}$$

where $Z_{max} = Z_0(l)$ and $Z_{min} = Z_0(0)$. The via to the ground plane shows a zero impedance and can be replaced by a quarter-wavelength radial stub in our proposed structure. The effective electrical length of quarter-wavelength grants 90° phase shift between two ends of the stub. Therefore, the input port of an open-circuited stub sees a short circuit to the ground.

Figure 3.17 shows the geometry of an open-circuited quarter-wavelength radial stub and figure 3.18 presents the input impedance of proposed radial stub optimized over 50 to 70GHz to works as a short-circuit to ground plane. The optimized parameters are $Rs = 375um$, $Lg = 150um$ and $T = 50°$. This is just an example; although, we need to perform the optimization again when we integrate the radial stub with the unit-cell. It is noticeable in the figure 3.18 that the input impedance of radial stub is not completely zero over the bandwidth; but a via also is not perfect in the grounding task due to its inductance at the high frequency.

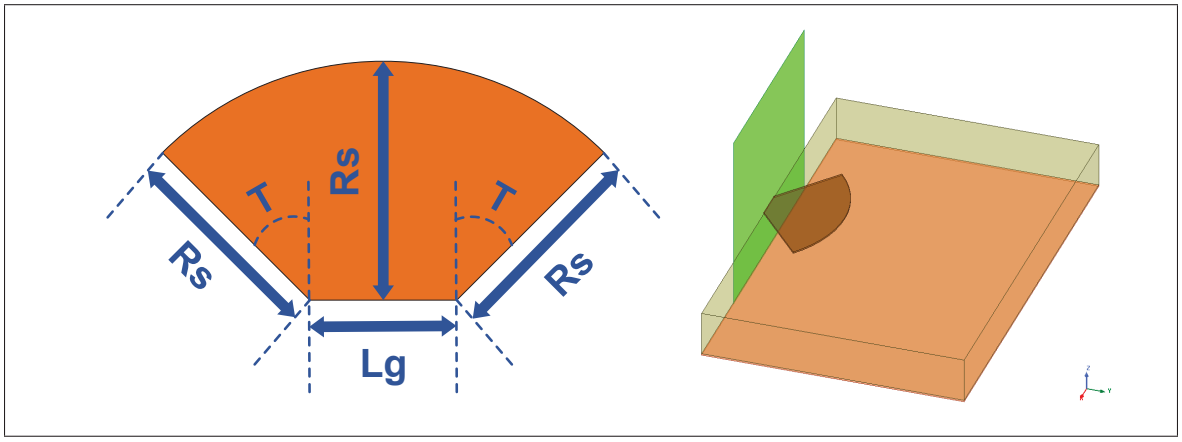

Figure 3.17 Geometry of an open-circuited quarter-wavelength radial stub.

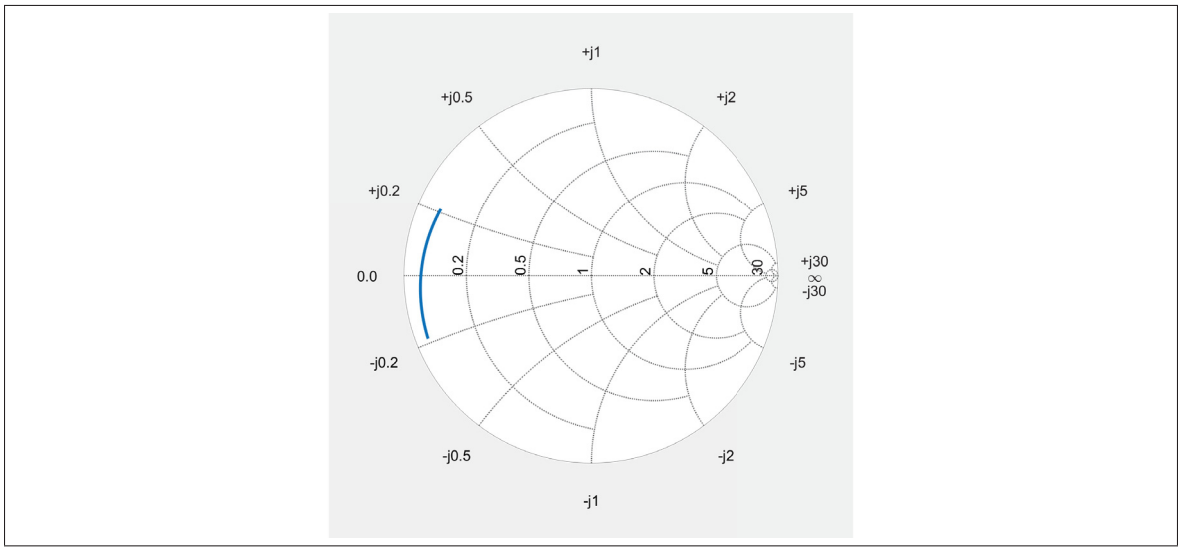

Figure 3.18 Impedance of quarter-wavelength radial stub optimized for 50 to 70GHz.

3.4.2 Number of radial stubs and unit-cell's structure

We can replace the via with open-circuited quarter-wavelength radial stub in our proposed unit-cell in different ways. Figure 3.19 presents three proposed configurations. The simple structure is the best candidate for the fabrication but it has one input parameter less than normal structure which makes it more complicated to achieve the optimized unit-cell. On the other hand, the complex structure has two more input parameters for the optimization but it is really difficult to fabricate. Therefore, we select the normal structure as our proposed alternative periodic LWA which is best comparable to our original design with via.

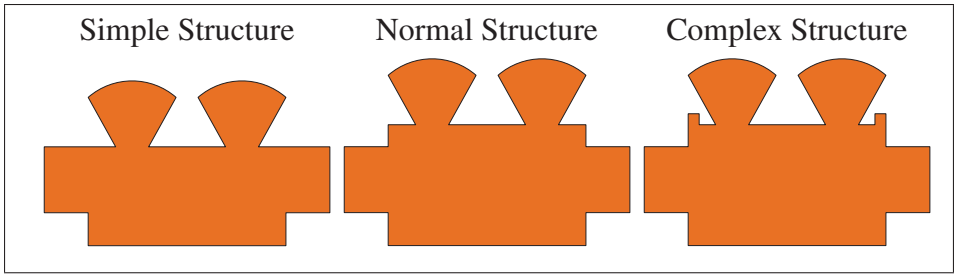

Figure 3.19 Proposed antenna structures with two radial stubs.

The number of radial stubs can vary like the number of vias in the unit-cells (figure 3.20). We covered this part at the section "Study on the number of via". However, unlike via, the radial stub is a little bulky. Therefore, fitting three radial stubs in one unit-cell does not seem feasible. On the other hand, one stub has a very wide input port which may not provide a constant impedance over entire bandwidth. So, we choose the unit-cell with two radial stub for now and try to optimize the structure. We will review this matter after finalization of the design.

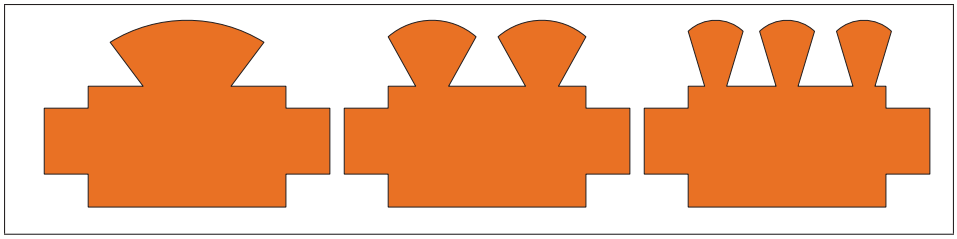

Figure 3.20 Antenna structures with different radial stub number.

3.4.3 Proposed alternative structure

Figure 3.21 shows the proposed alternative periodic LWA with two open-circuited quarter-wavelength radial stubs. Considering this new design, we performed all the optimization procedure explained in section "Unit-Cell design" for one UC, five UCs and the whole structure to obtain our desired features. Here, we have nine input parameters to be optimized which makes the solution more complicated. The optimized input parameters are presented in table 3.8.

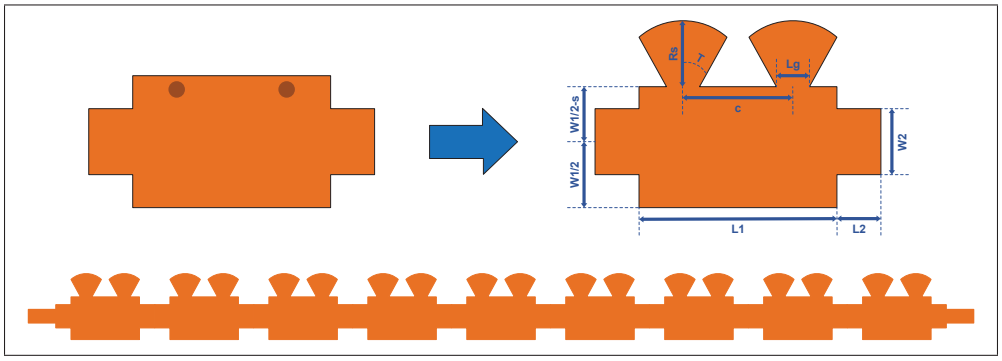

Figure 3.21 Dimension parameters of proposed periodic LWA with two quarter-wavelength radial stubs.

Figure 3.22 shows the return loss, insertion loss and input impedance of a single unit-cell and the propagation constant of a cascade of five unit-cells for the antenna introduced in table 3.8. Figure 3.23 presents performance parameters of the antenna with 9 unit-cells. Figure 3.24 demonstrates scanning properties of antenna in three frequencies through antenna's 3-D gain. We can observe that all features of the alternative design are almost in the same range or better. Only the Axial Ratio of antenna with radial stub is a little high and needs improvement.

It is noticeable that the parameter c in the optimized unit-cell is so small that two redial stubs have an overlap. Actually, this overlapped area is large enough to consider these two stub as one. We filled all the gap between two radial stubs and try to solve the solution again by keeping all parameters constant. The new structure has almost the same properties as old one because no radiating current passes through this part of metal corresponding to the gap. Therefore, a unit-cell with one radial stub is working just as fine as two radial stubs.

Table 3.8 Parameters of an optimized UC with two radial stubs.

Parameter	Value	unit	Parameter	Value	unit	Parameter	Value	unit
L_1	1.030	mm	L_2	0.420	mm	L_g	0.150	mm
W_1	1.050	mm	W_2	0.380	mm	R_s	0.370	mm
s	0.180	mm	c	0.340	mm	T	35	deg

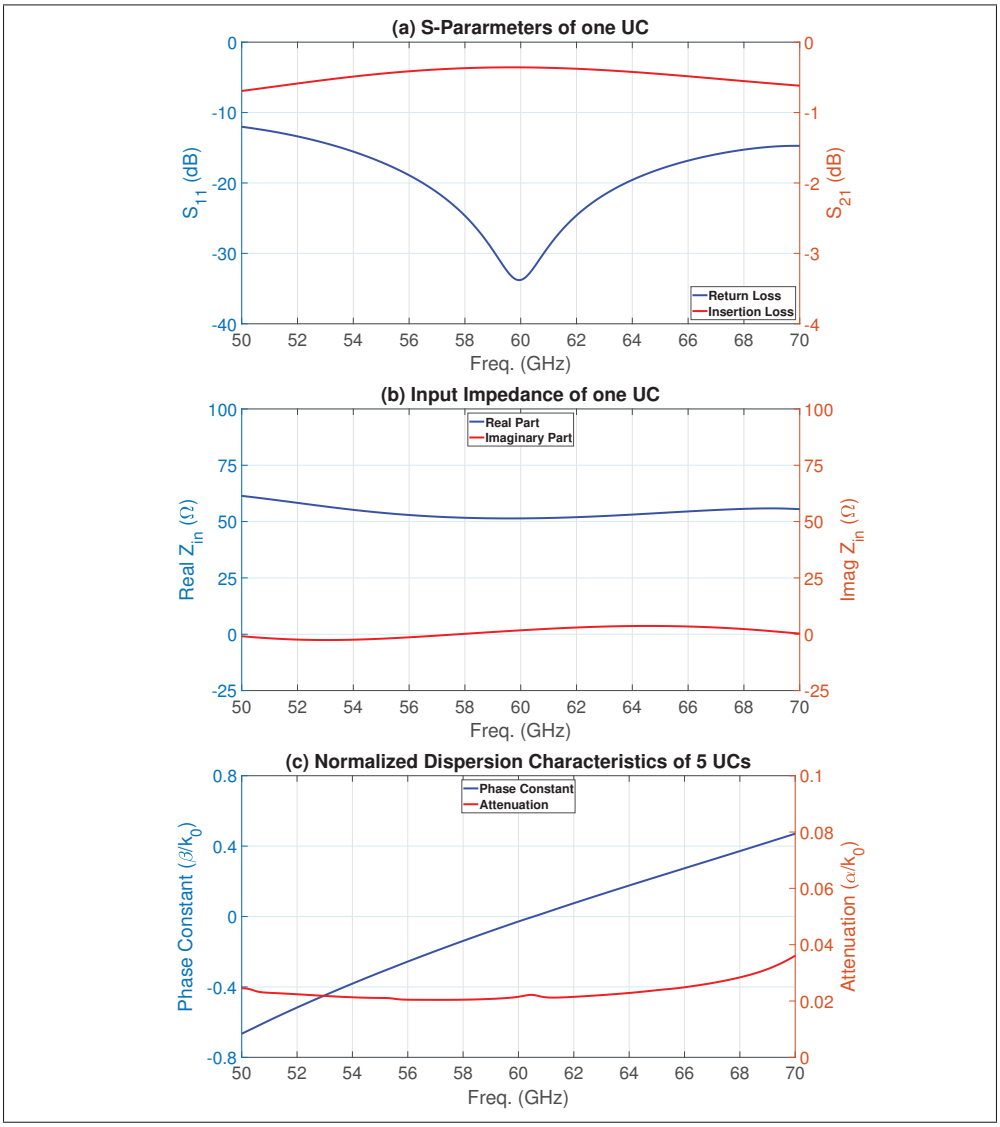

Figure 3.22 (a) S-Parameters of single UC (b) Input impedance of single UC (c) Normalized propagation constant of a cascade of 5 UCs.

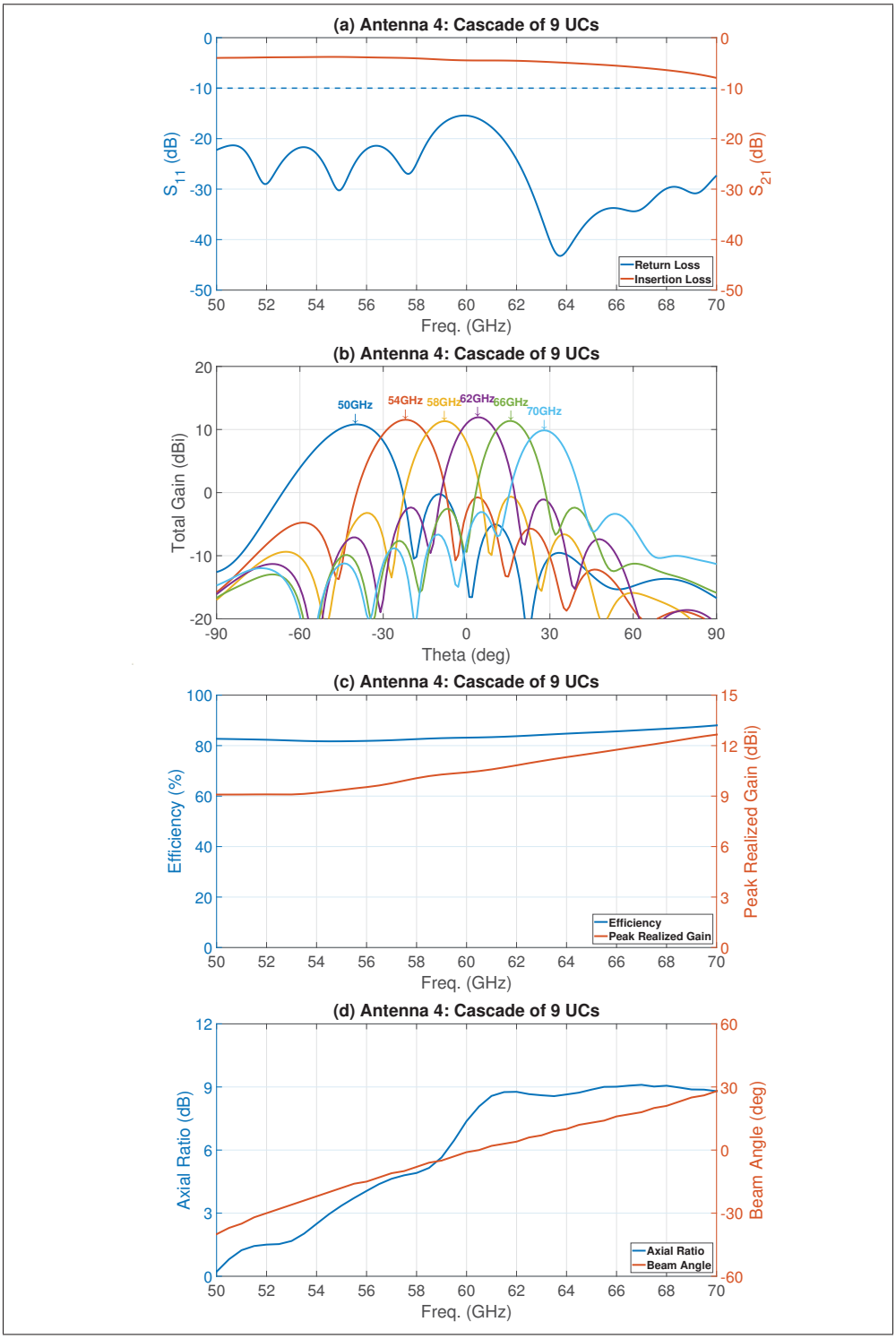

Figure 3.23 Performance of the Antenna in table 3.8.

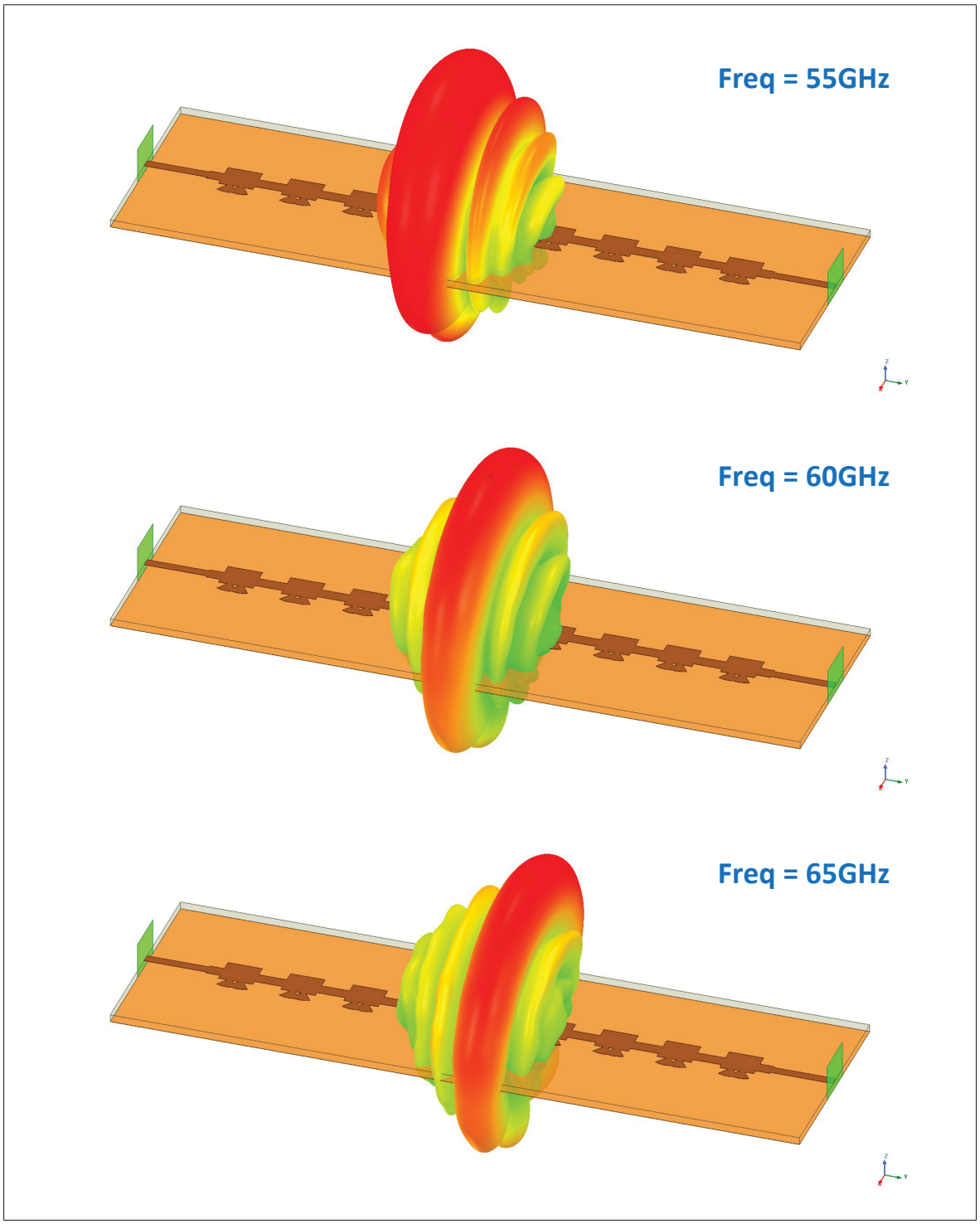

Figure 3.24 3D Gain of Antenna in table 3.8 at 55GHz, 60GHz and 65GHz (backward to forward beam scanning with frequency).

3.5 Array of antennas

As mentioned earlier, at 60 GHz band the attenuation level is very large due to the interaction of oxygen molecules in the atmosphere with the RF waves. Therefore, we need an antenna with higher gain and directivity for the communication. To cover more space with the narrow radiation beam, it is necessary to have a 2-D beam scanning system. The leaky-wave structure already provides us the scanning with frequency in one direction (direction of wave propagation in the antenna). The beam steering in the second direction (perpendicular to the direction of wave propagation) can be achieved by a planar Beam Forming Network (BFN).

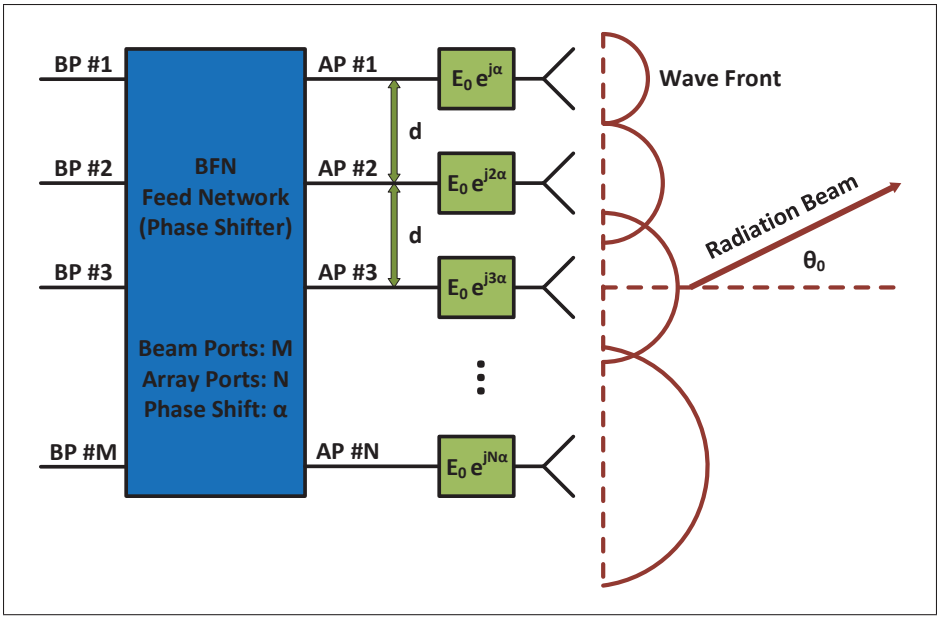

Figure 3.25 Description of phased-array operation.

Figure 3.25 demonstrates the operation of a typical BFN named phased-array network with M inputs (beam port) and N outputs (array port). When an incident wave is applied to one of the beam ports, the BFN distributes the input power equally in magnitude with a specified phase to the array ports. The array ports deliver a portion of the incident wave with a specific phase shift (α) to N radiating elements (the array of antennas). The input phase difference between each array elements causes a constant delay in wave-front, produced by the radiating elements, which leads to a tilt (θ_0) of the main beam from broadside (Hansen, 2009).

Considering (α) as the phase difference between two adjacent radiating elements and (θ_0) as the deviation angle of the superposition of all elements' radiation beams relating to broadside, we will have (Stutzman & Thiele, 2012):

$$\alpha = -k\,d\,sin\theta_0 = -2\pi\,(\frac{d}{\lambda})\,sin\theta_0 \tag{3.13}$$

Where $k = 2\pi/\lambda$ is the wavenumber and d is the element spacing of phased-array. The element spacing is the physical distance between two adjacent radiating elements. Now by taking ψ as:

$$\psi = k\,d\,sin\theta + \alpha = 2\pi\,(\frac{d}{\lambda})\,(sin\theta - sin\theta_0) \tag{3.14}$$

we will find the normalized array factor (AF) for an N elements, uniformly excited, equally spaced linear array that is centered about the coordinate origin as (Stutzman & Thiele, 2012):

$$AF = \frac{sin(N\,\psi/2)}{N\,sin(\psi/2)} \tag{3.15}$$

When the number of radiating elements in an array increases (Stutzman & Thiele, 2012):

1. The main lobe will become narrower (more directive).
2. The numbers of side lobes will increase.
3. The Side Lope Level (SLL) will decrease.
4. The total gain will increase.

Generally, it is better to have more radiating elements in the phased-array, but we should also consider the physical dimension of the structure; so, we found $N = 5$ good enough for our purpose. Other parameter that should be determined is the element spacing. The best value

for element spacing is $d = \lambda/2$, because it covers optimum area from the visible horizon. Any value greater than this, will produce more gating lobes and the smaller value will increase the chance of missing a part of the main lobe (Hansen, 2009).

Figure 3.26 shows an array of 5 identical periodic LWAs presented in table 3.6, consisting of 9 unit-cells. These antennas are placed in $d = \lambda/2$ distance from each other and fed by the wave-port with unit amplitude and the phase difference of α between two adjacent ports.

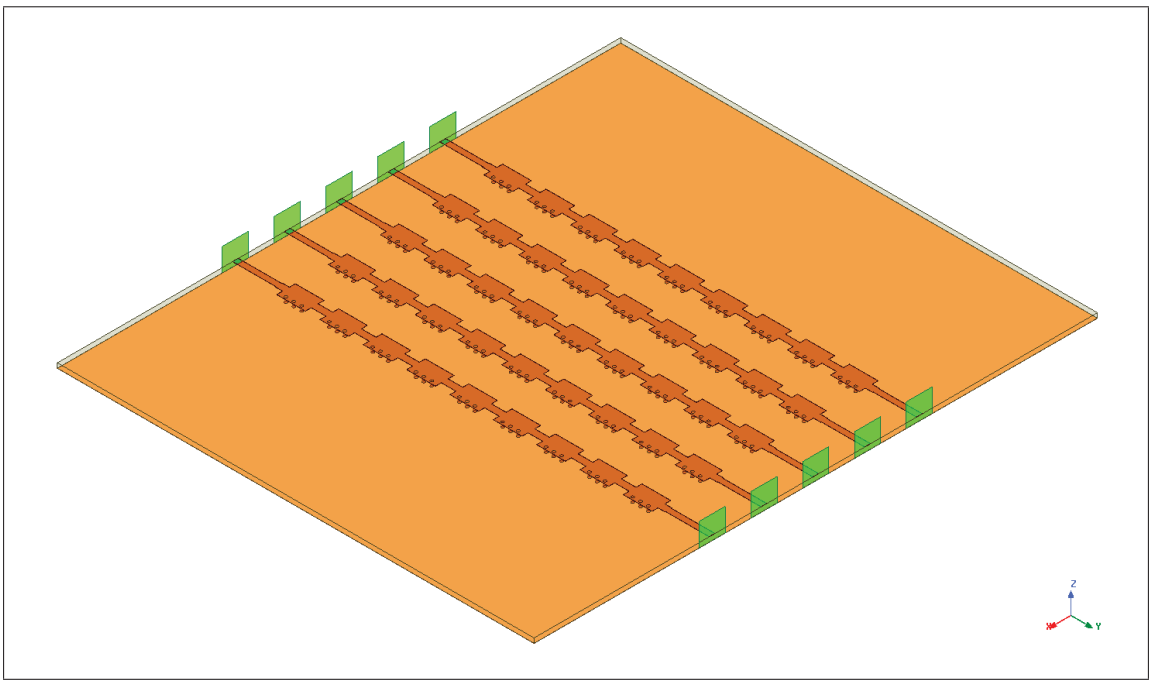

Figure 3.26 Array of 5 proposed antennas consisting of 9 UCs.

Figure 3.27 presents the return loss of input ports and the insertion loss of output ports for the aforementioned phased-array. It is noticeable that the return loss of the phased-array is different than figure 3.5(b) which is for a single antenna. That is because of the mutual effect of antenna on each other in the array structure. Moreover, the return loss of each antenna is different to others in one array, especially in lower and higher band. The position of an antenna in the array changes the configuration of mutual coupling with other antennas. Besides, the asymmetry in the structure of unit-cell leads to different mutual coupling in both side of antenna. Same logic applies to the insertion loss of output ports which are a little lower than expected.

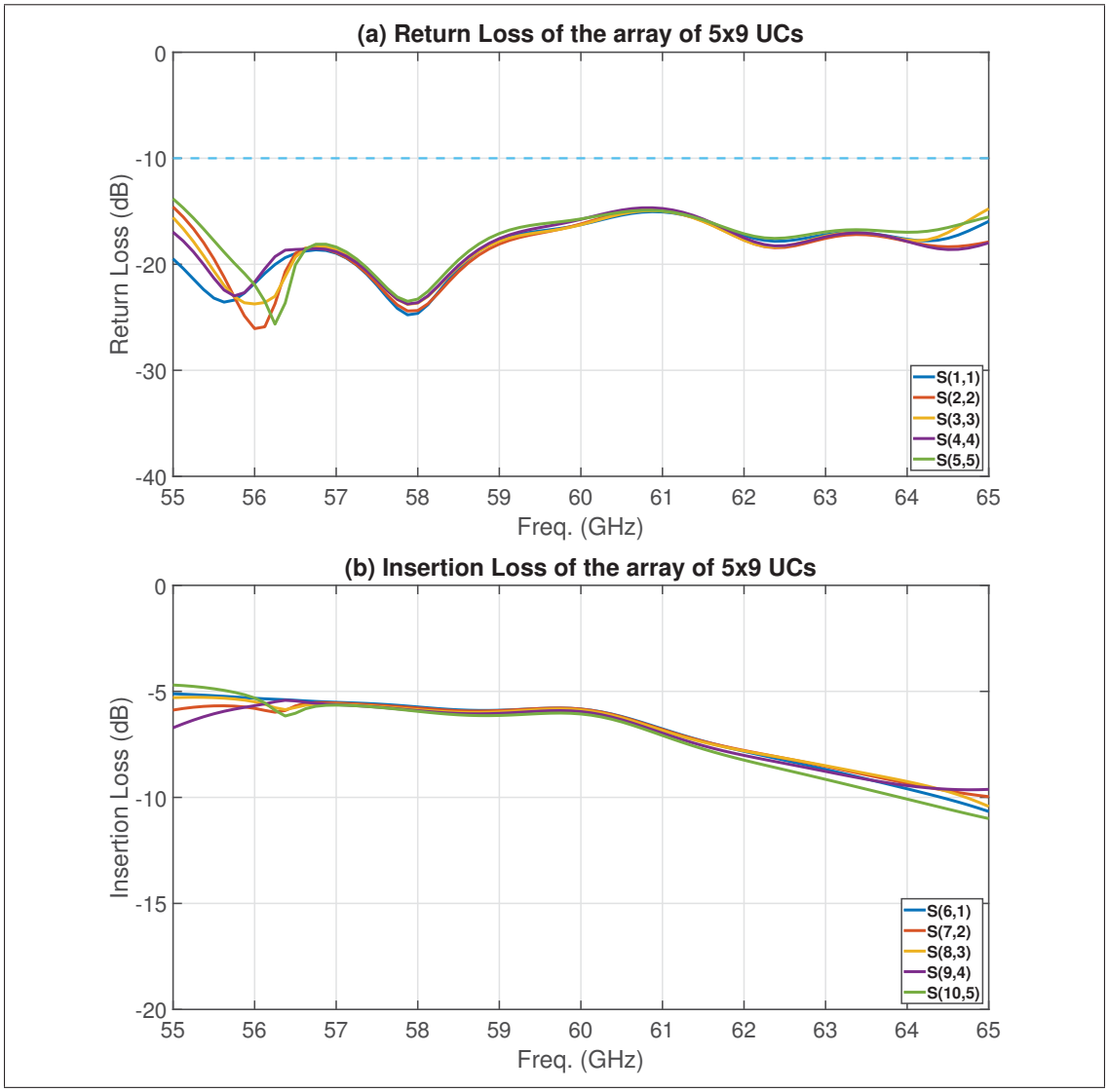

Figure 3.27 Return Loss and Insertion Loss of array of 5×9 UCs in table 3.6.

Figure 3.28 represents the scanning ability of the 5×9 UCs phased-array of the proposed LWA antenna with frequency in the Y-Z plane ($\Phi = 90°$). Considering $\alpha = 0°$, the radiation beams are presented for three frequencies of $55\,GHz$, $60\,GHz$ and $65\,GHz$ to demonstrate backward, broadside and forward beam scanning respectively. The max total gain for $55\,GHz$ is $18.2\,dB$ in $\theta = -18.5°$, for $60\,GHz$ is $19.8\,dB$ in $\theta = 0°$ and for $65\,GHz$ is $19.8\,dB$ in $\theta = 15°$.

Figure 3.29 shows the scanning ability of the same phased-array structure with different input phase shift in the X-Z plane ($\Phi = 0°$) for frequency of $60\,GHz$. At this frequency, we have a

broadside radiation; so, max radiation will be in X-Z plane. The radiation beams are presented for three phase shifts (α) of $-45°$, $0°$ and $+45°$. According to equation 3.13, the radiation beam angle (θ_0) will be $+14.5°$, $0°$ and $-14.5°$ respectively, considering $d = \lambda/2$, that is the exact angle observed in this figure. The maximum total gain for all of these angles is $19.8\,dB$.

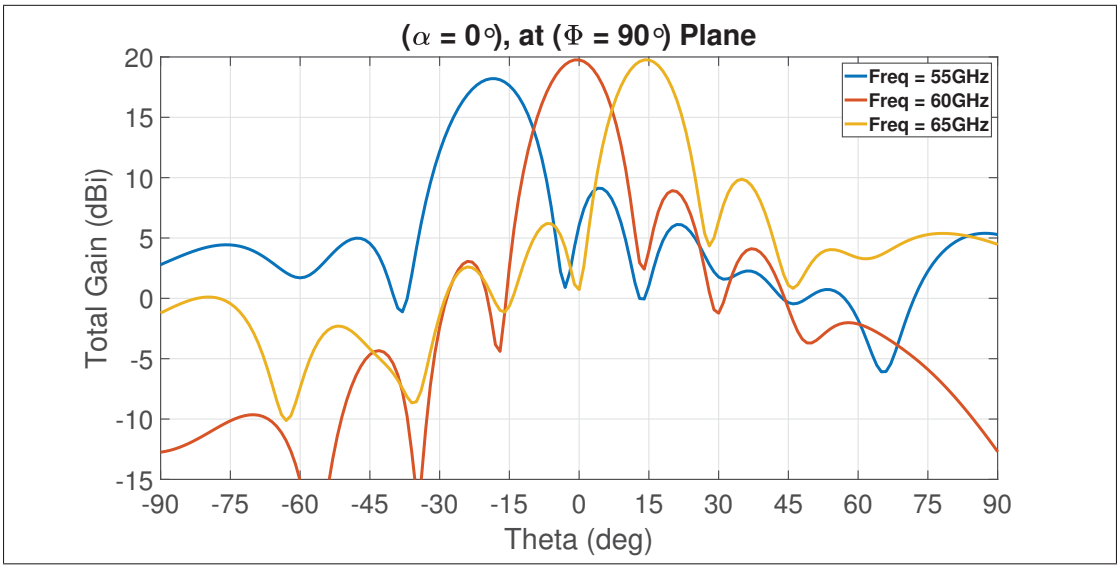

Figure 3.28 Beam scanning vs frequency at plane $\Phi = 90°$ for Antenna Array 5×9.

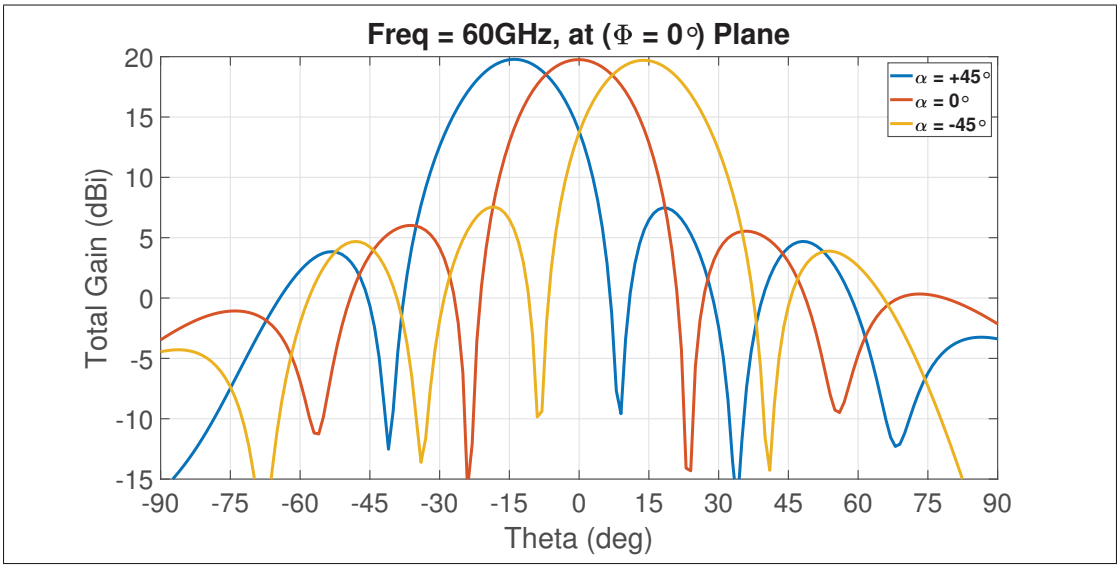

Figure 3.29 Beam scanning vs phase shift at plane $\Phi = 0°$ for Antenna Array 5×9.

Figure 3.30 shows 2-D radiation beam scanning feature of the phased-array presented in figure 3.26 with the frequency in Y-Z Plane and the input phase shift in X-Z Plane. 3-D gain of the array is demonstrated just for three frequencies (55 GHZ, 60 GHZ and 65 GHZ) and three phase shifts ($-45°$, $0°$ and $+45°$) over the layout of array structure.

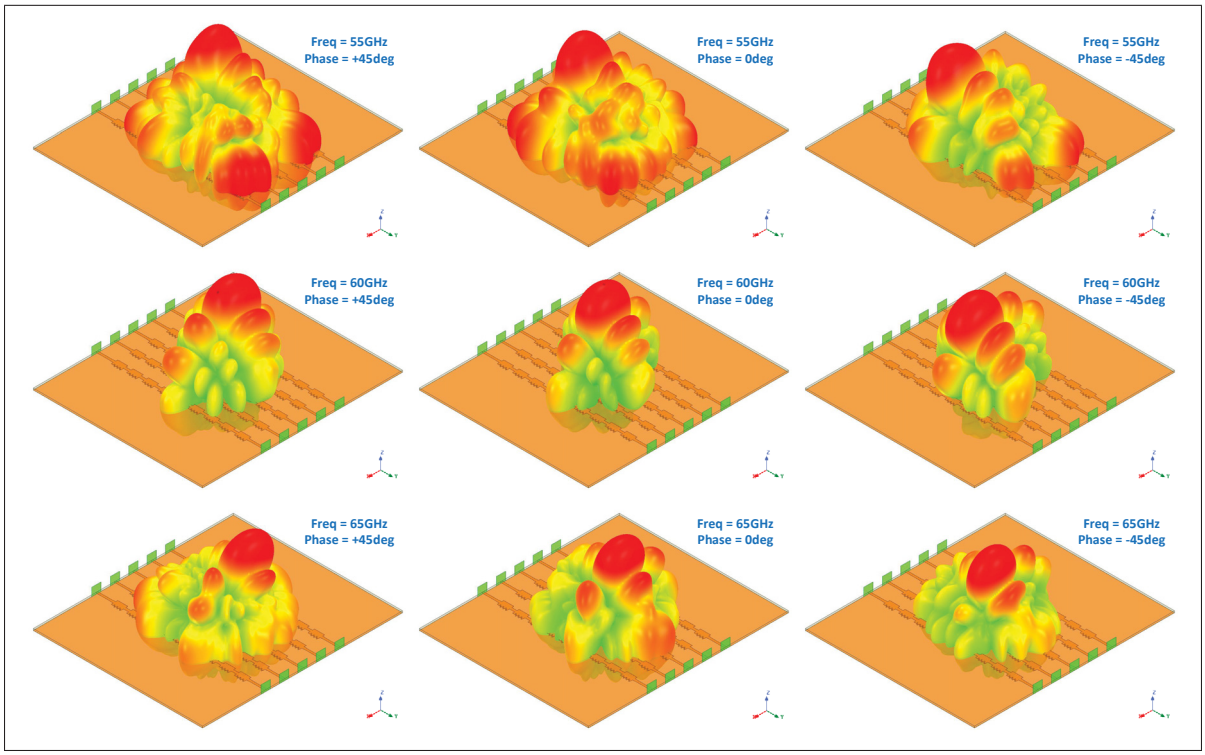

Figure 3.30 3D Beam scanning vs frequency and phase shift for Antenna Array 5×9.

3.6 Rotman lens design

In the previous section, we introduced the Beamformers as the feeding network of an array of the antennas. An acceptable BFN ideally should be ultra wideband (to match with our proposed LWA) to cover the desired frequency bandwidth and also be independent of the input frequency to maintain a constant, reliable beam steering. Moreover, it preferably has a low-profile and low-cost structure to be integrated with the antennas in a multi-layer package. So, we suggest to employ a structure with only the passive elements that are printable on the LTCC substrate. Two possible BFN solutions that fit this description are Butler Matrix and Rotman Lens.

The Butler matrix (Butler, 1961) consists of an $n \times n$ matrix of hybrid couplers and fixed-value phase shifters. This feeding network has n input ports (beam ports) and n output ports (array ports), where n normally is some power of 2. Unfortunately, the Butler matrix has a fix scanning angle and the practical number of ports is limited by a 16×16 matrix. Besides, it is considered relatively narrow-band compared to other BFNs such as the Rotman lens.

The Rotman lens, which first was introduced by (Rotman & Turner, 1963), takes advantage of the geometrical rules to produce the desired phase difference between array ports from received incident power on the excited beam port. This beamformer is a true time delay BFN which is suitable for a linear array element structure. The Rotman lens has a small footprint on the substrate with a wideband performance which is ideal for our application. Theoretically, the radiation beam direction created by the array elements with this BFN should be constant versus the frequency (Hansen, 2009), but in real world a small variation is observable.

Figure 3.31 illustrates the beamforming function of a Rotman lens. A typical Rotman lens consists of three major operation regions: feed contour, array contour and outer contour. The feed contour is a semicircular focal arc that traces the contour of beam ports. The array contour or inner contour is a curved line which follows the contour of the array ports. Finally, the outer contour is a straight line which locates the position of the array elements.

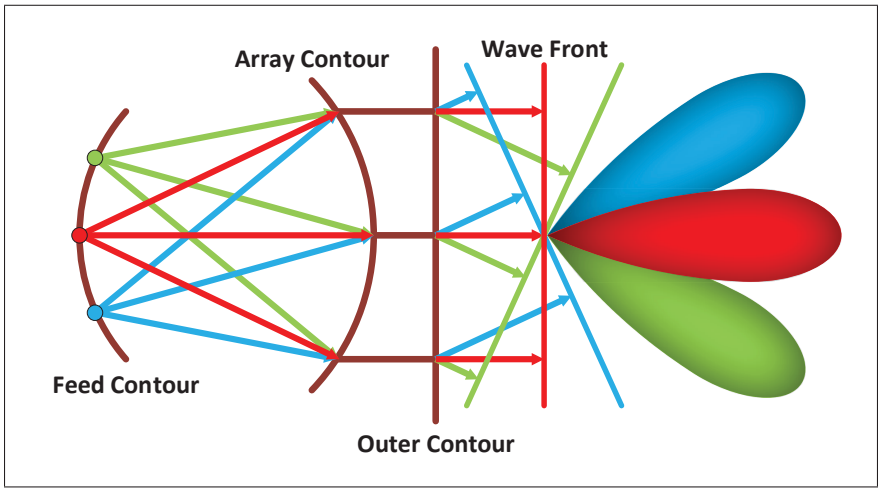

Figure 3.31 Beamforming operation of the Rotman Lens.

Ideally, when one beam port on the feed contour is excited, each array port on the array contour receives an equal portion of the incident wave with a specific phase which is proportional to the electrical path length between the beam port and the array port. The electrical path lengths will vary linearly from one beam port to each array ports, result in a linear phase distribution and consequently, a steered radiation beam from the broadside. It should be mentioned that the electrical length between all array ports and array elements on the outer contour is constant.

The Geometry parameters of the Rotman Lens is presented in Figure 3.32. We can modify the semicircular focal arc slightly to be elliptical to reduce aberration, phase error, and side lobes of the array factor (Mailloux, 1994). Also, some additional matched dummy ports must be devised on the sidewalls of Rotman lens to minimize the reflection. Theoretically, there is no limitation on the number of feed inputs and the steering angles in this BFN. Moreover, the electrical path length's phase error is very low which is one of its geometrical advantage. A comprehensive investigation on the geometrical parameters of the Rotman lens such as the lens shape, the position of the ports, and the phase error is presented in Hansen (1991).

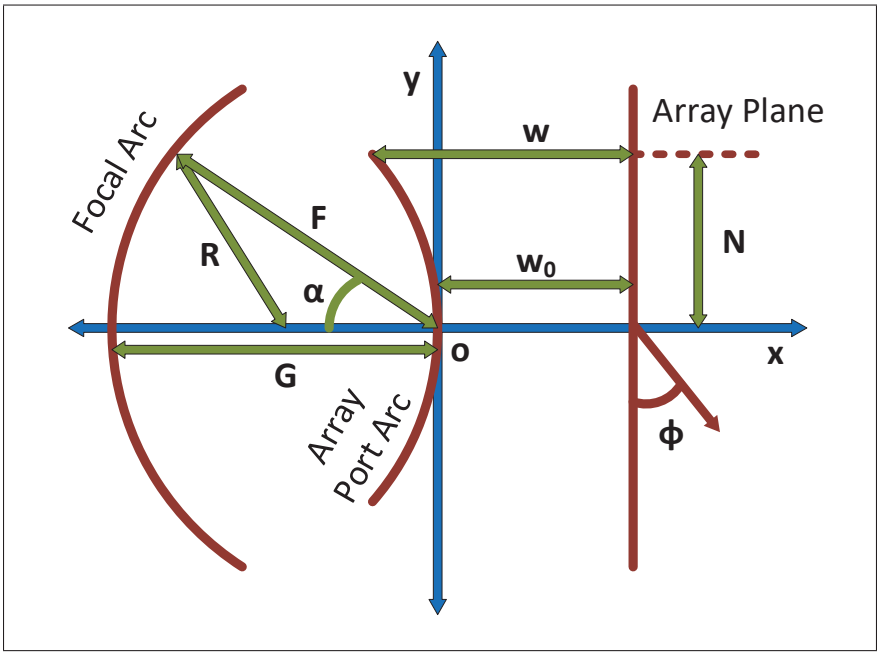

Figure 3.32 Geometry parameters of the Rotman Lens.

Considering the structure in figure 3.32, we can find the geometrical design parameters of the Rotman lens employing the equations presented in Rotman & Turner (1963). In these equations, the normalized value of the parameters by the focal length F is used for simplicity. So, we define the normalized parameters as:

$$n = \frac{N}{F} \; , \; x = \frac{X}{F} \; , \; y = \frac{Y}{F} \; , \; w = \frac{w - w_o}{F} \; , \; g = \frac{G}{F} \tag{3.16}$$

$$a_0 = cos\alpha \; , \; b_0 = sin\alpha \; , \; a_1 = cos\phi \; , \; b_1 = sin\phi \tag{3.17}$$

$$\varepsilon_{eff} = \frac{\varepsilon_r + 1}{2} + \frac{\varepsilon_r - 1}{2} \frac{1}{\sqrt{1 + \frac{12d}{w}}} \tag{3.18}$$

First, for the given design parameters of α, ϕ, g and ε_r, we can calculate w using:

$$a = \frac{\varepsilon_{eff}}{\varepsilon_r} - n^2 (\frac{b_1}{b_0})^2 \frac{\varepsilon_{eff}}{\varepsilon_r^2} - \frac{\varepsilon_{eff}}{\varepsilon_r} \frac{(g-1)^2}{(g-a_0)^2} \tag{3.19}$$

$$b = 2\frac{\sqrt{\varepsilon_{eff}}}{\sqrt{\varepsilon_r}} \frac{g(g-1)}{(g-a_0)} - \frac{\sqrt{\varepsilon_{eff}}}{\varepsilon_r \sqrt{\varepsilon_r}} \frac{(g-1) b_1^2 n^2}{(g-a_0)^2} + 2\frac{\sqrt{\varepsilon_{eff}}}{\varepsilon_r \sqrt{\varepsilon_r}} (\frac{b_1}{b_0})^2 - 2\frac{\sqrt{\varepsilon_{eff}}}{\sqrt{\varepsilon_r}} g \tag{3.20}$$

$$c = \frac{(b_1 n)^2 \, g}{\varepsilon_r \, (g - a_0)} - \frac{(b_1 n)^4}{4\varepsilon_r^2 \, (g - a_0)^2} - (\frac{b_1}{b_0})^2 \frac{n^2}{\varepsilon_r} \tag{3.21}$$

$$aw^2 + bw + c = 0 \tag{3.22}$$

Then, parameters of x and y can be found by these equations:

$$y = \frac{b_1}{b_0}\, n\,(\frac{1}{\sqrt{\varepsilon_r}} - \frac{\sqrt{\varepsilon_{eff}}}{\varepsilon_r}) \tag{3.23}$$

$$x^2 + y^2 + 2gx = \frac{\varepsilon_{eff}}{\varepsilon_r}\, w^2 - 2\frac{\sqrt{\varepsilon_{eff}}}{\sqrt{\varepsilon_r}}\, gw \tag{3.24}$$

Aforementioned equations are formulated in a Matlab code which accepts the input parameters and prepares the geometry of the Rotman lens in DXF format. The input parameters of our design are listed in the table 3.9. We want to design a Rotman lens at the center frequency of 60 GHz on the substrate with dielectric constant of 7.1. This Rotman lens has 5 beam ports, 5 array ports and 4 dummy ports with element spacing of half-wavelength and is able to steer the radiation beam from $-30°$ to $+30°$ relating to the broadside. The output file will provide the position and direction of all ports and the tapering to the $50\,\Omega$ transmission line.

The next step is to import this DXF file in the Keysight ADS (Keysight, 2020) software and append the $50\,\Omega$ transmission lines for the ports connection to the rest of circuit. It is important to notice that the electrical path length of the transmission lines between the array ports and the radiating elements must be the same. In this way, we keep the phase shift between the array contour and the outer contour constant and the phase error will be minimum. To achieve this goal, we should bend the shorter transmission lines in the middle part to obtain the desired electrical length. On the other hand, the length of transmission lines for the beam ports and the dummy ports are not very important. Keysight ADS momentum provides some tools that make it easy to calculate the electrical length of transmission line at desired frequency.

Table 3.9 Input parameters of the designed Rotman Lens for 60GHz band.

Beam Port	**Array Port**	**Dummy Port**	**Element Spacing**	**Array Steering Angle**	**Focal Angle (α)**	**Focal Ratio (g)**	**Expansion Factor** $sin(\phi)/sin(\alpha)$
5	5	4	0.5λ	$\pm 30°$	$30°$	0.9	1.05

Then we can run a full-wave simulation in the Keysight ADS momentum or export the layout to HFSS software and simulate in more detail there. The layout of designed Rotman lens with and without the 50 Ω transmission lines in ADS and HFSS is presented in figure 3.33.

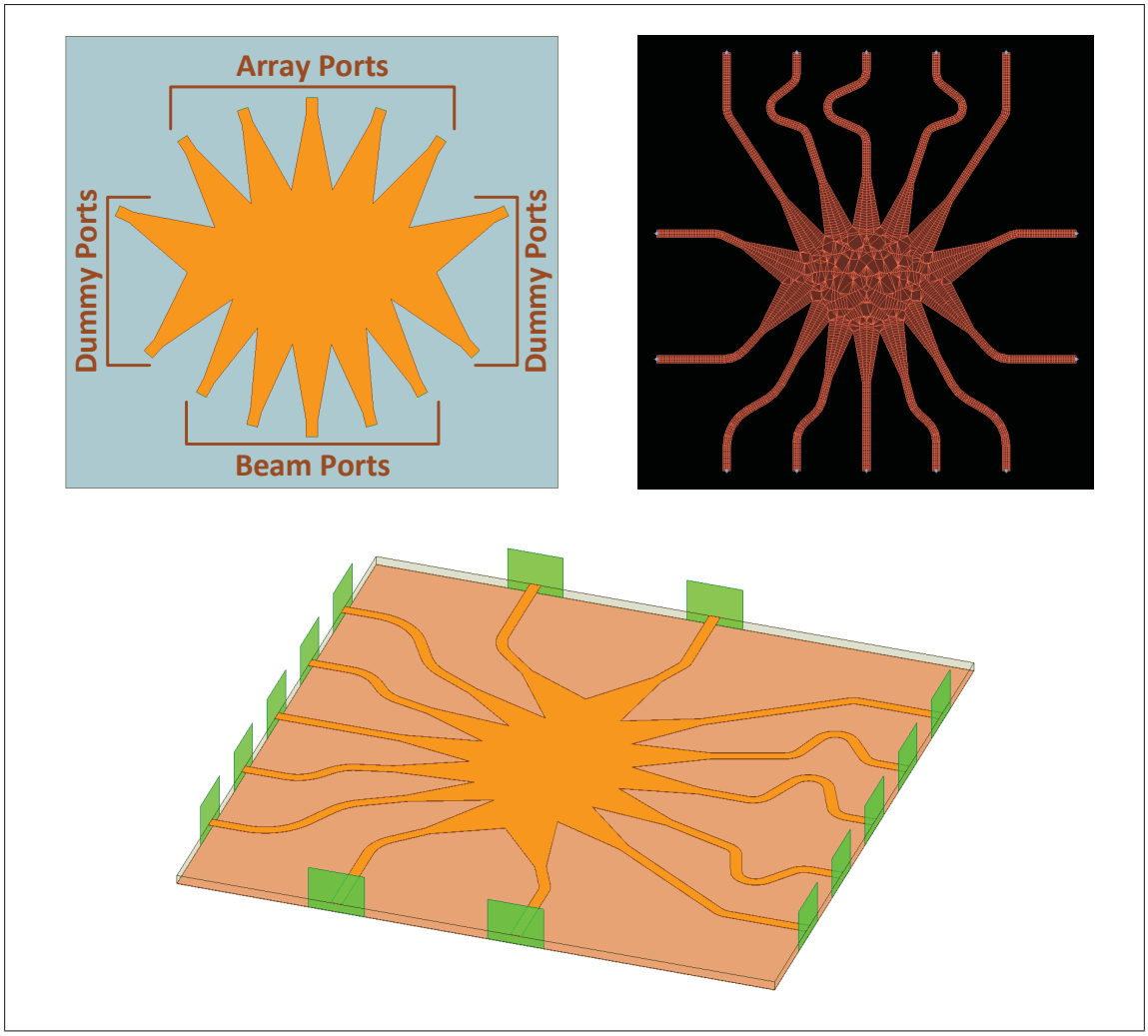

Figure 3.33 Designed Rotman Lens with and without transmission lines.

(Rahmani, 2017) and (Attaran *et al.*, 2016) followed the same procedure to design the Rotman lens for the center frequency of 25 GHz and 60 GHz respectively. Figures 3.34 to 3.38 presents the simulation results of designed Rotman lens. Figure 3.37 displays the total insertion loss and the phase shift of array ports when one input is excited. Considering the Array Factor in figure 3.38, it is noticeable that the scanning over frequency is stable with acceptable SLL.

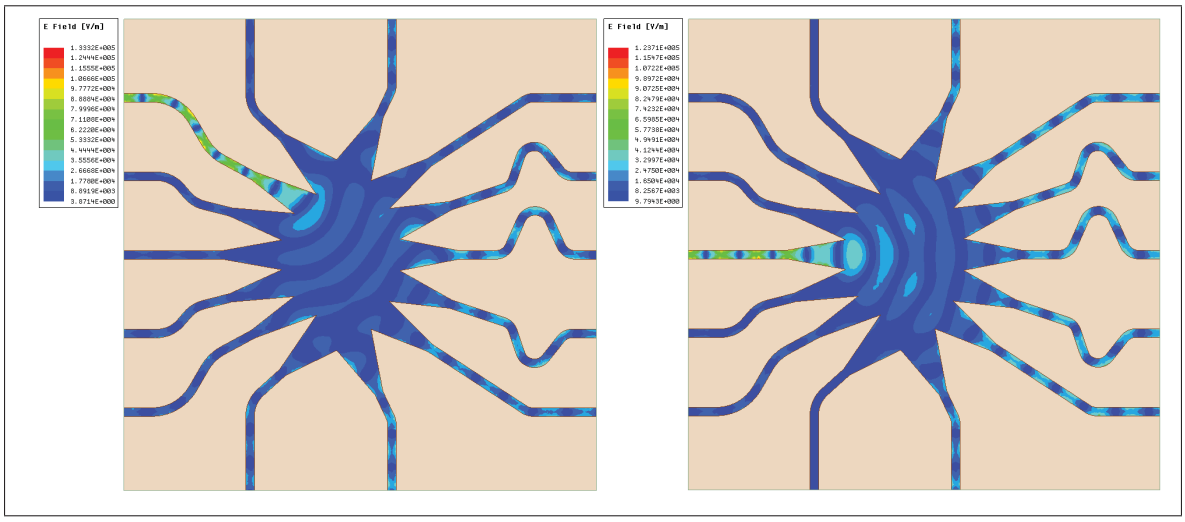

Figure 3.34 Electrical wave propagation in the substrate under the Rotman Lens when the beam ports 1 and 3 are excited.

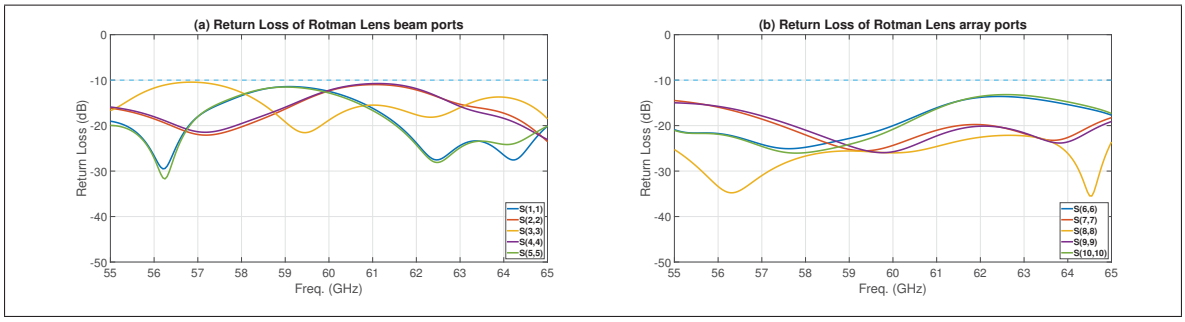

Figure 3.35 Return loss of the beam ports and array ports of Rotman Lens.

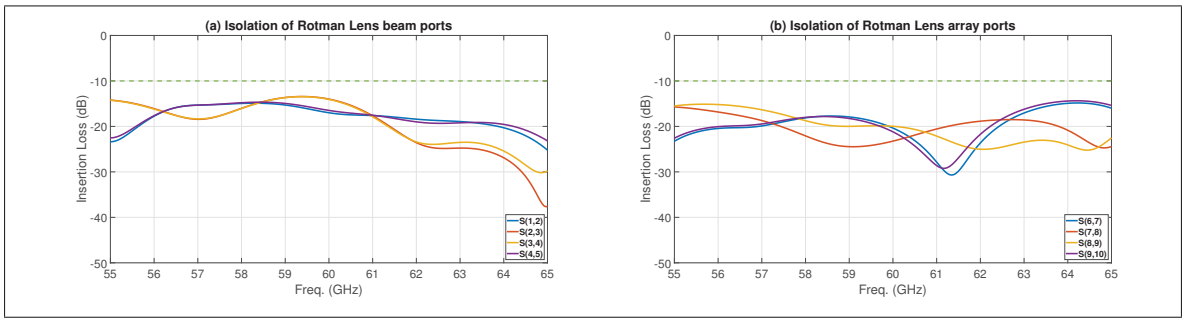

Figure 3.36 Isolation of the beam ports and array ports of Rotman Lens.

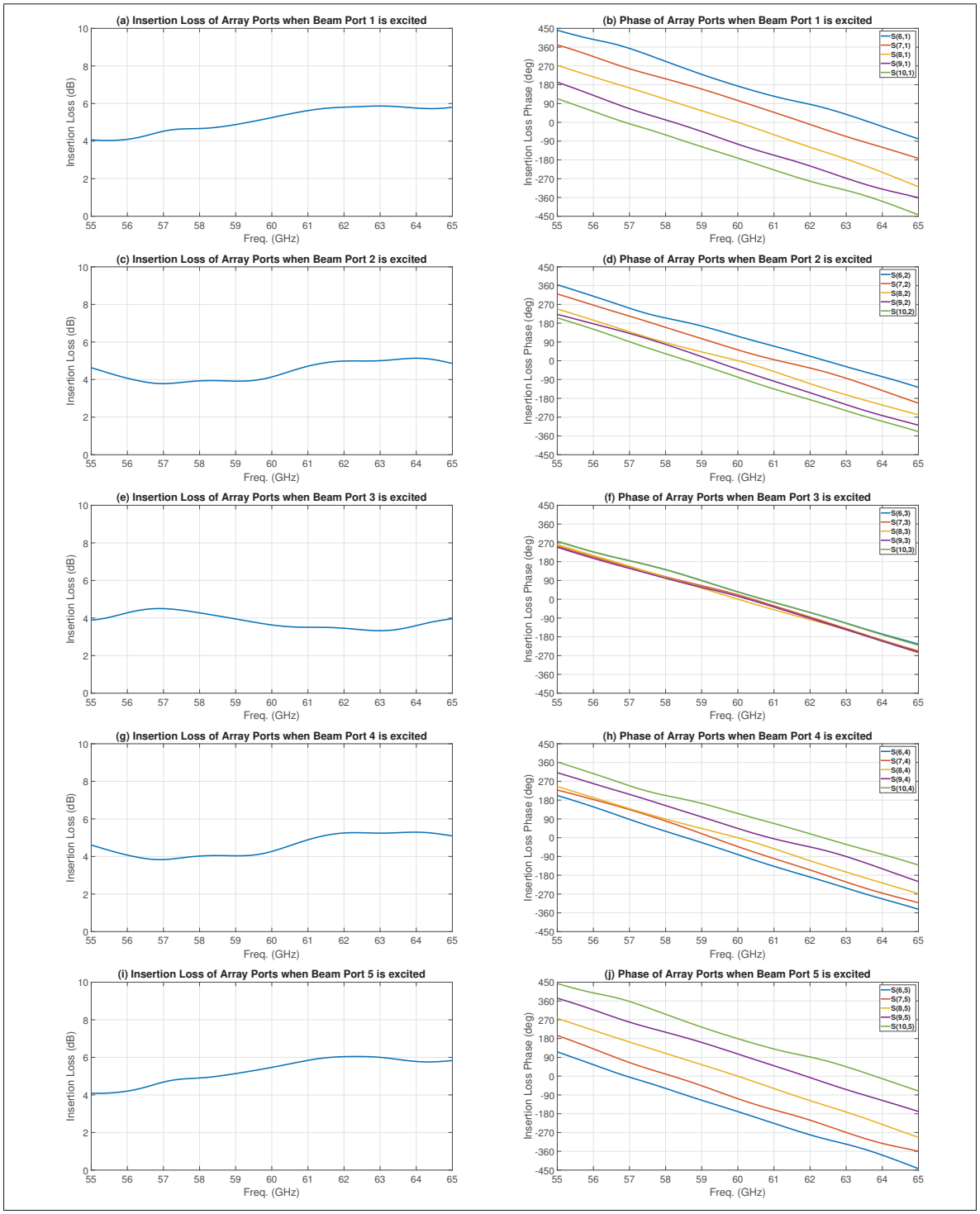

Figure 3.37 Total Insertion Loss and individual output phase of the array ports when one beam port is excited.

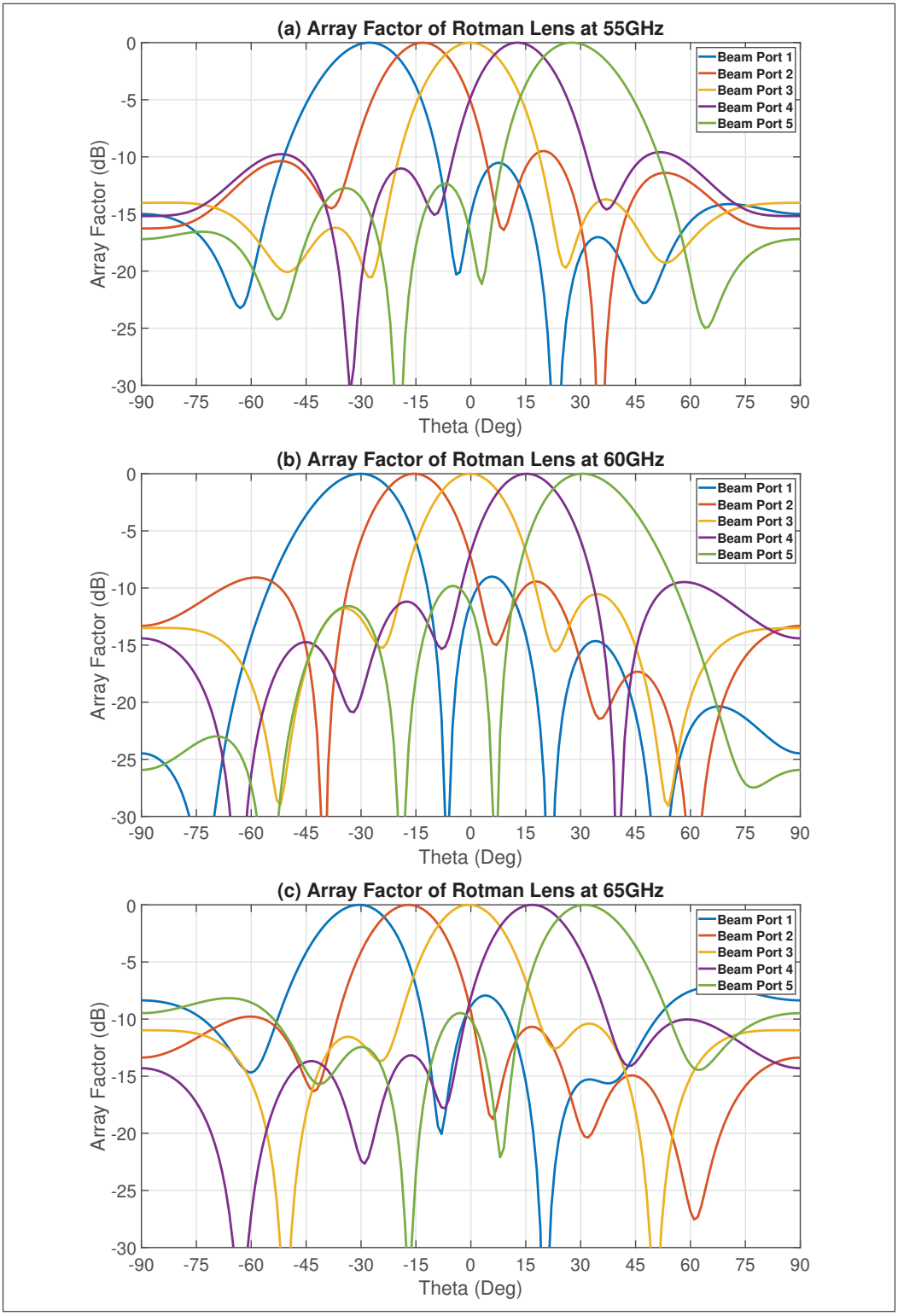

Figure 3.38 Array Factor of the simulated Rotman Lens at 55GHz, 60GHz and 65GHz when different beam ports are excited.

3.7 Complete proposed structure

So far, in all the previous sections of this chapter, we have explained each part of our proposed structure in detail. Here, we are going to put all these pieces together and present a complete design structure for two introduced periodic LWAs. Figures 3.39 and 3.40 display the layout of complete design structure for the original proposed antenna presented in table 3.6 with three vias and the alternative proposed antenna presented in table 3.8 with two quarter-wavelength radial stubs respectively. These layouts include an array of 5 LWA antennas with 9 unit-cells, a Rotman lens and all the necessary 50 Ω transmission lines connection between them and ports.

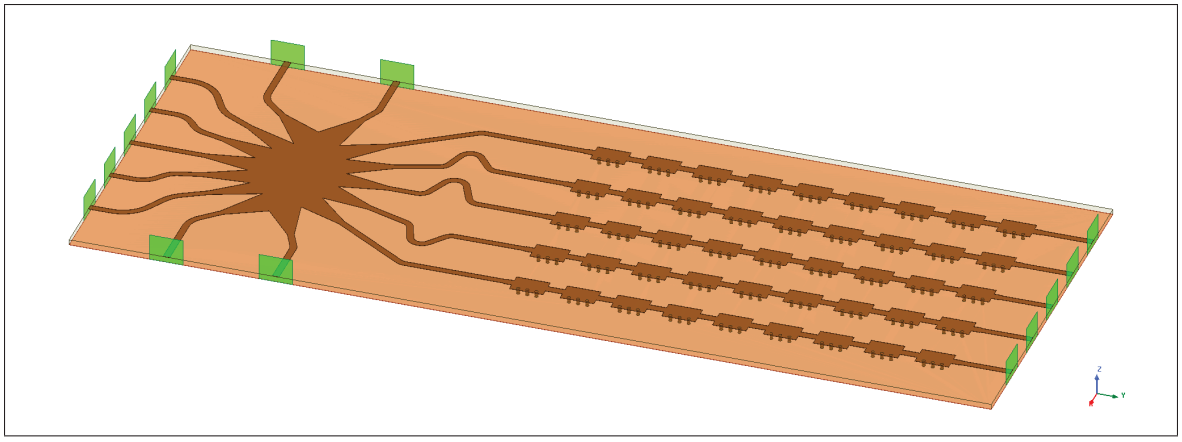

Figure 3.39 Complete design structure layout for the antenna in table 3.6 (with via).

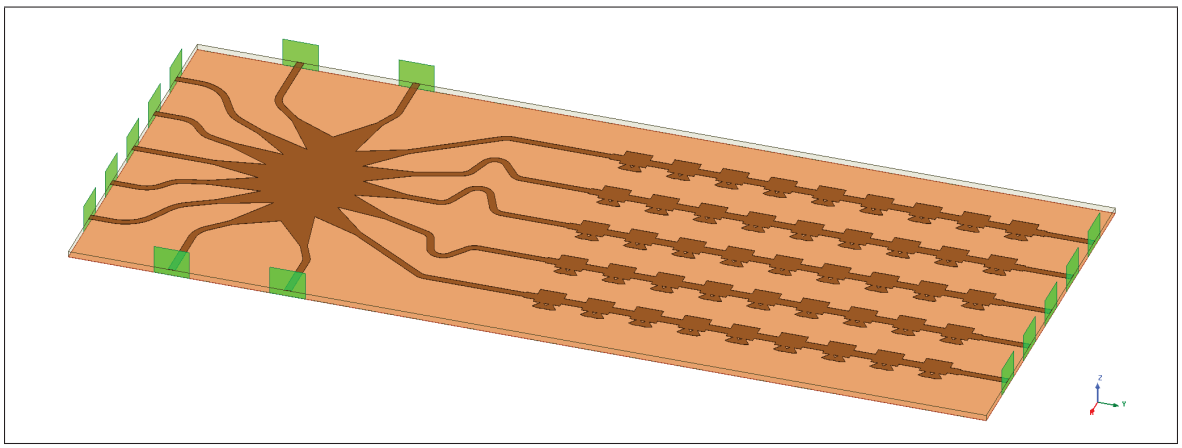

Figure 3.40 Complete design structure layout for the antenna in table 3.8 (with stub).

The complete solution was simulated in HFSS software with discrete sweep type from 50 GHz to 70 GHZ in 1 GHz step. Ports 1 to 5 are the input ports, which are connected directly to the beam ports of the Rotman lens and are excited one at a time. Ports 6 to 10 are the output ports that are connected to the end of antennas array and matched by 50 Ω load. Finally, ports 11 to 14 are the Rotman lens dummy ports, matched by load as well to minimize the reflection. Figure 3.41 presents the return loss of input ports and the insertion loss of output ports relating to each input ports for the structure in figure 3.39. As we can see, the input return losses are better than 10 dB; so, the reflection on the input ports are minimum. Also, the insertion loss of all the output ports are above 10 dB, which means most part of the incident power from the input port dissipates through radiation (almost nothing reaches to the other side of antennas).

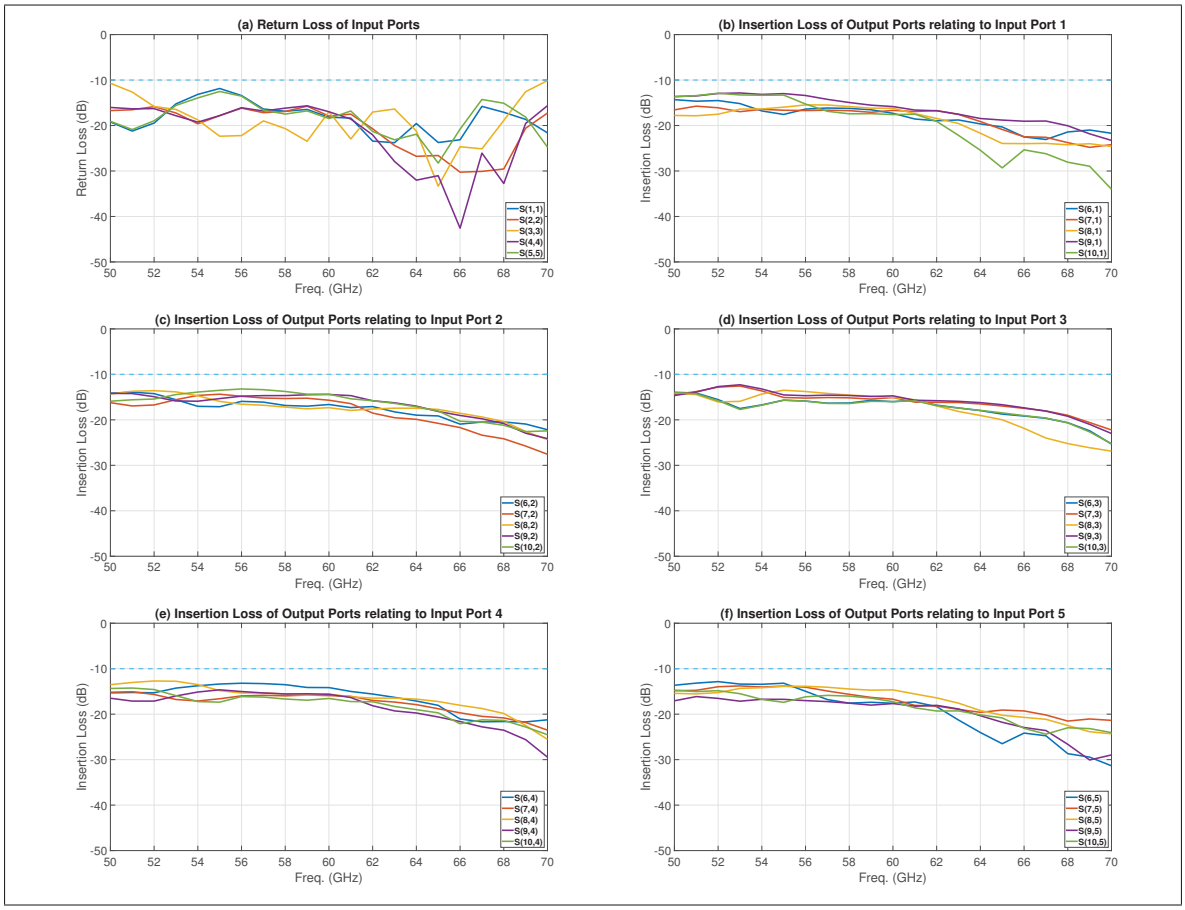

Figure 3.41 Return Loss of the input ports and Insertion Loss of the output ports for the whole structure in figure 3.39.

Figure 3.42 presents the return loss of input ports and the insertion loss of output ports relating to each input ports individually for the structure introduced in figure 3.40. Once again, the input return losses and the output insertion losses are better than 10 dB. Therefore, the reflection coefficient on the input ports are acceptable and most portion of the incident power from the input port dissipates through radiation. It is noticeable that the insertion losses in this figure are more flat compared to the previous one, especially at higher frequencies.

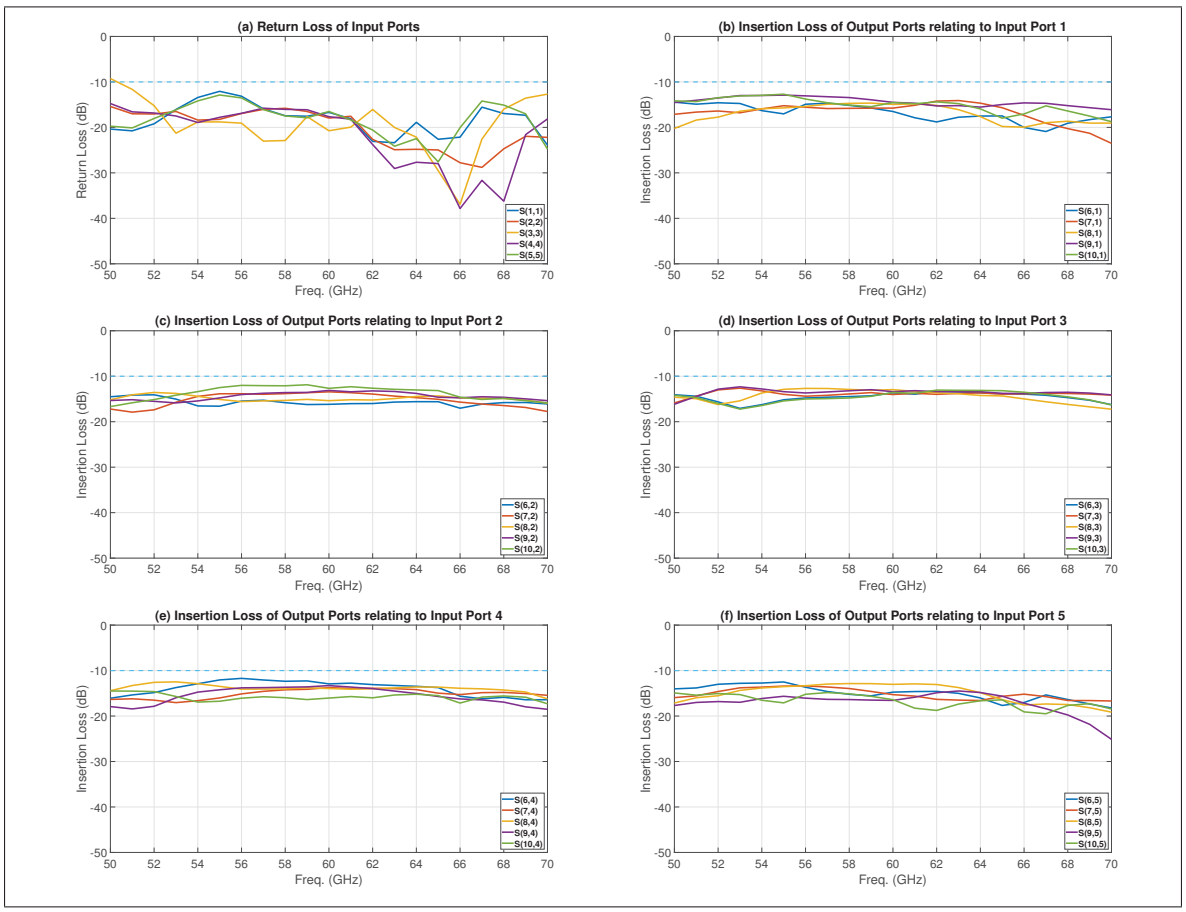

Figure 3.42 Return Loss of the input ports and Insertion Loss of the output ports for the whole structure in figure 3.40.

Figures 3.43 and 3.44 demonstrate the radiation beam scanning of the structures presented in figures 3.39 and 3.40 respectively versus the frequency on the Y-Z plane ($\Phi = 90°$) while the input port 3 is excited. In the proposed configuration, if we feed the input port 3, the locus of the maximum radiation points with frequency will be on the Y-Z plane. The max total gain

of the first structure at $54\,GHz$ is $15.7\,dB$ in $\theta = -24°$, at $60\,GHz$ is $17.1\,dB$ in $\theta = -1°$ and at $66\,GHz$ is $18.1\,dB$ in $\theta = +18°$. The max total gain of the second structure at $54\,GHz$ is $15.2\,dB$ in $\theta = -24°$, at $60\,GHz$ is $15.8\,dB$ in $\theta = -2°$ and at $66\,GHz$ is $16.8\,dB$ in $\theta = +15°$.

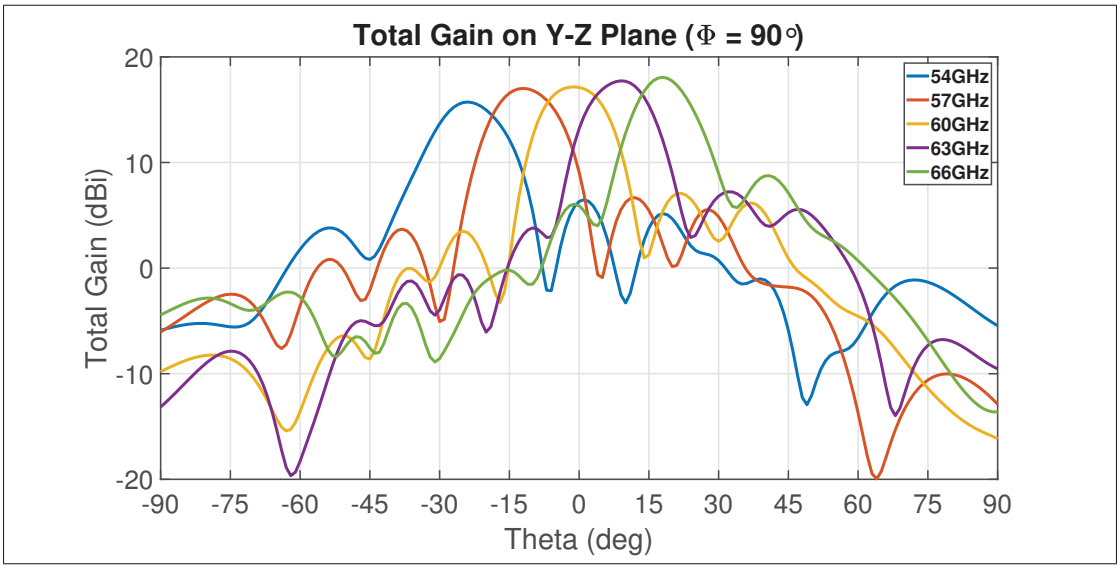

Figure 3.43 Beam scanning vs frequency on the Y-Z plane ($\Phi = 90°$) for the whole structure in figure 3.39 when input port 3 is excited.

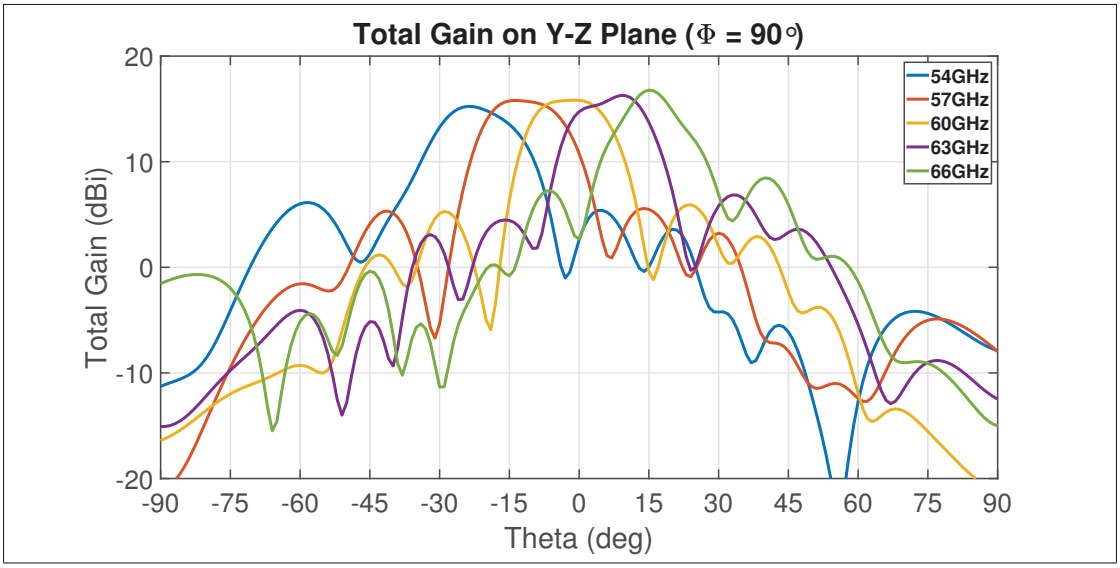

Figure 3.44 Beam scanning vs frequency on the Y-Z plane ($\Phi = 90°$) for the whole structure in figure 3.40 when input port 3 is excited.

Figures 3.45 and 3.46 illustrate the radiation beam scanning of two structures versus the excited input port on the X-Z plane ($\Phi = 0°$) at 60 GHz. The scanning angle for the first structure is from $\theta = -30°$ to $\theta = +28°$ and for the second structure is from $\theta = -28°$ to $\theta = +28°$.

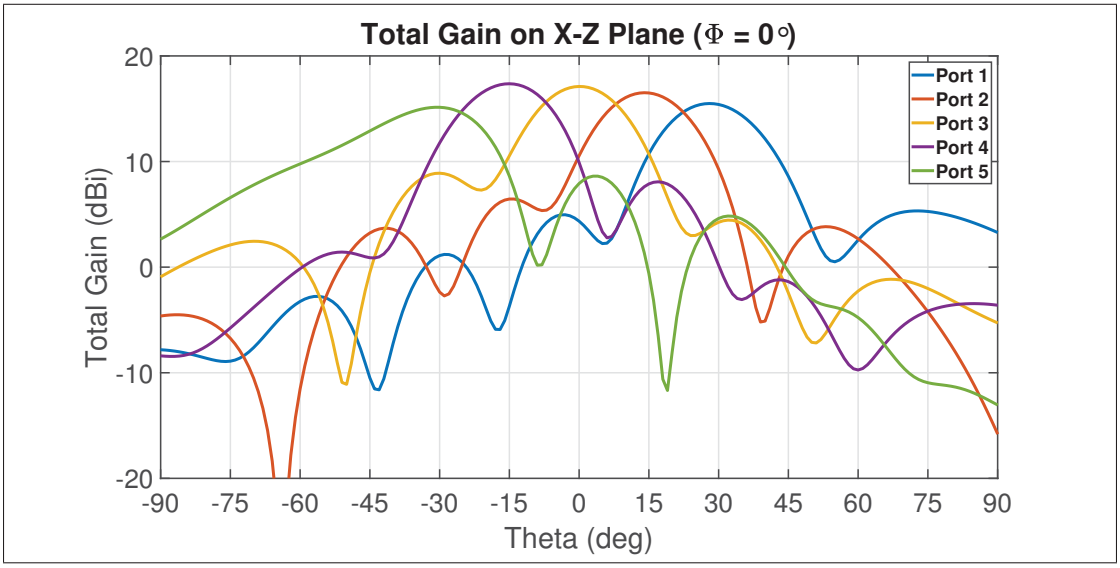

Figure 3.45 Beam scanning vs input ports on the X-Z plane ($\Phi = 0°$) for the whole structure in figure 3.39 at 60 GHz.

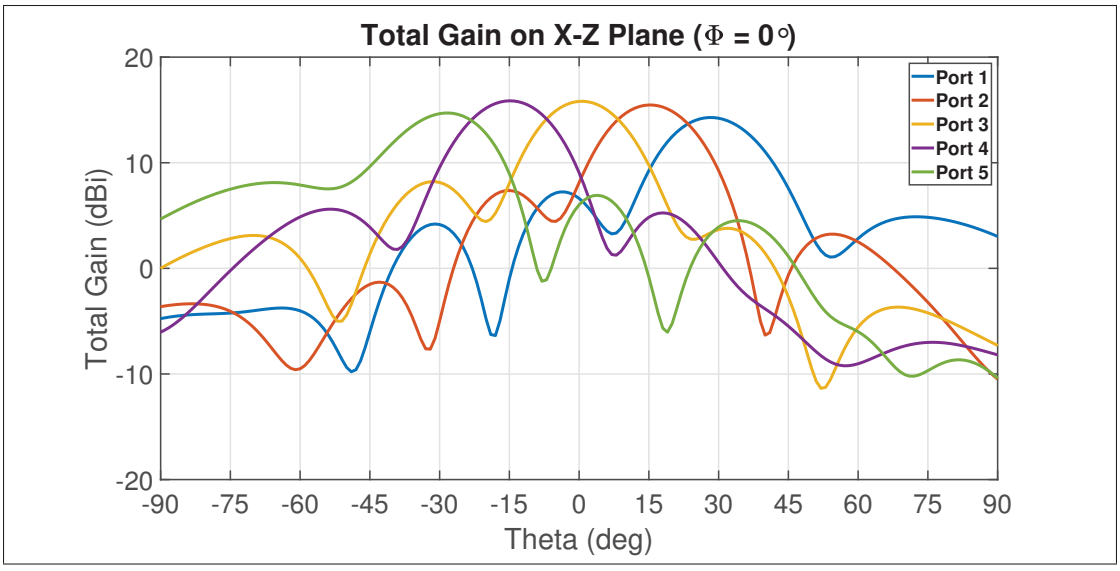

Figure 3.46 Beam scanning vs input ports on the X-Z plane ($\Phi = 0°$) for the whole structure in figure 3.40 at 60 GHz.

Figures 3.47 and 3.48 present the total efficiency of two structures versus the excited input port. The average efficiency for all input ports in the first structure over the frequency bandwidth is from 64% to 83% and in the second structure, which is more flat over the frequencies, is from 70% to 79%. But, both of them are almost 72% efficient at the center frequency.

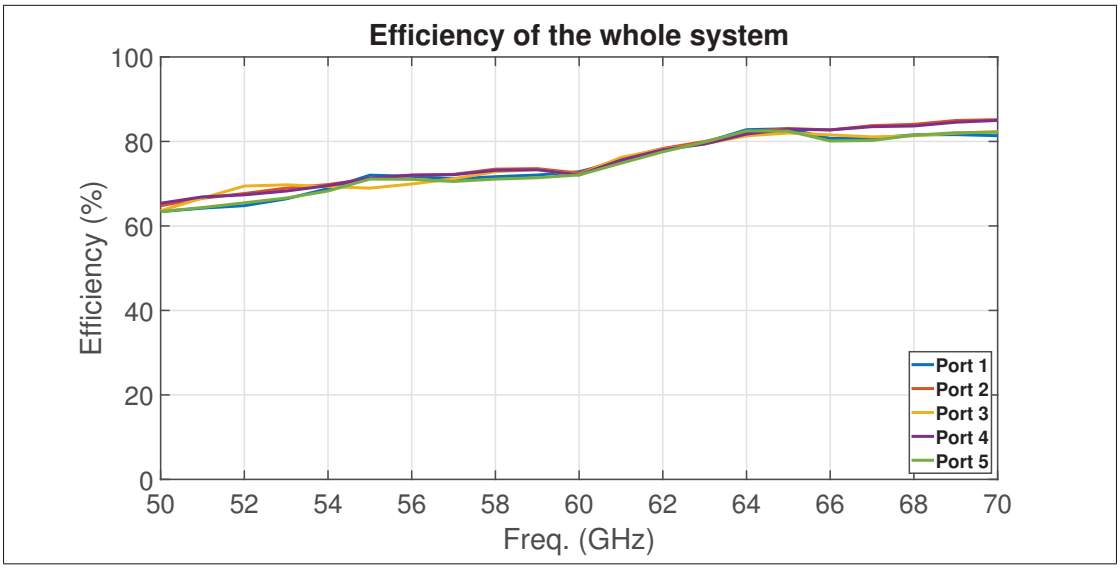

Figure 3.47 Efficiency vs input ports for the whole structure in figure 3.39.

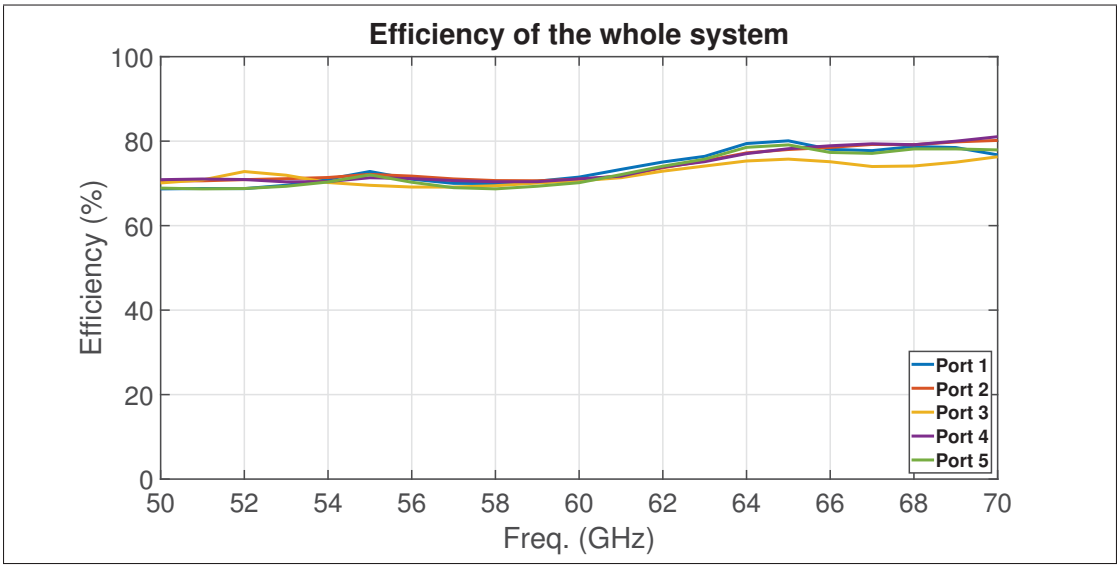

Figure 3.48 Efficiency vs input ports for the whole structure in figure 3.40.

Figures 3.49 and 3.50 present the total peak realized gain of two structures versus the excited input port. The average peak realized gain for all input ports in the first structure over the frequency bandwidth is from 9.5 dB to 14.5 dB and in the second structure, which is more flat over the frequencies (not in the higher frequencies), is from 10.5 dB to 12.5 dB.

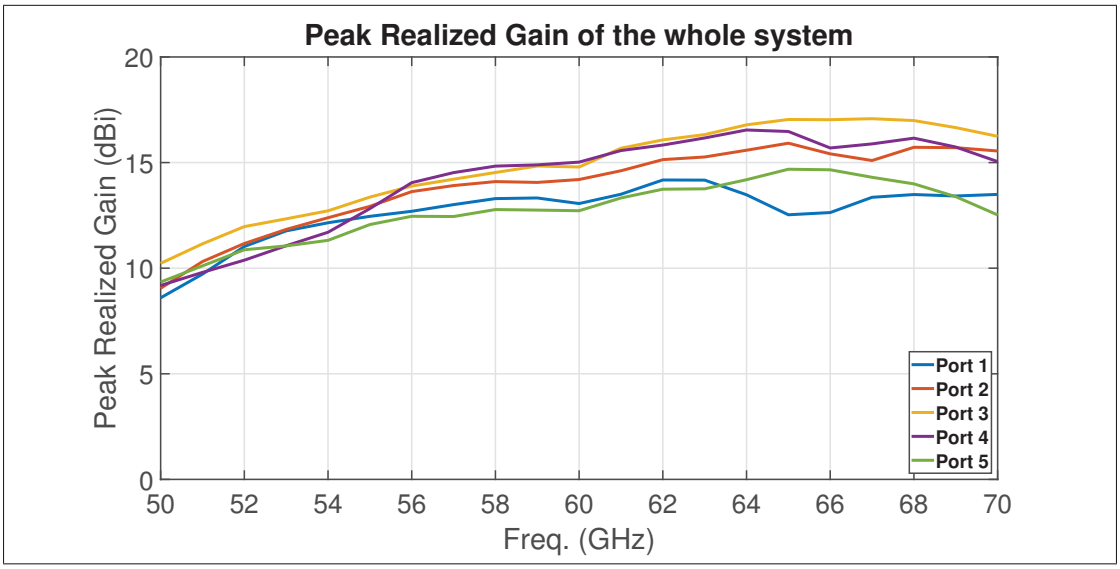

Figure 3.49 Peak Realized Gain vs input ports for the whole structure in figure 3.39.

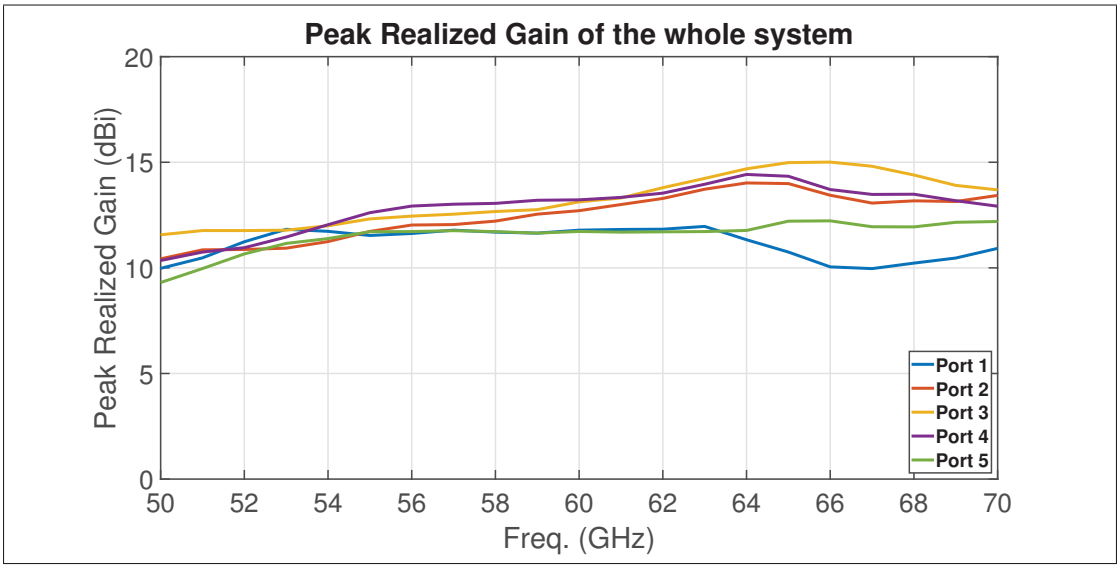

Figure 3.50 Peak Realized Gain vs input ports for the whole structure in figure 3.40.

Figures 3.51 and 3.52 present the axial ratio and the radiation beam angle of two structures when the input port 3 is excited. The axial ratio for the first structure is a little higher than expected and need an improvement but for the second structure is in the acceptable range.

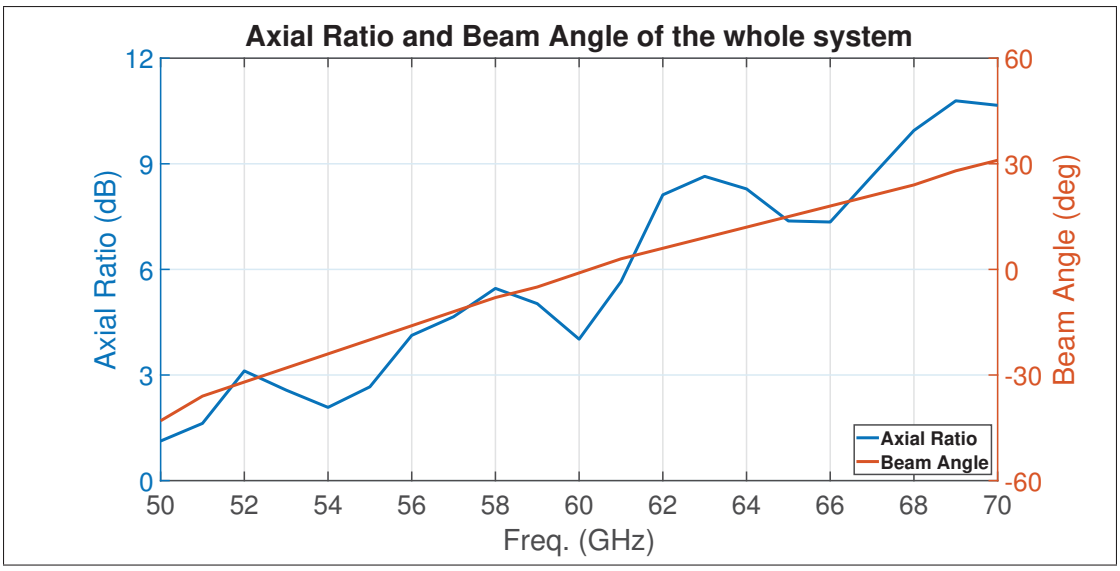

Figure 3.51 Axial Ratio and Beam Angle for the whole structure in figure 3.39 when input port 3 is excited.

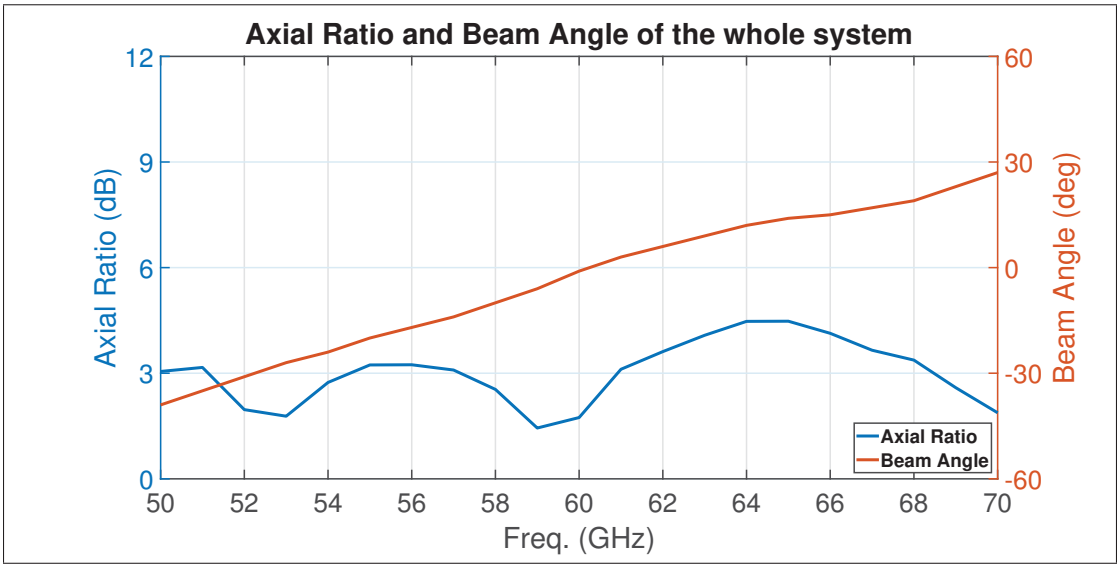

Figure 3.52 Axial Ratio and Beam Angle for the whole structure in figure 3.40 when input port 3 is excited.

Figures 3.53 shows the Surface Current Density distribution on the metal body of the structure presented in figure 3.39 at the frequency of 60 GHz when the input ports 3 and 5 are excited.

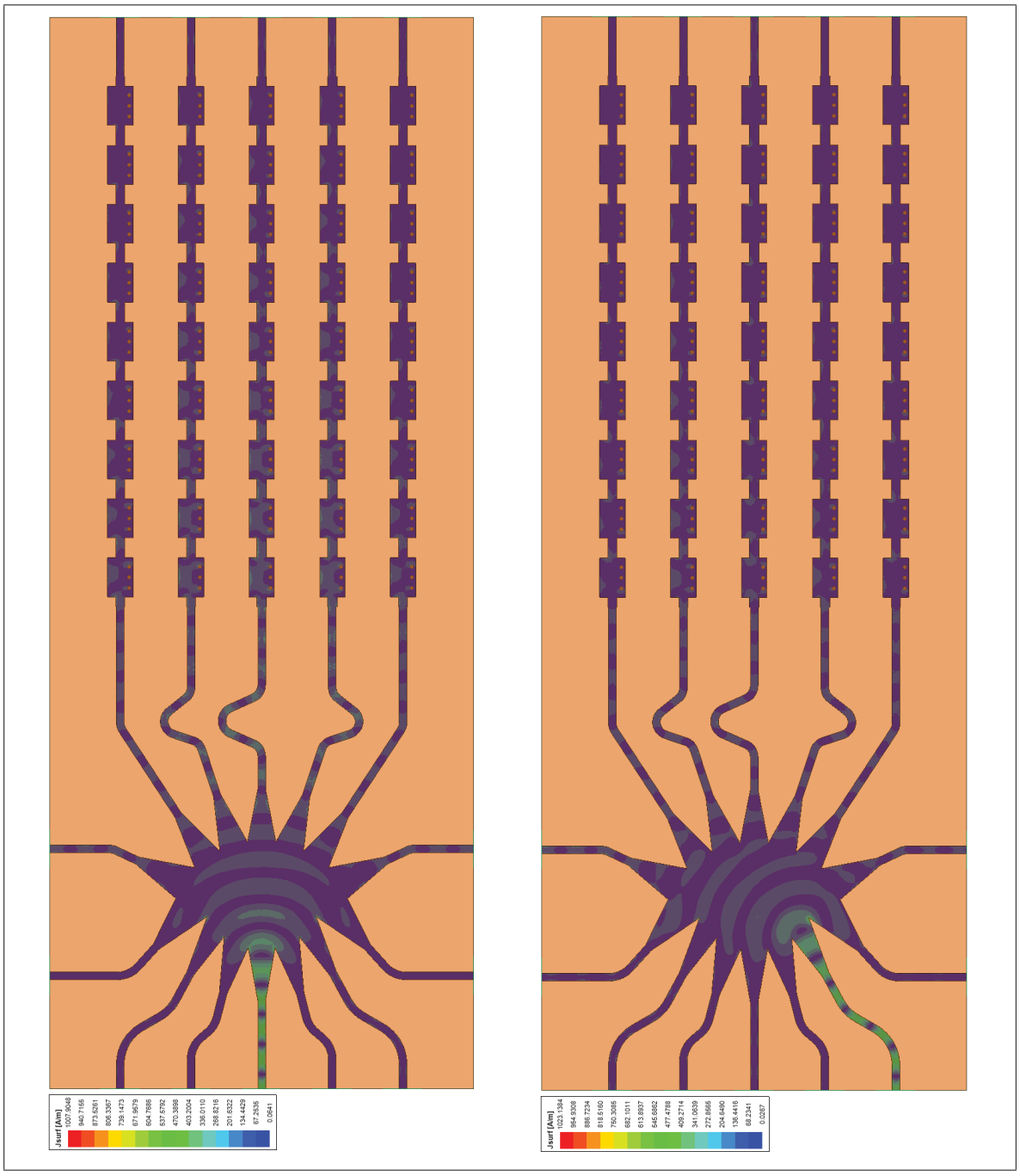

Figure 3.53 Surface Current Density distribution for the whole structure in figure 3.39 when the input ports 3 and 5 are excited.

Figures 3.54 shows the Surface Current Density distribution on the metal body of the structure presented in figure 3.40 at the frequency of 60 GHz when the input ports 3 and 5 are excited.

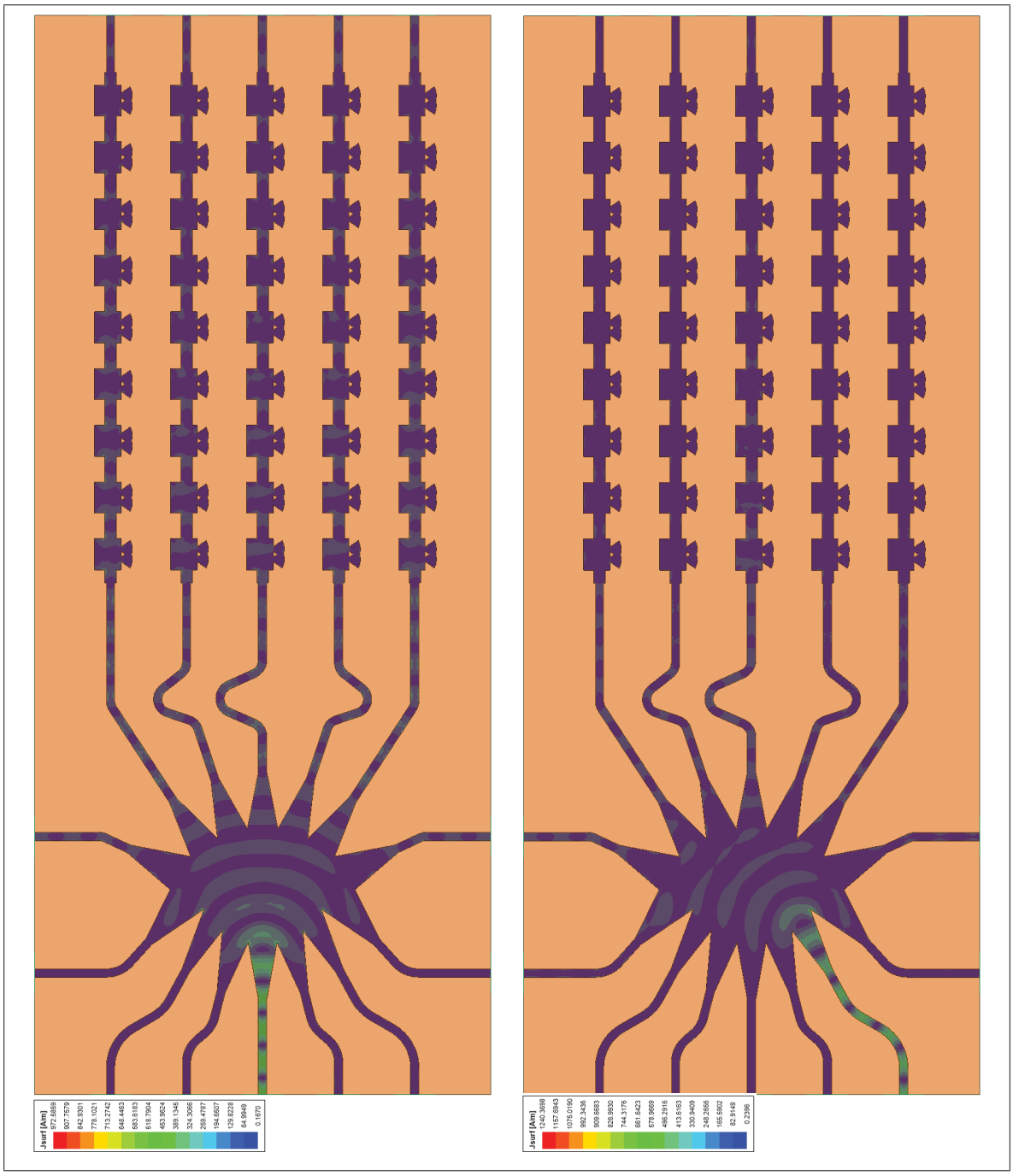

Figure 3.54 Surface Current Density distribution for the whole structure in figure 3.40 when the input ports 3 and 5 are excited.

Figures 3.55 displays the 3-D radiation pattern of the structure presented in figure 3.39 for five excited input ports at three frequencies of 55 GHz, 60 GHZ and 65 GHz. These radiation patterns demonstrate seamless beam steering capability of the proposed structure with the input frequency in the Y-Axis direction (direction of the wave propagation in the antenna) and the excited input port in the X-Axis direction (direction of the array elements) by means of 3-D total gain of the system. The SLL of the radiation patterns are mostly better than 10 dB.

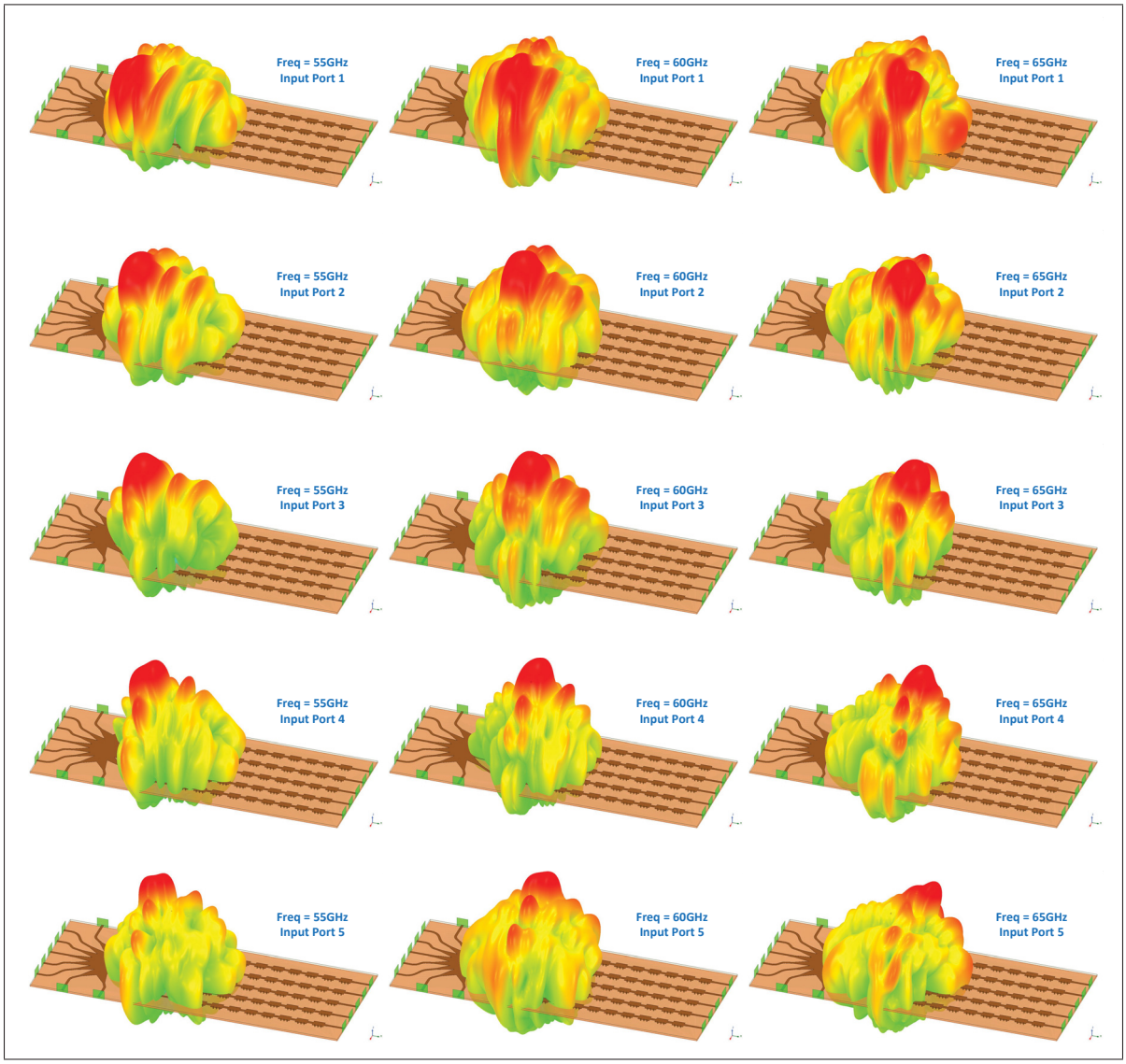

Figure 3.55 3-D Beam scanning vs the frequency and the input ports for the whole structure in figure 3.39.

Figures 3.56 displays the 3-D radiation pattern of the structure presented in figure 3.40 for five excited input ports at three frequencies of 55 GHz, 60 GHZ and 65 GHz. These radiation patterns demonstrate seamless beam steering capability of the proposed structure with the input frequency in the Y-Axis direction (direction of the wave propagation in the antenna) and the excited input port in the X-Axis direction (direction of the array elements) by means of 3-D total gain of the system. The SLL of the radiation patterns are mostly better than 10 dB.

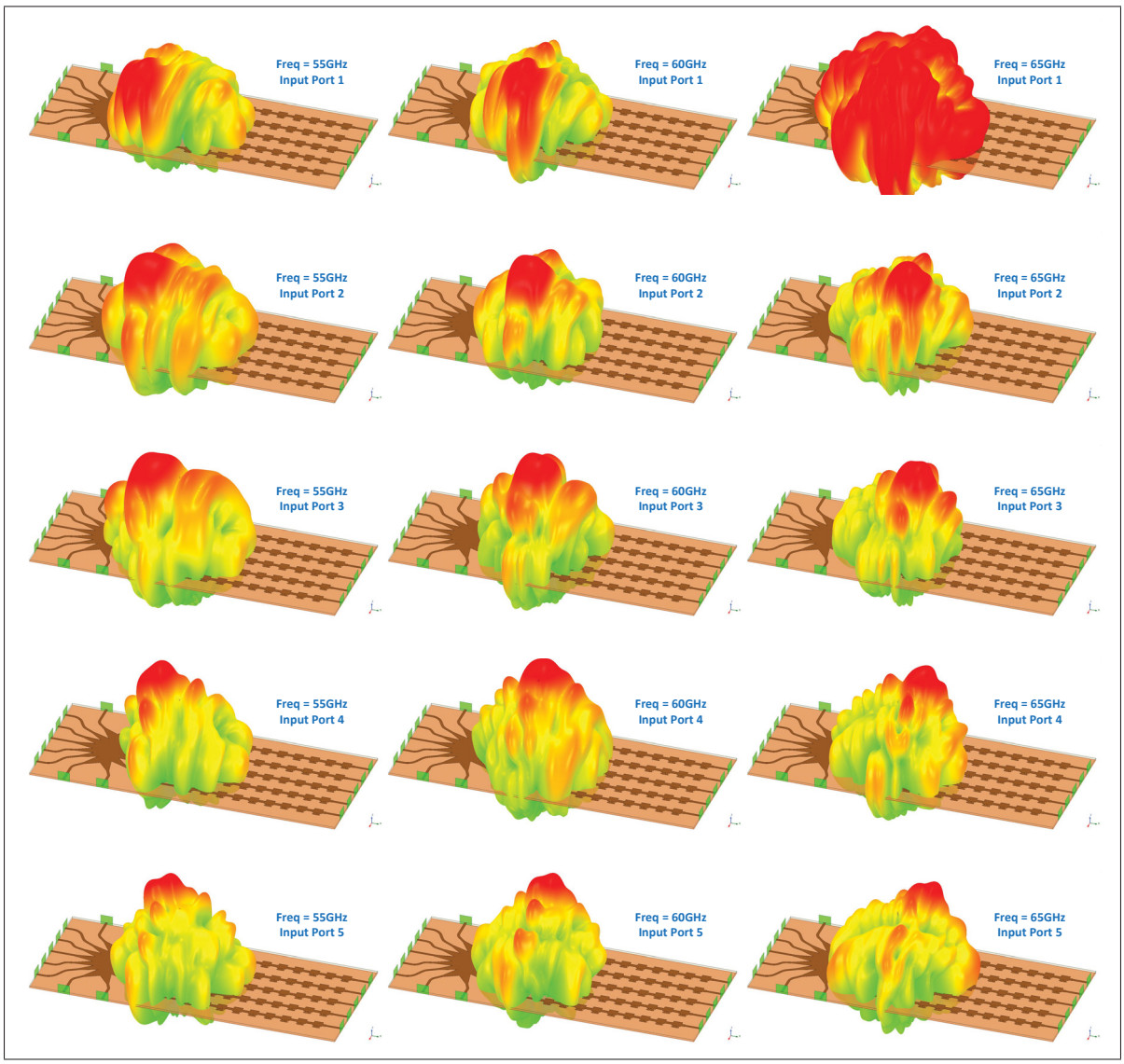

Figure 3.56 3-D Beam scanning vs the frequency and the input ports for the whole structure in figure 3.40.

3.8 Conclusion

In this chapter, we presented the whole design procedure from a single unit-cell design, the parametric optimization and simulation to the construction of the complete structure with all passive, printable components in order to have a reconfigurable radiation pattern, steering in two perpendicular directions. A simple geometry of the unit-cell with three vias on the side was proposed as the basic building block of a periodic leaky-wave antenna. The input parameters and the expected output features of the optimization process were investigated. Three periodic LWAs, optimized with different objectives were presented and the effect of the number of via and the ground plane's size on the structure were studied.

Then, an alternative design structure was suggested by replacing the via in the unit-cell with the open-circuited quarter-wavelength radial stub. Eliminating the drilling part and the extra alignment procedure, simplifies the fabrication process which leads to a great saving in the time and the budget. Besides, this alternative structure almost shows the same performance as the original proposed one. The summary of the performance of two proposed antennas over the frequency range of 50 GHz to 70 GHz are presented in the table 3.10.

Table 3.10 Performance of two proposed periodic LWAs on the frequency range of 50 GHz to 70 GHz.

Parameter	**Original Periodic LWA**	**Alternative Periodic LWA**
Average Efficiency	87.42%	86.06%
Average Total Gain	12.37 *dBi*	11.45 *dBi*
Average Peak Realized Gain	11.25 *dBi*	10.59 *dBi*
Beam Steering Angle	$-43°to+34°$	$-39°to+28°$
Average Axial Ratio	6.33 *dB*	6.38 *dB*

As we demonstrated with the gain plots, the designed PLWA has the ability to seamlessly steer the radiated beam pattern in the direction of wave propagation throughout the antenna from backward to forward including the broadside by varying its input frequency. It has the circular polarization and low side lobe level (SLL) that are the key features for any practical WPAN system. A linear phased-array of the periodic LWAs was employed to make the radiation beam steering in the second direction possible. The Rotman lens was introduced as the beamformer network (BFN) to feed this linear phased-array of antennas. Beam scanning on the orthogonal plane to the direction of propagation will be performed by the excitation of the beam ports of Rotman lens. The summary of the performance of two proposed complete structures, including an array of antenna, a Rotman lens and all connecting transmission lines, over the frequency range of 50 GHz to 70 GHz are presented in the table 3.11.

Table 3.11 Performance of two proposed complete structures on the frequency range of 50 GHz to 70 GHz.

Parameter	**Original Complete Structure**	**Alternative Complete Structure**	**Condition**
Average Efficiency	75.1%	73.4%	All input ports combined
Average Total Gain on Y-Z plane	16.84 *dBi*	15.77 *dBi*	Input ports 3 excited
Average Total Gain on X-Z plane	16.32 *dBi*	15.23 *dBi*	All input ports combined
Average Peak Realized Gain	13.63 *dBi*	12.25 *dBi*	All input ports combined
Beam Steering on Y-Z plane	$-43°to+31°$	$-39°to+27°$	Input ports 3 excited
Beam Steering on X-Z plane	$-31°to+28°$	$-28°to+28°$	All input ports combined
Average Axial Ratio	5.81 *dB*	3.02 *dB*	Input ports 3 excited

The proposed structure has many beneficial properties which makes it a good candidate for the WiGig application. It is made of only small, passive, printable components that makes it very low-cost, low-profile and easy to fabricate on the LTCC substrate. Besides, it has really advantageous performance in terms of efficiency, gain and beam scanning angle, as we can see in the table 3.11. It supports the circular polarization; although, the value of axial ratio in some frequencies is a little higher than expected, but it could be improved by new optimization. Finally, the side lobe level (SLL) is mostly below -10 dB for our desired bandwidth.

Total dimension of the original proposed antenna itself with 9 unit-cells is $0.9\,mm \times 18.81\,mm$ and for the alternative antenna with the same configuration is $1.05\,mm \times 16.83\,mm$. The whole structure of original design printed on one layer of the LTCC substrate has the dimension of $15\,mm \times 38\,mm$ and the alternative design is $15\,mm \times 35.5\,mm$. The whole structure's size can be reduced by multilayer design implementation which makes it more fit for the SIP applications.

It should be mentioned that we can improve the efficiency and gain of the system by adding extra unit-cells to the PLWA or using more antenna in the phased-array. Also, the beam steering angle can be expanded on the Y-Z plane by increasing the value of relative permittivity of the substrate and on the X-Z plane by redesigning the Rotman lens. Adding more beam ports and array ports, we could achieve more control on the steering and better angular resolution.

CHAPTER 4

FABRICATION ON THE LTCC SUBSTRATE

4.1 Introduction

In this chapter, we are going to cover the fabrication process of our proposed PLWA structure on the LTCC substrate and its challenges. We performed the whole procedure from constructing the circuit mask to the LTCC baking in the Microelectronics and Communications Research Lab (LaCIME - Laboratoire de communication et d'intégration de la microélectronique) of École de Technologie Supérieure (LTCC@ÉTS, 2020). Our LTCC lab in ÉTS is equipped with all kinds of machinery needed for this process, including the metal printing and ablation, via drilling and metal filling, stacking and laminating the layers of the substrates, cutting, LTCC firing and etc. Also, we have access to some inspection and measurement instruments like the measurement microscope, X-Ray machine and high frequency Vector Network Analyzer.

We will introduce the advantages of using a LTCC technology and what range of options we have for choosing a suitable substrate. Then, a summary of our fabrication process will be presented step by step, covering some tips and guidelines in each stage. For connecting the measurement instruments to our structure, some sort of transition and special tools are necessary. Researcher take advantage of many different techniques for this purpose based on the operating frequency band, available technologies and instruments, costs of implementation and etc. Here, we employed two methods of connection which are best fit to our goal.

We planed our fabrications in three batches to check the overall functionality and performance of the proposed system. Each one of them designed for a specific objective. In the next section, we are going to explain these designed phases and their objective. Also, the inspections after the fabrication and before the measurement are discussed to review the quality of manufacturing and its effect on the performance of the structure. We will talk about the performance in more details in the next chapter, while we present the results of the measurements. Finally, we will share our practical fabrication experiences, obtained while working in the lab.

4.2 LTCC substrate

Co-fired ceramic substrates, including low temperature (LTCC) and high temperature (HTCC), have been used extensively in the fabrication of monolithic microelectronic devices, where the whole structure with all passive components are baked in an oven at the same time. The technology is mostly exploited for multilayer integration and packaging of electronic components for industrial applications, such as military electronics, MEMS, microprocessor and RF circuits, because it is cheap and easy to be reproduced in mass production.

Low Temperature Co-Fired Ceramic (LTCC) technology offers a low-loss dielectric property, good thermal conductivity, and a high degree of passive components integration. That makes it a favorable substrate for many AiP (Antenna in Package) fabrications (Zhang & Mao, 2019). However, this technology is considered rather expensive for prototyping, which could be an issue for some applications. Therefore, some state-of-the-art technologies, known as High Density Interconnect (HDI), are recently developed specifically for low-cost mass production of mm-Wave AiPs. Simultaneous stacking of several layers of the industrial-level substrates with different thickness varying from tens of micrometers to 100 μm are possible using these modern technologies, which provides unprecedented design flexibility (Zhang & Mao, 2019).

LTCC-based structures are manufactured exploiting the ceramic tapes and metal pastes. The technology is, although a little expensive, but fairly attainable for the prototyping. However, the mass production can take advantage of the casting services to reduce the costs. The thickness, dielectric constant, and loss tangent of co-fired ceramic can vary from 12.5 to 250 μm , 4 to 75, and 0.0004 to 0.006, respectively by different manufacturers (Gaynor, 2006). Copper, silver, gold and even nickel are available as the metallic pastes of the structure body which will be printed onto the unfired “green” ceramic tapes. After printing all layers of the structure, stacking and laminating them together, they are fired in an oven at a sintering temperature below 900 °C. Normally, using a standard fabrication process, the conductor line-width and spacing of 100 μm, the via diameter and via-line pitch of 100 μm, and via pitch of 300 μm are easily achievable. Hence, LTCC has been popular in fabricating AiP (Zhang & Mao, 2019).

HTCC structures are made of alumina oxide tapes with tungsten and moly manganese metallization. They have the advantage of hermeticity, good electrical performance, good thermal conductivity, high strength, and perfect metal adhesion. But, they have high conductive loss of tungsten and moly manganese compared to gold and silver. In addition, high firing temperature and being costly are some of disadvantages of HTCC technology (Sturdivant, 2010). On the other hand, LTCC has better electrical performance and lower conductive loss at microwave and mm-Wave frequencies. However, the firing temperature of LTCC (about 850°C) is still higher than tolerable temperature of the active devices. Therefore, the active components must be assembled on the structure after firing process (Zhang & Liu, 2009).

We already mentioned all the LTCC substrates and pastes that we have available at LACIME lab (figure 4.1) in the previous chapter, because we needed the substrate's properties for the optimization procedure. DuPont GreenTape™ 9K7 is designed for advanced high-frequency, microwave, and millimeter wave electronic circuit applications. It is a low loss glass ceramic dielectric tape for high frequency applications up to 100 GHz and beyond. The dielectric tape is both cadmium and lead free. These are some advantages of working with DuPont 9K7:

- Superior high frequency performance
- Demonstrated reliability
- Smaller package size
- Stable in harsh environments
- Controlled impedance structures
- Thermal management
- Lower total system cost
- Compatible with plating
- Stable mechanical, electrical and thermal properties

Figure 4.1 LACIME LTCC Lab in ETS

4.3 LTCC fabrication process

Although, the fabrication process on LTCC is not a part of our research project, knowing the procedure gives a beneficial insight and fruitful perspective for improving the design. For example, we can better understand what is possible in the fabrication and what is not, which part is the most important to focus on and what are the tolerances and limitations of process. Here, we share the summary of our experiences in the fabrication process step by step:

1. **Fabrication files**: in the first step, we should prepare some fabrication files in the requested format. In our case, we imported our design from HFSS into ADS, defining required layers in a standard template and exporting Gerber/DXF files for different phases of fabrication. We must scale the structure based on the LTCC shrinkage after firing. In addition, the process accuracy tolerances should be take into account while preparing the design files. A few marks such as fiducials for the alignment, 3 mm holes for the indexing and some guidelines for the cutting also should be appended. To fortify the structure, some dummy layers are used to increase the structure thickness (normally more than 1 mm), because it will become very fragile after baking. Finally, we have to use the available area of LTCC sheet wisely and efficiently. Generally, we need to prepare these four types of files:

   - Drilling file: for vias and other round holes.
   - Mask file: for metal printing.
   - Laser ablation: for removing excessive metal around precise structures.
   - Cavity file: fugitive tape for large cavities and fugitive paste for small cavities.

2. **Stencil and Mask**: normally, stencil is used for the via filling. Although, it is reasonable for mass production, but a little costly for prototyping. Hence, we did not make the stencil, using a method named back-filling. The mask is made from a scaled version of the metal part of the structure for printing. The excessive metal will be removed later during laser ablation. It is made by UV exposure on the emulsion mesh while the positive film is on top of it and later wash off with water. The mask height determines the metal thickness t.

3. **Preconditioning**: DuPont recommends to preheat the 9K7 GreenTape™ 9K7 sheet in the oven for 20 minutes at 100 °C before starting the fabrication process.

4. **Drilling holes**: we have two options for drilling of vias and other holes in the structure: punch machine and laser machine. Laser machine is more accurate in the positioning of vias and it can creates any size or shape of the holes even cavities. However, it is much slower method. The holes are not always in a nice and clean shapes that we expect such as perfect circle. It could burn the LTCC tape and creates edge's burr around the holes which makes the via filling more difficult. Sometimes, two sides of the cylindrical hole are different in size and shape, because the laser beam may expose not perpendicularly to the sheet. On the other hand, the punch machine creates nice and clean vias very fast. But, if we want holes with new dimension or other shapes, we must order a new drill head which is costly. During drilling process, we add $4 \times 3\,mm$ holes for the indexing and $4 \times 150\,\mu m$ holes as fiducial for later alignments.

5. **Via filling**: this process normally is done by an automatic via filling machine using the stencil. But it is expensive for prototyping and suitable for mass production. Instead, we take advantage of the back filling method, using plastic Mylar on the backside of LTCC GreenTape to manually apply the metal paste and fill up the vias. Later, we will remove the Mylar before stacking process. If the sheet is too thick (more than 10 mil) or holes are not perfect, sometime it is difficult to perform back filling method. In these cases, we prepare a plastic stencil which is not expensive and try to fill the via from the top manually.

6. **Metal printing**: for metal printing process, we put the LTCC sheet and the mask in the machine and try to align them precisely using four fiducial holes. It is not easy to align them, because the unfired LTCC sheet is an elastic fabric. We should point out that the standard thickness of metal attained in this process is 8 µm and the paste for metal printing is different than one we used for the via filling. After printing, we have to let it dry in room temperature for one day or put it in the oven at low temperature (30 minutes at 60 °C).

7. **Laser ablation**: metal printing with the mask is not very accurate especially for small structures designed for high frequency applications. For example, thin conductor line-

width and the spacing of less than 100 μm is not feasible through the mask printing process. To achieve the most accurate dimensions and shapes on the structure we employ the laser ablation process. Generally, we print out the wider metal lines with mask to be sure nothing is missing in the structure body. Then, we will engrave the desired, sized structure by removing extra printed metal paste through the laser ablation.

8. **Stacking**: we deposit the prepared layers of LTCC structure face-down into the stacking machine, starting from top layer. We must remove the Mayar from the sheet before putting it inside. The machine takes the sheets, one layer at the time by vacuum pump and stacks it on top of the structure precisely using the indexing holes for the alignment. Then, it uses a small force (150 psi) to press the layers together and makes them like one layer.

9. **Lamination**: after stacking process, the layers need to be laminated together by heating and pressing. For lamination process, we used an Hot Isostatic Press with hydraulic pressure force. we put the sealed, stacked structure in the machine (in the water) for 15 minutes at 70 °C and then press it for 12 minutes using a 108 pascal pressure. After pressing, we should check the dimension of the metal printed on the structure, because sometimes it expand more than accepted tolerance. In this case, we can repeat the laser ablation only for the top layer to adjust the dimension. fortunately, our structure has only one layer.

10. **Cutting**: in one batch of the fabrication, we put different copies of the design structure together to use the most part of the sheet. LTCC tape will be a fragile ceramic after the firing. So, we need to cut it into the pieces we want before baking. Using the guidelines we already dedicated for the cutting purpose in the mask, we cut the separate structures by a guillotine machine. This will deliver a fast and clean cut. However, we can use the laser machine for cutting the complicated shapes as well.

11. **Baking**: each manufacturer recommends a profile or recipe for the firing of its GreenTape LTCC. The programmable oven accepts this recipe and follows its temperature instructions to bake the LTCC structure. Sometimes, they suggest to use the nitrogen gas to prevent the metal oxidation during the procedure which does not apply to our case. DuPont GreenTape 9K7 firing takes almost one day to be completed.

4.4 Ports connection

For S-Parameter measurement using Vector Network Analyser (VNA) and the radiation pattern measurement in the RF Anechoic Chamber, we need a medium to convey the electromagnetic waves between the measurement instrument and the structure's ports. Hence, different types of mediums are available for this purpose at high frequency bands. The microstrip transmission lines, waveguides and coaxial cables are typical solutions, depending on the frequency range, accessible measurement tools and our structure configuration. Sometimes, a mix of methods would be necessary; therefore, a transition between these mediums will be needed.

As we presented earlier, our proposed structure is designed based on the passive microstrip components. Therefore, the access to our structure will be through the microstrip transmission lines. On the other hand, in our measurement for the S-parameter, the VNA could work either using the coaxial cable up to 67GHz or through the WR10 waveguide from 70GHz to 110GHz. The coaxial cable comes with the standard 150µm pitch GSG (Ground-Signal-Ground) Probe or the V-Type 1.85mm Connector which both can be easily connected to our structure. But, if we want to perform the measurement for higher frequencies, the WR10 waveguide and a transition kit from waveguide to microstrip line is necessary that will be costly and inconvenient.

For measuring the radiation pattern, the coaxial cable with 1.85mm V-Connector was available in the frequency range up to 67GHz. Higher frequencies measurements would be possible using the WR15 waveguide (from 50GHz to 75GHz) and WR10 waveguide (from 75GHz to 110GHz). However, using the Probe measurement is only feasible starting at 70GHz.

Based on our application's frequency range (57GHz to 64GHz), bandwidth of our simulated antenna (43GHz to 72GHz) and aforementioned criteria on the instruments, we decided to perform the measurements from **50GHz** to **67GHz** using the coax cable with the 150µm pitch GSG Probe for the S-Parameter and with the 1.85mm V-Connector for the radiation pattern. The Probe has smaller footprint and lower electrical loss which makes it more accurate method for S-Parameter's measurements. Also, it needs shorter transmission line and is less expensive comparing to the connector because no bulky component is needed on the structure's side.

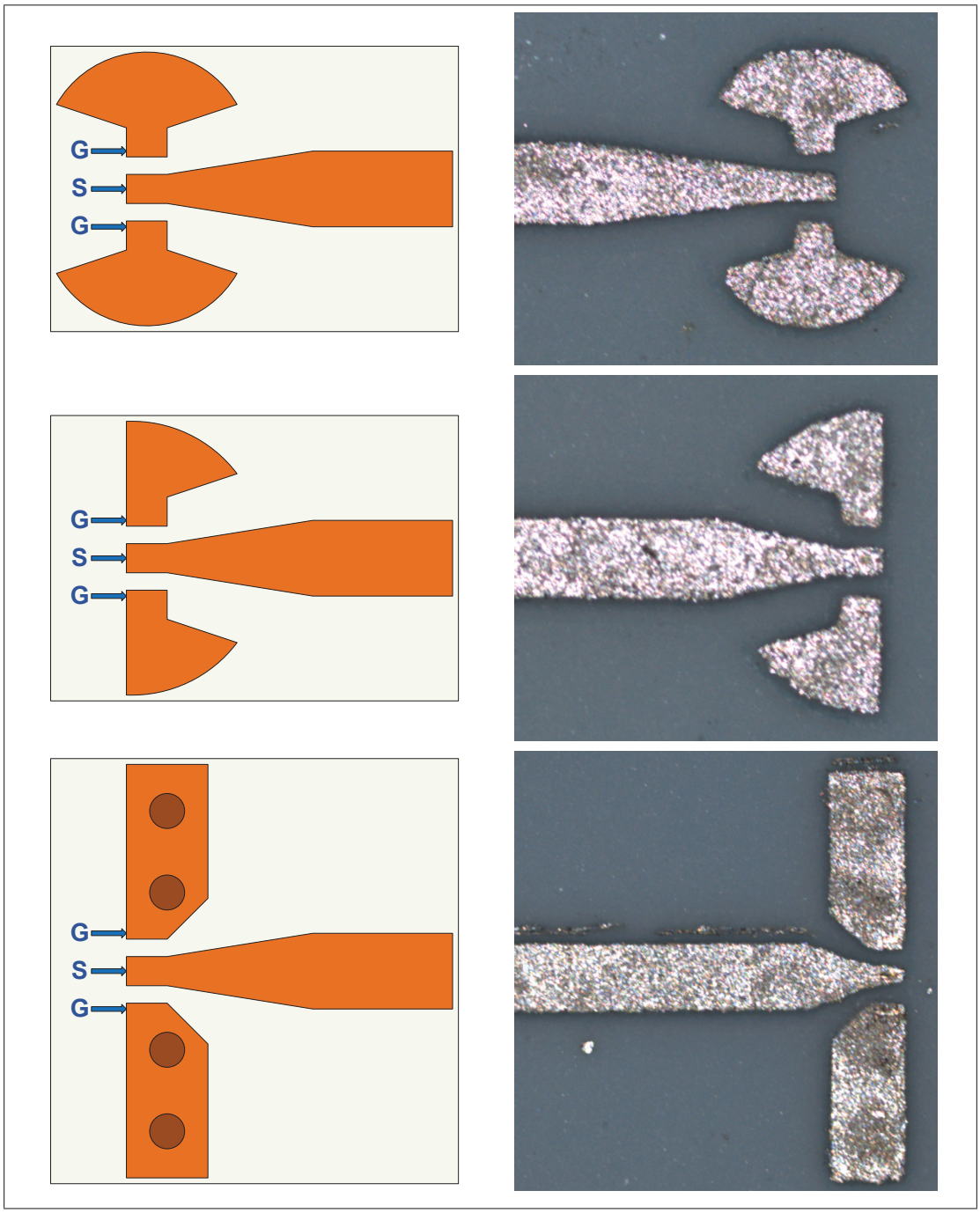

Figure 4.2 Three types of port used for GSG Probe connection

We have to devise a port's footprint on our structure for both Probe and Connector. The Probe connection needs a ground plane in the same layer as the antenna's ports. The whole structure is designed on a two layers substrate: the antennas on top and the ground plane on bottom layer.

As we mentioned, the 10 mil LTCC substrate is too fragile and could be easily broken during the measurements. Thus, in order to strengthen the structure and increase the robustness, we have added four dummy layers which leaves the ground plane in the middle and inaccessible. The simplest way to bring the ground on top is to use vias. However, via connection can add an extra inductance to the return path which its value will increase at the higher frequencies and may affect the measurement's results (Hammou *et al.*, 2016).

Figure 4.2 illustrates three different GSG ports that we designed for the 150μm pitch Probe connection. The first two ports take advantage of a virtual ground using the open-circuited quarter-wavelength radial stub (Hammou *et al.*, 2016) and the third port has via connection to the ground plane. The quarter-wavelength radial stub has smaller footprint, does not change the inductance of the path and provides the zero potential over a wide range of frequencies.

For the footprint of connector assembly on the structure, we just follow the manufacturer's recommendation on the datasheet. We ordered a female 1.85mm V-Connector from "END LUNCH (0.012)w/1.85J LP" series with model number "1892-03A-6" of Southwest Microwave Inc. for the structure's side (SouthwestMicrowave, 2018).

4.5 Calibration kit

De-embedding is used to compensate all the losses due to the mediums and connections on the path. It justifies the measurement point to an arbitrary location on the structure and increases the accuracy of S-Parameters measurements. Instead of using company's calibration kit, it is better to fabricate our own on the same substrate layer as the structure. In this way, the kit will have the same exact properties as the antenna and will be more accurate. In addition, we can set the measurement plane precisely at the antenna's ports. Two most common calibration kits are Open-Short-Load-Through (SOLT) and Thru-Reflect-Line (TRL). We chose TRL calibration kit for our measurements to avoid using the matched load or the short-circuit.

Figure 4.3 shows the designed and fabricated two ports TRL calibration kit. We expected that the port with the radial stub to have an improved performance in measurements comparing to

the port with the via. But in reality, it is more dependent on the tolerances of the fabrication. There would always be some imperfections in the shape and the dimension of the port due to metal printing and laser ablation, which leads to inaccuracy in the calibration and measurement. Moreover, Probe measurement accuracy with radial stub port is more sensitive to the placement of Probe on the circuit. However, our results with all three methods were almost the same.

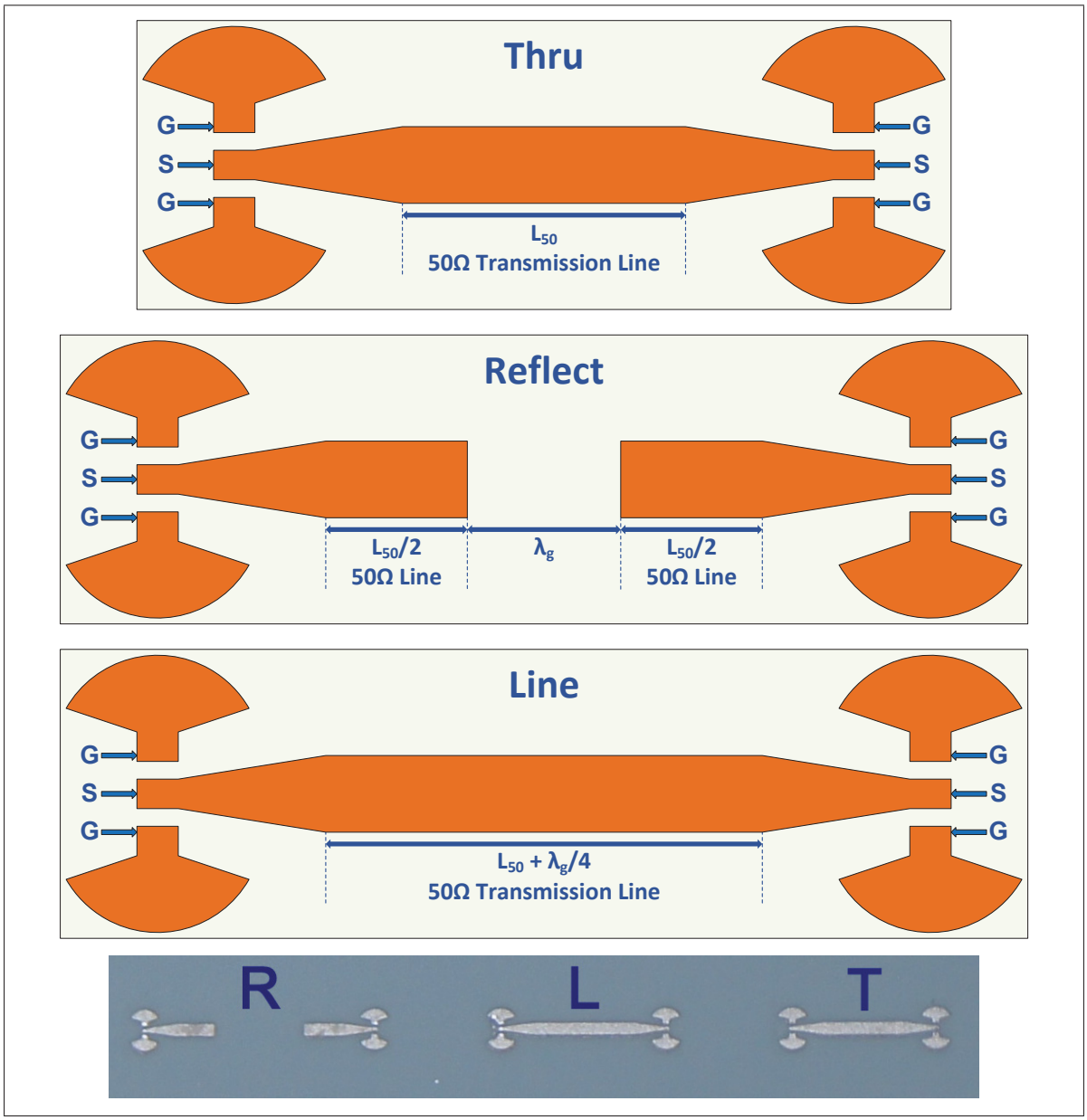

Figure 4.3 Two ports TRL Calibration Kit.

4.6 Fabrication Batches

Our fabrications were planed on three batches with certain objectives, as follows:

4.6.1 First Fabrication

For the first batch, we targeted the proof of concept and the fabrication's tolerances. We wanted to check if the fabricated proposed antenna's performance is close to the result of simulations. In addition, what is the best procedure that should be followed to fabricate an antenna on DuPont 9K7 substrate at 60GHz. Hence, we prepared two optimized antennas with 2-vias and 15-UCs long presented in table 4.1 and 4.2. We intended to measure just S-Parameters for this batch. Thus, only ports for the 150 µm pitch Probe were devised on the layout. As mentioned, three types of port were designed to compare their performance at 60GHz. The calibration kits with different ports also were fabricated on the same LTCC sheet. Some via's holes were created by the laser machine and others by the punch machine for the comparison of methods. Some antennas were made using the laser ablation and the rest only printed by the mask.

Table 4.1 Parameters of the UC with 2-vias for Antenna #1.

Parameter	**Value**	**unit**	**Parameter**	**Value**	**unit**
L_1	1.283	mm	L_2	0.385	mm
W_1	1.025	mm	W_2	0.387	mm
s	0.138	mm	c	0.877	mm

Table 4.2 Parameters of the UC with 2-vias for Antenna #2.

Parameter	**Value**	**unit**	**Parameter**	**Value**	**unit**
L_1	1.325	mm	L_2	0.383	mm
W_1	1.043	mm	W_2	0.424	mm
s	0.178	mm	c	0.973	mm

Figure 4.4 shows the design plan and the layout of the first batch prepared in keysight ADS. Figure 4.5 presents some antennas and TRL calibration kits fabricated in the first batch.

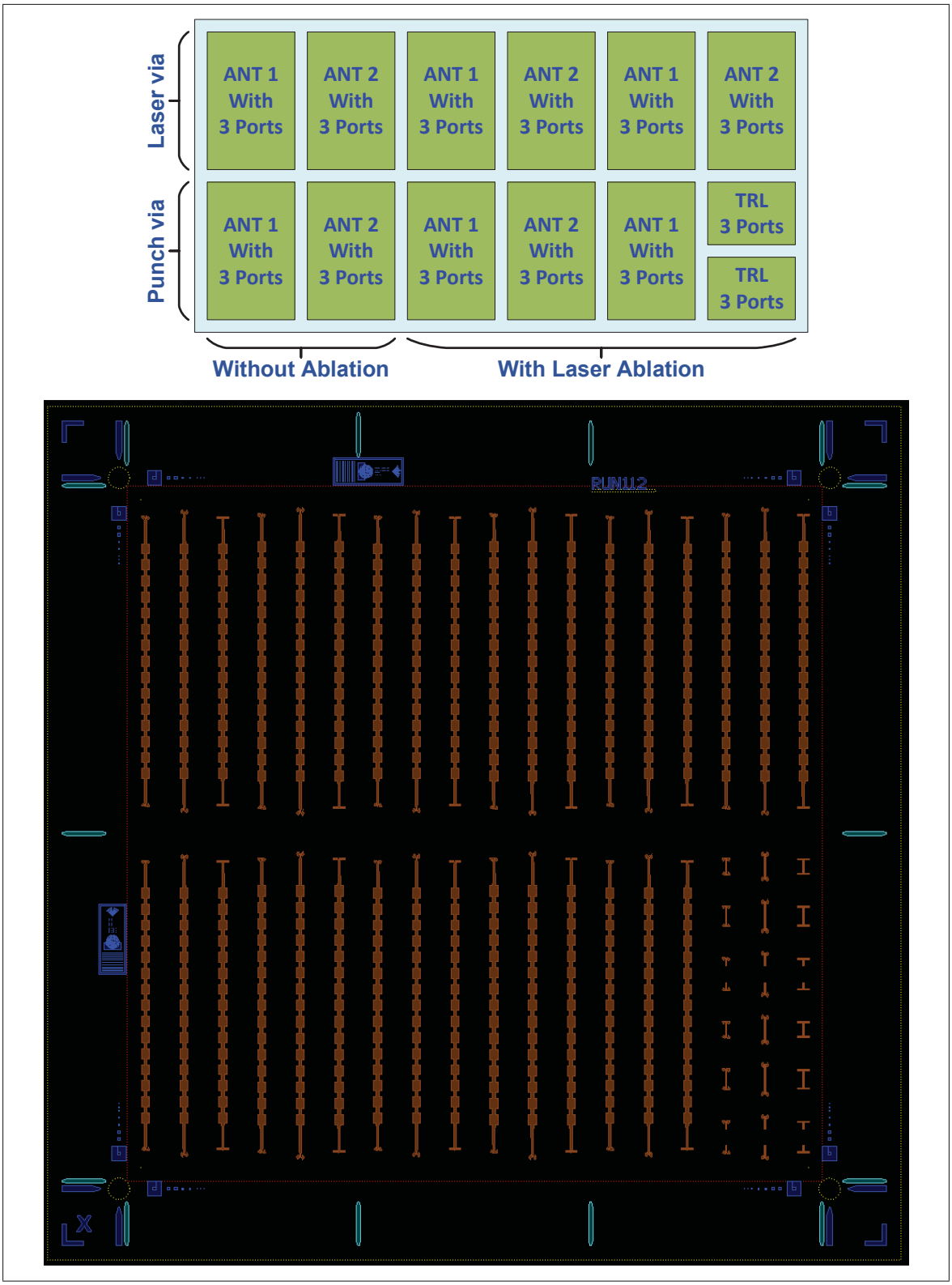

Figure 4.4 First fabrication's design plan and layout.

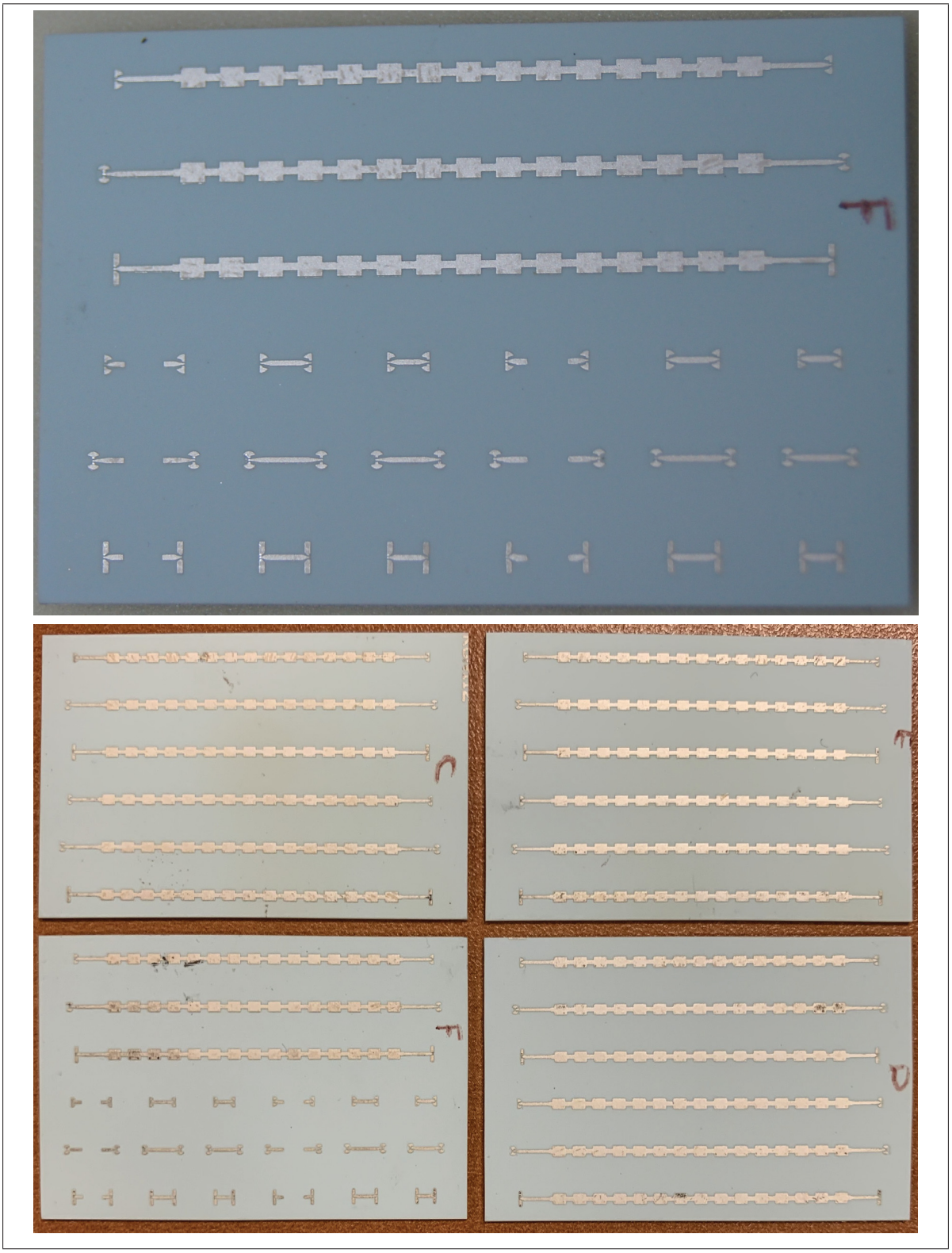

Figure 4.5 Fabricated structures in the first batch.

4.6.2 Second Fabrication

After successful fabrication and promising results of the first batch, we defined the objective of the second batch to have more specific, accurate structure and perform the full measurements. Hence, we improved the performance of our antenna a little by new optimizations which is presented in table 4.3 and 4.4. These two antennas were fabricated in the 2-vias/3-vias and the 9-UCs/11-UCs long versions in the second batch. For VNA connection, the ports for 150 µm pitch Probe with via were dedicated on the layout and also, the 1.85mm female V-Connector was devised for the radiation pattern measurement. Again, the calibration kits with Probe ports and V-Connector were fabricated on the same LTCC sheet. The whole structure was engraved using the laser ablation and the punch created all the holes on structure except the 2mm holes of the connectors, because the drill head was not available for the punching.

Table 4.3 Parameters of the UC with 2-vias for Antenna #3.

Parameter	**Value**	**unit**	**Parameter**	**Value**	**unit**
L_1	1.290	mm	L_2	0.385	mm
W_1	1.030	mm	W_2	0.390	mm
s	0.136	mm	c	0.442	mm

Table 4.4 Parameters of the UC with 2-vias for Antenna #4.

Parameter	**Value**	**unit**	**Parameter**	**Value**	**unit**
L_1	1.386	mm	L_2	0.352	mm
W_1	0.900	mm	W_2	0.330	mm
s	0.136	mm	c	0.375	mm

Figure 4.6 shows the design plan and the layout of the second batch prepared in keysight ADS. The size of DuPont GreenTape 9K7 sheet which we have in the lab is $97.8mm \times 97.8mm$ before the firing that will shrink to $88.9mm \times 88.9mm$ after the baking. We filled up the sheet with different copies of our design to make the most use out of it. Figure 4.7 presents some antennas with the connector assembled and TRL calibration kits fabricated in the second batch.

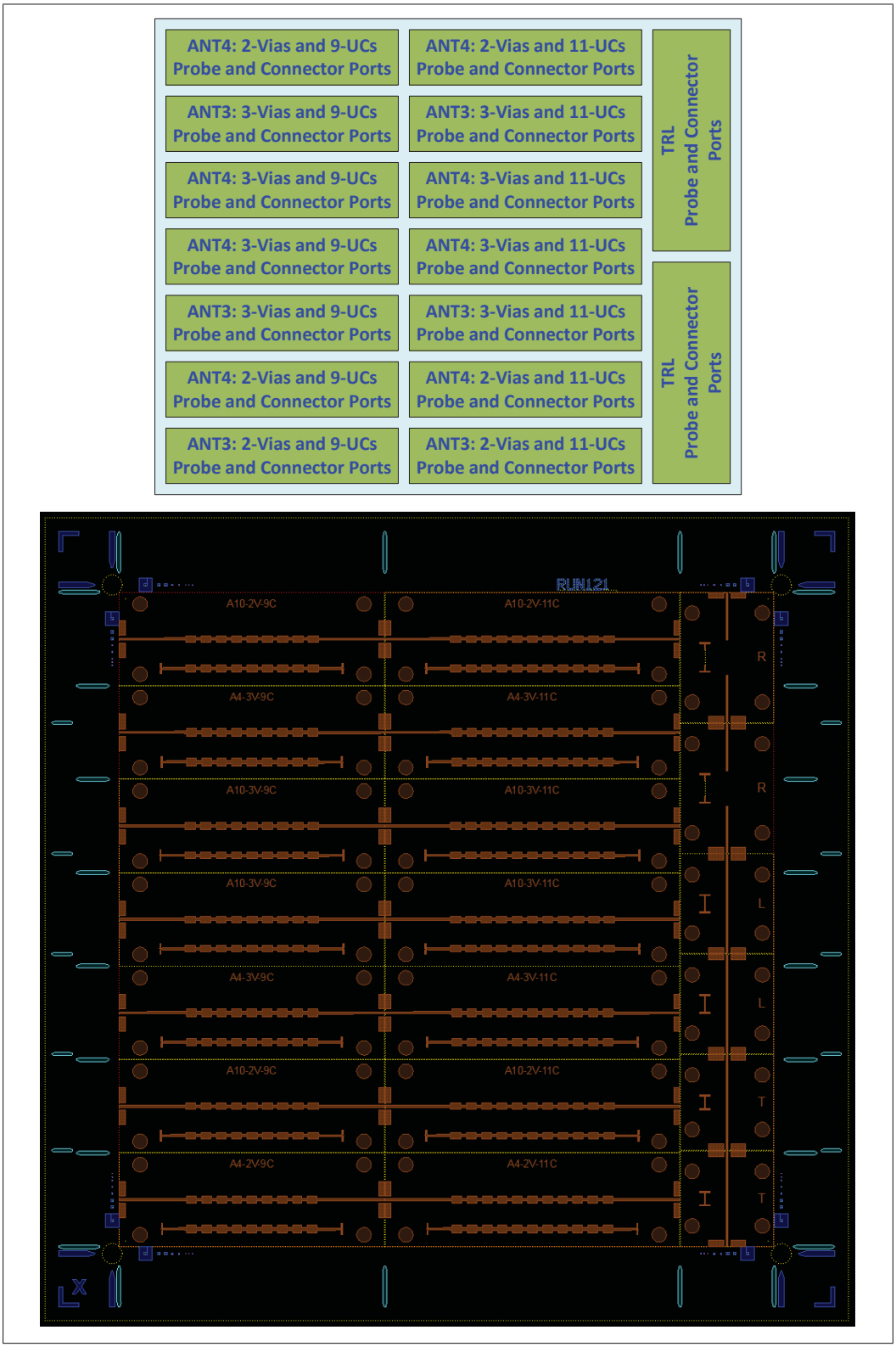

Figure 4.6 Second fabrication's design plan and layout.

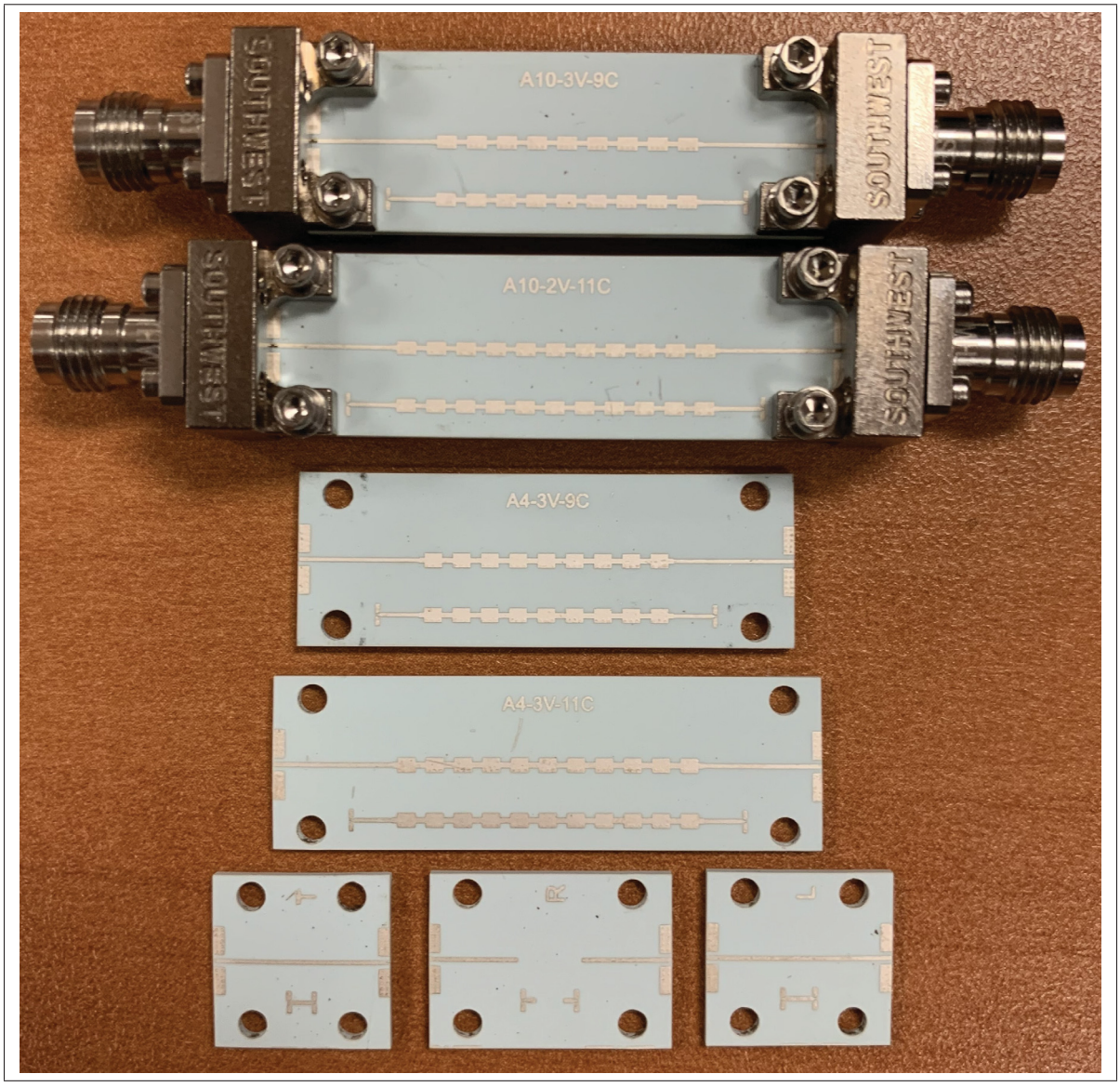

Figure 4.7 Fabricated structures in the second batch.

4.6.3 Third Fabrication

In the third step of the fabrication, we intended to make a prototype of the complete design structure, including a phased-array of the antennas, a Rotman lens, all the transmission line connections, the ports and matched loads. Although, we prepared the layout but we did not fabricate the third batch. You can just refer to the simulation results in the previous chapter at the section "Complete proposed structure". However, we already fabricated and tested the

most important part, which is the antenna itself, at 60GHz on the LTCC substrate. A similar Rotman lens structure at 60 GHz was fabricated on a 127 (121 fired) μm thick DuPont 9K7 LTCC substrate utilizing gold conductor and tested in the same lab recently (Attaran *et al.*, 2016). Moreover, a complete design structure similar to ours with 3-D scanning was fabricated on a RO3006 substrate with $\varepsilon_r = 6.15$ and a thickness of 0.25 mm using copper conductor at 25 GHz on one layer and multilayer versions with band-pass filter (Rahmani, 2017).

4.7 Fabrication inspection

After fabricating the structure and before performing the measurements, we followed these three steps to verify the quality of the fabricated antennas in our lab:

4.7.1 Visual inspection

Visual inspection will be performed right after taking out the LTCC structure out of the firing oven by means of a microscope to check the physical qualities of the fabrication and the shape of structure. In this step, we are looking for the missing parts of the conductor through poor printing process, unremoved metal parts after the laser ablation, disconnected parts especially the via and the metal patch, unwanted short-circuits, undesirable flaws, holes and cavities in the substrate and etc. Figure 4.8 illustrates ten images of these flaws from the first batch's visual inspection. Despite these flaws, the structures surprisingly still have satisfying performance.

4.7.2 Dimension inspection

The size of structure in the fabrication would be affected by the conductor printing process, the laser ablation process and the shrinkage of LTCC substrate after the firing. We verified the physical dimensions of the structure under a special microscope. This microscope is equipped by a gauge on its screen for the length measurement including the different lenses to scale the accuracy of measurements. We expected the length tolerances less than 5 μm using laser machine, which in reality, was about 20-30 μm for the first batch and 10 μm for the second one.

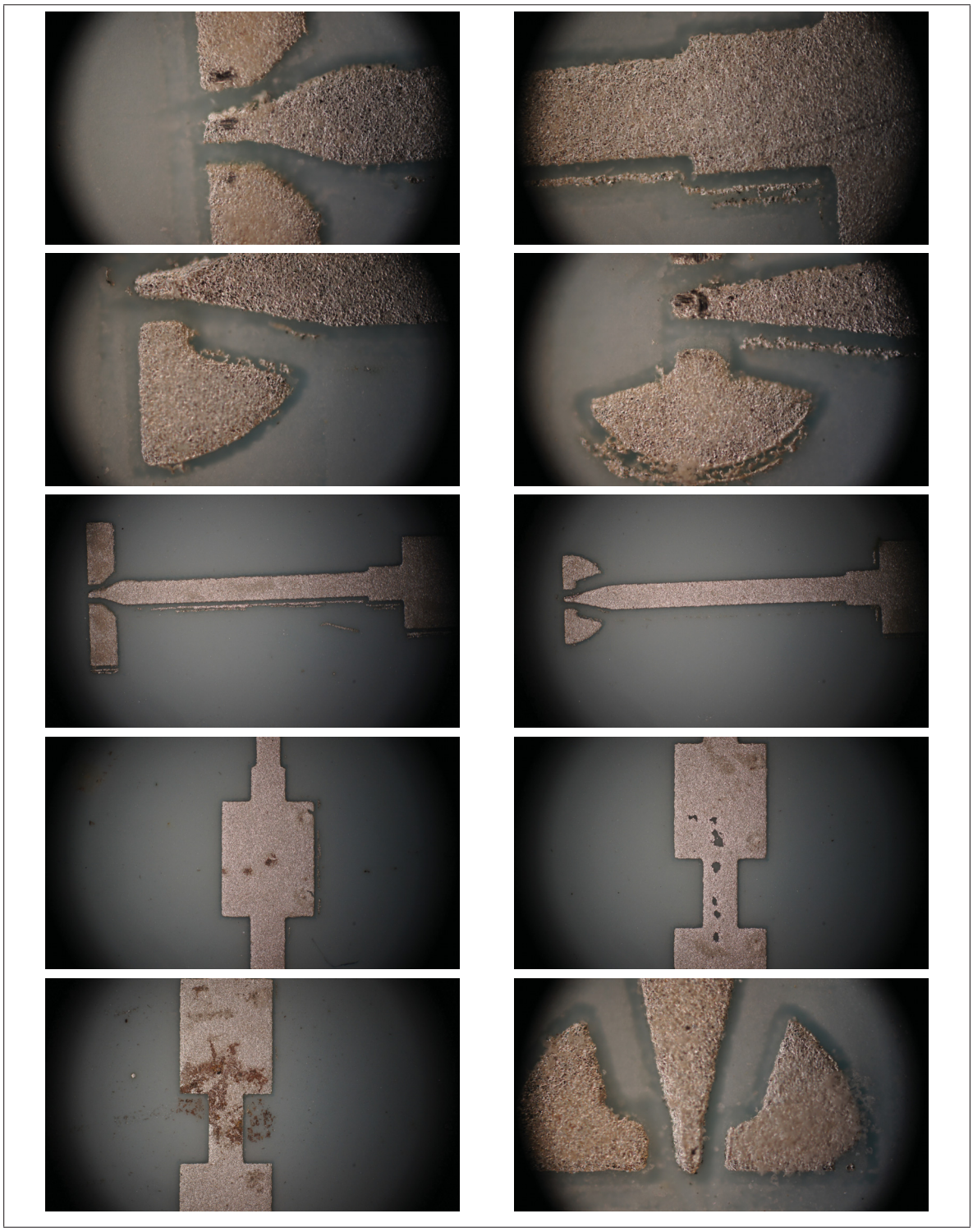

Figure 4.8 Visual inspection under microscope: check the quality of first fabrication.

4.7.3 X-Ray inspection

We used X-Ray machine to check the connection of vias. Figure 4.9 shows some X-Ray images of the first batch's inspection. As we can see, all the vias are filled and connected to both layers perfectly. However, the vias that are created by the laser machine are a little out of shape.

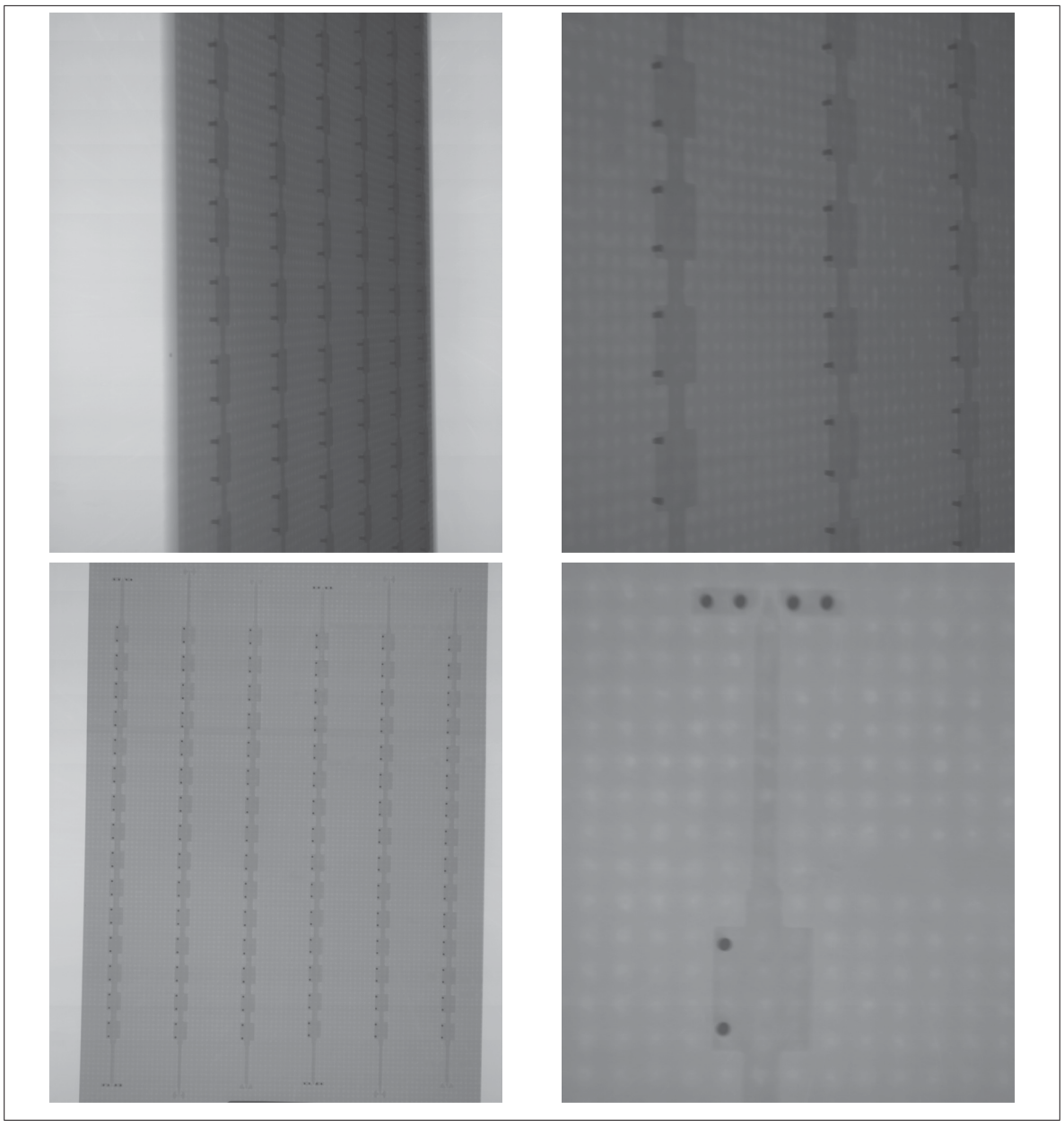

Figure 4.9 X-Ray images: inspecting the via's connection.

4.8 Practical experiences

In this section, we are going to share some of our practical experiences obtained from the fabrication and the inspection processes while working in the lab:

1. Try to design a simple structure and avoid the complicated shapes and the sharp edges. Because in mm-Wave application, the structures are normally in the scale of hundreds of micron and it will be so difficult to fabricate the complicated shapes with sharp edges. Hence, the results will be really far from the simulations.

2. Consider the actual tolerances of the fabrication, not the provided datasheet. Then, try to simulate the structure for the worse case scenario out of the fabrication and be prepared.

3. Don't waste too much time for the fine tuning of the structure. We are not going to achieve that accuracy due to the fabrication tolerances. Instead, work on a design which is more sustainable against the dimension variations. For example, our proposed antenna structure is dependent mostly to the relation between the lengths not just the absolute value of them. Therefore, if two values are scaled a little, the performance will not change so much. We will discuss this concept in the next chapter, while presenting the measurement results.

4. Find the proper process of the fabrication and right ingredients. Then, stick to it for future.

5. The LTCC GreenTape is elastic like a fabric tissue, but after the baking it will shrink and become fragile like a ceramic. Therefore, the alignment during the fabrication process is difficult because of its elasticity. Extra caution should be taken into account during this process. Also, due to its fragility nature after the firing, it must be handled carefully.

6. Always strengthen the structure by adding a few dummy layers on the bottom to have the final structure with at least 1 mm thickness.

7. Try to perform all the measurements as soon as possible. Because, the conductor (especially silver) is prone to fast oxidation. This will cause problem for port connection and affect the results. The coating also will change the properties of the structure.

4.9 Conclusion

In this chapter, we investigated a little around the LTCC technologies and its advantages in the mm-Wave applications and packaging. Then, we presented a summary of the fabrication process in the ETS LACIME Lab to give a better understanding of the differences between the simulated and the fabricated structure. In addition, it could be really beneficial for the future design improvement to consider what is actually possible and what is not; especially, in the fabrications of low-profile structures for the mm-Wave applications like WiGig.

Next, the ports connecting the structure to the measurement tools and the calibration kit for S-Parameter measurement were explained. The 150 µm pitch Probe is used for S-Parameter measurement through VNA and the 1.85 mm V-Connector employed for the radiation pattern measuring at the anechoic chamber. Although, V-Connector can be used for the connection to the VNA, but the measurement would be less accurate due to the losses. The TRL calibration kit were fabricated on the same sheet as the structure to have the most precise results.

Three planed batches of the fabrications were introduced to achieve a certain goal in each one. The design plan and the design layout along with some fabricated prototypes were presented for the first and second batches. Also, three steps of inspection, after LTCC firing and before the measurement, were articulated to verify the quality of the fabrications, encompassing some images of the inspections. It must be mentioned that the second batch of the fabrication had more clean, precise instances of our design. At last, we shared our actual experiences of the fabrication which could be beneficial for future.

CHAPTER 5

MEASUREMENTS AND RESULTS

5.1 Introduction

So far, we introduced the mathematical model, the design's simulation and optimization, the fabrication process and the inspection for our proposed periodic LWA. Now, we are going to present the measurement results in this chapter. Generally, the performance of an antenna is measured in two steps. First, S-Parameter measurement using a Vector Network Analyzer to check the matching of the antenna. Second, the radiation pattern measurement in an Anechoic Chamber to verify other antenna's features such as gain, main beam angle and polarization. We performed the S-Parameter measurement in the LACIME LTCC Lab of ETS and the radiation pattern measurement in the anechoic chamber of Polytechnique Montréal.

Normally, the measurement at high frequencies is accomplished using waveguides. We tried to avoid the waveguide, because it needs a complicated structure for the microstrip to waveguide transition. Hence, we confined our measurements from 50GHz to 67GHz duo to the limitation of the coaxial cable. We have already covered all the constraints of our available measurement instruments in the previous chapter while designing the connection ports for the measurement tools. The S-Parameter measurements is done by a VNA using a standard 150 μm pitch GSG Probe from 50GHz to 67GHz and the radiation pattern of antenna was measured in an anechoic chamber using a 1.85 mm V-Connector at the same frequency range. As mentioned earlier, the measurement with a GSG Probe is more accurate due to its lower loss, but this option was not available for the radiation pattern measurement on the desired frequency band.

We have fabricated our proposed antenna structure in two batches, as we presented in chapter 4. The first one was intended to verify the proof of concept and check the fabrication's tolerances. Therefore, for this batch, we only measured the S-Parameter to verify the matching of antenna. But, for the second batch, which was fabricated with the Probe and the V-Connector ports, we performed both measurements to investigate all features of the proposed structure.

5.2 Measurement's setup

5.2.1 Vector Network Analyzer

The S-parameter was measured by a VNA using the 150 µm pitch GSG Probe at the LACIME Lab of École de Technologie Supérieure (LTCC@ÉTS, 2020). The VNA model was Keysight N5247A PNA-X Microwave Network Analyzer (Keysight, 2019), that can measure 4-channels S-Parameters up to 67 GHz. Figure 5.1 shows the setup for the S-Parameters measurement and the placement of two GSG Probes on both side of the antenna for two ports measurement.

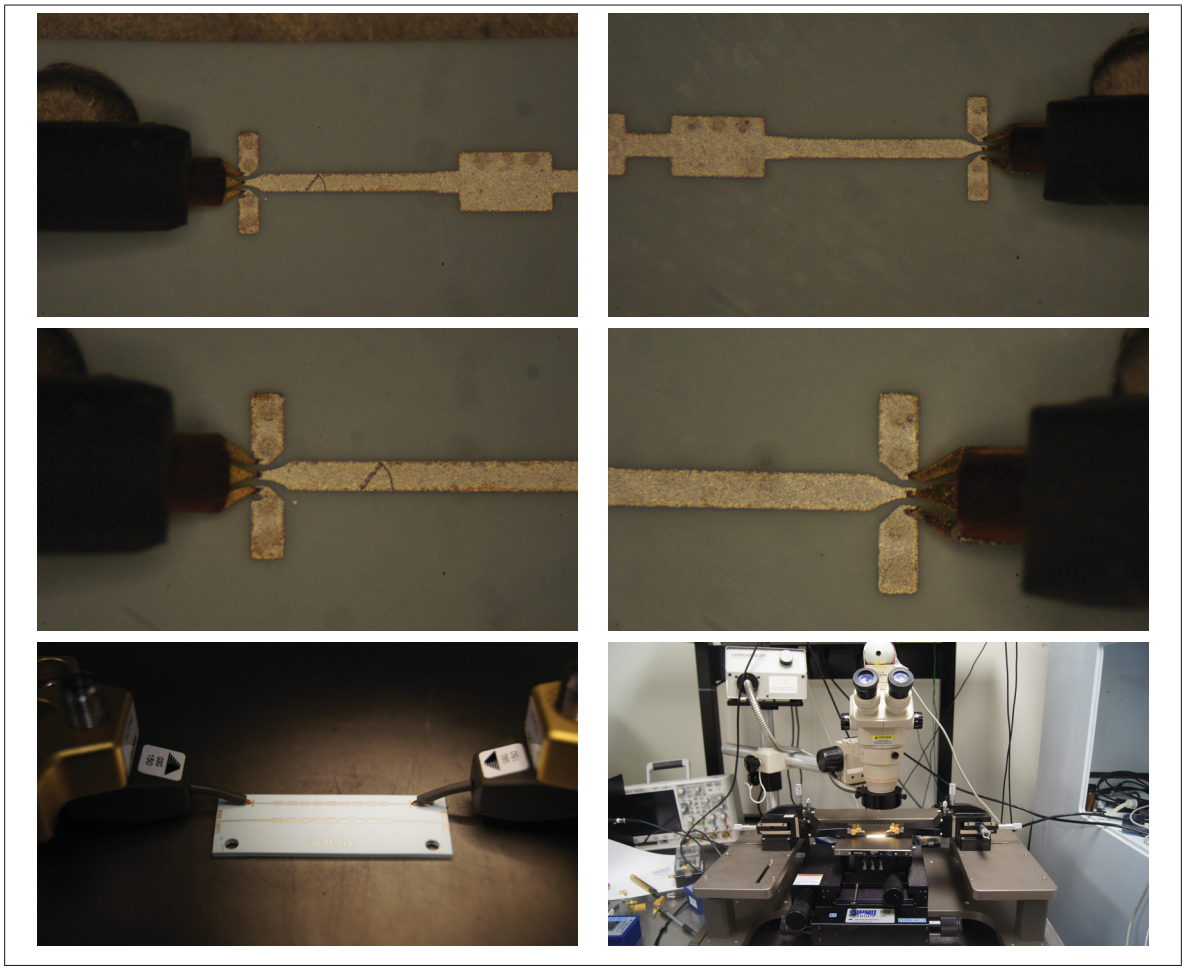

Figure 5.1 Antenna's S-Parameter measurement setup by 150 µm pitch GSG Probe at LACIME of École de Technologie Supérieure.

Using the GSG Probe while is more precise method for the measurement, it is also extremely dependent on proper placement of the Probe on dedicated antenna's ports. If the Probe moves a little or misplaces relating to the calibration process, the result will change. Therefore, special care must be taken to ensure the suitable Probe's placement. Another factor that can affect the result of measurement with a Probe is the quality of port's fabrication. Because, de-embedding is performed using such a port through calibration process, all of ports must be as similar as possible and any difference or flaw among them will lead to inaccuracy of the results.

5.2.2 Anechoic Chamber

The radiation pattern was measured in the anechoic chamber of Polytechnique Montréal using the 1.85mm V-Connector. The measurement setup is presented in figure 5.2, while one side of the antenna is matched by a $50\,\Omega$ load and the other side is connected to the transceiver through a V-Cable. A HO15 horn antenna is used as the second antenna of the measurement setup for the communication. The specification of this antenna is provided by the Lab for the calibration.

Normally, the radiation pattern should be measured on a hemisphere space, but it is very costly and time-consuming procedure. Instead, we only measured the radiation pattern of our antenna in two perpendicular planes of X-Z and Y-Z. The Y-Z ($\Phi = 90°$) plane illustrates the scanning feature of the periodic LWA with the frequency. The phased-array beam steering ability can be displayed on the X-Z ($\Phi = 0°$) plane, but we did not fabricate the array structure. Hence, it can be used to demonstrate the main beam shape of a single antenna in the broadside radiation.

It should be mentioned that a separate radiation pattern measurement was perform with the same setup using two HO15 horn antennas for the calibration purpose. This result plus the specification of the HO15 antenna were used to adjust the results of measurements on our antennas. An M-file code was developed on MATLAB to perform this task automatically.

In addition, some ripples on the measured radiation pattern are observable. These noises exist because all the equipment on the Lab are a little old. Despite these ripples, the tools are calibrated and certified and the results of the measurements are trust-worthy.

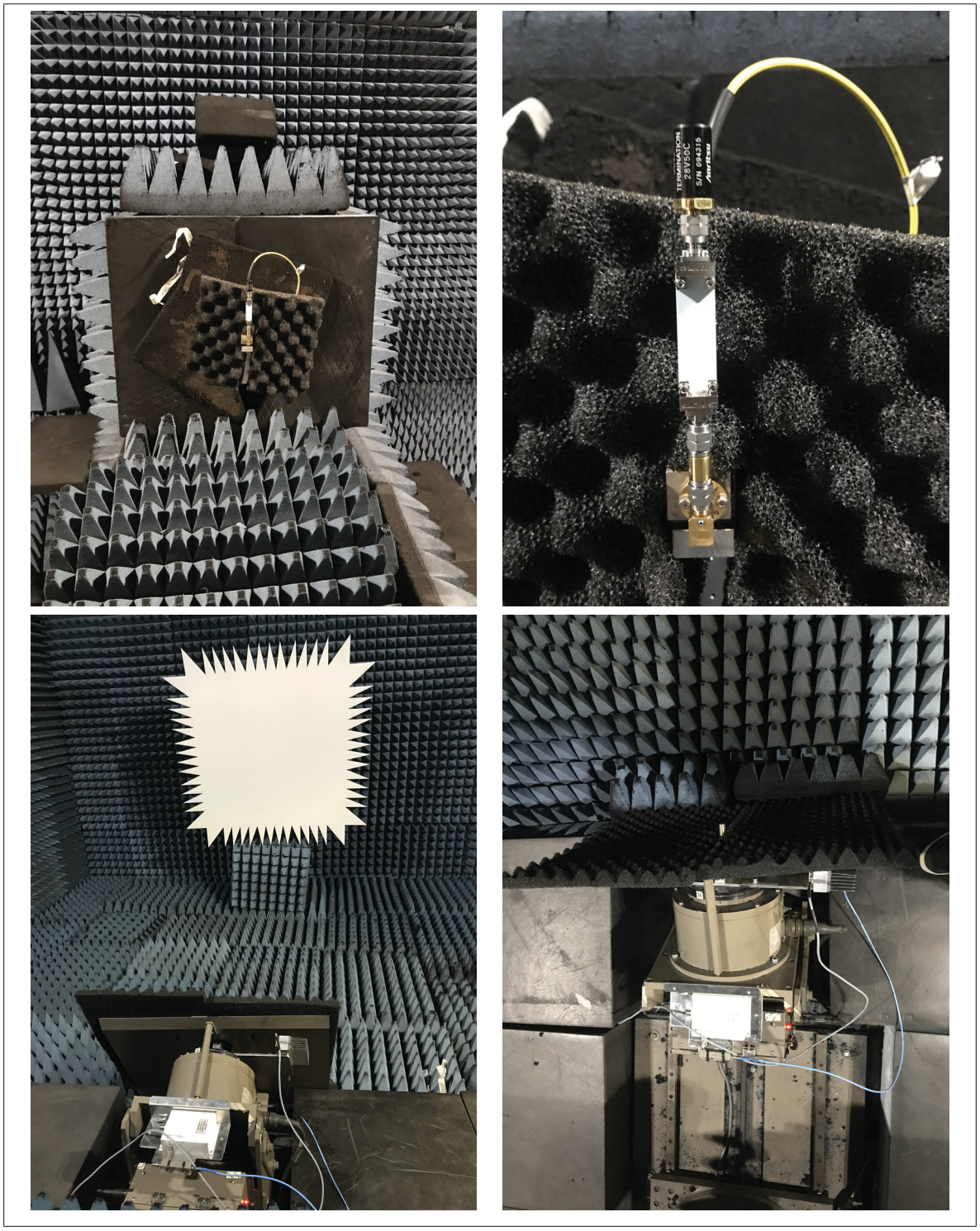

Figure 5.2 Antenna's radiation pattern measurement setup in the anechoic chamber of Polytechnique Montréal.

5.3 Measurement's results

5.3.1 First Fabrication

5.3.1.1 S-Parameter measurement

As mentioned in the previous chapter, in the first batch, we fabricated two optimized antennas (presented in the tables 4.1 and 4.2) containing 2-vias in the unit-cell with 15-UCs length. 33 instances of these antennas were made on LTCC substrate with 3 different types of ports (radial stub and via ports) accompanied by 2 series of the TRL calibration kit for each one. Antenna's vias were created using the punch machine and the laser for the comparison of the methods.

Almost half of the prototypes were fabricated just by the mask metal printing and the other half using the laser ablation process for more precise and clean structure. The instances who were made without the laser ablation did not show satisfactory features in the measurements. Thus, we are not presenting their measurement results here. But, the other half had a promising performance that was a proof of concept for further investigation in the second batch.

Figure 5.3 shows the S-Parameters of four antenna's instances whose their vias are created by the laser machine. The results are presented for two antennas (Antenna #1 and Antenna #2) with the radial stub port (only one of the radial stub) and the via port. Figure 5.4 displays the S-Parameters of the same prototypes of the antennas which the vias are created using the punch machine. The simulation results also plotted in these figures for the comparison.

All the antennas almost are matched over the measured range of frequency (50GHz to 67GHz), looking at the S_{11} and S_{22}. Although, S_{11} and S_{22} have to be the same duo to the symmetry of the antenna, but in reality, they are not because of the fabrication's tolerances. The results with the via port seem to be better due to the challenges in the measurement using the radial stub ports. Also, there is no significant difference between the result of instances created by the punch and the laser. However, working the punch is faster and it creates more precise vias. As we can see, there is a good agreement between the measurement and the simulation results.

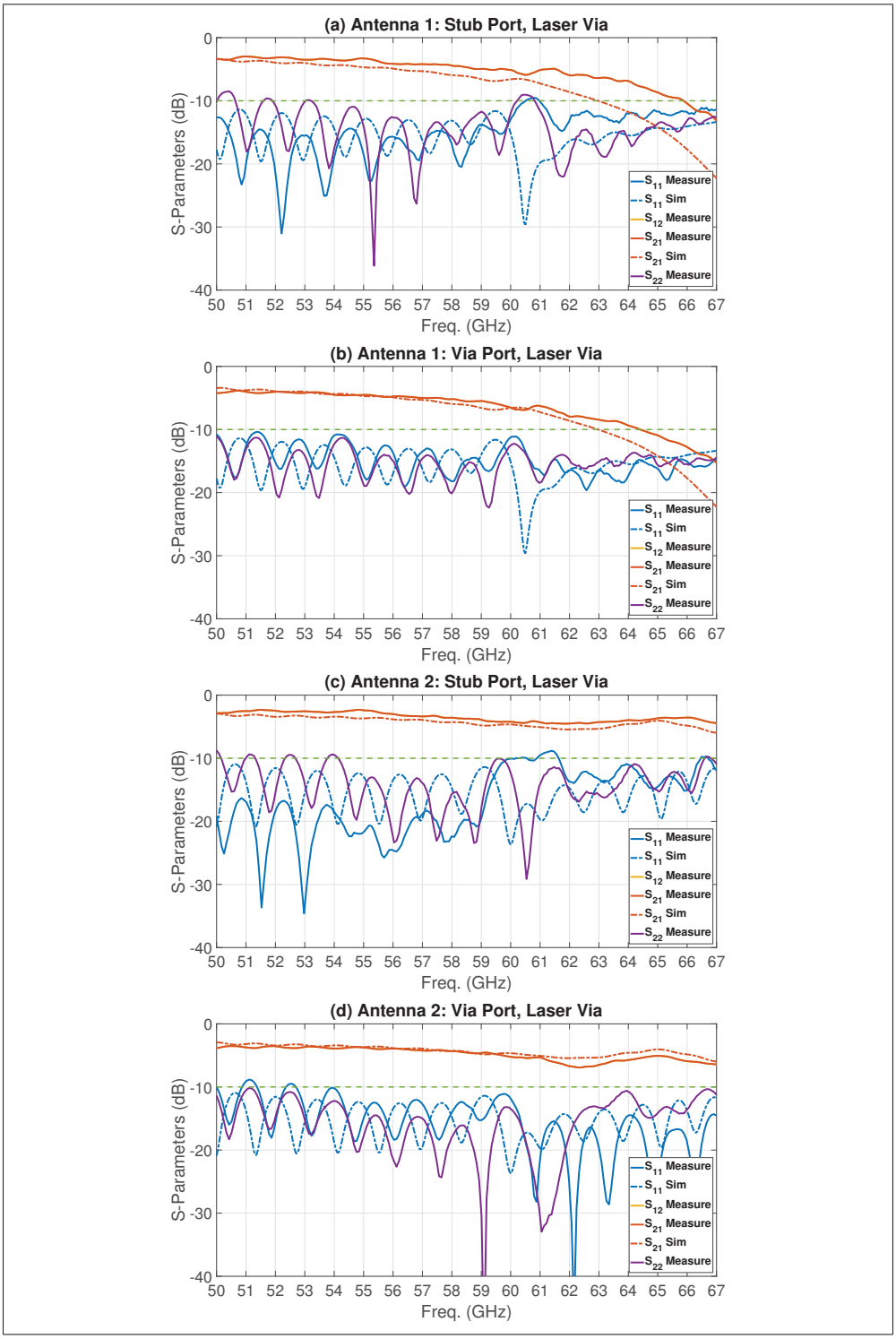

Figure 5.3 S-Parameter of the first batch with laser via.

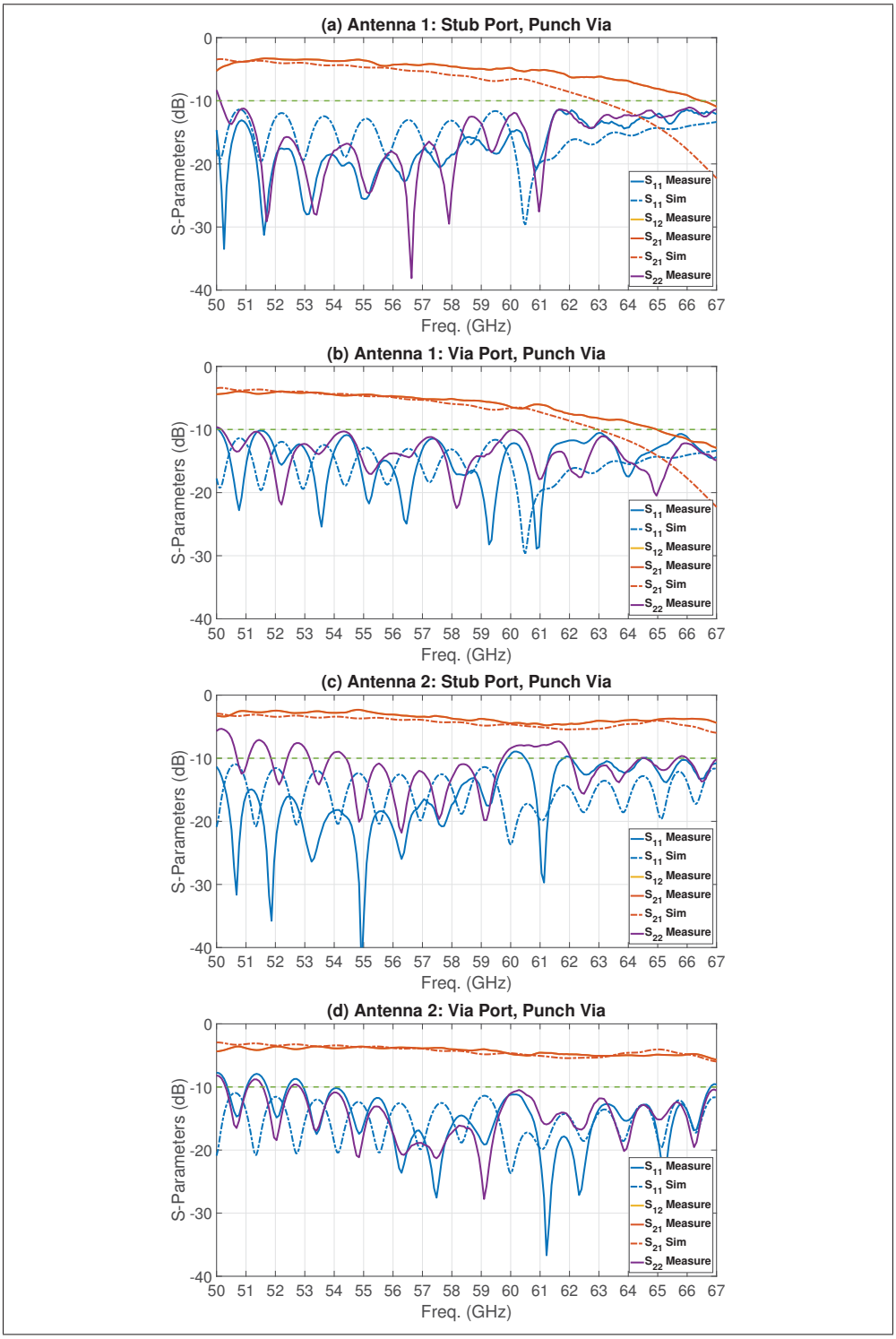

Figure 5.4 S-Parameter of the first batch with punch via.

5.3.2 Second Fabrication

5.3.2.1 S-Parameter measurement

In the second batch, 28 antenna's instances were fabricated along with 4 TRL calibration kits. Half of them including the calibration kits have the V-Connector port and the other half have the via port. Two optimized antennas (Antenna #3 and Antenna #4) were made in 2-vias and 3-vias configurations with the length of 9-UCs and 11-UCs. Also, two prototypes of each antenna were fabricated (Sample A and B) using the laser ablation process and the punch machine.

Figure 5.5 shows the S-Parameters of the Sample A of the Antenna #3 with 2-vias and 3-vias unit-cells and the length of 9-UCs and 11-UCs, measured using the 150 μm pitch GSG Probe. Figures 5.6 and 5.7 present the S-Parameters of the Antenna #4 with the same configurations for the Sample A and B respectively. Finally, figure 5.8 displays the measurement results for the Sample B of the Antenna #3 with 3-vias, measured using the Probe, along with one result for antenna #3 and one for antenna #4, measured using the V-Connector for the comparison.

Looking at the S-Parameters, we can see that the structure with 3-vias has better performance than the structure with 2-vias. Although, the structure with 11-UCs in the simulation shows better matching, but there is not significant difference between 9-UCs and 11-UCs length in the measurement. Again, there is a good agreement between the simulation and the measurement results, except for the measurement that performed by the connector has more loss in the S_{21}.

5.3.2.2 Radiation pattern measurement

We measured the radiation pattern of 6 prototypes of the second batch in the anechoic chamber using the V-Connector. Figures 5.9 to 5.14 display the radiation pattern of these antennas on the Y-Z and X-Z planes, the peak realized gain, the axial ratio and the main beam angle versus the frequency. The radiation pattern on the Y-Z plane is presented for five frequencies to show the beam steering feature of the antenna with the frequency. Only the broadside radiation pattern is plotted on the X-Z plane because other frequencies' main beam do not locate on this plane.

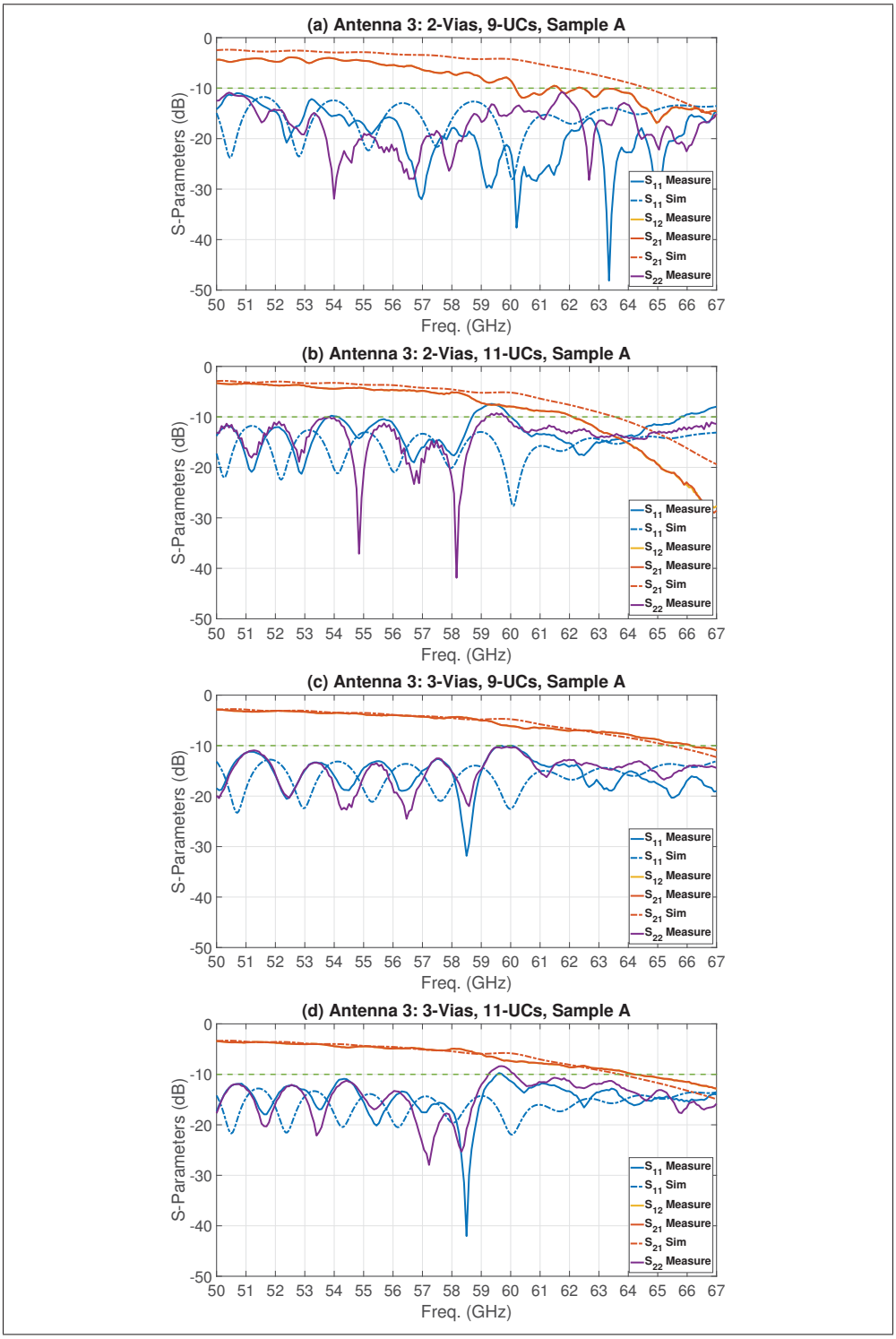

Figure 5.5 S-Parameter of the second batch, Antenna #3 Sample A.

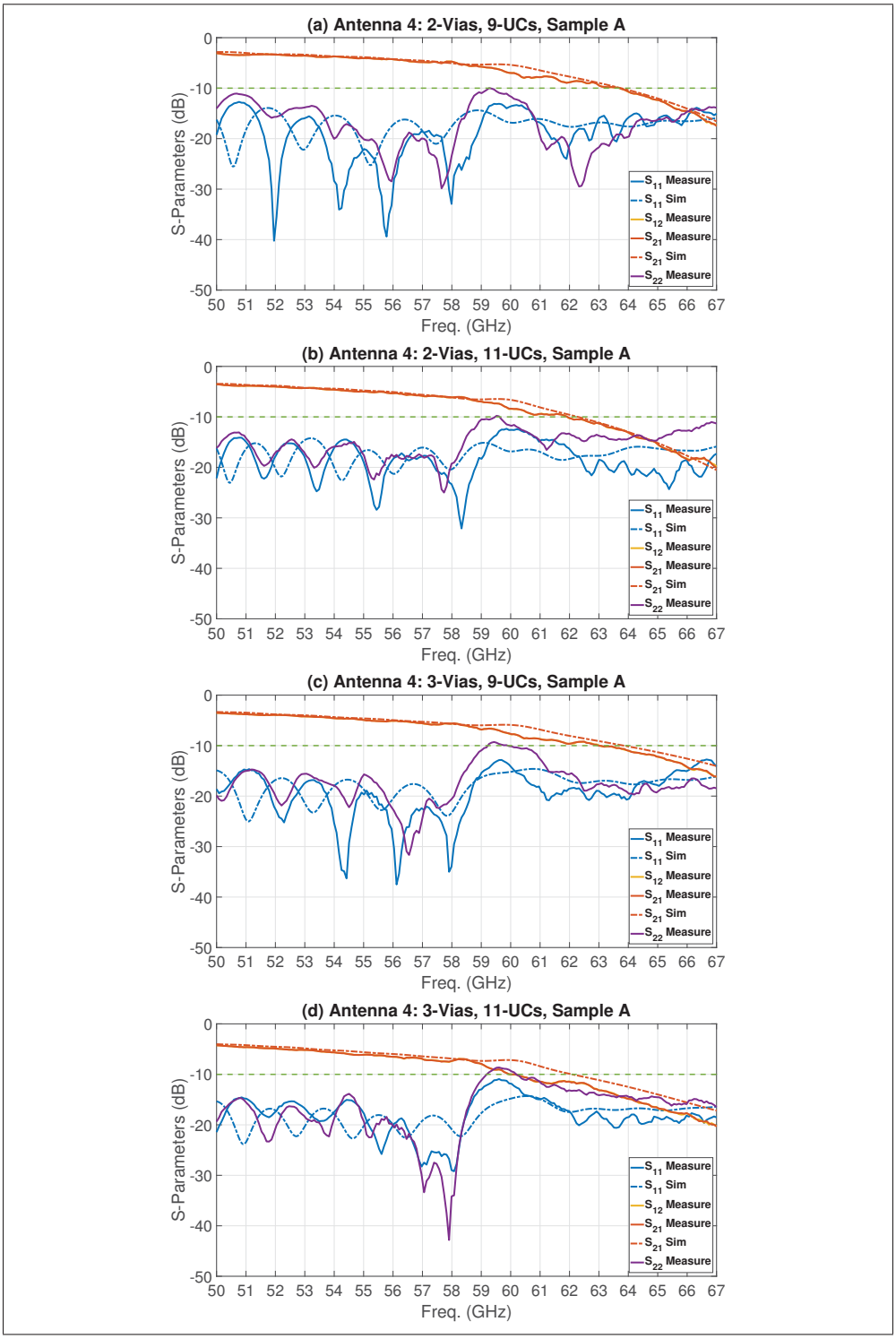

Figure 5.6 S-Parameter of the second batch, Antenna #4 Sample A.

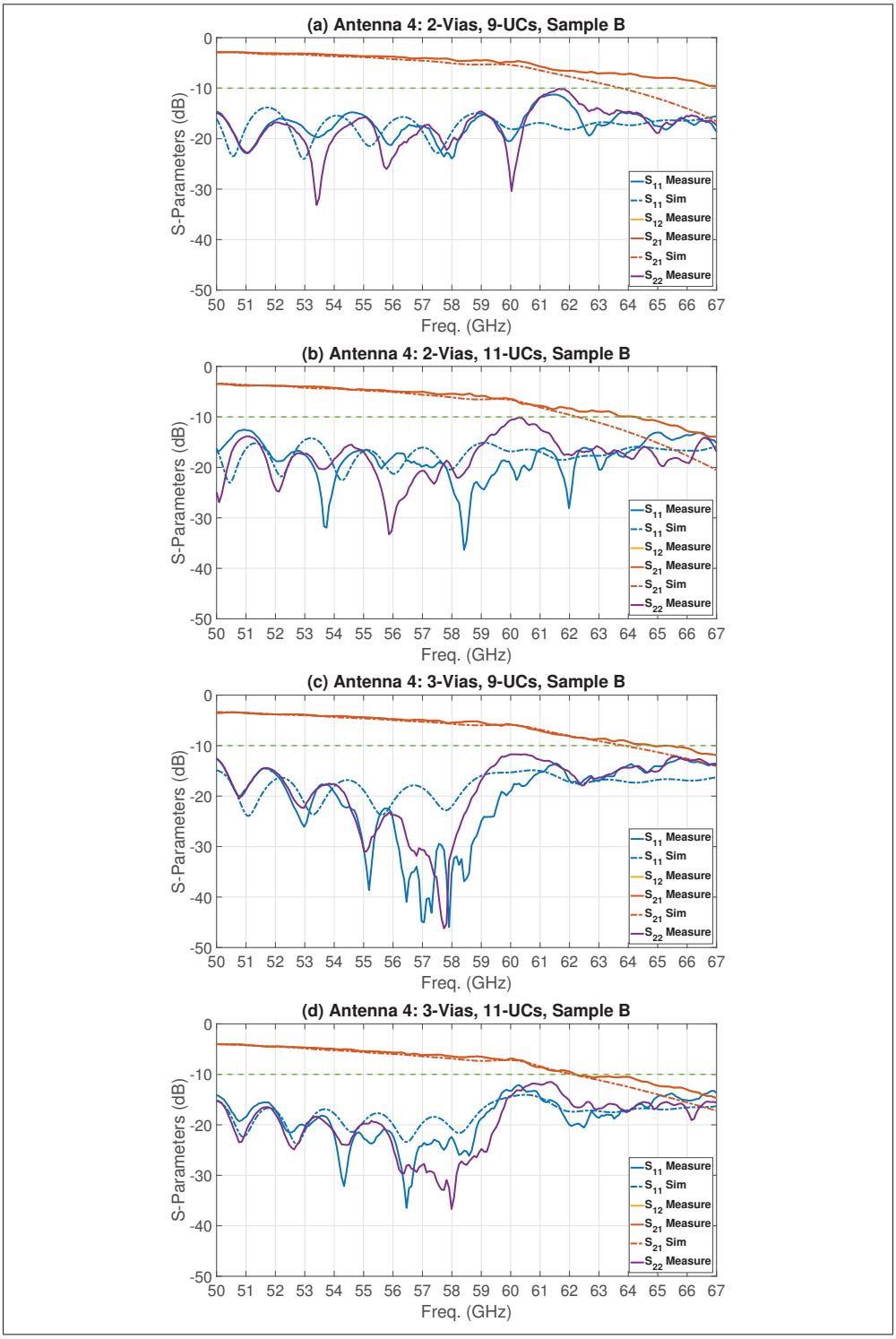

Figure 5.7 S-Parameter of the second batch, Antenna #4 Sample B.

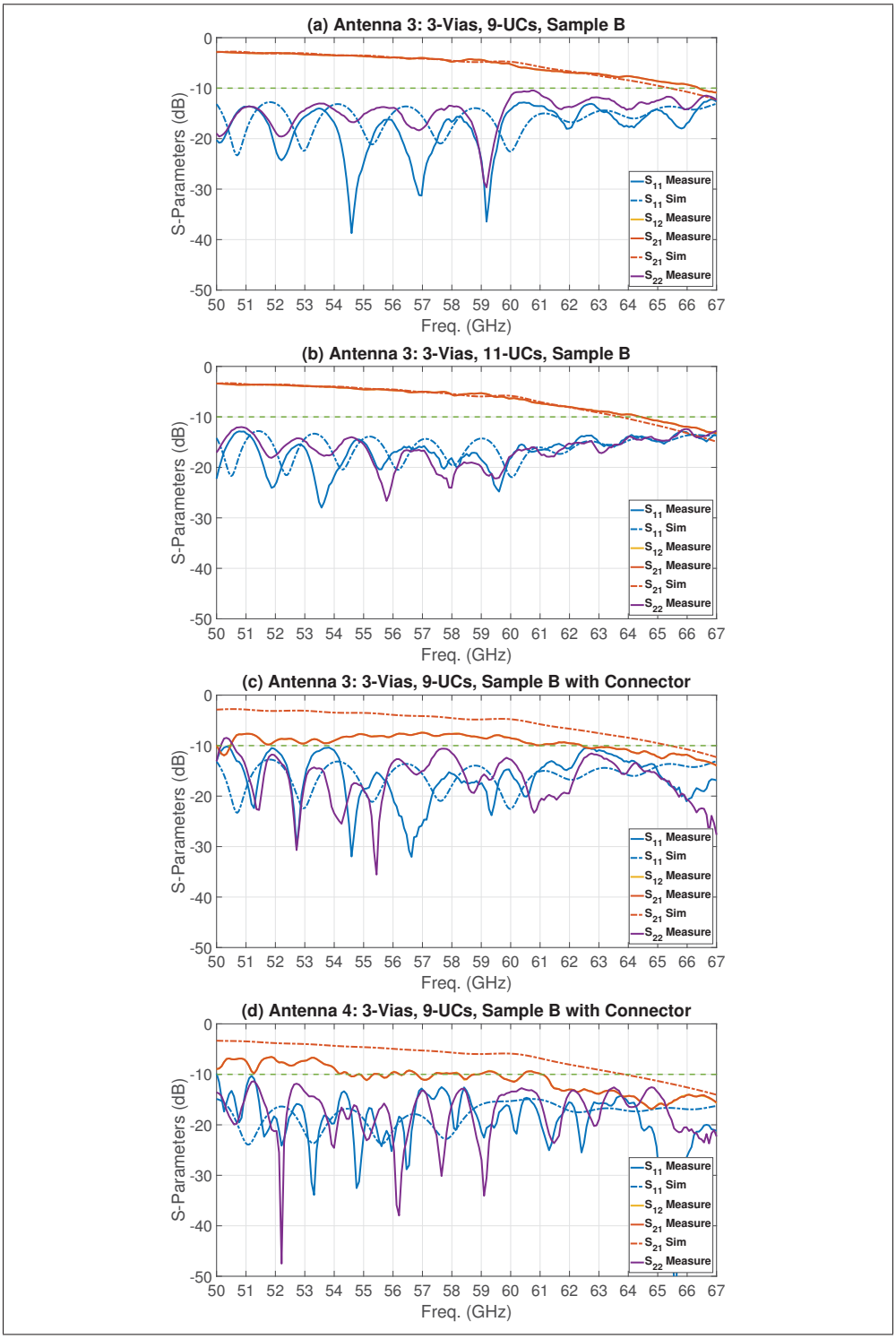

Figure 5.8 S-Parameter of the second batch, Probe vs Connector.

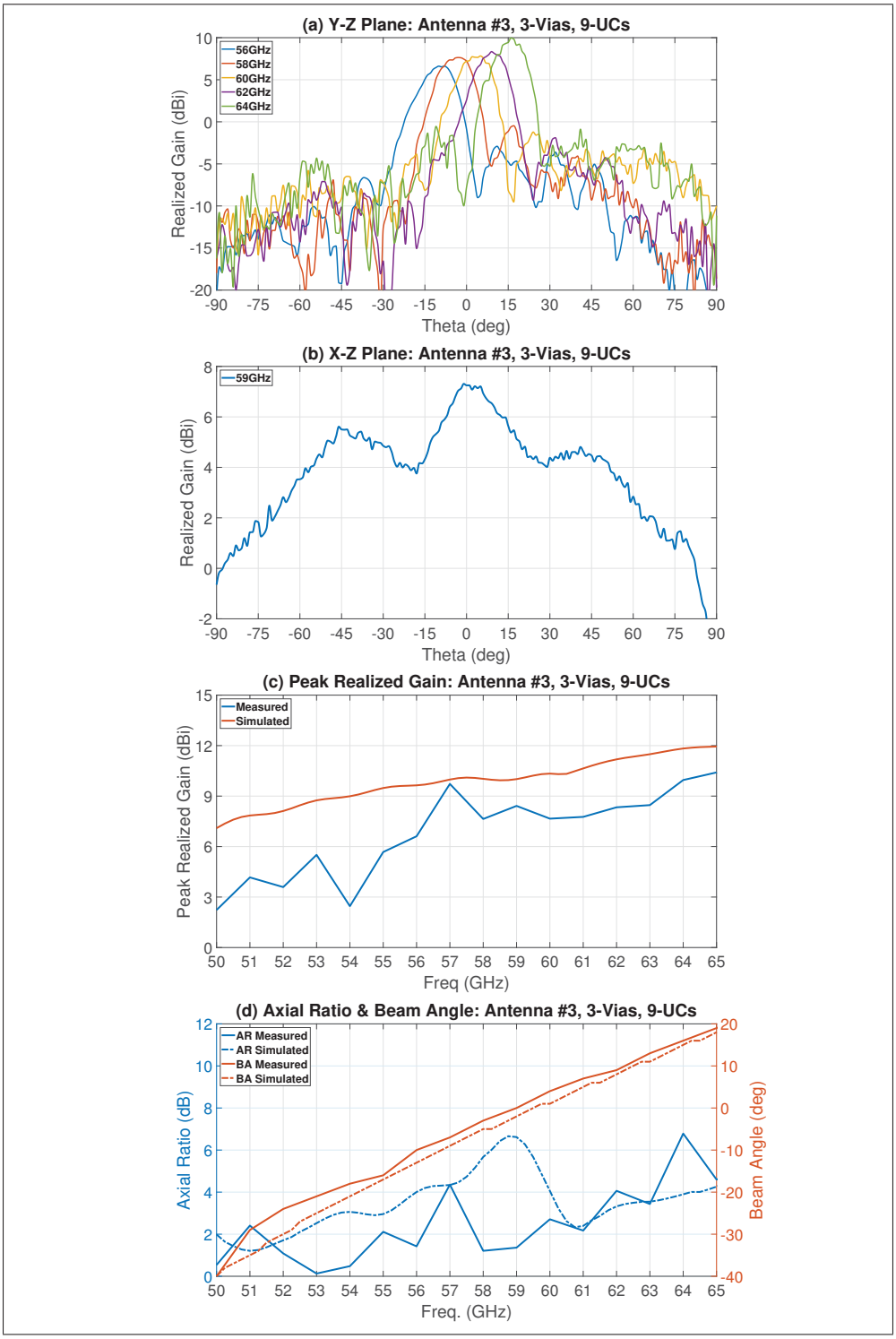

Figure 5.9 Radiation Pattern of antenna #3 with 3-vias and 9-UCs.

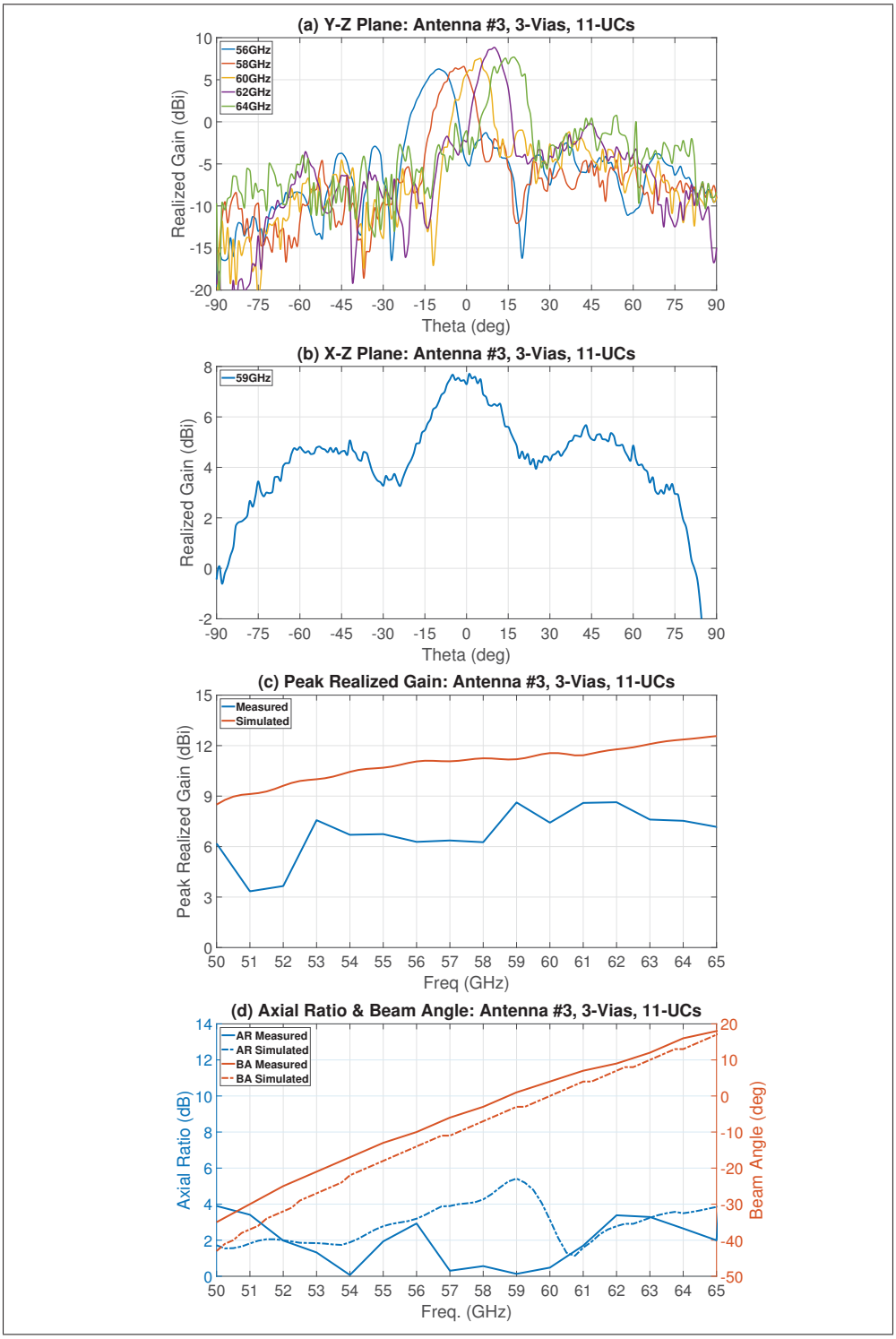

Figure 5.10 Radiation Pattern of antenna #3 with 3-vias and 11-UCs.

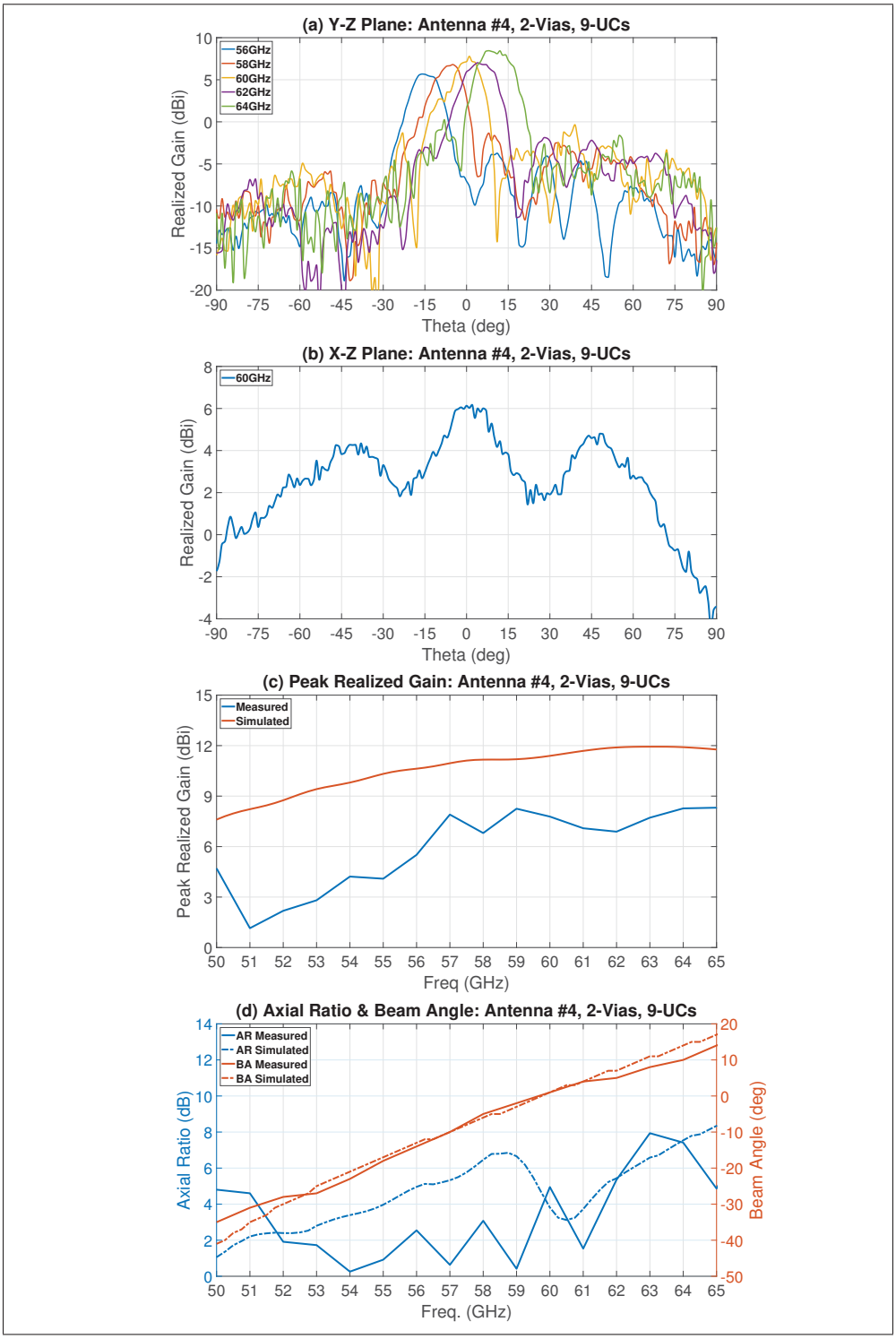

Figure 5.11 Radiation Pattern of antenna #4 with 2-vias and 9-UCs.

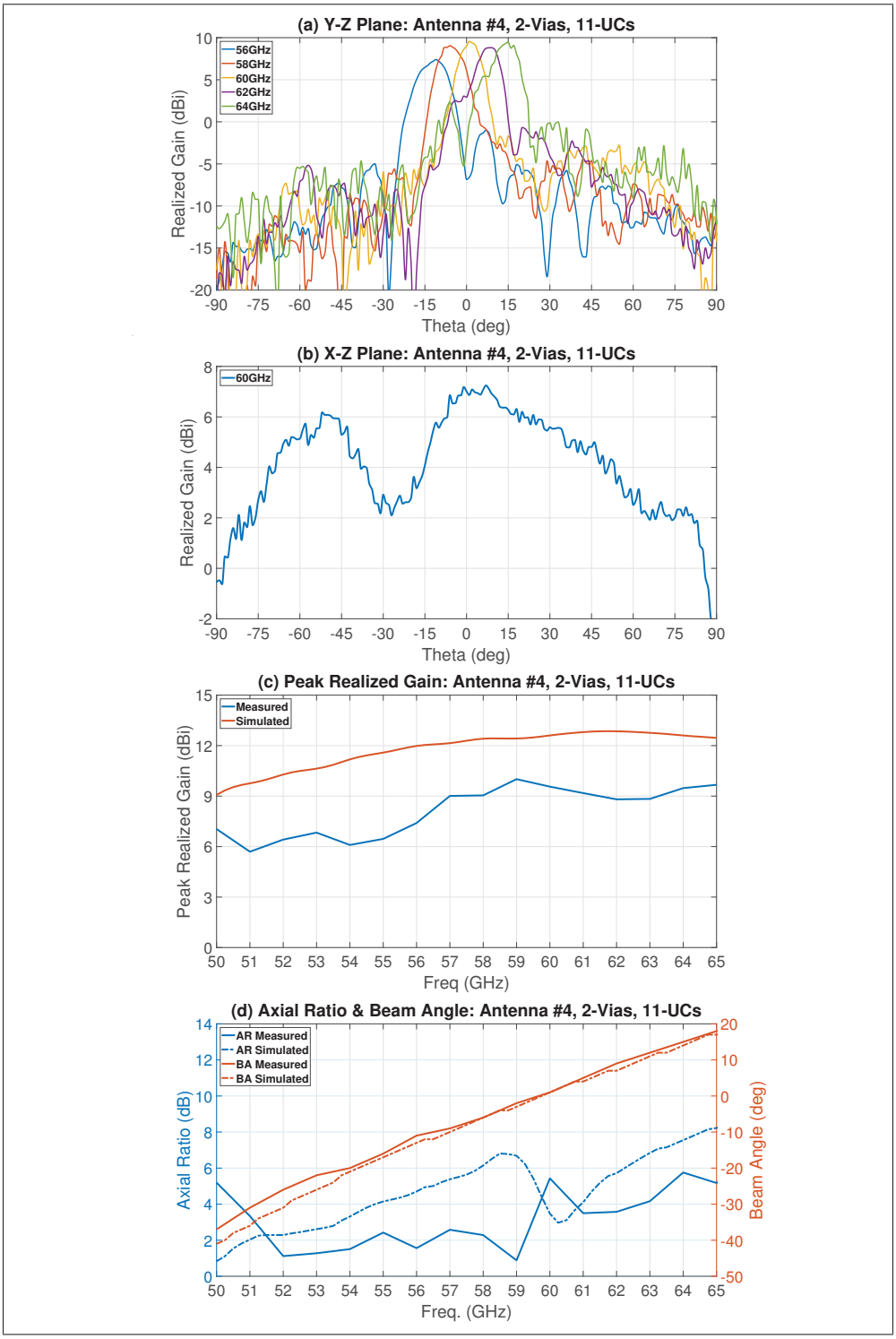

Figure 5.12 Radiation Pattern of antenna #4 with 2-vias and 11-UCs.

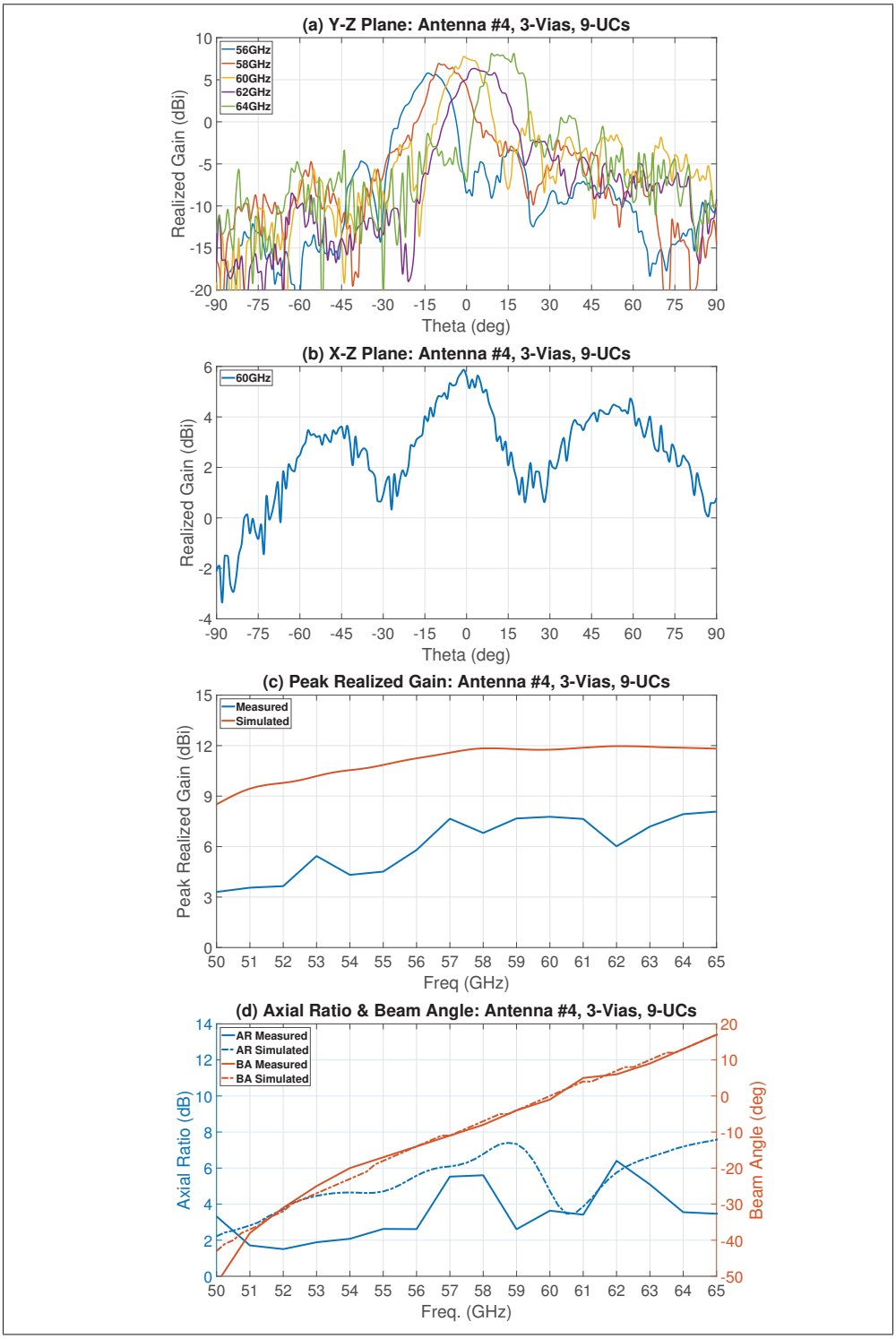

Figure 5.13 Radiation Pattern of antenna #4 with 3-vias and 9-UCs.

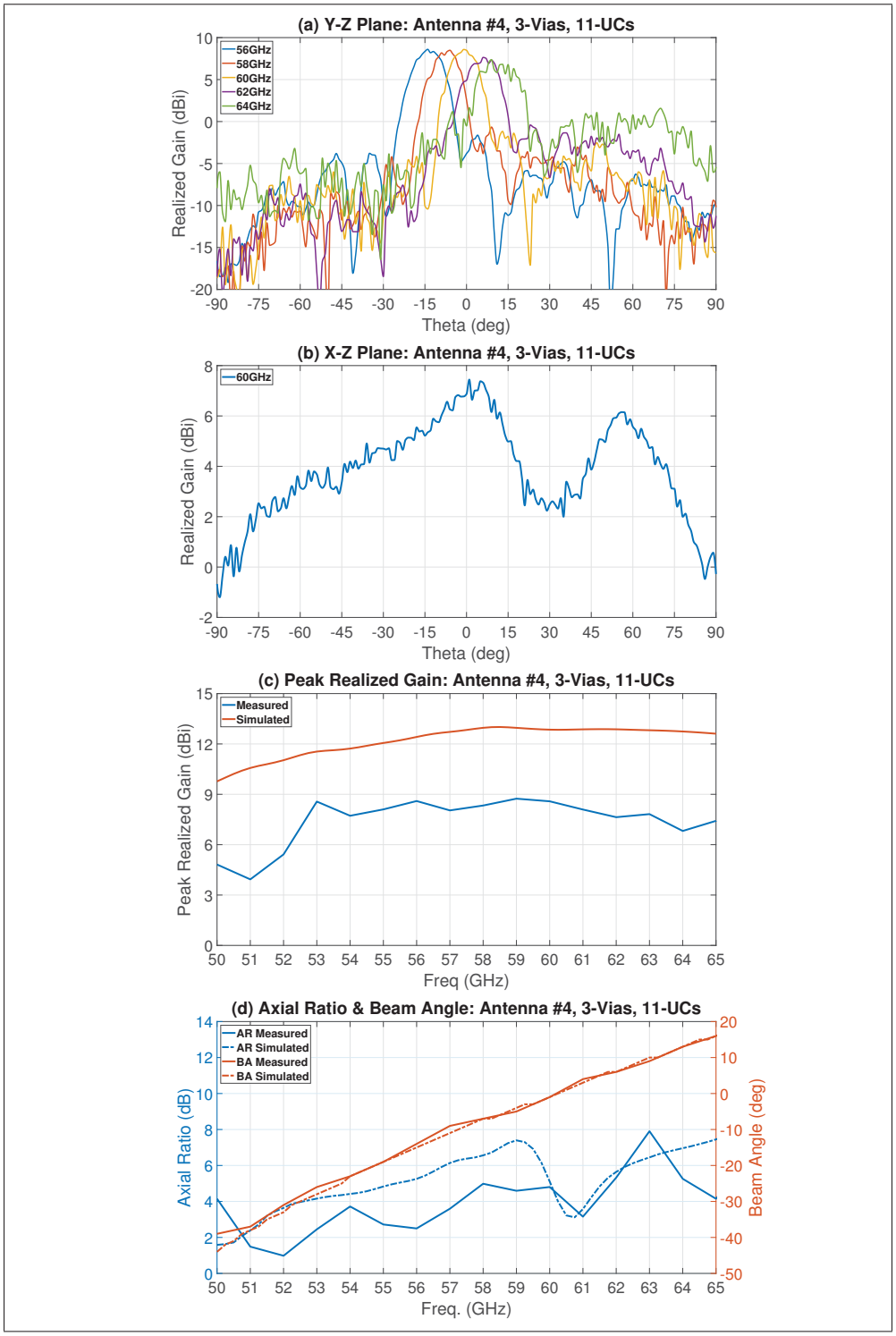

Figure 5.14 Radiation Pattern of antenna #4 with 3-vias and 11-UCs.

5.4 Conclusion

In this chapter, we introduced the setup for the S-Parameter measurement by a Vector Network Analyzer using two 150 µm pitch GSG Probe and the setup for the radiation pattern measurement in an anechoic chamber using the 1.85 mm V-Connector. Then, the result of S-Parameter measured at the LACIME LTCC Lab (LTCC@ÉTS, 2020) were presented for 8 prototypes of the first fabrication batch and 16 prototypes of the second batch. The results were compared with the simulation results which there was a good agreement between them. All the antenna's prototypes showed a wideband matching over the measured frequency band. The insertion loss should be improved a little by increasing the length of the antenna using more unit-cells.

The radiation pattern for six prototypes of the antenna, that were fabricated with V-Connector in the second fabrication batch, were illustrated on the Y-Z plane plus the broadside radiation on the X-Z plane. The pattern on the Y-Z plane clearly demonstrated the beam steering ability of the proposed periodic LWA with the frequency. The peak realized gain, the axial ratio and the main beam angle were calculated and plotted over the frequency band for the maximum radiation on the Y-Z plane, which is the direction of the wave propagation. The comparison to the result of the simulation were made for these features. The efficiency cannot be estimated because we didn't measure the pattern over the entire radiation sphere. Looking at the presented radiation pattern plots, all of the performance parameters are premising as expected.

Table 5.1 summarizes the measured radiation pattern of these six prototypes. We can compare the performance of two antennas (Antenna #3 and Antenna #4) with different configurations using this table. However, we should consider that some differences between the results are duo to the quality of the fabrication, not the design parameters. It is noticeable that the scanning angle over our desired frequency band (57GHz to 64GHz) are limited right now. But, it can be improved using a substrate with higher value of the dielectric constant. The average gain, even with the 9-UCs antenna, seems enough for our WiGig application which needs a very short distance communication. The axial ratio is actually better than the simulation results. This will support an effective circular polarization in the telecommunication.

Table 5.1 Summary of measured antenna's performance.

Sample	**Scanning Angle on 50GHz 67GHz**	**Scanning Angle on 57GHz 64GHz**	**Average Gain on 50GHz 67GHz**	**Average Gain on 57GHz 64GHz**	**Average AR on 50GHz 67GHz**	**Average AR on 57GHz 64GHz**
ANT3 3-vias 9-UCs	$-40°$ $+26°$	$-7°$ $+16°$	7.56 *dBi*	8.49 *dBi*	2.57 *dB*	3.26 *dB*
ANT3 3-vias 11-UCs	$-35°$ $+26°$	$-6°$ $+16°$	7.41 *dBi*	7.63 *dBi*	3.68 *dB*	1.56 *dB*
ANT4 2-vias 9-UCs	$-35°$ $+21°$	$-10°$ $+10°$	6.68 *dBi*	7.59 *dBi*	3.63 *dB*	3.91 *dB*
ANT4 2-vias 11-UCs	$-37°$ $+25°$	$-9°$ $+15°$	8.72 *dBi*	9.24 *dBi*	3.29 *dB*	3.52 *dB*
ANT4 3-vias 9-UCs	$-52°$ $+22°$	$-11°$ $+13°$	6.86 *dBi*	7.33 *dBi*	3.64 *dB*	4.48 *dB*
ANT4 3-vias 11-UCs	$-39°$ $+23°$	$-9°$ $+13°$	8.11 *dBi*	8.01 *dBi*	4.08 *dB*	4.95 *dB*

CONCLUSION AND RECOMMENDATIONS

6.1 Main contributions of this research project

Recently, demand for the applications on the 5G unlicensed 60GHz band is increasing because of its wide range of bandwidth. This becomes a perfect solution for future fast data steaming in short range telecommunications at homes and small offices. However, due to high values of the attenuation in these frequencies, the communications would be challenging. To overcome these limitations, the antennas that are designed for these applications usually able to provide high radiation gain levels with high impedance bandwidth. Moreover, they must be extremely efficient structures with reduced Side Lobe Level (SLL) that support the circular polarization, which is a necessary part for a Wireless Personal Area Network (WPAN) communication.

In this research project, we introduced an efficient periodic LWA structure with a high directive, reconfigurable radiation pattern in two directions (2-D beam steering). This antenna has a very simple and small-footprint structure, designed for the LTCC technology, which makes it easy to fabricate for the mm-Wave AiP applications and allows the budget-efficient repeatability of the mass production for a commercially suitable product. Moreover, it supports the circular polarization. Here, we presented an empirical model for the proposed antenna, the design and optimization process, the fabrication's challenges on the LTCC substrate and the considerations for the measurements. The main features of the proposed periodic LWA structure are:

- It is a low-profile and low-cost periodic LWA structure fabricated on the Dupont 9K7 LTCC substrate that makes it an ideal candidate for the AiP applications at mm-Wave frequencies.
- It has a really simple structure compared to similar designs, which reduces the complexity of the fabrication and increases the similarity of the designed and fabricated product's features.
- A 2-D scanning antenna system that can be implemented in multi-layer configuration.

- Only passive components are used in a microstrip structure to minimize the cost and size of total system and make it ready for easy integration in a package.
- The center frequency of the proposed periodic LWA is set to 60GHz. This antenna specially designed, optimized and tested for the WiGig application band (57GHz to 64GHz).
- It has an ultra-wide fractional impedance bandwidth of 48.3%. The matching bandwidth of the antenna based on the simulation is 29GHz from 43GHz to 72GHz. In the measurements over the frequency range of 50GHz to 67GHz, the antenna showed a good matching as well.
- The average total radiation gain and average peak realized gain of the antenna according to the simulation over the frequency range of 50GHz to 70GHz are 12.37 dBi and 11.25 dBi respectively. The average peak realized gain measured from 50GHz to 67GHz for the same fabricated antenna is 7.56 dBi. This value can reach up to 20 dBi for the whole structure containing a phased-array of five antennas.
- The efficiency is very high and almost constant over the desired frequencies. The average efficiency of the proposed antenna simulated from 50GHz to 70GHz is 87.42 %.
- The antenna has the beam steering ability with the input frequency on the Y-Z plane. The beam scanning angle on this plane simulated for frequencies of 50GHz to 70GHz is $-43°$ to $+34°$. The measured scanning angle for frequencies of 50GHz to 67GHz is $-40°$ to $+26°$.
- A phased-array of antennas fed by a Rotman lens has the beam steering ability with the input port on the X-Z plane which can be designed for any desired beam angle. Our proposed structure designed for the beam scanning angle of $-31°$ to $+28°$ on the X-Z plane.
- The antenna supports the circular polarization as an essential requirement for a WPAN device. Although, the average simulated Axial Ratio from 50GHz to 70GHz is 5.81 dB, but the average measured Axial Ratio is 2.57 dB from 50GHz to 67GHz.

- Side Lobe Level (SLL) for the simulation and the measurement is less than -10dB.
- The proposed structure showed a consistent flexibility toward the fabrication's inaccuracies which challenges the repeatability of the results at the high frequencies. Despite all the flaws in the structure due to bad fabrication, it still displayed an acceptable performance.
- There is no need for a separate interconnection network between the antenna and the active radio chip. They could be integrated easily is a single package.

6.2 Recommendations and Future Works

6.2.1 Third fabrication

The first step of the future works is to fabricate the whole structure containing a phased-array of the antenna with a Rotman lens that we presented in the chapter 3 and measure the radiation pattern over the entire radiation sphere to verify the scanning feature of the structure in two directions. All fabrication design files are already prepared and ready to prove the concept.

6.2.2 Improve the design features of the proposed antenna

There rooms for improvement of the current proposed structure. For example, better axial ratio values can be achieved to have an enhanced circular polarization over desired frequency band; or the insertion loss could be raised up to 10dB by increasing the attenuation level. Using more advanced optimization and new trade-off, we can design an antenna with improved features.

6.2.3 Improve the fabrication process

We should find the optimum procedure for the fabrication on the desired LTCC substrate. When we succeed to improve the repeatability of the fabrication, we will have a better quality structure, lower costs, faster process and a product with enhanced features.

6.2.4 Increase the scanning angle

Right now, the beam scanning angle of the proposed LWA is about 24° (from $-11°$ to $+13°$ for the antenna presented in table 3.6) over the application bandwidth of 57GHz to 64GHz. This beam scanning angle is not enough for covering the whole hemisphere. We suggest to increase this scanning angle at least to 90° for better coverage, considering the Half Power (HP) beam width (HP for the the antenna presented in table 3.6 with 9-UCs is about 30°).

To increase the beam scanning angle, we have to increase the slope of phase constant β versus the input frequency. This would be possible with the higher values of the dielectric constant. However, special care must be taken to keep only one space harmonic element (β_{-1}) in the radiation region. Refer to the chapter 2 for more details about the space harmonics.

6.2.5 Aperture coupling and multi-layer design

Like the structure presented in Rahmani (2017), we can work on a multi-layer design to make the footprint even smaller. In this way, it would be a better fit for the mmWave SiP applications. Figure 6.1 illustrates this structure containing a Rotman lens on the bottom layer and a phased-array of the antennas on the top layer. The wave propagates from bottom to top layer through an aperture coupling with an embedded band-pass filter. The dedicated band-pass filter allows the rejection of undesired signals and reduces the complexity of the transceiver circuit.

6.2.6 Antenna integration with the transceiver in a package

The final objective of this research project is to have a low-profile structure which can be integrated with its transceiver chip in a single package. If we are able to design a small multi-layer structure based on the microstrip LTCC substrate, they can be packaged with no separate interconnection network between the antenna and the active radio chip. Moreover, it is possible to embed the band-pass filter through the aperture coupling in the multi-layer structure.

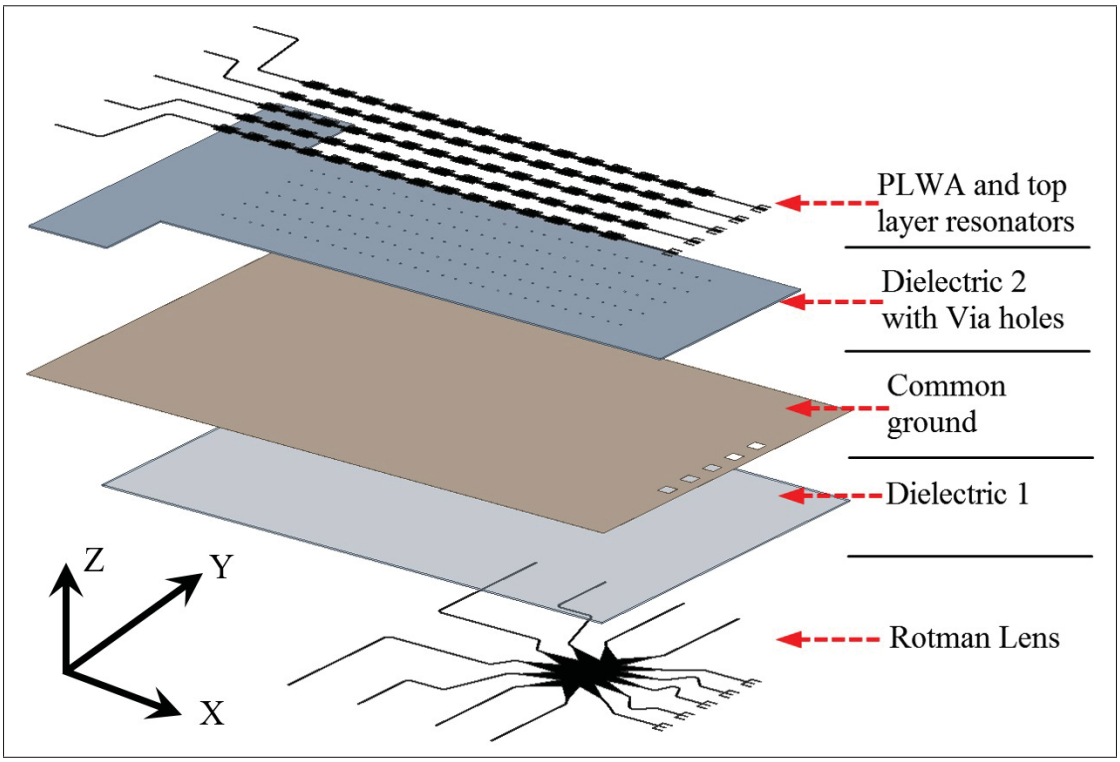

Figure 6.1 Multi-layer design structure Taken from Rahmani (2017).

6.2.7 Ring Structure

The complete proposed antenna structure has the ability of beam scanning in two directions using two control variables: the input frequency and the excited port. The half power (HP) beam width is almost constant on every direction and we don't have control on it. But, some applications may need a changeable directivity such as a pencil beam pattern.

In figure 6.2, we proposed another structure which has the same 2-D scanning feature without a Rotman lens or a phased-array, plus the ability to change the main beam directivity. It has a smaller footprint than the proposed structure because it does not need an array of antenna. In addition to the input frequency and the excited port, it takes advantage of the phase shift on the exited ports to control the directivity of main beam. As we can see in the figure 6.2, The excitation is performed by some microstrip transmission lines through the aperture coupling.

It should be mentioned that the feeding network of this structure will be more complicated than the original proposed structure. A lot of feeding configurations for this structure are possible. Here, we present the structure with 18-UCs and 6 excitation ports. It is possible to excite only one port or multiple ports with phase shift. The simulation results that we have for this structure are primitive but still very promising. More investigations are needed to reach a robust design.

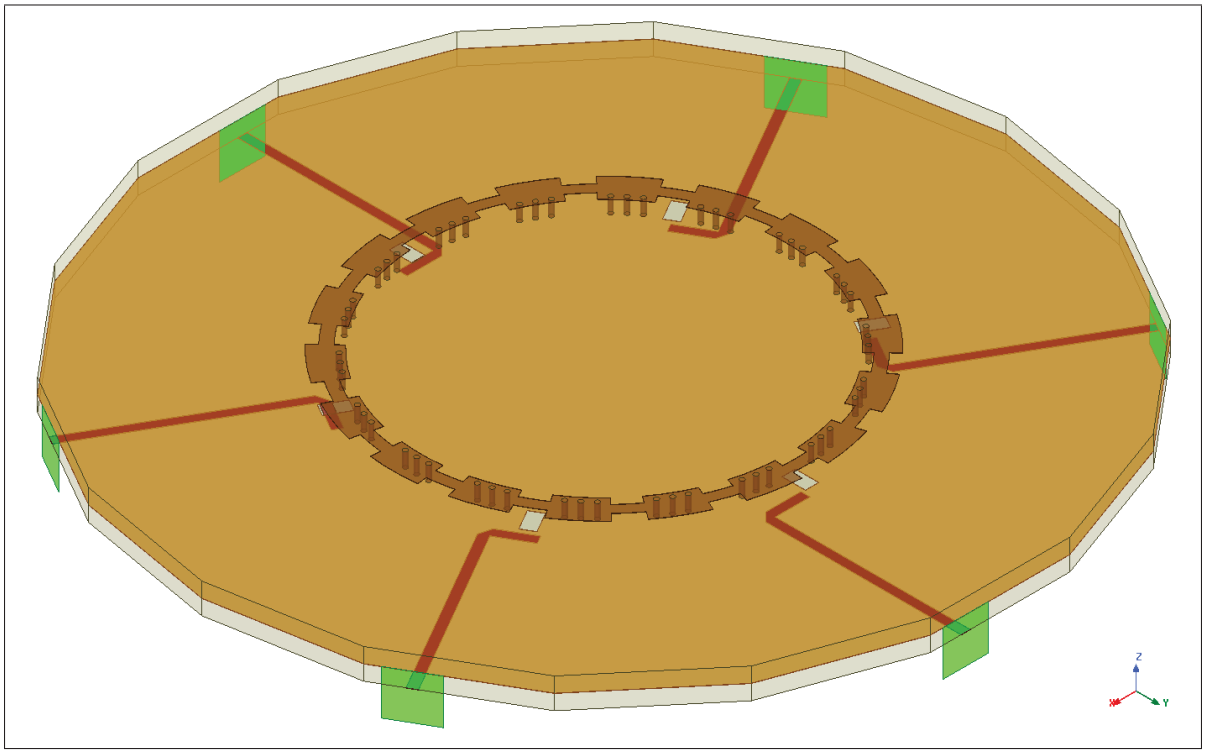

Figure 6.2 Proposed ring design structure with 6 feed lines.

BIBLIOGRAPHY

Aboufoul, T., Parini, C., Chen, X. & Alomainy, A. (2013). Pattern-Reconfigurable Planar Circular Ultra-Wideband Monopole Antenna. *IEEE Transactions on Antennas and Propagation*, 61(10), 4973-4980. doi: 10.1109/TAP.2013.2274262.

Aboufoul, T., Chen, X., Parini, C. G. & Alomainy, A. (2014). Multiple-parameter reconfiguration in a single planar ultra-wideband antenna for advanced wireless communication systems. *IET Microwaves, Antennas and Propagation*, 8(11), 849–857. doi: 10.1049/iet-map.2013.0690.

Al-Alem, Y. & Kishk, A. A. (2019). Wideband Millimeter-Wave Dielectric Resonator Antenna. *2019 IEEE International Symposium on Antennas and Propagation and USNC-URSI Radio Science Meeting*, pp. 653-654. doi: 10.1109/APUSNCURSINRSM.2019.8888809.

Alexeff, I., Anderson, T., Parameswaran, S., Pradeep, E., Hulloli, J. & Hulloli, P. (2006). Experimental and theoretical results with plasma antennas. *IEEE Transactions on Plasma Science*, 34(2), 166-172. doi: 10.1109/TPS.2006.872180.

Ansoft, H. (2020). ANSYS® Electromagnetics Suite (Version 2020-R1). Southpointe, 2600 ANSYS Drive, Canonsburg, PA 15317: ANSYS, Inc.

Attaran, A., Rashidzadeh, R. & Kouki, A. (2016). 60 GHz Low Phase Error Rotman Lens Combined With Wideband Microstrip Antenna Array Using LTCC Technology. *IEEE Transactions on Antennas and Propagation*, 64(12), 5172-5180. doi: 10.1109/TAP.2016.2618479.

Aziz, I., Öjefors, E., Dahlbäck, R., Rydberg, A., Engblom, G. & Dancila, D. (2019). Broadband Connected Slots Phased Array Feeding a High Gain Lens Antenna at 60 GHz. *2019 49th European Microwave Conference (EuMC)*, pp. 718-721. doi: 10.23919/EuMC.2019.8910856.

Bisharat, D. J., Liao, S. & Xue, Q. (2016). High Gain and Low Cost Differentially Fed Circularly Polarized Planar Aperture Antenna for Broadband Millimeter-Wave Applications. *IEEE Transactions on Antennas and Propagation*, 64(1), 33-42. doi: 10.1109/TAP.2015.2499750.

Borg, G. G., Harris, J. H., Miljak, D. G. & Martin, N. M. (1999). Application of plasma columns to radiofrequency antennas. *Applied Physics Letters*, 74(22), 3272-3274. doi: 10.1063/1.123317.

Butler, J. (1961). Beam-forming matrix simplifies design of electronically scanned antennas. *Electronic design*, 12, 170-173.

Caloz, C. & Itoh, T. (2004). Array factor approach of leaky-wave antennas and application to 1-D/2-D composite right/left-handed (CRLH) structures. *IEEE Microwave and Wireless Components Letters*, 14(6), 274-276.

Chiao, J.-C., Fu, Y., Chio, I. M., DeLisio, M. & Lin, L.-Y. (1999). MEMS reconfigurable Vee antenna. *1999 IEEE MTT-S International Microwave Symposium Digest (Cat. No.99CH36282)*, 4, 1515-1518 vol.4. doi: 10.1109/MWSYM.1999.780242.

Collin, R. E. & Zucker, F. J. (1969). *Antenna Theory* (ed. 2). New York: McGraw-Hill.

Deslandes, D. & Ke Wu. (2006). Accurate modeling, wave mechanisms, and design considerations of a substrate integrated waveguide. *IEEE Transactions on Microwave Theory and Techniques*, 54(6), 2516-2526.

Deslandes, D. & Wu, K. (2001). Integrated microstrip and rectangular waveguide in planar form. *IEEE Microwave and Wireless Components Letters*, 11(2), 68-70.

Ding, C., Guo, Y. J., Qin, P., Bird, T. S. & Yang, Y. (2014). A Defected Microstrip Structure (DMS)-Based Phase Shifter and Its Application to Beamforming Antennas. *IEEE Transactions on Antennas and Propagation*, 62(2), 641-651. doi: 10.1109/TAP.2013.2290802.

Dubal, S. & Chaudhari, A. (2020). Mechanisms of Reconfigurable Antenna: A Review. *2020 10th International Conference on Cloud Computing, Data Science Engineering (Confluence)*, pp. 576-580. doi: 10.1109/Confluence47617.2020.9057998.

Emami, M., Rahmani, M. H. & Deslandes, D. (2018, Sep.). A LTCC ultra-wideband periodic leaky-wave antenna with wide scanning range at 60 GHz. *2018 IEEE-APS Topical Conference on Antennas and Propagation in Wireless Communications (APWC)*, pp. 916-919. doi: 10.1109/APWC.2018.8503672.

Erdil, E., Topalli, K., Unlu, M., Civi, O. A. & Akin, T. (2007). Frequency Tunable Microstrip Patch Antenna Using RF MEMS Technology. *IEEE Transactions on Antennas and Propagation*, 55(4), 1193-1196. doi: 10.1109/TAP.2007.893426.

Gardner, D. W. (1987). *A Closed-form Model for Radial-line Stub Elements in Microstrip Circuits*. University of Colorado at Colorado Springs. Consulted at https://books.google.ca/books?id=B6UmOAAACAAJ.

Gardner, D. W. & Wickert, M. A. (1988). Microwave filter design using radial line stubs. *IEEE Region 5 Conference, 1988: 'Spanning the Peaks of Electrotechnology'*, pp. 68-72.

Gaynor, M. P. (2006). *System-in-package RF Design and Applications*. Artech House.

Gomez-Tornero, J. L., Martinez, A. T., Rebenaque, D. C., Gugliemi, M. & Alvarez-Melcon, A. (2005). Design of tapered leaky-wave antennas in hybrid waveguide-planar technology for millimeter waveband applications. *IEEE Transactions on Antennas and Propagation*, 53(8), 2563-2577.

Grzyb, J., Liu, D. & Gaucher, B. (2007). Packaging effects of a broadband 60 GHz cavity-backed folded dipole superstrate antenna. *2007 IEEE Antennas and Propagation Society International Symposium*, pp. 4365-4368. doi: 10.1109/APS.2007.4396509.

Gulati, N. & Dandekar, K. R. (2014). Learning State Selection for Reconfigurable Antennas: A Multi-Armed Bandit Approach. *IEEE Transactions on Antennas and Propagation*, 62(3), 1027-1038. doi: 10.1109/TAP.2013.2276414.

GUO, Q.-Y. & WONG, H. (2019). A Fabry-Pérot Cavity Antenna for Millimeter-Wave Application. *2019 Cross Strait Quad-Regional Radio Science and Wireless Technology Conference (CSQRWC)*, pp. 1-2. doi: 10.1109/CSQRWC.2019.8799287.

Hammou, D., Djerafi, T., Nedil, M. & Tatu, S. O. (2016). Considerations for On-Wafer Millimeter-Wave Measurements on Thin Ceramic Substrate. *IEEE Transactions on Instrumentation and Measurement*, 65(2), 441-447.

Hansen, C. J. (2011). WiGiG: Multi-gigabit wireless communications in the 60 GHz band. *IEEE Wireless Communications*, 18(6), 6-7. doi: 10.1109/MWC.2011.6108325.

Hansen, R. C. (1991). Design trades for Rotman lenses. *IEEE Transactions on Antennas and Propagation*, 39(4), 464-472.

Hansen, R. C. (2009). Phased Array Antennas: Second Edition. *Phased Array Antennas: Second Edition*, 1-547. doi: 10.1002/9780470529188.

Harrington, R. (1978). Reactively controlled directive arrays. *IEEE Transactions on Antennas and Propagation*, 26(3), 390-395. doi: 10.1109/TAP.1978.1141852.

Henry, R. & Okoniewski, M. (2016). A Broadside Scanning Substrate Integrated Waveguide Periodic Phase-Reversal Leaky-Wave Antenna. *IEEE Antennas and Wireless Propagation Letters*, 15, 602-605. doi: 10.1109/LAWP.2015.2462733.

Hong, W., Goudelev, A., Baek, K.-h., Arkhipenkov, V. & Lee, J. (2011). 24-Element Antenna-in-Package for Stationary 60-GHz Communication Scenarios. *IEEE Antennas and Wireless Propagation Letters*, 10, 738-741. doi: 10.1109/LAWP.2011.2162640.

Hong, W., Baek, K.-h. & Goudelev, A. (2013). Grid Assembly-Free 60-GHz Antenna Module Embedded in FR-4 Transceiver Carrier Board. *IEEE Transactions on Antennas and Propagation*, 61(4), 1573-1580. doi: 10.1109/TAP.2012.2232635.

Huff, G. & Bernhard, J. (2008). Reconfigurable Antennas. In Balanis, C. A. (Ed.), *Modern Antenna Handbook* (ch. 8, pp. 369-398). Wiley.

Hum, S. V. & Perruisseau-Carrier, J. (2014). Reconfigurable Reflectarrays and Array Lenses for Dynamic Antenna Beam Control: A Review. *IEEE Transactions on Antennas and Propagation*, 62(1), 183-198. doi: 10.1109/TAP.2013.2287296.

Huynh, M. C. & Stutzman, W. (2003). Ground plane effects on planar inverted-F antenna (PIFA) performance. *IEE Proceedings - Microwaves, Antennas and Propagation*, 150(4), 209-213.

Ibrahim, M. S. (2019). Low-Cost, Circularly Polarized, and Wideband U-Slot Microstrip Patch Antenna with Parasitic Elements for WiGig and WPAN Applications. *2019 13th European Conference on Antennas and Propagation (EuCAP)*, pp. 1-4.

Itoh, T. (1989). *Numerical techniques for microwave and millimeter-wave passive structures*. Hoboken, NJ, USA: Wiley.

Jackson, D. R. & Oliner, A. A. (2008). Leaky-Wave Antennas. In Balanis, C. A. (Ed.), *Modern Antenna Handbook* (ch. 7, pp. 325-367). Wiley.

Jackson, D. R., Caloz, C. & Itoh, T. (2012). Leaky-Wave Antennas. *Proceedings of the IEEE*, 100(7), 2194-2206. doi: 10.1109/JPROC.2012.2187410.

Kai Chang, Ming-yi Li, Tae-Yeoul Yun & Rodenbeck, C. T. (2002). Novel low-cost beam-steering techniques. *IEEE Transactions on Antennas and Propagation*, 50(5), 618-627. doi: 10.1109/TAP.2002.1011227.

Kam, D. G., Liu, D., Natarajan, A., Reynolds, S., Chen, H.-C. & Floyd, B. A. (2011). LTCC Packages With Embedded Phased-Array Antennas for 60 GHz Communications. *IEEE Microwave and Wireless Components Letters*, 21(3), 142-144. doi: 10.1109/LMWC.2010.2103932.

Keysight. [VNA]. (2019). N5247A PNA-X Microwave Network Analyzer, 67 GHz [Datasheet]. Consulted at https://www.keysight.com/en/pdx-x201825-pn-N5247A/pna-x-microwave-network-analyzer-67-ghz/.

Keysight. (2020). Advanced Design System (ADS) (Version 2020-Update 2). Santa Rosa, California, United States: Keysight Technologies Inc.

Kim, H. Y., Lee, J. H., Song, I. S. & Park, C. S. (2014). Compact LTCC Yagi-Uda type end-fire antenna-in-package for 60 GHz wireless communications. *2014 IEEE MTT-S International Microwave Symposium (IMS2014)*, pp. 1-3. doi: 10.1109/MWSYM.2014.6848628.

Kumar, R. & Bora, D. (2010). A reconfigurable plasma antenna. *Journal of Applied Physics*, 107(5), 053303. doi: 10.1063/1.3318495.

Lei Liu, Caloz, C. & Itoh, T. (2002). Dominant mode leaky-wave antenna with backfire-to-endfire scanning capability. *Electronics Letters*, 38(23), 1414-1416.

Li, J., Matos, C. & Ghalichechian, N. (2021). A Low-Cost Vertically Integrated Antenna Array at 60 GHz With 85% Efficiency. *IEEE Antennas and Wireless Propagation Letters*, 20(4), 513-517. doi: 10.1109/LAWP.2021.3055726.

Liao, S. & Xue, Q. (2017). Dual Polarized Planar Aperture Antenna on LTCC for 60-GHz Antenna-in-Package Applications. *IEEE Transactions on Antennas and Propagation*, 65(1), 63-70. doi: 10.1109/TAP.2016.2630723.

Liao, S., Wu, P., Shum, K. M. & Xue, Q. (2015). Differentially Fed Planar Aperture Antenna With High Gain and Wide Bandwidth for Millimeter-Wave Application. *IEEE Transactions on Antennas and Propagation*, 63(3), 966-977. doi: 10.1109/TAP.2015.2389256.

Liu, C., Guo, Y.-X., Bao, X. & Xiao, S.-Q. (2012). 60-GHz LTCC Integrated Circularly Polarized Helical Antenna Array. *IEEE Transactions on Antennas and Propagation*, 60(3), 1329-1335. doi: 10.1109/TAP.2011.2180351.

Liu, D., Akkermans, J. A. G., Chen, H.-C. & Floyd, B. (2011). Packages With Integrated 60-GHz Aperture-Coupled Patch Antennas. *IEEE Transactions on Antennas and Propagation*, 59(10), 3607-3616. doi: 10.1109/TAP.2011.2163760.

Liu, L. & Langley, R. (2008). Liquid crystal tunable microstrip patch antenna. *Electronics Letters*, 44, 1179 - 1180. doi: 10.1049/el:20081995.

LTCC@ÉTS. [LaCIME]. (2020). Process and Capabilitiess [PDF]. Consulted at https://www.etsmtl.ca/Unites-de-recherche/LTCC/Services-offerts/processV2.pdf.

Mailloux, R. (1994). *Phased Array Antenna Handbook*. Boston, MA, USA: Artech House.

Mookiah, P. & Dandekar, K. R. (2009). Metamaterial-Substrate Antenna Array for MIMO Communication System. *IEEE Transactions on Antennas and Propagation*, 57(10), 3283-3292. doi: 10.1109/TAP.2009.2028638.

Moulder, W. F., Khalil, W. & Volakis, J. L. (2010). 60-GHz Two-Dimensionally Scanning Array Employing Wideband Planar Switched Beam Network. *IEEE Antennas and Wireless Propagation Letters*, 9, 818-821. doi: 10.1109/LAWP.2010.2070056.

Murano, K., Watanabe, I., Kasamatsu, A., Suzuki, S., Asada, M., Withayachumnankul, W., Tanaka, T. & Monnai, Y. (2017). Low-Profile Terahertz Radar Based on Broadband Leaky-Wave Beam Steering. *IEEE Transactions on Terahertz Science and Technology*, 7(1), 60-69. doi: 10.1109/TTHZ.2016.2624514.

Nikfalazar, M., Sazegar, M., Mehmood, A., Wiens, A., Friederich, A., Maune, H., Binder, J. R. & Jakoby, R. (2017). Two-Dimensional Beam-Steering Phased-Array Antenna With Compact Tunable Phase Shifter Based on BST Thick Films. *IEEE Antennas and Wireless Propagation Letters*, 16, 585-588. doi: 10.1109/LAWP.2016.2591078.

Oliner, A. & Lee, K. (1986). Microstrip leaky wave strip antennas. *1986 Antennas and Propagation Society International Symposium*, 24, 443-446.

Otto, S., Chen, Z., Al-Bassam, A., Rennings, A., Solbach, K. & Caloz, C. (2014). Circular Polarization of Periodic Leaky-Wave Antennas With Axial Asymmetry: Theoretical Proof and Experimental Demonstration. *IEEE Transactions on Antennas and Propagation*, 62(4), 1817-1829. doi: 10.1109/TAP.2013.2297169.

Panagamuwa, C., Chauraya, A. & Vardaxoglou, J. (2006). Frequency and beam reconfigurable antenna using photoconducting switches. *IEEE Transactions on Antennas and Propagation*, 54(2), 449-454. doi: 10.1109/TAP.2005.863393.

Paulotto, S., Baccarelli, P., Frezza, F. & Jackson, D. R. (2009). A Novel Technique for Open-Stopband Suppression in 1-D Periodic Printed Leaky-Wave Antennas. *IEEE Transactions on Antennas and Propagation*, 57(7), 1894-1906.

Pozar, D. M. (2011). *Microwave engineering* (ed. 4). Wiley.

Pringle, L., Harms, P., Blalock, S., Kiesel, G., Kuster, E., Friederich, P., Prado, R., Morris, J. & Smith, G. (2004). A reconfigurable aperture antenna based on switched links between electrically small metallic patches. *IEEE Transactions on Antennas and Propagation*, 52(6), 1434-1445. doi: 10.1109/TAP.2004.825648.

Rafiei, V., Karamzadeh, S. & Saygin, H. (2018). Millimeter-Wave High-Gain Circularly polarized SIW End-Fire Bow-tie Antenna by utilizing Semi Planar Helix Unit Cell. *Electronics Letters*, 54(7), 411–412. doi: 10.1049/el.2018.0022.

Rahmani, M. H. (2017). *Study, design and fabrication of a two-dimension beam scanning antenna in package*. (Ph.D. thesis, École de technologie supérieure).

Rahmani, M. H. & Deslandes, D. (2017). Backward to Forward Scanning Periodic Leaky-Wave Antenna With Wide Scanning Range. *IEEE Transactions on Antennas and Propagation*, 65(7), 3326-3335. doi: 10.1109/TAP.2017.2705021.

Reddy Kota, M., Abejide, A. E., Pandey, S., Aboderin, O. & Teixeira, A. (2020). Silicon nitride 60 GHz antenna for IoT applications. *2020 12th International Symposium on Communication Systems, Networks and Digital Signal Processing (CSNDSP)*, pp. 1-5. doi: 10.1109/CSNDSP49049.2020.9249629.

Rodrigo, D., Jofre, L. & Cetiner, B. A. (2012). Circular Beam-Steering Reconfigurable Antenna With Liquid Metal Parasitics. *IEEE Transactions on Antennas and Propagation*, 60(4), 1796-1802. doi: 10.1109/TAP.2012.2186235.

Rodrigo, D., Cetiner, B. A. & Jofre, L. (2014). Frequency, Radiation Pattern and Polarization Reconfigurable Antenna Using a Parasitic Pixel Layer. *IEEE Transactions on Antennas and Propagation*, 62(6), 3422-3427. doi: 10.1109/TAP.2014.2314464.

Rotman, W. & Turner, R. (1963). Wide-angle microwave lens for line source applications. *IEEE Transactions on Antennas and Propagation*, 11(6), 623-632.

Shen, T.-M., Kao, T.-Y. J., Huang, T.-Y., Tu, J., Lin, J. & Wu, R.-B. (2012). Antenna Design of 60-GHz Micro-Radar System-In-Package for Noncontact Vital Sign Detection. *IEEE Antennas and Wireless Propagation Letters*, 11, 1702-1705. doi: 10.1109/LAWP.2013.2239957.

Simons, R., Chun, D. & Katehi, L. (2002). Polarization reconfigurable patch antenna using microelectromechanical systems (MEMS) actuators. *IEEE Antennas and Propagation Society International Symposium (IEEE Cat. No.02CH37313)*, 2, 6-9 vol.2. doi: 10.1109/APS.2002.1016015.

SouthwestMicrowave. [V-Connector]. (2018). End Launch 1.85mm (V) 67 GHz Jack (Female) Standard Block [Datasheet]. Consulted at https://mpd.southwestmicrowave.com/product/1892-03a-6-end-launch-1-85mm-v-67-ghz-jack-female-standard-block/.

Sturdivant, R. (2010). Fundamentals of Packaging at Microwave and Millimeter-Wave Frequencies. In Kuang, K., Kim, F. & Cahill, S. S. (Eds.), *RF and Microwave Microelectronics Packaging* (pp. 1–23). Boston, MA: Springer US. doi: 10.1007/978-1-4419-0984-8_1.

Stutzman, W. L. & Thiele, G. A. (2012). *Antenna Theory and Design* (ed. 3). Wiley.

Sun, H., Guo, Y.-X. & Wang, Z. (2013). 60-GHz Circularly Polarized U-Slot Patch Antenna Array on LTCC. *IEEE Transactions on Antennas and Propagation*, 61(1), 430-435. doi: 10.1109/TAP.2012.2214018.

Tekkouk, K., Hirokawa, J., Sauleau, R. & Ando, M. (2017). Wideband and Large Coverage Continuous Beam Steering Antenna in the 60-GHz Band. *IEEE Transactions on Antennas and Propagation*, 65(9), 4418-4426. doi: 10.1109/TAP.2017.2723663.

Townley, A., Swirhun, P., Titz, D., Bisognin, A., Gianesello, F., Pilard, R., Luxey, C. & Niknejad, A. M. (2017). A 94-GHz 4TX–4RX Phased-Array FMCW Radar Transceiver With Antenna-in-Package. *IEEE Journal of Solid-State Circuits*, 52(5), 1245-1259. doi: 10.1109/JSSC.2017.2675907.

Walter, C. H. (1965). *Traveling Wave Antennas*. New York: McGraw-Hill.

Wanchu Hong, Tai-Lee Chen, Chi-Yang Chang, Sheen, J. . & Yu-De Lin. (2003). Broadband tapered microstrip leaky-wave antenna. *IEEE Transactions on Antennas and Propagation*, 51(8), 1922-1928.

Weily, A. R. & Guo, Y. J. (2009). Circularly Polarized Ellipse-Loaded Circular Slot Array for Millimeter-Wave WPAN Applications. *IEEE Transactions on Antennas and Propagation*, 57(10), 2862-2870. doi: 10.1109/TAP.2009.2029305.

Williams, J. T., Baccarelli, P., Paulotto, S. & Jackson, D. R. (2013). 1-D Combline Leaky-Wave Antenna With the Open-Stopband Suppressed: Design Considerations and Comparisons With Measurements. *IEEE Transactions on Antennas and Propagation*, 61(9), 4484-4492. doi: 10.1109/TAP.2013.2271234.

Wu, K., Yao, Y., Cheng, X., Yu, J. & Chen, X. (2019). Design of High Efficiency Linearly Polarized 8 × 8 Millimeter-Wave Antenna Array. *2019 IEEE Asia-Pacific Microwave Conference (APMC)*, pp. 735-737. doi: 10.1109/APMC46564.2019.9038470.

Xia, H., Zhang, T., Li, L. & Zheng, F.-C. (2020). A 1 × 2 Taper Slot Antenna Array With Flip-Chip Interconnect via Glass-IPD Technology for 60 GHz Radar Sensors. *IEEE Access*, 8, 61790-61796. doi: 10.1109/ACCESS.2020.2983485.

Yang, N., Caloz, C. & Wu, K. (2010). Full-Space Scanning Periodic Phase-Reversal Leaky-Wave Antenna. *IEEE Transactions on Microwave Theory and Techniques*, 58(10), 2619-2632. doi: 10.1109/TMTT.2010.2065890.

Yang, X.-S., Wang, B.-Z., Wu, W. & Xiao, S. (2007). Yagi Patch Antenna With Dual-Band and Pattern Reconfigurable Characteristics. *IEEE Antennas and Wireless Propagation Letters*, 6, 168-171. doi: 10.1109/LAWP.2007.895292.

Yoshida, S., Suzuki, Y., Ta, T. T., Kameda, S., Suematsu, N., Takagi, T. & Tsubouchi, K. (2013). A 60-GHz Band Planar Dipole Array Antenna Using 3-D SiP Structure in Small Wireless Terminals for Beamforming Applications. *IEEE Transactions on Antennas and Propagation*, 61(7), 3502-3510. doi: 10.1109/TAP.2013.2257643.

Zhang, B., Titz, D., Ferrero, F., Luxey, C. & Zhang, Y. P. (2013). Integration of Quadruple Linearly-Polarized Microstrip Grid Array Antennas for 60-GHz Antenna-in-Package Applications. *IEEE Transactions on Components, Packaging and Manufacturing Technology*, 3(8), 1293-1300. doi: 10.1109/TCPMT.2013.2255333.

Zhang, Y. & Mao, J. (2019). An Overview of the Development of Antenna-in-Package Technology for Highly Integrated Wireless Devices. *Proceedings of the IEEE*, 107(11), 2265-2280.

Zhang, Y. P. & Liu, D. (2009). Antenna-on-Chip and Antenna-in-Package Solutions to Highly Integrated Millimeter-Wave Devices for Wireless Communications. *IEEE Transactions on Antennas and Propagation*, 57(10), 2830-2841.

Zhang, Y. P. & Liu, D. (2009). Antenna-on-Chip and Antenna-in-Package Solutions to Highly Integrated Millimeter-Wave Devices for Wireless Communications. *IEEE Transactions on Antennas and Propagation*, 57(10), 2830-2841. doi: 10.1109/TAP.2009.2029295.

Zhang, Y. P., Sun, M., Chua, K. M., Wai, L. L. & Liu, D. (2009). Antenna-in-Package Design for Wirebond Interconnection to Highly Integrated 60-GHz Radios. *IEEE Transactions on Antennas and Propagation*, 57(10), 2842-2852. doi: 10.1109/TAP.2009.2029290.

Zhang, Y. P., Sun, M., Liu, D. & Lu, Y. (2011). Dual Grid Array Antennas in a Thin-Profile Package for Flip-Chip Interconnection to Highly Integrated 60-GHz Radios. *IEEE Transactions on Antennas and Propagation*, 59(4), 1191-1199. doi: 10.1109/TAP.2011.2109358.

Zhang, Y., Sun, M., Chua, K., Wai, L. & Liu, D. (2008). Integration of slot antenna in LTCC package for 60 GHz radios. *Electronics Letters*, 44, 330 - 331. doi: 10.1049/el:20083352.

Zhu, J., Li, S., Liao, S., Yang, Y. & Zhu, H. (2018). 60 GHz Substrate-Integrated-Waveguide-Fed Patch Antenna Array With Quadri-Polarization. *IEEE Transactions on Antennas and Propagation*, 66(12), 7406-7411. doi: 10.1109/TAP.2018.2869255.

Zhu, J., Yang, Y., Li, S., Liao, S. & Xue, Q. (2019). Single-Ended-Fed High-Gain LTCC Planar Aperture Antenna for 60 GHz Antenna-in-Package Applications. *IEEE Transactions on Antennas and Propagation*, 67(8), 5154-5162. doi: 10.1109/TAP.2019.2917591.

Zwick, T., Liu, D. & Gaucher, B. (2006). Broadband Planar Superstrate Antenna for Integrated Millimeterwave Transceivers. *IEEE Transactions on Antennas and Propagation*, 54(10), 2790-2796. doi: 10.1109/TAP.2006.882167.